U.PORTO
FEUP FACULDADE DE ENGENHARIA
UNIVERSIDADE DO PORTO

Computational efficient generation of microstructures towards the design of advanced multi-scale heterogeneous materials

Professors:
Francisco Manuel Andrade Pires
Bernardo Proença Ferreira

Student:
José Luís Passos Vila-Chã

Thesis submitted under the scope of
the Master's degree in Mechanical Engineering

Porto, June 2020

Page intentionally left blank.

To my parents and my brother

Page intentionally left blank.

Abstract

Nowadays, the design and modeling of advanced materials calls for the understanding that these are hierarchical in nature, i.e. their macroscopic properties and mechanical response result from the interaction between heterogeneous structures spanning over multiple length scales. Examples of important materials from an industrial standpoint that benefit from this multi-scale approach are polymer blends and composite materials. In this view, the method of computational homogenization emerged as an effective way of modeling multi-scale heterogeneous materials by performing an homogenization procedure over a representative volume element (RVE) of the microstructure. However, in order to accurately capture the macroscopic behavior, it is crucial that the RVE contains enough morphological and topological information about the microstructural heterogeneities and is representative in an average sense.

This work presents a computational robust and efficient program in Python, based on a molecular dynamics simulation with a multi-temperature isokinetic scheme, that is able to generate an RVE from a given set of material and geometrical input descriptors. In general, these may characterize the material matrix, particles/inclusions, voids and fibers, e.g. radius, ellipsoid axes magnitude and orientation, spatial position, and the corresponding phase in the heterogeneous material, volume fraction and number of particles. The geometrical parameters characterizing the inclusions may be specified by the user as fixed values or be made to vary according to different statistical distributions. Multiple phases are also supported allowing for great flexibility in the modeling of real materials.

The microstructures generated are evaluated using the Minkowski structure metrics of their Voronoi cells. These are a very versatile tool in the detection of unwanted order or clustering, both undesirable properties in a microstructure whose purpose is to plausibly mimic real matrix-composite materials. Using this technique, the microstructures generated through the proposed approach are validated as it pertains to their "quality".

After the generation procedure, various RVEs are discretized in a suitable finite element mesh in order to perform microscale analyses through computational homogenization. The various examples considered are created keeping the volume fraction constant and increasing the number of inclusions within the RVE. Submitting the microstructures to various loading conditions and employing different boundary conditions, it is concluded that an increase in the number of particles included leads to a more representative volume element. Isotropic responses are also achieved for microstructures containing only Disks and Spheres, as more inclusions are considered.

Page intentionally left blank.

Resumo

Nos dias de hoje, o projeto e modelação de materiais avançados exige a perceção de que estes são compostos por estruturas hierárquicas, isto é, as suas propriedades macroscópicas e a sua resposta mecânica resultam da interação entre estruturas heterogéneas que se apresentam a múltiplas escalas. Materiais de grande importância a nível industrial que beneficiam deste tipo de análise a várias escalas são, por exemplos, as misturas de polímeros e os materiais compósitos. Nesta perspetiva, o método da homogeneização computacional surgiu como uma técnica eficaz de modelar materiais heterogéneos a múltiplas escalas, através de um procedimento de homogeneização ao longo de um elemento de volume representativo (RVE) da microestrutura. Todavia, de modo a capturar com precisão o seu comportamento macroscópico é crucial que o RVE contenha um conjunto de informação morfológica e topológica sobre as heterogeneidades à micro escala, sendo representativo do comportamento do material em média.

Esta tese apresenta um programa computacionalmente robusto e eficiente, escrito em Python, baseado em simulações de dinâmica molecular com esquema isocinético multi temperatura, que é capaz de gerar RVEs a partir de um conjunto de descritores materiais de geométricos de entrada. Em geral, estes podem caraterizar a matriz do material, as sua inclusões, vazios ou fibras, especificando, por exemplo, o raio das partículas, e a fase correspondente, através da sua fração volúmica e numero de inclusões. Dado que um número arbitrário de fases é permitido, obtém-se uma ferramenta muito flexível na modelação de materiais reais.

As microestruturas geradas são avaliadas utilizando as métricas estruturais de Minkowski das suas células Voronoi. Estas são uma ferramenta versátil na deteção de estruturas ordenadas ou aglomerados indesejáveis de partículas, ambas caraterísticas inconvenientes em microestruturas cujo propósito é imitar de forma plausível materiais compósitos reais. Utilizando esta técnica, validaram-se as microestruturas geradas através da abordagem proposta quanto à sua "qualidade".

Depois de gerados, discretizaram-se vários RVEs em malhas de elementos finitos apropriadas com o objetivo de levar a cabo análises à micro escala por homogeneização computacional. Os vários exemplos considerados são criados mantendo a fração volúmica constante, mas aumentando o número de inclusões dentro do RVE. Concluí-se, submetendo as microestruturas a vários esquemas de carregamento mediante diferentes condições fronteira, que um aumento no número de partículas incluídas leva a um volume elementar mais representativo. Verificam-se ainda respostas isotrópicas por parte de microestruturas que contêm apenas Discos e Esferas, à medida que mais inclusões são consideradas.

Page intentionally left blank.

Acknowledgments

I wish to thank both my supervisors, Prof. Francisco Pires and Bernardo Ferreira for their guidance and help during this work. I hope to have fulfilled the goals set forth for this MSc thesis and to have meaningfully contributed to the work developed by the CM2S group.

I am profoundly thankful for all the support and encouragement from my parents and my brother. All my achievements, big and small, in the journey that lead me here can be traced to their unwavering belief in me.

To all the CM2S work group, I wish to express a sincere "thank you" for all the help you provided me.

Page intentionally left blank.

Contents

Page intentionally left blank.

List of Figures

Page intentionally left blank.

List of Tables

Page intentionally left blank.

Notation

General abbreviations

BVP	**B**oundary **V**alue **P**roblem
DOF	**D**egrees **O**f **F**reedom
FEM	**F**inite **E**lement **M**ethod
PMVP	**P**rinciple of **M**ulti-scale **V**irtual **P**ower
RVE	**R**epresentative **V**olume **E**lement

Accents

$\dot{(\cdot)}$	First order time derivative
$\ddot{(\cdot)}$	Second order time derivative
$\widehat{(\cdot)}$	Incremental constitutive function

Sets, domains and boundaries

$\mathscr{E}$	Euclidean space
$\mathscr{K}$	Set of kinematically admissible macroscopic displacements
$\mathscr{K}_\mu$	Set of kinematically admissible minimally constrained microscopic displacements
$\tilde{\mathscr{K}_\mu}$	Set of kinematically admissible minimally constrained microscopic displacements fluctuations
$\mathscr{V}$	Set of virtual displacements
$\mathscr{V}_\mu$	Set of virtual displacements fluctuations
υ	Local (or natural) normalized domain
Ω	Body domain in current configuration

$\partial\Omega$	Body domain boundary in current configuration
Ω_0	Body domain in reference configuration
$\partial\Omega_0$	Body domain boundary in reference configuration
Ω_μ	RVE domain in current configuration
$\partial\Omega_\mu$	RVE domain boundary in current configuration
$\Omega_{\mu,0}$	RVE domain in reference configuration
$\partial\Omega_{\mu,0}$	RVE domain boundary in reference configuration

General notation

a	Scalar
$\boldsymbol{a}$	First order tensor
$\boldsymbol{A}$	Second order tensor
$\mathbf{a}$	Finite Element Method vector
$\mathbf{A}$	Finite Element Method matrix
$\mathscr{A}$	Body, space or set

Operators and symbols

$(\cdot) * (\cdot)$	Appropriate product
$(\cdot) : (\cdot)$	Tensorial double contraction
$(\cdot) \cdot (\cdot)$	Tensorial dot product
$(\cdot) \otimes (\cdot)$	Tensorial product
$\mathsf{A}_{(\cdot)}$	Finite Element Method assembly operator
$\delta(\cdot)$	Variation
$\langle(\cdot)\rangle$	Ensemble average
$\ln(\cdot)$	Natural logarithm
$\boldsymbol{I}$	Second order identity tensor
$\det(\cdot)$	Determinant
$\mathrm{div}(\cdot)$	Spatial divergence operator
$\mathrm{div}_0(\cdot)$	Material divergence operator
$\mathrm{tr}(\cdot)$	Matrix trace
$\nabla(\cdot)$	Spatial gradient operator
$\nabla_0(\cdot)$	Material gradient operator
$\partial(\cdot)/\partial a$	Partial derivative with respect to a
$\mathrm{d}(\cdot)$	Infinitesimal

Subscripts and superscripts

$(\cdot)^{(0)}$	Reference material related quantity
$(\cdot)^{(e)}$	Elemental quantity
$(\cdot)^{g}$	Global quantity
$(\cdot)_0$	Reference configuration, initial time
$(\cdot)_\mu$	Microscale related quantity
$(\cdot)_d$	Deviatoric component
$(\cdot)_h$	Hydrostatic component
${}^{h}(\cdot)$	Discretized domain, interpolated field

Variables

Δt	Time step
ℓ	Mean free path
λ_i	Eigenvalue of the right and left Cauchy-Green strain tensor
$\boldsymbol{\sigma}$	Cauchy stress tensor
$\boldsymbol{\tau}$	Kirchhoff stress tensor
$\boldsymbol{B}$	Left Cauchy-Green strain tensor
$\boldsymbol{C}$	Right Cauchy-Green strain tensor
$\boldsymbol{D}$	Rate of deformation tensor
$\boldsymbol{E}^{(m)}$	Strain tensor from the Lagrange family
$\boldsymbol{e}^{(m)}$	Strain tensor from the Eulerian family
$\boldsymbol{F}$	Deformation gradient
$\boldsymbol{P}$	First Piola-Kirchhoff stress tensor
$\boldsymbol{R}$	Proper orthogonal rotation tensor
$\boldsymbol{U}$	Symmetric positive right stretch tensor
$\boldsymbol{V}$	Symmetric positive left stretch tensor
$\mathbf{B}$	Discrete symmetric gradient operator
$\mathbf{f}^{\text{ext}}$	Vector of internal forces
$\mathbf{f}^{\text{int}}$	Vector of external forces
$\mathbf{G}$	Discrete global gradient operator
$\mathbf{N}$	Interpolation matrix
$\mathscr{O}$	System observable
$\mathscr{B}$	General body
Ω	Sample space
ω	Realization of the random medium

$\mathcal{F}$	σ-algebra of subsets of the sample space
$\mathcal{I}^{(i)}$	Indicator function for phase i
$\mathcal{P}$	Probability measure
ϕ	Volume fraction
π	Probability distribution
ψ	Specific Helmholtz free energy
ψ_s	Irreducible Minkowski Tensor of degree s
$\psi_{s,m}$	Irreducible Minkowski tensor of degree s and order m
ρ	Material density
ρ_K	Normal density function of shape K
ρ_n	n-particle probability density function
σ	Effective cross-sectional length/area
σ	Standard deviation
θ	Temperature field
$\boldsymbol{\alpha}$	Set of macroscopic internal variables
$\boldsymbol{\beta}$	Set of microscopic internal variables
$\boldsymbol{\eta}$	Virtual displacements
$\boldsymbol{\zeta}$	Natural coordinate
$\boldsymbol{A}$	Set of thermodynamics forces
$\boldsymbol{b}$	Body forces
$\boldsymbol{E}_i$	Material orthonormal basis
$\boldsymbol{e}_i$	Spatial orthonormal basis
$\boldsymbol{E}_i^*$	Lagrangian principal directions
$\boldsymbol{e}_i^*$	Eulerian principal directions
$\boldsymbol{f}$	Force acting on a particle
$\boldsymbol{g}$	Spatial gradient of the temperature field
$\boldsymbol{m}$	Unitary vector normal to the surface or boundary in deformed configuration
$\boldsymbol{n}$	Unitary vector normal to the surface or boundary in reference configuration
$\boldsymbol{n}_k$	Outer normal vector to the kth edge or face of a polygon or polyhedron, respectively
$\boldsymbol{q}$	Heat flux
$\boldsymbol{t}$	Cauchy stress vector
$\boldsymbol{u}$	Displacement field
$\boldsymbol{v}$	Velocity of a particle
$\boldsymbol{X}$	Material macroscopic position vector
$\boldsymbol{x}$	Position of a particle
$\boldsymbol{x}$	Spatial macroscopic position vector
$\boldsymbol{Y}$	Material microscopic position vector
$\boldsymbol{y}$	Spatial microscopic position vector

Ξ	Dissipation potential
ξ	Structure function
e	Specific internal energy
g_2	Pair correlation function
g_n	n-particle correlation function
H_P	Nearest neighbor function
J	Determinant of the deformation gradient
K	Geometrical shape
$K(r)$	Ripley's K function
k_b	Boltzmann constant
$L^{(i)}$	Lineal path function of phase i
L_k	Length of the kth edge of a polygon
m	Mass of a particle
n_{dim}	Number of degrees of freedom per node
N_{DOF}	Number of degrees of freedom per particle
n_{nodes}	Number of nodes of a finite element
n_{points}	Total number of nodes in the finite element mesh
N_i	Shape function associated with node i
N_p	Number of particles in the system
p	Hydrostatic pressure
P_N	N-particle probability density function
q_s	Minkowski structure metric of degree s
r	Density of heat production
s	Specific entropy
$S_n^{(i)}$	n-point probability function for phase i
T	Absolute temperature of a system of particles
t	Time instant
w	Gauss sampling point weight
$\ell_{\text{RVE}\,i}$	Length of the RVE in the i direction

Page intentionally left blank.

Chapter 1

Introduction

1.1 Contextualization

Nowadays, the design and modeling of advanced materials calls for the understanding that these are hierarchical in nature, i.e. their macroscopic properties and mechanical response result from the interaction between heterogeneous structures spanning over multiple length scales. More precisely, the microstructural features determining the properties of a heterogeneous material are:

1. properties of the constituent(s),
2. geometry of the constituent(s): their distribution, orientation, shape and volume fraction,
3. nature and characteristics of the interfaces between different constituents.

These are often controlled by fabrication, alloying, and processing (Bargmann et al., 2018). The present work focus exclusively on point 2.

Highlighting the importance of this multi-scale approach to material modeling, it must be noted that at a small enough scale, all natural and synthetic materials are heterogeneous. For example, laminated composite materials can be analyzed from a mechanical standpoint at three different scales, according to the task at hand (Melro, 2011):

Micro-scale The heterogeneity in the composite is present at this scale. Analyses performed at this scale focus on the mechanical behavior of the constituents. These are considered as individual homogeneous materials.

Meso-scale The scale of the ply thickness. The ply is taken as the building block of the composite, being considered as a homogeneous material with transverse isotropy in the case of unidirectional long fibre composites.

Macro-scale The scale corresponding to the laminate itself and to the structure. The material is assumed homogeneous and the effects of the constituent materials are represented only by averaged apparent properties of the composite material.

There are several materials of great practical importance from an industrial point of view, whose modeling and design benefit from this approach. One such class of

materials are the matrix-inclusion composites. These are characterized by non-overlapping particles embedded in topologically interconnected matrix. The presence of inclusions is meant to improve the mechanical properties, such as specific strength in lightweight construction, e.g. in short and long fiber reinforced materials, fracture toughness, e.g. in polymer blends, or it originates from the manufacturing process, e.g. injection molding or sintering (Bargmann et al., 2018).

An example of marked manufacturing importance are the polymer blends. For instance, polycarbonate (PC) blends with acrylonitrile butadiene styrene (ABC) find ample use in molding applications, particularly in the automotive industry (Lombardo et al., 1994). In these blends, the size and distribution of the rubber particles have a appreciable impact on the mechanical properties, e.g. thoughness. Moreover, the particular structure of the blend changes with the distance from the surface (Lombardo et al., 1994; Bärwinkel et al., 2016).

Regarding the characterization of the microstructure of these materials, volume fraction and geometry of inclusions, typically idealized as convex bodies, are critical. Different materials are better described using diverse geometrical shapes. For example, rubber particles in polymer blends are generally modeled using spherical or ellipsoidal inclusions (see Figure 1.1a). Convex polyhedra are typically employed to mimic inclusions in concrete or asphalt as well as metal matrix composites. Also, short fiber reinforcements, approximated by cylinders and spherocylinders, are widely used in lightweight constructions, such as boats, automobiles, water tanks, pipes or external skins, by mixing glass fibers or carbon fibers with polymers. Long fiber reinforced composites, in turn, are commonly approximated by cylinders, and are common in automotive and aerospace application, where glass and carbon fiber mats are embedded in polymers (see Figure 1.1b). However, due to their waviness, most natural fibers cannot be satisfactorily approximated as cylinders (Bargmann et al., 2018). Also, in order to closely approximate the real materials, it is important to mimic the statistical distribution of the geometrical parameters characterizing the idealized shapes that model the inclusions, e.g. the orientation or aspect ratio of elliptical particles. Adding support for multiple material phases, great flexibility can be provided in the modeling of actual matrix-composite materials.

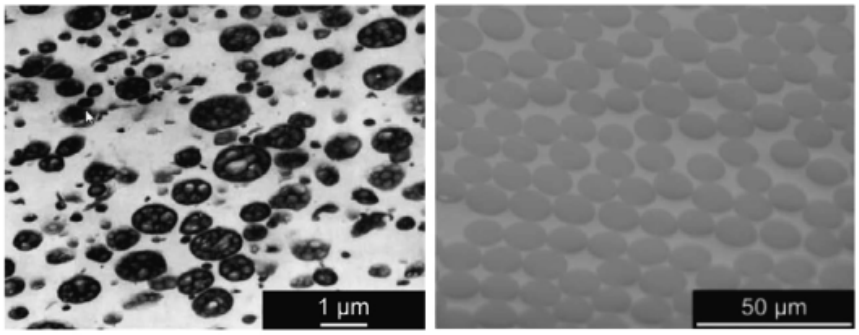

(a) (b)

Figure 1.1: (a): Polymer blend ABS with ellipsoidal shape inclusions. (b): Fiber-reinforced composite with cylindrical shape inclusions (Adapted from Bargmann et al. (2018)).

Another set of materials that can be modeled in a similar way are matrix-dilute pore systems. As the name suggests, they consist of a matrix material which contains isolated voids. These voids are approximated using convex bodies, such as spheres or ellipsoids, in the same way as inclusions in matrix-composite materials. The source of dilute pores can be natural or synthetic. Examples of dilute pore systems are most metallic alloys with casting defects in the form of micro- or macro-voids of various sizes and shapes (see Figure 1.2). Their presence is crucial to explain material failure in such materials, and it also tends to lead to a decrease in stiffness, strength and ductility (Bargmann et al., 2018). Despite this, there are circumstances in which the presence of voids is beneficial. For example, in nanoporous metallic glasses a more favorable failure mechanism can be induced by the presence of these voids (Şopu et al., 2016). Another instance where voids are desirable are designed materials with periodically introduced dilute pores of various shapes and sizes. Dilute pore systems with porosity as low as 1% can feature very desirable properties regarding wave attenuation, and thus can be suitable for vibration control (Javid et al., 2016).

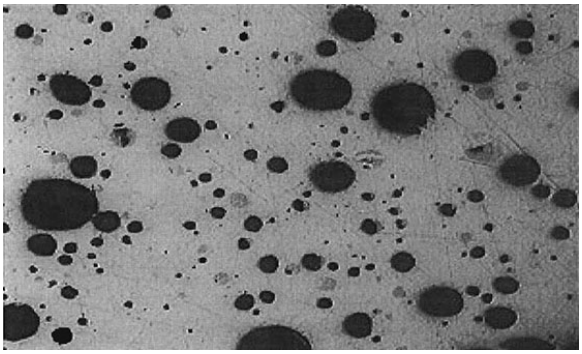

Figure 1.2: Pure gas porosity in die casting. The high concentration of gas bubbles probably caused by too much lubricant or from water leaking into the die. (Adapted from (Walkington and Association, 2003)).

Having understood the importance of considering the material behavior at multiple scales, the method of computational homogenization emerged as an effective way of modeling multi-scale heterogeneous materials by performing an homogenization procedure over a representative volume element (RVE) of the microstructure. The concept of RVE was introduced by Hill (1963) defining it as region of the microstructure that is representative of the entire microstructure in an average sense. Thus, the RVE must be

1. structurally representative of the mixture of constituents on average, and

2. contain a sufficient number of inclusions for the apparent overall moduli to be effectively independent of the surface values of traction and displacement, as long as these are "macroscopically uniform".

A later definition by Drugan and Willis (1996) describes the RVE as the smallest material volume element of the composite for which the usual spatially constant "overall modulus" macroscopic constitutive representation is a sufficiently accurate model to represent the mean constitutive response.

From its definition, it's not possible to determine the size of RVE straight away. It can not comprise too large a volume, as that would hinder the possibility of analyzing it through numerical methods. On the other hand, the volume can't be too small either, so that it is representative of the material under analysis, as the definition of the RVE demands (Melro, 2011). Moreover, the dimensions of the RVE depend on the problem at hand, i.e. on the geometric features and mechanical properties of the phases and on the type of analysis performed, being generally determined empirically (Drugan and Willis, 1996; Trias et al., 2006).

A quick and simple solution for the generation of RVEs would be to model it as periodic, tilling a small volume of particles, until a desired volume has been reached. This approach, however, leads to inaccurate predictions when applied to failure/damage related analysis (Pyrz, 1994; Trias et al., 2006; Hojo et al., 2009). Therefore, the need arises to generate RVEs, whose morphology is "random", avoiding the presence of clusters or ordered arrangements of particles, so that it properly represents the materials under analysis.

The main objective of the present work is then to implement a computational robust and efficient program in Python that is able to generate RVEs based on a given set of material and geometrical input descriptors. In general, these may characterize the material matrix, particles/inclusions, voids and fibers (e.g. radius, ellipsoid axes magnitude and orientation, spatial position, etc.) and the corresponding phase in the heterogeneous material (e.g. volume fraction, number of particles, etc.), being also necessary to account for their deterministic or stochastic nature. After the generation procedure, the RVE should be discretized in a suitable finite element mesh in order to perform microscale analyses through computational homogenization.

The computational efficient generation of microstructures can be used towards the design of advanced multi-scale heterogeneous materials in a framework for data-driven analysis of materials under uncertainty, as proposed by Bessa et al. (2017). This framework consists of three general steps

1. design of experiments, where the input variables describing material geometry (microstructure), phase properties and external conditions are sampled;
2. efficient computational analysis of each design sample, leading to the creation of a material response database;
3. machine learning applied to this database to obtain a new design or response model.

Data-driven approaches for the design of advanced heterogeneous materials, such as the one mentioned in the previous paragraph, attempt to improve the efficiency and efficacy of this highly iterative process. The search for an optional design regarding chosen quantities of interest can be a pain-staking process, due to the large dimension of the engineering design space. There are too many combinations of the design variables to conduct experimental investigations for every design point. The proposed program meets the need of generating the design samples, as dictated by the design of experiments, for later computational analysis. In this away, a large database of material behavior as function of the material descriptors can be created and using machine learning techniques a complete relationship between the key descriptors of each design and the quantities of interest is approximated, enabling its used for distinct purposes. For example, finding general constitutive model for materials as a function of their microstructure and phase properties, or predicting the global optimum design for the material within a sample space (Bessa et al., 2017).

1.2 Objectives

The objectives of the work developed in the present MSc thesis are:

- Theoretical review of the Finite Element Method (FEM), computational homogenization and computational generation of microstructures;
- Design of a program to generate an RVE ranging from the specification of the input descriptors to the finite element discretization of the spatial domain;
- Implementation of the program in an object-oriented Python framework, allowing for the generation of 2D RVEs with simple geometrical features, such as circles and ellipses, as well as 3D RVEs containing spherical and ellipsoidal inclusions. Further requirements are the support for multiple phases and the assurance of stochasticity regarding the spatial positioning of the particles and their geometrical descriptors;
- Validation and assessment of the efficiency of the developed program;
- Analysis of the quality of the microstructures generated using the proposed approach;
- Results compilation and analyses: critical assessment of the RVE representativeness based on the homogenized response.

1.3 Computational implementations and numerical simulations

The computational implementations and numerical simulations performed in the scope of the present work are carried out in several programs described in what follows.

All the numerical simulations based on the Finite Element Method (FEM) based on computational homogenization are held in the in-house Fortran (IBM Mathematical Formula Translation System) program LINKS (Large Strain Implicit Non-linear Analysis of Solids Linking Scales), a multi-scale finite element code for implicit infinitesimal and finite strain analyses of hyperelastic and elastoplastic solids that is continuously developed by the CM2S research group (Computational Multi-Scale Modeling of Solids and Structures) at the Faculty of Engineering of University of Porto.

All the microstructure generation and analysis is done using the proposed program developed in Python. This program is later described in a dedicated chapter of this document.

As it relates to the generation of the nonconform meshes used for FEM analysis of the microstructures generated, these were obtained using the free software Gmsh.

1.4 Document structure

The present document is structured as follows:

Chapter 2

In Chapter 2 the fundamental concepts required to describe the behavior of a solid undergoing large deformations are introduced along with some of the formalism relevant to the constitutive theory based on thermodynamics with internal variables. The application of the Finite Element Method to the solution of a mechanical initial boundary value equilibrium problem is then detailed.

Chapter 3

In Chapter 3 the fundamental concepts behind a first order hierarchical multiscale model based on computational homogenization are outlined, including the scale transition theory and the microscale boundary conditions. The microscale equilibrium problem is then properly defined and its solution through the Finite Element Method is briefly covered.

Chapter 4

In Chapter 4 a systematic approach for the description of random heterogeneous materials is presented. It includes a definition of such materials and a diverse array of techniques for their characterization.

Chapter 5

In Chapter 5 an overview of computational microstructure methods is provided, including microstructure reconstruction from experimental data, physics based microstructure generation and geometrical generation methods. It is followed by a detailed comparison of their appropriateness for the task at hand, providing the motivation for the final choice made regarding the proposed program.

Chapter 6

In Chapter 6 the suggested approach, a time-driven molecular dynamics simulation, is more fully fleshed out. It includes the algorithms used in the proposed program, from its general structure to the computation of the interaction between the particles and the integration of the equations of motion. A new approach for faster generation of microstructure is put forth in the form of a multi-temperature isokinetic scheme.

Chapter 7

In Chapter 7 three sets of results are presented. The first concerns the validation of the proposed approach and an analysis of its efficiency. The second regards the quality of the microstructures generated, using the Minkowski structure metrics. Lastly, the third provides application examples in the form of multi-scale analyses based on computational homogenization.

Chapter 8

In Chapter 8 the main conclusions are summed up and some further research topics are discussed.

Chapter 2

Continuum Mechanics and Finite Element Method

This chapter deals with the concepts needed to describe the behavior of a solid undergoing large deformation as well as the conservation principles that ensure its mechanical equilibrium. A brief overview of the Finite Element Method as a tool to solve mechanical initial value equilibrium problem is also presented. These topics are broadly covered in the literature and here the approach used follows de Souza Neto et al. (2011a).

2.1 Kinematics of Deformation

2.1.1 Motion

Let a deformable body $\mathscr{B}$ occupy an open region Ω_0 of the tridimensional Euclidean space $\mathscr{E}$ with a regular boundary $\partial\Omega_0$ in its reference configuration. Its motion (see Figure 2.1) is defined by a smooth one-to-one function

$$\boldsymbol{\varphi}\colon \Omega \times \mathscr{R} \to \mathscr{E}, \tag{2.1}$$

mapping each material particle of coordinates $\boldsymbol{X}$ in the reference configuration to its position $\boldsymbol{x}$ in the deformed configuration, for a given instant of time t, as

$$\boldsymbol{x} = \boldsymbol{\varphi}(\boldsymbol{X}, t). \tag{2.2}$$

Thus, the displacement field is defined as

$$\boldsymbol{u}(\boldsymbol{X}, t) = \boldsymbol{\varphi}(\boldsymbol{X}, t) - \boldsymbol{X}, \tag{2.3}$$

and, since the function that defines the motion is one-to-one, the reference configuration can be recovered as

$$\boldsymbol{X} = \boldsymbol{\varphi}^{-1}(\boldsymbol{x}, t) = \boldsymbol{x} - \boldsymbol{u}(\boldsymbol{\varphi}^{-1}(\boldsymbol{x}, t), t), \tag{2.4}$$

where $\boldsymbol{\varphi}^{-1}$ is the reference mapping function.

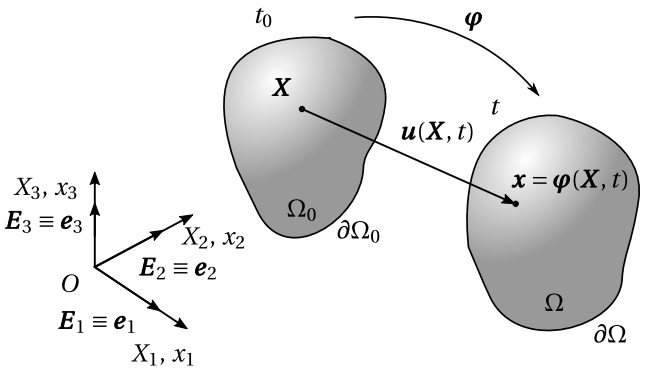

Figure 2.1: Motion

2.1.2 Material and spatial descriptions

When dealing with finite deformations, the behavior of the body under analysis can be described with respect to the reference configuration, using the so-called material or Lagrangian description, or to the deformed configuration, using the so-called spatial or Eulerian description.

In the Lagrangian description, any field defined over the body, be it scalar, vectorial or tensorial, is expressed as a function of the reference configuration, $\boldsymbol{X} \in \Omega_0$. On the other hand, the Eulerian description of the same field is done using the deformed configuration, $\boldsymbol{x} \in \Omega$.

Let $\alpha(\boldsymbol{x},t)$ be a spatial field and $\beta(\boldsymbol{X},t)$ a material field. Their material and spatial descriptions, α_m and β_s, respectively, are given by

$$\alpha_m(\boldsymbol{X},t) = \alpha(\boldsymbol{\varphi}(\boldsymbol{X},t),t), \tag{2.5}$$

$$\beta_s(\boldsymbol{x},t) = \beta(\boldsymbol{\varphi}^{-1}(\boldsymbol{x},t),t), \tag{2.6}$$

noting that any field associated with a motion of $\mathscr{B}$ can be expressed as a function of time and material or spatial position.

The same distinction between material and spatial descriptions applies to operators such as the divergence and the gradient. The spatial and material gradients, ∇ and ∇_0, respectively, are defined as

$$\nabla\alpha = \frac{\partial}{\partial \boldsymbol{x}}\alpha(\boldsymbol{x},t), \quad \nabla_0\beta = \frac{\partial}{\partial \boldsymbol{X}}\beta(\boldsymbol{X},t), \tag{2.7}$$

where the derivatives are taken with respect to the spatial and reference configuration accordingly.

2.1.3 Deformation gradient

The deformation gradient, a second order tensor denoted by $\boldsymbol{F}$, is defined as

$$\boldsymbol{F}(\boldsymbol{X},t) \equiv \nabla_0 \boldsymbol{\varphi}(\boldsymbol{X},t) = \frac{\partial \boldsymbol{x}}{\partial \boldsymbol{X}}, \tag{2.8}$$

or, taking into account that

$$\boldsymbol{x} = \boldsymbol{X} + \boldsymbol{u}(\boldsymbol{X},t), \tag{2.9}$$

it can be expressed as

$$\boldsymbol{F}(\boldsymbol{X},t) = \boldsymbol{I} + \nabla_0 u. \tag{2.10}$$

The deformation gradient relates the relative position between two neighboring material particles before and after deformation. To see this, let $\boldsymbol{X}$ be the coordinates of some material particle in the reference configuration and $\boldsymbol{X} + d\boldsymbol{X}$ the coordinates of some material particle in its neighborhood. Their corresponding coordinates in the deformed configuration are given, respectively, by

$$\boldsymbol{X} = \boldsymbol{x} + \boldsymbol{u}(\boldsymbol{X},t), \tag{2.11}$$

$$\boldsymbol{X} + d\boldsymbol{X} = \boldsymbol{x} + d\boldsymbol{x} + \boldsymbol{u}(\boldsymbol{X} + d\boldsymbol{X},t). \tag{2.12}$$

Subtracting Equation (2.11) from Equation (2.12), it is found that

$$d\boldsymbol{X} = d\boldsymbol{x} + \boldsymbol{u}(\boldsymbol{X} + d\boldsymbol{X},t) - \boldsymbol{u}(\boldsymbol{X},t) \tag{2.13}$$

$$= (\boldsymbol{I} + \nabla_0 \boldsymbol{u}(\boldsymbol{X},t))\, d\boldsymbol{x} \tag{2.14}$$

$$= \boldsymbol{F}\, d\boldsymbol{x}. \tag{2.15}$$

Due to this relation, it can be shown that the determinant of the deformation gradient has a physical meaning. It is the local unit volume change, that is,

$$J \equiv \det \boldsymbol{F} = \frac{\mathrm{d}v}{\mathrm{d}v_0}, \tag{2.16}$$

where $\mathrm{d}v_0$ is an infinitesimal volume of the body in its reference configuration and $\mathrm{d}v$ the infinitesimal volume after deformation.

Isochoric/Volumetric decomposition

Any deformation can be locally decomposed in volumetric and isochoric (or distortional) components. From Equation (2.16) it can be gathered that an isochoric deformation is characterized by $J = 1$. As such, the deformation gradient can be decomposed as

$$\boldsymbol{F} = \boldsymbol{F}_{\mathrm{iso}} \boldsymbol{F}_{\mathrm{vol}} = \boldsymbol{F}_{\mathrm{vol}} \boldsymbol{F}_{\mathrm{iso}}, \tag{2.17}$$

where the isochoric and volumetric components are defined by

$$\boldsymbol{F}_{\mathrm{iso}} = (\det \boldsymbol{F})^{-\frac{1}{3}}, \quad \boldsymbol{F}_{\mathrm{vol}} = (\det \boldsymbol{F})^{\frac{1}{3}} \boldsymbol{I}. \tag{2.18}$$

Polar decomposition

The deformation gradient can also be decomposed in rotation and stretch components, the so-called polar decomposition, defined as

$$\boldsymbol{F} = \boldsymbol{R}\boldsymbol{U} = \boldsymbol{V}\boldsymbol{R}, \tag{2.19}$$

where $\boldsymbol{R}$ is the proper orthogonal rotation tensor and $\boldsymbol{U}$ and $\boldsymbol{V}$ are the symmetric positive right and left stretch tensors, respectively.

Equation (2.19) has a physical interpretation with the right polar decomposition ($\boldsymbol{F} = \boldsymbol{R}\boldsymbol{U}$) corresponding to a stretch mapping followed by a rotation, and the left polar decomposition ($\boldsymbol{F} = \boldsymbol{V}\boldsymbol{R}$) corresponding to a rotation followed by a stretch mapping. The right $\boldsymbol{U}$ and left $\boldsymbol{V}$ stretch tensors are related through the rotation matrix $\boldsymbol{R}$ as

$$\boldsymbol{V} = \boldsymbol{R}\boldsymbol{U}\boldsymbol{R}^T, \tag{2.20}$$

and can be obtained from deformation gradient by

$$\boldsymbol{C} \equiv \boldsymbol{U}^2 = \boldsymbol{F}^T\boldsymbol{F}, \quad \boldsymbol{B} \equiv \boldsymbol{V}^2 = \boldsymbol{F}\boldsymbol{F}^T, \tag{2.21}$$

where $\boldsymbol{C}$ and $\boldsymbol{B}$ are the right and left Cauchy-Green strain tensors.

Since $\boldsymbol{U}$ and $\boldsymbol{V}$ are symmetric tensors, they admit the spectral decomposition

$$\boldsymbol{U} = \sum_{i=1}^{3} \lambda_i \boldsymbol{E}_i^* \otimes \boldsymbol{E}_i^*, \quad \boldsymbol{V} = \sum_{i=1}^{3} \lambda_i \boldsymbol{e}_i^* \otimes \boldsymbol{e}_i^*, \tag{2.22}$$

where λ_i, $i = 1,2,3$, are the eigenvalues of both $\boldsymbol{U}$ and $\boldsymbol{V}$ and $\boldsymbol{E}_i^*$ and $\boldsymbol{e}_i^*$ are the respective eigenvectors.

The eigenvectors of left $\boldsymbol{V}$ and right $\boldsymbol{U}$ stretch tensors are related through

$$\boldsymbol{e}_i^* = \boldsymbol{R}\boldsymbol{E}_i^*. \tag{2.23}$$

forming two orthogonal bases. These vectors define the Lagrangian and Eulerian principal directions, respectively, allowing for the expression of the local stretching from a material particle, associated with any deformation, as a superposition of stretches along the three mutual orthogonal directions.

2.2 Strain tensors

In Continuum Mechanics there are two main families of strain tensors derived from the deformation gradient and used to describe the body deformation. The Lagrange family strain tensors are defined as

$$\boldsymbol{E}^{(m)} = \begin{cases} \dfrac{1}{m}(\boldsymbol{U}^m - \boldsymbol{I}), & m \neq 0, \\ \ln(\boldsymbol{U}), & m = 0, \end{cases} \tag{2.24}$$

where m is a real number, and likewise, the Euler family strain tensors are defined as

$$\boldsymbol{\varepsilon}^{(m)} = \begin{cases} \dfrac{1}{m}(\boldsymbol{V}^m - \boldsymbol{I}), & m \neq 0, \\ \ln(\boldsymbol{V}), & m = 0, \end{cases} \tag{2.25}$$

where m is also real number.

In particular, choosing $m = 0$, one obtains the so-called material and spatial logarithmic strain tensors

$$\boldsymbol{E}^{(0)} \equiv \ln[\boldsymbol{U}] = \sum_{i=1}^{3} \ln \lambda_i \boldsymbol{E}_i^* \otimes \boldsymbol{E}_i^*, \tag{2.26}$$

$$\boldsymbol{e}^{(0)} \equiv \ln[\boldsymbol{V}] = \sum_{i=1}^{3} \ln \lambda_i \boldsymbol{e}_i^* \otimes \boldsymbol{e}_i^*. \tag{2.27}$$

2.3 Forces and stress measures

The deformation of a body is intrinsically related to the forces acting on it. These forces can be divided in two classes from a purely mechanical point of view: volume (or body) forces, proportional to the mass contained in a volume element, thus, measured in force per unit volume, and surface forces, acting on the surface of a volume element, measured as force per unit area. Related to the latter is the concept of stress, usually described mathematically by second order tensors with different definitions.

Cauchy stress tensor

According to Cauchy's theorem, the relation between the so-called Cauchy stress vector, $\boldsymbol{t}(\boldsymbol{x},\boldsymbol{n})$ and the unitary outward vector normal to the deformed surface under analysis, $\boldsymbol{n}$, is linear, and given by

$$\boldsymbol{t}(\boldsymbol{x},\boldsymbol{n}) \equiv \boldsymbol{\sigma}(\boldsymbol{x})\boldsymbol{n}, \tag{2.28}$$

where $\boldsymbol{\sigma}$ is the second order Cauchy stress tensor.

The Cauchy stress vector is naturally associated with the deformed configuration and thus, expressed in a spatial description and measured in force per unit deformed area. It must also be noted that, as a consequence of the balance of angular momentum, the Cauchy stress tensor is symmetric.

First Piola-Kirchhoff stress tensor

The First Piola-Kirchhoff stress tensor, $\boldsymbol{P}$, can be regarded as the material counterpart of the Cauchy stress tensor, as it establishes a linear dependence between the stress vector $\boldsymbol{t}_0(\boldsymbol{X},\boldsymbol{m})$, measured in force per unit reference area, and the unitary outward vector normal to the undeformed surface under analysis, $\boldsymbol{m}$,

$$\boldsymbol{t}_0 = \boldsymbol{P}\boldsymbol{m}, \tag{2.29}$$

which is related to the Cauchy stress vector by

$$\boldsymbol{t}_0 = \frac{\mathrm{d}a}{\mathrm{d}a_0}\boldsymbol{t} = \frac{\mathrm{d}a}{\mathrm{d}a_0}\boldsymbol{\sigma}\boldsymbol{n}, \tag{2.30}$$

where $\mathrm{d}a$ is the infinitesimal deformed area normal to the unitary vector $\boldsymbol{n}$ and $\mathrm{d}a_0$ the corresponding undeformed area normal to $\boldsymbol{m}$. It can be shown that the relation between $\mathrm{d}a$ and $\mathrm{d}a_0$ is

$$\frac{da}{da_0}\boldsymbol{n} = J\boldsymbol{F}^{-T}\boldsymbol{m}, \tag{2.31}$$

and substitution in the equation above motivates the following definition

$$\boldsymbol{P} \equiv J\boldsymbol{\sigma}\boldsymbol{F}^{-T}, \tag{2.32}$$

where J is the determinant of the deformation gradient $\boldsymbol{F}$ and $\boldsymbol{\sigma}$ is the Cauchy stress tensor. From Equation (2.32), one gathers that, in general, the First Piola-Kirchhoff stress tensor is not symmetric.

Kirchhoff stress tensor

The Kirchhoff stress tensor, $\boldsymbol{\tau}$, is a widely used symmetric tensor, defined as

$$\boldsymbol{\tau} \equiv J\boldsymbol{\sigma}. \tag{2.33}$$

Deviatoric/Hydrostatic decomposition

The Cauchy stress tensor, $\boldsymbol{\sigma}$, can be split as

$$\boldsymbol{\sigma} = \boldsymbol{\sigma}_d - p\boldsymbol{I}, \tag{2.34}$$

where p is the hydrostatic pressure defined as

$$p \equiv -\frac{1}{3}\text{tr}\,[\boldsymbol{\sigma}], \tag{2.35}$$

and $\boldsymbol{\sigma}_d$ is the deviatoric stress defined as

$$\boldsymbol{\sigma}_d \equiv \boldsymbol{\sigma} - p\boldsymbol{I}. \tag{2.36}$$

2.4 Fundamental conservation principles

In Continuum Mechanics, there is a set of conservation principles and thermodynamic laws that, irrespective of the quantities used to describe the mechanical behavior of a body undergoing large deformations, must always be satisfied.

Principle of mass conservation

The principle of mass conservation can be stated as

$$\dot{\rho} + \rho\,\text{div}\,\dot{\boldsymbol{u}}(\boldsymbol{x}) = 0, \tag{2.37}$$

where ρ is the material density measured in mass per unit deformed volume.

Principle of linear momentum conservation

The principle of linear momentum conservation can be stated in both material and spatial description. In a spatial description it reads

$$\begin{cases} \operatorname{div} \boldsymbol{\sigma}(\boldsymbol{x}) + \boldsymbol{b} = \rho \ddot{\boldsymbol{u}}(\boldsymbol{x}), & \forall \boldsymbol{x} \in \Omega, \\ \boldsymbol{t}(\boldsymbol{x}, \boldsymbol{n}) = \boldsymbol{\sigma}(\boldsymbol{x}) \boldsymbol{n}, & \forall \boldsymbol{x} \in \partial\Omega, \end{cases} \tag{2.38}$$

where $\boldsymbol{b}$ is the body force field measured as per unit deformed volume.

One can also write the principle of linear momentum conservation in material coordinates, as

$$\begin{cases} \operatorname{div}_0 \boldsymbol{P}(\boldsymbol{X}) + \boldsymbol{b}_0 = \rho_0 \ddot{\boldsymbol{u}}(\boldsymbol{X}), & \forall \boldsymbol{x} \in \Omega_0, \\ \boldsymbol{t}_0(\boldsymbol{X}, \boldsymbol{m}) = \boldsymbol{P}(\boldsymbol{X}) \boldsymbol{m}, & \forall \boldsymbol{x} \in \partial\Omega_0, \end{cases} \tag{2.39}$$

where $\boldsymbol{b}_0$ is the body forces field, measured in force per unit undeformed volume, and ρ_0 is the material density, measured in mass per unit undeformed volume. Both these quantities can be found from their spatial counterparts as

$$\boldsymbol{b}_0 = J\, \boldsymbol{b}, \quad \rho_0 = J\, \rho. \tag{2.40}$$

Equations (2.38) and (2.39) are the so-called strong, point-wise or local equilibrium equations, as they enforce the mechanical equilibrium at every material particle of the body.

First principle of thermodynamics

$$\rho \dot{e} = \boldsymbol{\sigma} : \boldsymbol{D} + \rho r - \operatorname{div} \boldsymbol{q}, \tag{2.41}$$

where e is the specific internal energy field, r is the density of heat production field and $\boldsymbol{q}$ is the heat flux vector field. The second order tensor $\boldsymbol{D}$ denotes a strain rate measure, such that the double contraction $\boldsymbol{\sigma} : \boldsymbol{D}$ represents the stress power per unit volume in the deformed configuration of body.

Second principle of thermodynamics

The second principle of thermodynamics postulates that changes in entropy in the universe can never be negative, which is mathematically expressed as

$$\rho \dot{s} + \operatorname{div} \left[\frac{\boldsymbol{q}}{\theta} \right] - \frac{\rho r}{\theta} \geq 0, \tag{2.42}$$

where θ and s are the temperature and specific entropy fields, respectively.

Clausius-Duhem inequality

Combining the first and second thermodynamic principles yields

$$\rho \dot{s} + \operatorname{div} \left[\frac{\boldsymbol{q}}{\theta} \right] - \frac{1}{\theta} (\rho \dot{e} - \boldsymbol{\sigma} : \boldsymbol{D} + \operatorname{div} \boldsymbol{q}) \geq 0, \tag{2.43}$$

From the definition of the specific Helmholtz free energy

$$\psi \equiv e - \theta s, \tag{2.44}$$

and defining the temperature field gradient as $\boldsymbol{g} = \nabla\theta$, it is possible to establish the so-called Clausius-Duhem inequality in the spatial description as

$$\boldsymbol{\sigma} : \boldsymbol{D} - \rho\left(\dot{\psi} + s\dot{\theta}\right) - \frac{1}{\theta}\boldsymbol{q}\cdot\boldsymbol{g} \geq 0, \tag{2.45}$$

where the identity

$$\operatorname{div}\left[\frac{\boldsymbol{q}}{\theta}\right] = \frac{1}{\theta}\operatorname{div}\boldsymbol{q} - \frac{1}{\theta^2}\boldsymbol{q}\cdot\nabla\theta. \tag{2.46}$$

is used.

From a physical point of view, the Clausius-Duhem inequality states that the energy dissipation per unit deformed volume is always non-negative.

Equation (2.45) can also be written as

$$\boldsymbol{\tau} : \boldsymbol{D} - \rho_0\left(\dot{\psi} + s\dot{\theta}\right) - \frac{J}{\theta}\boldsymbol{q}\cdot\boldsymbol{g} \geq 0, \tag{2.47}$$

multiplying it by J and attending to the definition of the Kirchhoff stress tensor, where the left hand side represents now the energy dissipation per unit reference volume.

2.5 Weak equilibrium equations

From a practical standpoint, finding the exact solution to the strong equilibrium equations in the context of real engineering problems is most often nearly or completely impossible. To circumvent this problem, most numerical methods are formulated to obtain approximate solutions to the so-called weak equilibrium equations. These result from relaxing the strong equilibrium equations, so that the solutions need only to satisfy the equilibrium equations in an average sense, instead of satisfying the equilibrium equations pointwise, This is as result of an integration over the body volume. More precisely, the weak equilibrium equations can be found making use of several energetic and weighted residual methods, such as the Virtual Work Principle used here.

Spatial description

For a quasi-static motion, such that the inertial terms can be neglected, the Virtual Work Principle states, in a spatial description, that the body is in equilibrium if and only if the Cauchy stress field satisfies

$$\int_\Omega [\boldsymbol{\sigma} : \nabla\boldsymbol{\eta} - \boldsymbol{b}\cdot\boldsymbol{\eta}]\,\mathrm{d}v - \int_{\partial\Omega} \boldsymbol{t}\cdot\boldsymbol{\eta}\,\mathrm{d}a = 0, \quad \forall\boldsymbol{\eta} \in \mathscr{V}, \tag{2.48}$$

where $\mathscr{V}$ is the space of virtual displacement of the body. It is defined by the space of sufficiently regular arbitrary displacements

$$\boldsymbol{\eta}\colon \Omega \to \mathscr{U}, \tag{2.49}$$

where $\mathscr{U}$ is the n-dimension vector associated with $\mathscr{E}$.

Spatial description

Likewise, in a material description, the Virtual Work Principle states that the body is in equilibrium if and only if the First Piola-Kirchhoff stress field satisfies

$$\int_{\Omega_0} [\boldsymbol{P} : \nabla_0 \boldsymbol{\eta} - \boldsymbol{b}_0 \cdot \boldsymbol{\eta}] \, \mathrm{d}v - \int_{\partial\Omega_0} \boldsymbol{t}_0 \cdot \boldsymbol{\eta} \, \mathrm{d}a = 0, \quad \forall \boldsymbol{\eta} \in \mathscr{V}, \tag{2.50}$$

where $\mathscr{V}$ is the space of virtual displacement of the body, defined by the space of sufficiently regular arbitrary displacements

$$\boldsymbol{\eta} : \Omega \to \mathscr{U}. \tag{2.51}$$

2.6 Mechanical constitutive initial value problem

In Continuum Mechanics, a constitutive model is a set of equations, also called constitutive equations, establishing the stress-strain relation for a given material. Before going further, it is important to define a thermokinetic process of a body $\mathscr{B}$ as

$$\text{thermokinetic process:} \quad \{\boldsymbol{\varphi}(\boldsymbol{X}, t), \theta(\boldsymbol{X}, t)\}, \tag{2.52}$$

and a calorodynamic process of $\mathscr{B}$ as

$$\text{calorodynamic process:} \quad \{\boldsymbol{\sigma}(\boldsymbol{X}, t), e(\boldsymbol{X}, t), s(\boldsymbol{X}, t), r(\boldsymbol{X}, t), \boldsymbol{b}(\boldsymbol{X}, t), \boldsymbol{q}(\boldsymbol{X}, t)\}, \tag{2.53}$$

which satisfies the fundamental conservation principles previously introduced.

It is also important to note that any constitutive model must satisfy a set of constitutive axioms, explained in detail by de Souza Neto et al. (2011a). As these are too general to be used directly in practice, a particular case of the general history functional-based constitutive theory based on the thermodynamics with internal variables approach is used.

2.6.1 Thermodynamics with internal variables

In the thermodynamics with interval variables approach, the thermodynamic state at a given material particle, i.e. $\boldsymbol{\sigma}$, ψ, s and $\boldsymbol{q}$ at that material particle, at a given instant of the calorodynamic process is assumed to be completely defined by the instantaneous values of a finite number of state variables

$$\{\boldsymbol{F}, \theta, \boldsymbol{g}, \boldsymbol{\alpha}\}. \tag{2.54}$$

where

$$\boldsymbol{\alpha} = \{\alpha_k\} \tag{2.55}$$

is a set of internal variables (scalar or tensorial in nature) associated with dissipative mechanisms.

The accuracy of the constitutive model depends strongly on the appropriate choice of the set of internal variables, as these contain the relevant information about the material thermodynamical history.

Accordingly, the specific Helmholtz free energy is postulated to be

$$\psi = \psi(\boldsymbol{F}, \theta, \boldsymbol{\alpha}). \tag{2.56}$$

To find the constitutive equations for the stress tensor and the entropy, one can substitute

$$\dot{\psi} = \frac{\partial \psi}{\partial \boldsymbol{F}} : \dot{\boldsymbol{F}} + \frac{\partial \psi}{\partial \dot{\theta}} \dot{\theta} + \frac{\partial \psi}{\partial \alpha_k} \dot{\alpha}_k, \tag{2.57}$$

found from the chain rule, on the Clausius-Duhem equation, Equation (2.45), obtaining

$$\left(\boldsymbol{\sigma} \boldsymbol{F}^{-T} - \rho \frac{\partial \psi}{\partial \boldsymbol{F}} \right) : \dot{\boldsymbol{F}} - \rho \left(s + \frac{\partial \psi}{\partial \theta} \right) \dot{\theta} - \rho \frac{\partial \psi}{\partial \alpha_k} \dot{\alpha}_k - \frac{1}{\theta} \boldsymbol{q} \cdot \boldsymbol{g} \geq 0, \tag{2.58}$$

where the velocity gradient is adopted to set the work conjugacy as

$$\boldsymbol{\sigma} : \boldsymbol{D} = \boldsymbol{\sigma} : \boldsymbol{L} = \boldsymbol{\sigma} : \dot{\boldsymbol{F}} \boldsymbol{F}^{-1} = \boldsymbol{\sigma} \boldsymbol{F}^{-T} : \boldsymbol{F}. \tag{2.59}$$

Since the Clausius-Duhem inequality must hold for any thermokinetic process and remain valid for any set $\{\dot{\boldsymbol{F}}(t), \dot{\theta}(t)\}$, it implies the following Cauchy stress and entropy constitutive equations

$$\boldsymbol{\sigma} = \rho \frac{\partial \psi}{\partial \boldsymbol{F}} \boldsymbol{F}^T, \tag{2.60}$$

$$s = -\frac{\partial \psi}{\partial \theta}. \tag{2.61}$$

It is also possible to write the constitutive equations for the Kirchhoff stress tensor as

$$\boldsymbol{\tau} = J \rho \frac{\partial \psi}{\partial \boldsymbol{F}} \boldsymbol{F}^T, \tag{2.62}$$

multiplying Equation (2.60) by J, and the first Piola-Kirchhoff stress tensor as

$$\boldsymbol{P} = \rho_0 \frac{\partial \psi}{\partial \boldsymbol{F}}, \tag{2.63}$$

multiplying Equation (2.58) also by J.

For each internal variable α_k of the set $\boldsymbol{\alpha}$ of internal variables, the conjugate thermodynamical forces are defined to be

$$A_k \equiv \rho_0 \frac{\partial \psi}{\partial \alpha_k}, \tag{2.64}$$

so that the Clausius-Duhem equation can be written in a reduced form as

$$-\boldsymbol{A} * \dot{\boldsymbol{\alpha}} - \frac{J}{\theta} \boldsymbol{q} \cdot \boldsymbol{g} \geq 0, \tag{2.65}$$

where $\boldsymbol{A}$ is the set of conjugate thermodynamical forces and $*$ denotes the appropriate product operation.

To completely define the constitutive model, one still needs to postulate the constitutive equations for the flux variables $\dot{\boldsymbol{\alpha}}$ and $\frac{1}{\theta}\boldsymbol{q}$. These are given by

$$\dot{\boldsymbol{\alpha}} = f(\boldsymbol{F}, \theta, \boldsymbol{g}, \boldsymbol{\alpha}), \tag{2.66}$$

$$\frac{1}{\theta}\boldsymbol{q} = g(\boldsymbol{F}, \theta, \boldsymbol{g}, \boldsymbol{\alpha}). \tag{2.67}$$

A sufficient condition for the previous constitutive functions to satisfy the Clausius-Duhem inequality is the hypothesis of normal dissipativity, whereby one defines the constitutive functions for the flux variables as

$$\dot{\alpha}_k = -\frac{\partial \Xi}{\partial A_k}, \quad \frac{1}{\theta}\boldsymbol{q} = -\frac{\partial \Xi}{\partial \boldsymbol{g}}, \tag{2.68}$$

where the dissipation potential is

$$\Xi = \Xi(\boldsymbol{A}, \boldsymbol{g}; \boldsymbol{F}, \theta, \boldsymbol{\alpha}), \tag{2.69}$$

a convex function with respect to each A_k and $\boldsymbol{g}$, and zero valued at the origin, $\{\boldsymbol{A}, \boldsymbol{g}\} = \{\boldsymbol{0}, \boldsymbol{0}\}$. Note that in the previous definition the state variables appear only as parameters.

2.6.2 Mechanical constitutive initial value problem

In the purely mechanical case, where all the quantities related to the thermal domain may be removed, a constitutive model based on internal variables can be established by the following set of equations

$$\boldsymbol{P} = \rho_0 \frac{\partial \psi}{\partial \boldsymbol{F}}, \tag{2.70}$$

$$\psi = \psi(\boldsymbol{F}, \boldsymbol{\alpha}), \tag{2.71}$$

$$\dot{\boldsymbol{\alpha}} = f(\boldsymbol{F}, \boldsymbol{\alpha}). \tag{2.72}$$

Thus, the spatial mechanical constitutive initial value problem can be stated as follows

Problem 2.1 | Spatial mechanical constitutive initial value problem.

Given the initial values of the internal variables, $\boldsymbol{\alpha}(t_0)$, and the history of the deformation gradient

$$\boldsymbol{F}(t), \quad t \in [t_0, t_{\text{end}}], \tag{2.73}$$

find the functions for $\boldsymbol{\sigma}(t)$ and $\boldsymbol{\alpha}(t)$ such that the constitutive equations

$$\boldsymbol{\sigma} = \rho \frac{\partial \psi}{\partial \boldsymbol{F}} \boldsymbol{F}^T, \tag{2.74}$$

$$\psi = \psi(\boldsymbol{F}, \boldsymbol{\alpha}), \tag{2.75}$$

$$\dot{\boldsymbol{\alpha}} = f(\boldsymbol{F}, \boldsymbol{\alpha}), \tag{2.76}$$

are satisfied for every $t \in [t_0, t_{\text{end}}]$.

Likewise, in a material description it can be stated as

Problem 2.2 | Material mechanical constitutive initial value problem.

Given the initial values of the internal variables, $\boldsymbol{\alpha}(t_0)$, and the history of the deformation gradient

$$\boldsymbol{F}(t), \quad t \in [t_0, t_{\text{end}}], \tag{2.77}$$

find the functions for $\boldsymbol{P}(t)$ and $\boldsymbol{\alpha}(t)$ such that the constitutive equations

$$\boldsymbol{P} = \rho_0 \frac{\partial \psi}{\partial \boldsymbol{F}}, \tag{2.78}$$

$$\psi = \psi(\boldsymbol{F}, \boldsymbol{\alpha}), \tag{2.79}$$

$$\dot{\boldsymbol{\alpha}} = f(\boldsymbol{F}, \boldsymbol{\alpha}), \tag{2.80}$$

are satisfied for every $t \in [t_0, t_{\text{end}}]$.

It is now possible to pose the quasi-static mechanical constitutive initial value problem in its weak form. To do it one assumes that a body $\mathscr{B}$ is made from a generic material, characterized by a given constitutive model, whose internal variables are known at the initial time t_0 (see Figure 2.2). In addition, it is assumed that the interior of the body is subjected to a prescribed history of body forces, $\boldsymbol{b}(\boldsymbol{X}, t)$, $t \in [t_0, t_{\text{end}}]$, and to the following boundary conditions:

- **Natural (or Neumann) boundary condition:** t The boundary portion $\Omega_{\text{traction, 0}}$ of $\mathscr{B}$ is subjected to a prescribed history of traction forces, $\boldsymbol{t}_{\text{presc}}(\boldsymbol{X}, t)$, $\boldsymbol{X} \in \partial\Omega_{\text{traction,0}}$, $t \in [t_0, t_{\text{end}}]$,

- **Essential (or Dirichlet) boundary condition:** The boundary portion $\Omega_{\text{motion, 0}}$ of $\mathscr{B}$ is subjected to a prescribed displacement field history, $\boldsymbol{u}_{\text{presc}}(\boldsymbol{X}, t)$, such that[1].

$$\boldsymbol{\varphi}(\boldsymbol{X}, t) = \boldsymbol{X} + \boldsymbol{u}_{\text{presc}}(\boldsymbol{X}, t), \quad \boldsymbol{X} \in \partial\Omega_{\text{motion, 0}}, \quad t \in [t_0, t_{\text{end}}].$$

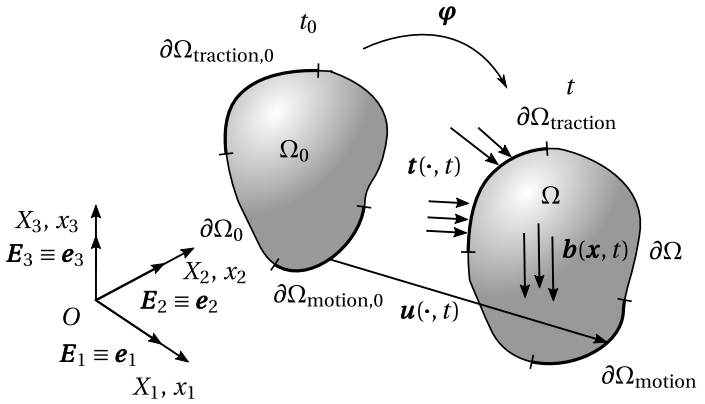

Figure 2.2: Quasi-static mechanical constitutive initial boundary value problem.

It is also convenient to define the set of kinematically admissible displacements of $\mathscr{B}$ as the set of all sufficiently regular displacement functions that satisfy the essential boundary condition (de Souza Neto et al., 2011a),

[1] For simplicity, it is assumed that $\partial\Omega_{\text{traction,0}} \cap \partial\Omega_{\text{motion,0}} = \varnothing$

$$\mathscr{K} \equiv \{\boldsymbol{u} : \Omega \times \mathscr{R} \to \mathscr{U} \mid \boldsymbol{u}(\boldsymbol{X}, t) = \boldsymbol{u}_{\text{presc}}(\boldsymbol{X}, t), \quad \boldsymbol{X} \in \partial\Omega_{\text{motion},0}, \quad t \in [t_0, t_{\text{end}}]\}. \tag{2.81}$$

So the weak form of the quasi-static mechanical constitutive initial boundary value problem can be stated in a spatial description as follows

Problem 2.3 | Spatial quasi-static mechanical initial BVP.

Find a kinematically admissible displacement function, $\boldsymbol{u} \in \mathscr{K}$, such that for every $t \in [t_0, t_{\text{end}}]$, the body $\mathscr{B}$ is in equilibrium as stated by the Virtual Work Principle

$$\int_\Omega [\boldsymbol{\sigma} : \nabla\boldsymbol{\eta} - \boldsymbol{b} \cdot \boldsymbol{\eta}] \, \mathrm{d}v - \int_{\partial\Omega} \boldsymbol{t} \cdot \boldsymbol{\eta} \, \mathrm{d}a = 0, \quad \forall \boldsymbol{\eta} \in \mathscr{V}, \tag{2.82}$$

where the space of virtual displacements at time t is defined by

$$\mathscr{V} \equiv \left\{\boldsymbol{\eta} : \Omega \to \mathscr{U} \mid \boldsymbol{\eta} = \boldsymbol{0} \quad \text{in} \quad \partial\Omega_{\text{motion},0}\right\}, \tag{2.83}$$

and, at each point of $\mathscr{B}$, the Cauchy stress tensor is the solution of spatial mechanical constitutive initial value problem.

and in the material description as

Problem 2.4 | Material quasi-static mechanical initial BVP.

Find a kinematically admissible displacement function, $\boldsymbol{u} \in \mathscr{K}$, such that for every $t \in [t_0, t_{\text{end}}]$, the body $\mathscr{B}$ is in equilibrium as stated by the Virtual Work Principle

$$\int_{\Omega_0} [\boldsymbol{P} : \nabla_0\boldsymbol{\eta} - \boldsymbol{b}_0 \cdot \boldsymbol{\eta}] \, \mathrm{d}v - \int_{\partial\Omega_0} \boldsymbol{t}_0 \cdot \boldsymbol{\eta} \, \mathrm{d}a = 0, \quad \forall \boldsymbol{\eta} \in \mathscr{V}, \tag{2.84}$$

where the space of virtual displacements at time t is defined by

$$\mathscr{V} \equiv \left\{\boldsymbol{\eta} : \Omega_0 \to \mathscr{U} \mid \boldsymbol{\eta} = \boldsymbol{0} \quad \text{in} \quad \partial\Omega_{\text{motion},0}\right\}, \tag{2.85}$$

and, at each point of $\mathscr{B}$, the First Piola-Kirchhoff stress tensor is the solution of material mechanical constitutive initial value problem.

2.7 Time descretization

In a generic path-dependent model, the stress state does not depend only on the instantaneous deformation state but also on the deformation history. For such a model, the solution of the constitutive initial value problem for a given set of initial conditions is usually not known for complex strain paths $\boldsymbol{F}(t)$. Thus, there is a need to use an appropriate numerical algorithm for the integration of the rate constitutive equations.

In general, the algorithms for the integration of rate constitutive equations are obtained by adopting some kind of time (or pseudo-time) discretisation along with some hypothesis on the deformation path between adjacent time instants.

In the present document, it is adopted an algorithm based on approximated incremental constitutive functions. Attending to the mechanical constitutive initial boundary value problem and considering the time increment $[t_n, t_{n+1}]$, this approach is comprised by the two following requeriments:

- **Cauchy and First Piola-Kirchhoff stress tensors.** Considering a time increment $[t_n, t_{n+1}]$ and given the set $\boldsymbol{\alpha}_n$ of internal variables at t_n, the deformation gradient $\boldsymbol{F}_{n+1}$ at time t_{n+1} determines the stress $\boldsymbol{\sigma}_{n+1}$ uniquely through

$$\boldsymbol{\sigma}_{n+1} = \widehat{\boldsymbol{\sigma}}(\boldsymbol{\alpha}_n, \boldsymbol{F}_{n+1}), \tag{2.86}$$

  where $\widehat{\boldsymbol{\sigma}}$ is the incremental constitutive function for the Cauchy stress tensor.

  Similarly, the First Piola-Kirchhoff stress tensor $\boldsymbol{P}_{n+1}$ must be uniquely determined by the prescribed deformation gradient $\boldsymbol{F}_{n+1}$ prescribed at t_{n+1} as

$$\boldsymbol{P}_{n+1} = \widehat{\boldsymbol{P}}(\boldsymbol{\alpha}_n, \boldsymbol{F}_{n+1}), \tag{2.87}$$

  where $\widehat{\boldsymbol{P}}$ is the incremental constitutive function for the First Piola-Kirchhoff stress tensor.

- **Set of internal variables.** Assuming that the set of internal variables $\boldsymbol{\alpha}_n$ is known at t_n, the set of internal variables must be uniquely determined by the prescribed deformation gradient $\boldsymbol{F}_{n+1}$ prescribed at t_{n+1} as

$$\boldsymbol{\alpha}_{n+1} = \widehat{\boldsymbol{\alpha}}(\boldsymbol{\alpha}_n, \boldsymbol{F}_{n+1}), \tag{2.88}$$

  where $\widehat{\boldsymbol{\alpha}}$ is the incremental constitutive function for the set of internal variables.

Generally, the numerical constitutive laws are nonlinear and are expected to converge to the exact solution as the strain increments are reduced.

Making use of the aforementioned time discretization, the weak form of the quasi-static mechanical constitutive initial boundary value problem can then be stated in the spatial description as

Problem 2.5 | Spatial incremental quasi-static mechanical initial BVP.

Given the set of internal variables $\boldsymbol{\alpha}_n$ at t_n, the prescribed body and traction force fields $\boldsymbol{b}_{n+1}$ and $\boldsymbol{t}_{n+1}$ at t_{n+1}, and the prescribed deformating gradient $\boldsymbol{F}_{n+1}$ at t_{n+1}, find the kinematically admissible displacement field $\boldsymbol{u}_{n+1} \in \mathscr{K}_{n+1}$ such that

the body $\mathscr{B}$ is in equilibrium as stated by the virtual Work Principle

$$\int_{\Omega_{n+1}} [\widehat{\boldsymbol{\sigma}}(\boldsymbol{F}_{n+1}, \boldsymbol{\alpha}_n) : \nabla\boldsymbol{\eta} - \boldsymbol{b}_{n+1} \cdot \boldsymbol{\eta}] \, \mathrm{d}v - \int_{\partial\Omega_{n+1}} \boldsymbol{t}_{n+1} \cdot \boldsymbol{\eta} \, \mathrm{d}a = 0, \quad \forall \boldsymbol{\eta} \in \mathscr{V}, \tag{2.89}$$

where the space of kinematically admissible displacement fields $\mathscr{K}_{n+1}$ is defined by

$$\mathscr{K}_{n+1} \equiv \{\boldsymbol{u} : \Omega \times \mathscr{R} \to \mathscr{U} \mid \boldsymbol{u}_{n+1}(\boldsymbol{X}) = \boldsymbol{u}_{\text{presc},n+1}(\boldsymbol{X}),\ \boldsymbol{X} \in \partial\Omega_{\text{motion},0}\}. \tag{2.90}$$

and in the material description as

Problem 2.6 | Material incremental quasi-static mechanical initial BVP.

Given the set of internal variables $\boldsymbol{\alpha}_n$ at t_n, the prescribed body and traction force fields $\boldsymbol{b}_{0,n+1}$ and $\boldsymbol{t}_{0,n+1}$ at t_{n+1}, and the prescribed deformating gradient $\boldsymbol{F}_{n+1}$ at t_{n+1}, find the kinematically admissible displacement field $\boldsymbol{u}_{n+1} \in \mathscr{K}_{n+1}$ such that the body $\mathscr{B}$ is in equilibrium as stated by the virtual Work Principle

$$\int_{\Omega_{n+1}} [\widehat{\boldsymbol{P}}(\boldsymbol{F}_{n+1}, \boldsymbol{\alpha}_n) : \nabla_0\boldsymbol{\eta} - \boldsymbol{b}_{0,n+1} \cdot \boldsymbol{\eta}] \, \mathrm{d}v - \int_{\partial\Omega_{n+1}} \boldsymbol{t}_{0,n+1} \cdot \boldsymbol{\eta} \, \mathrm{d}a = 0, \quad \forall \boldsymbol{\eta} \in \mathscr{V}, \tag{2.91}$$

where the space of kinematically admissible displacement fields $\mathscr{K}_{n+1}$ is defined by

$$\mathscr{K}_{n+1} \equiv \{\boldsymbol{u} : \Omega \times \mathscr{R} \to \mathscr{U} \mid \boldsymbol{u}_{n+1}(\boldsymbol{X}) = \boldsymbol{u}_{\text{presc},n+1}(\boldsymbol{X}),\ \boldsymbol{X} \in \partial\Omega_{\text{motion},0}\}. \tag{2.92}$$

2.8 Finite Element Method

With the incremental weak form of the quasi-static mechanical constitutive initial boundary value problem now established, an approximated solution can be found making use of the Finite Elment Method.

2.8.1 Finite element concept

The first step in the Finite Element method is the discretization of the continuum domain Ω in a finite set of n_{elem} mutually exclusive subdomains called finite elements $\Omega^{(e)}$. The discretized domain, ${}^h\Omega$, is therefore an approximation to the continuum domain expressed by

$$\Omega \approx {}^h\Omega \equiv \bigcup_{e=1}^{n_{\text{elem}}} \Omega^{(e)}. \tag{2.93}$$

The space of virtual displacements $\mathscr{V}$, as well as, the space of kinematically admissible displacement fields $\mathscr{K}$, are also discretized in the same manner, with their discretized forms denoted by ${}^h\mathscr{V}$ and ${}^h\mathscr{K}$.

2.8.2 Interpolation functions

Let e be a generic finite element with n_{nodes} nodes, where each node i of coordinates $\boldsymbol{x}_i$ is associated with an interpolation function $N_i^{(e)}$. These interpolation functions are

often called shape functions and perform the required field interpolations inside the element domain $\Omega^{(e)}$.

Letting $a(\boldsymbol{x})$ be a generic field defined over $\Omega^{(e)}$, its interpolation at any point $\boldsymbol{x}$ inside the element is defined by the element shape functions as

$$a(\boldsymbol{x}) \approx {}^h a(\boldsymbol{x}) \equiv \sum_{i=1}^{n_{\text{nodes}}} a(\boldsymbol{x}_i) N_i^{(e)}(\boldsymbol{x}). \tag{2.94}$$

If, instead, $a(\boldsymbol{x})$ is a generic field defined over the global domain Ω, the interpolation of $a(\boldsymbol{x})$ at any point $\boldsymbol{x}$ is defined by the global shape functions, N^g, as

$$a(\boldsymbol{x}) \approx {}^h a(\boldsymbol{x}) \equiv \sum_{i=1}^{n_{\text{points}}} a(\boldsymbol{x}_i) N_i^g(\boldsymbol{x}), \tag{2.95}$$

where n_{points} is the total number of nodes of the finite element mesh. The discretized spaces ${}^h\mathscr{V}$ and ${}^h\mathscr{K}$ can now be defined as

$${}^h\mathscr{K} \equiv \left\{ {}^h\boldsymbol{u}(\boldsymbol{x}) = \sum_{i=1}^{n_{\text{points}}} \boldsymbol{u}(\boldsymbol{x}_i) N_i^g(\boldsymbol{x}) \mid \boldsymbol{u}(\boldsymbol{x}_i) = \boldsymbol{u}_{\text{presc}}(\boldsymbol{x}_i) \quad \text{if } \boldsymbol{x}_i \in \partial\Omega_{\text{motion},0} \right\}, \tag{2.96}$$

$${}^h\mathscr{V} \equiv \left\{ {}^h\boldsymbol{\eta}(\boldsymbol{x}) = \sum_{i=1}^{n_{\text{points}}} \boldsymbol{\eta}(\boldsymbol{x}_i) N_i^g(\boldsymbol{x}) \mid \boldsymbol{\eta}(\boldsymbol{x}_i) = \boldsymbol{0} \quad \text{if } \boldsymbol{x}_i \in \partial\Omega_{\text{motion},0} \right\}. \tag{2.97}$$

2.8.3 Interpolation matrix and discrete gradient operators

The global shape functions can be conveniently assembled in the so-called global interpolation matrix as

$$\mathbf{N}^g(\boldsymbol{x}) \equiv \left[\text{diag}[N_1^g(\boldsymbol{x})] \; \text{diag}[N_2^g(\boldsymbol{x})] \; \cdots \; \text{diag}[N_{n_{\text{points}}}^g(\boldsymbol{x})] \right], \tag{2.98}$$

where $\text{diag}[N_i^g]$ is a diagonal matrix $n_{\text{dim}} \times n_{\text{dim}}$

$$\text{diag}[N_i^g(\boldsymbol{x})] \equiv \begin{bmatrix} N_i^g & 0 & \cdots & 0 \\ 0 & N_i^g & \cdots & 0 \\ \vdots & \vdots & \ddots & \vdots \\ 0 & 0 & \cdots & N_i^g \end{bmatrix} \tag{2.99}$$

where n_{dim} is the number of degrees of freedom per node.

Defining the global vector of nodal displacements as

$$\mathbf{u} = \left[u_1^1, \ldots, u_{n_{\text{dim}}}^1, \ldots, u_1^{n_{\text{points}}}, \ldots, u_{n_{\text{dim}}}^{n_{\text{points}}} \right]^T, \tag{2.100}$$

the displacement field $\boldsymbol{u}(\boldsymbol{x})$ defined over the global domain Ω, can be found from Equation (2.95) at any point $\boldsymbol{x}$ as

$${}^h\boldsymbol{u}(\boldsymbol{x}) \equiv \mathbf{N}^g(\boldsymbol{x})\mathbf{u}, \quad {}^h\boldsymbol{u} \in {}^h\mathscr{K}. \tag{2.101}$$

2.8.4 Spatial discretization

Applying the aforementioned finite element discretization to the incremental quasi-static mechanical constitutive initial boundary value problem, it can then be written in the spatial description as

$$\int_{^h\Omega} \left[\widehat{\boldsymbol{\sigma}}^T \mathbf{B}^g \boldsymbol{\eta} - \mathbf{b}_{n+1} \cdot \mathbf{N}^g \boldsymbol{\eta} \right] \mathrm{d}v - \int_{\partial^h\Omega_{\text{traction}}} \mathbf{t}_{n+1} \cdot \mathbf{N}^g \boldsymbol{\eta} \, \mathrm{d}a = 0, \quad \forall \boldsymbol{\eta} \in {}^h\mathscr{V}, \tag{2.102}$$

where $\mathbf{B}^g$ is the discrete symmetric global gradient operator, defined for a 2D problem in Cartesian coordinates as

$$\mathbf{B}^g \equiv \begin{bmatrix} \dfrac{\partial N_1^g}{\partial x} & 0 & \dfrac{\partial N_2^g}{\partial x} & 0 & \cdots & \dfrac{\partial N_{n_{\text{points}}}^g}{\partial x} & 0 \\ 0 & \dfrac{\partial N_1^g}{\partial y} & 0 & \dfrac{\partial N_2^g}{\partial y} & \cdots & 0 & \dfrac{\partial N_{n_{\text{points}}}^g}{\partial y} \\ \dfrac{\partial N_1^g}{\partial y} & \dfrac{\partial N_1^g}{\partial x} & \dfrac{\partial N_2^g}{\partial y} & \dfrac{\partial N_2^g}{\partial x} & \cdots & \dfrac{\partial N_{n_{\text{points}}}^g}{\partial y} & \dfrac{\partial N_{n_{\text{points}}}^g}{\partial x} \end{bmatrix}. \tag{2.103}$$

Equation (2.102) can be rewritten as

$$\left\{ \int_{^h\Omega} \left[\mathbf{B}^{g\,T} \widehat{\boldsymbol{\sigma}}(\boldsymbol{F}_{n+1}, \boldsymbol{\alpha}_n) - \mathbf{N}^{g\,T} \mathbf{b}_{n+1} \right] \mathrm{d}v - \int_{\partial^h\Omega_{\text{traction}}} \mathbf{N}^{g\,T} \mathbf{t}_{n+1} \, \mathrm{d}a \right\}^T \boldsymbol{\eta} = 0, \quad \forall \boldsymbol{\eta} \in {}^h\mathscr{V}, \tag{2.104}$$

and, since it must be satisfied for any $\boldsymbol{\eta} \in {}^h\mathscr{V}$, the incremental quasi-static discretized mechanical constitutive initial boundary value problem may, thus, be stated in the spatial description as

Problem 2.7 | Spatial incremental discretized quasi-static mechanical initial BVP.

Given the set of internal variables $\boldsymbol{\alpha}_n$ at t_n, the prescribed body and traction force fields $\mathbf{b}_{n+1}$ and $\mathbf{t}_{n+1}$, and the prescribed deformation gradient $\boldsymbol{F}_{n+1}$ at t_{n+1}, find the kinematically admissible nodal displacement field $\mathbf{u}_{n+1} \in {}^h\mathscr{K}_{n+1}$ such that the body $\mathscr{B}$ is in equilibrium as stated by the Virtual Work Principle

$$\boldsymbol{r}(\mathbf{u}_{n+1}) \equiv \mathbf{f}^{\text{int}}(\mathbf{u}_{n+1}) - \mathbf{f}_{n+1}^{\text{ext}} = \mathbf{0}, \tag{2.105}$$

where $\mathbf{f}^{\text{int}}$ e $\mathbf{f}_{n+1}^{\text{ext}}$ are the global vectors of internal and external forces defined as

$$\mathbf{f}^{\text{int}} \equiv \int_{^h\Omega_0} \mathbf{B}^{g\,T} \widehat{\boldsymbol{\sigma}}(\boldsymbol{F}_{n+1}, \boldsymbol{\alpha}_n) \, \mathrm{d}v, \tag{2.106}$$

$$\mathbf{f}_{n+1}^{\text{ext}} \equiv \int_{^h\Omega_0} \mathbf{N}^{g\,T} \mathbf{b}_{n+1} \, \mathrm{d}v + \int_{\partial^h\Omega_{\text{traction}}} \mathbf{N}^{g\,T} \mathbf{t}_{n+1} \, \mathrm{d}a. \tag{2.107}$$

In a material description, Equation (2.104) is written as

$$\left\{\int_{{}^h\Omega}\left[\mathbf{G}^{g\,T}\widehat{\boldsymbol{P}}(\boldsymbol{\alpha}_n,\boldsymbol{F}_{n+1})-\mathbf{N}^{g\,T}\mathbf{b}_{0,n+1}\right]\mathrm{d}v - \int_{\partial^h\Omega_{\text{traction},0}}\mathbf{N}^{g\,T}\mathbf{t}_{0,n+1}\,\mathrm{d}a\right\}^T\boldsymbol{\eta}=0,\quad\forall\boldsymbol{\eta}\in{}^h\mathscr{V},\tag{2.108}$$

where $\mathbf{G}^g$ is the discrete global gradient operator, defined for a 2D problem in Cartesian coordinates as

$$\mathbf{G}^g\equiv\begin{bmatrix}\frac{\partial N_1^g}{\partial x} & 0 & \frac{\partial N_2^g}{\partial x} & 0 & \cdots & \frac{\partial N_{n_{\text{points}}}^g}{\partial x} & 0\\ 0 & \frac{\partial N_1^g}{\partial x} & 0 & \frac{\partial N_2^g}{\partial x} & 0 & \cdots & \frac{\partial N_{n_{\text{points}}}^g}{\partial x}\\ \frac{\partial N_1^g}{\partial y} & 0 & \frac{\partial N_2^g}{\partial y} & \cdots & 0 & \frac{\partial N_{n_{\text{points}}}^g}{\partial y} & 0\\ 0 & \frac{\partial N_1^g}{\partial y} & 0 & \frac{\partial N_2^g}{\partial y} & \cdots & 0 & \frac{\partial N_{n_{\text{points}}}^g}{\partial y}\end{bmatrix}.\tag{2.109}$$

As for the spatial description, Equation (2.108) must be satisfied for any $\boldsymbol{\eta}\in{}^h\mathscr{V}$, the incremental quasi-static discretized mechanical constitutive initial boundary value problem may, thus, be stated in the material description as

Problem 2.8 | Material incremental discretized quasi-static mechanical initial BVP.

Given the set of internal variables $\boldsymbol{\alpha}_n$ at t_n, the prescribed body and traction force fields $\mathbf{b}_{0,n+1}$ and $\mathbf{t}_{0,n+1}$, and the prescribed deformation gradient $\boldsymbol{F}_{n+1}$ at t_{n+1}, find the kinematically admissible nodal displacement field $\mathbf{u}_{n+1}\in{}^h\mathscr{K}_{n+1}$ such that the body $\mathscr{B}$ is in equilibrium as stated by the Virtual Work Principle

$$\mathbf{r}(\mathbf{u}_{n+1})\equiv\mathbf{f}^{\text{int}}(\mathbf{u}_{n+1})-\mathbf{f}^{\text{ext}}_{n+1}=\mathbf{0},\tag{2.110}$$

where $\mathbf{f}^{\text{int}}$ e $\mathbf{f}^{\text{ext}}_{n+1}$ are the global vectors of internal and external forces defined as

$$\mathbf{f}^{\text{int}}\equiv\int_{{}^h\Omega_0}\mathbf{G}^{g\,T}\widehat{\boldsymbol{P}}(\boldsymbol{F}_{n+1},\boldsymbol{\alpha}_n)\,\mathrm{d}v,\tag{2.111}$$

$$\mathbf{f}^{\text{ext}}_{n+1}\equiv\int_{{}^h\Omega_0}\mathbf{N}^{g\,T}\mathbf{b}_{0,n+1}\,\mathrm{d}v+\int_{\partial^h\Omega_{\text{traction},0}}\mathbf{N}^{g\,T}\mathbf{t}_{0,n+1}\,\mathrm{d}a.\tag{2.112}$$

The global vectors for the internal and external forces are usually obtained by assemblage of their elemental counterparts as

$$\mathbf{f}^{\text{int}}=\mathop{\mathsf{A}}_{e=1}^{n_{\text{elem}}}\left(\mathbf{f}^{\text{int}}\right)^{(e)},\tag{2.113}$$

$$\mathbf{f}^{\text{ext}}=\mathop{\mathsf{A}}_{e=1}^{n_{\text{elem}}}\left(\mathbf{f}^{\text{ext}}\right)^{(e)},\tag{2.114}$$

where the elemental vectors in the spatial description are defined as

$$\left(\mathbf{f}^{\text{int}}\right)^{(e)} \equiv \int_{{}^{h}\Omega^{(e)}} \mathbf{B}^T \widehat{\boldsymbol{\sigma}}(\boldsymbol{F}_{n+1}, \boldsymbol{\alpha}_n)\, \mathrm{d}v, \tag{2.115}$$

$$\left(\mathbf{f}^{\text{ext}}_{n+1}\right)^{(e)} \equiv \int_{{}^{h}\Omega^{(e)}} \mathbf{N}^T \mathbf{b}_{n+1}\, \mathrm{d}v + \int_{\partial {}^{h}\Omega^{(e)}_{\text{traction}}} \mathbf{N}^T \mathbf{t}_{n+1}\, \mathrm{d}a, \tag{2.116}$$

and in material description as

$$\left(\mathbf{f}^{\text{int}}\right)^{(e)} \equiv \int_{{}^{h}\Omega^{(e)}_0} \mathbf{G}^T \widehat{\boldsymbol{P}}(\boldsymbol{F}_{n+1}, \boldsymbol{\alpha}_n)\, \mathrm{d}v, \tag{2.117}$$

$$\left(\mathbf{f}^{\text{ext}}_{n+1}\right)^{(e)} \equiv \int_{{}^{h}\Omega^{(e)}_0} \mathbf{N}^T \mathbf{b}_{0,n+1}\, \mathrm{d}v + \int_{\partial {}^{h}\Omega^{(e)}_{0,\text{traction}}} \mathbf{N}^T \mathbf{t}_{0,n+1}\, \mathrm{d}a. \tag{2.118}$$

The matrices **N**, **B** and **G** are the elemental interpolation matrix, the symmetric elemental gradient operator and the discrete elemental gradient operator, respectively.

2.8.5 Newton-Raphson Method

The equilibrium equation, Equation (2.105) in a spatial description and Equation (2.110) in a material description, is generally nonlinear due to geometrical and/or material nonlinearities. The Newton-Raphson Method is an efficient and robust iterative scheme with a quadratic convergence rate that is often use to solve the equilibrium equation at each time increment, t_n. Its application to this problem is detailed by de Souza Neto et al. (2011a).

2.8.6 Numerical integration

In the Finite Element Method, the integrations over the element domain are generally performed numerically using the Gaussian Quadrature Method. Stating it's application succinctly, let $a(\boldsymbol{x})$ be a generic field, if there is a coordinate transformation from a local (or natural) normalized domain Υ to the element domain $\Omega^{(e)}$, $\boldsymbol{x}\colon \Upsilon \to \Omega^{(e)}$, the integral of $a(\boldsymbol{x})$ over the domain $\Omega^{(e)}$ can be numerically determined as

$$\int_{\Omega^{(e)}} a(\boldsymbol{x})\, \mathrm{d}\boldsymbol{x} = \int_{\Upsilon} a(\boldsymbol{x}(\boldsymbol{\zeta}))\, j(\boldsymbol{\zeta})\, \mathrm{d}\boldsymbol{\zeta} \approx \sum_{i=1}^{n_{\text{GP}}} w_i\, a(\boldsymbol{x}(\boldsymbol{\zeta}_i))\, j(\boldsymbol{\zeta}_i), \tag{2.119}$$

where $\boldsymbol{\zeta}_i$ and w_i, $i = 1,\ldots,n_{\text{GP}}$ are the positions and weights of the Gauss sampling points in the domain Υ and $j(\boldsymbol{\zeta})$ is the determinant of the coordinate transformation's Jacobian defined as

$$j(\boldsymbol{\zeta}) = \det\left(\frac{\partial \boldsymbol{x}}{\partial \boldsymbol{\zeta}}\right). \tag{2.120}$$

Page intentionally left blank.

Chapter 3

First-order Homogenization-based Hierarchical Multi-scale Model

This chapter presents the formulation and numerical treatment of a first-order strain-driven hierarchical multi-scale model based on computational homogenization. The formulation adopted stems from the variational multi-scale constitutive theory established by de Souza Neto and coworkers (de Souza Neto and Feijóo, 2006, 2008; de Souza Neto et al., 2011b; Perić et al., 2011; Blanco et al., 2016).

3.1 The first order homogenized constitutive response

In a first-order hierarchical multi-scale model based on computational homogenization, the microscale analysis is included in the spatial (and material) incremental discretized quasi-static mechanical initial BVP (see Section 2.8.4). This is achieved by replacing the computation of the stress incremental constitutive function at a given point with the solution of a microscopic equilibrium problem over the RVE (see Section 1.1 for the definition of RVE) associated with same point. As stated in Section 2.8.6, the integrations over the element domain are generally performed numerically by means of the Gaussian Quadrature Method, thus, the stress incremental constitutive function must be computed at the Gauss integration points. Therefore, the total number of RVEs that must be considered is equal to the the total number of integration points required to integrate the macroscopic finite element domain.

The microscopic equilibrium problem just mentioned is driven by the macroscopic deformation gradient, $\boldsymbol{F}(\boldsymbol{x},t)$, and its solution must satisfy the assumed microscale boundary conditions. After the solution of the microscopic equilibrium problem is found, the computation of the macroscopic stress tensor, $\boldsymbol{P}(\boldsymbol{x},t)$ by computational homogenization allows one to return to the macroscale. The macroscopic solution procedure can then carry on in the standard way.

In order to clearly distinguish quantities associated with the two scales, the following notation is adopted henceforth. At the macroscale, the domain and its boundary are denoted by Ω and $\partial\Omega$, and the coordinates of a material point are given by $\boldsymbol{X}$ and $\boldsymbol{x}$ in the reference and deformed configurations, respectively, in accordance with the

previous chapter. At the microscale, the domain and its boundary are denoted by Ω_μ and $\partial\Omega_\mu$, and the coordinates of a material point are given by $\boldsymbol{Y}$ and $\boldsymbol{y}$ in the reference and deformed configurations, respectively. The subscript μ generally denotes microscale fields.

3.2 Scale Transition Theory

The three key assumptions underlying the hierarchical multi-scale models are the Principle of Scales Separation, associated with the RVE characteristic dimension, the kinematic multi-scale relations, relating the macroscopic and microscopic kinematic quantities, and the Principle of Multi-Scale Virtual Power, establishing the energetic equivalence between both scales.

3.2.1 Principle of Scales Separation

According to Hill (1963), the RVE must be large enough to be representative of the domain in an average sense. However, the RVE must also satisfy the so called Principle of Scales Separation, that is, the characteristic dimension of the RVE, denoted by l_{RVE}, must be simultaneously much smaller than the macroscopic characteristic dimension, l_{macro}, and much larger than the characteristic dimensions of the microstructure heterogeneities, l_{micro}. Stated symbolically as $l_{\text{micro}} \ll l_{\text{RVE}} \ll l_{\text{macro}}$.

3.2.2 Multi-scale kinematics

In order to formulate the multi-scale hierarchical model within the Method of Multi-Scale Virtual Power, the relation between the kinematic quantities of both scales are found from the procedures of kinematic insertion and kinematic homogenization.

Kinematic insertion

The procedure of kinematic insertion allows the downscale of the macroscopic quantities, finding their contribution to the microscale kinematics. Since the whole RVE is associated with some point $\boldsymbol{X}$ with a deformation gradient $\boldsymbol{F}(\boldsymbol{X},t)$, it is assumed that all the points in the RVE are subject to the associated linear displacement field, $\boldsymbol{u}^{\text{lin}}$, given by

$$\boldsymbol{u}_\mu^{\text{lin}} = \left[\boldsymbol{F}(\boldsymbol{X},t) - \boldsymbol{I}\right]\boldsymbol{Y}, \tag{3.1}$$

for some $\boldsymbol{Y}$ in Ω_μ. However, this displacement field leaves, in general, the RVE in a nonequilibrium state, thus, there is a need to consider an additional fluctuation component, $\tilde{\boldsymbol{u}}_\mu$, to ensure its equilibrium. Without loss of generality the displacement inside the RVE, $\boldsymbol{u}_\mu$, can be written as

$$\boldsymbol{u}_\mu(\boldsymbol{Y},t) = \boldsymbol{u}_\mu^{\text{lin}} + \tilde{\boldsymbol{u}}_\mu(\boldsymbol{Y},t), \tag{3.2}$$

Since the linear component of the displacement is fully known from the macroscopic deformation gradient, the unknowns of the microscopic equilibrium problem are the displacement fluctuations.

Accordingly, the microscopic deformation gradient can also be decomposed as

$$\boldsymbol{F}_\mu(\boldsymbol{Y},t) = \boldsymbol{F}(\boldsymbol{X},t) + \nabla_0\tilde{\boldsymbol{u}}_\mu(\boldsymbol{Y},t). \tag{3.3}$$

Kinematic homogenization

The kinematic homogenization is the procedure associated with the upscale of the microscopic kinematic quantities to their macroscopic counterparts and it is based on the volume averaging of the interest field over the RVE in its reference configuration.

Letting $\boldsymbol{A}(\boldsymbol{Y})$ be some generic tensorial field at the microscale, its macroscopic counterpart can be found from

$$\boldsymbol{A}(\boldsymbol{X}) = \frac{1}{v_{\mu,0}} \int_{\Omega_{\mu,0}} \boldsymbol{A}_{\mu}(\boldsymbol{Y}) \, \mathrm{d}v, \tag{3.4}$$

where $v_{\mu,0}$ denotes the RVE volume in the reference configuration. The macroscopic deformation gradient, which drives the microscale deformation, can then be defined as

$$\boldsymbol{F}(\boldsymbol{X}, t) = \frac{1}{v_{\mu,0}} \int_{\Omega_{\mu,0}} \boldsymbol{F}_{\mu}(\boldsymbol{Y}, t) \, \mathrm{d}v, \tag{3.5}$$

or directly from the displacement field as

$$\boldsymbol{F}(\boldsymbol{X}, t) = \boldsymbol{I} + \frac{1}{v_{\mu,0}} \int_{\Omega_{\mu,0}} \nabla_0 \boldsymbol{u}_{\mu}(\boldsymbol{Y}, t) \, \mathrm{d}v. \tag{3.6}$$

Making use of the so-called Gauss's theorem, the macroscopic deformation gradient can also be found from an integral along the surface of the RVE, as

$$\boldsymbol{F}(\boldsymbol{X}, t) = \boldsymbol{I} + \frac{1}{v_{\mu,0}} \int_{\partial\Omega_{\mu,0}} \boldsymbol{u}_{\mu}(\boldsymbol{Y}, t) \otimes \boldsymbol{n}(\boldsymbol{Y}) \, \mathrm{d}a, \tag{3.7}$$

where $\boldsymbol{n}(\boldsymbol{Y})$ is the outward unitary vector normal to the RVE boundary in its reference configuration.

Kinematic admissibility

As consequence of the multi-scale kinematic assumptions, the kinematic insertion and homogenization, there is a restriction on the microscopic displacement fluctuations. This restriction can be found substituting Equation (3.2) into Equation (3.6), obtaining

$$\boldsymbol{F}(\boldsymbol{X}, t) = \boldsymbol{F}(\boldsymbol{X}, t) + \frac{1}{v_{\mu,0}} \int_{\Omega_{\mu,0}} \nabla_0 \tilde{\boldsymbol{u}}_{\mu}(\boldsymbol{Y}, t) \, \mathrm{d}v, \tag{3.8}$$

which can be rewritten as

$$\int_{\Omega_{\mu,0}} \nabla_0 \tilde{\boldsymbol{u}}_{\mu}(\boldsymbol{Y}, t) \, \mathrm{d}v = 0. \tag{3.9}$$

Furthermore, aplying Gauss's theorem once again, one finds

$$\int_{\partial\Omega_{\mu,0}} \nabla_0 \tilde{\boldsymbol{u}}_{\mu}(\boldsymbol{Y}, t) \otimes \boldsymbol{n}(\boldsymbol{Y}) \, \mathrm{d}a = \boldsymbol{0}. \tag{3.10}$$

Therefore, the set of kinematically admissible minimally constrained microscopic displacement fluctuation can be defined as

$$\tilde{\mathscr{K}}_\mu \equiv \left\{ \tilde{\boldsymbol{u}}_\mu,\ \text{sufficiently regular} \,\middle|\, \int_{\partial\Omega_{\mu,0}} \nabla_0 \tilde{\boldsymbol{u}}_\mu(\boldsymbol{Y},t) \otimes \boldsymbol{n}(\boldsymbol{Y})\, \mathrm{d}a = \boldsymbol{0} \right\}. \tag{3.11}$$

3.2.3 Principle of Multi-Scale Virtual Power

The Principle of Multi-Scale Virtual Power establishes the connection between macro and microscales invoking power conservation between the two. It can be stated formally as

$$\boldsymbol{P}(\boldsymbol{X},t) : \delta\boldsymbol{F}(\boldsymbol{X},t) = \frac{1}{v_{\mu,0}} \int_{\Omega_{\mu,0}} \boldsymbol{P}_\mu(\boldsymbol{Y},t) : \delta\boldsymbol{F}_\mu(\boldsymbol{Y},t)\, \mathrm{d}v, \tag{3.12}$$

where $\delta\boldsymbol{F}(\boldsymbol{X},t)$ and $\delta\boldsymbol{F}_\mu(\boldsymbol{Y},t)$ are arbitrary macroscopic and microscopic deformation gradients, respectively. Furthermore, from the relation between the macroscopic and the microscopic deformation gradient, it is also found that

$$\boldsymbol{P}(\boldsymbol{X},t) : \delta\boldsymbol{F}(\boldsymbol{X},t) = \frac{1}{v_{\mu,0}} \int_{\Omega_{\mu,0}} \boldsymbol{P}_\mu(\boldsymbol{Y},t) : \left[\delta\boldsymbol{F}(\boldsymbol{X},t) + \nabla_0 \boldsymbol{\eta}_\mu \right] \mathrm{d}v, \tag{3.13}$$

for any virtual macroscopic deformation gradient, $\delta\boldsymbol{F}(\boldsymbol{X},t)$, and any admissible virtual microscopic displacement fluctuation, $\boldsymbol{\eta}_\mu$.

Assuming that $\delta\boldsymbol{F}(\boldsymbol{X},t) = \boldsymbol{0}$, the PMVP renders the weak microscale equilibrium equations in both spatial and material description as

$$\int_{\Omega_\mu} \boldsymbol{\sigma}_\mu(\boldsymbol{y},t) : \nabla\boldsymbol{\eta}_\mu\, \mathrm{d}v = 0, \quad \forall \boldsymbol{\eta}_\mu \in \mathscr{V}_\mu, \tag{3.14}$$

and

$$\int_{\Omega_{\mu,0}} \boldsymbol{P}_\mu(\boldsymbol{Y},t) : \nabla_0\boldsymbol{\eta}_\mu\, \mathrm{d}v = 0, \quad \forall \boldsymbol{\eta}_\mu \in \mathscr{V}_\mu, \tag{3.15}$$

respectively, where the virtual displacement fluctuations belong to the set admissible displacement fluctuations, $\mathscr{V}_\mu \subseteq \tilde{\mathscr{K}}_\mu$. The microscale equilibrium problem may, thus, be stated in the spatial description as

Problem 3.1 | Spatial quasi-static microscale mechanical initial BVP.

For a given macroscale material particle $\boldsymbol{x}$ and the associated macroscopic deformation gradient $\boldsymbol{F}(\boldsymbol{x},t)$, find a kinematically admissible microscopic displacement fluctuation function, $\tilde{\boldsymbol{u}} \in \tilde{\mathscr{K}}_\mu$, such that, for every $t \in [t_0, t_{\text{end}}]$, the RVE is in equilibrium as stated by the Virtual Work Principle

$$\int_{\Omega_\mu} \boldsymbol{\sigma}_\mu(\boldsymbol{y},t) : \nabla\boldsymbol{\eta}_\mu\, \mathrm{d}v = 0, \quad \boldsymbol{\eta}_\mu \in \mathscr{V}_\mu, \tag{3.16}$$

where the space of virtual displacements fluctuations, $\mathscr{V}_\mu$, at time t is defined by the set of kinematically admissible displacement fluctuations constrained by the adopted microscale boundary condition.

and in the material description

Problem 3.2 | Material quasi-static microscale mechanical initial BVP.

For a given macroscale material particle $\boldsymbol{X}$ and the associated macroscopic deformation gradient $\boldsymbol{F}(\boldsymbol{X},t)$, find a kinematically admissible microscopic displacement fluctuation function, $\tilde{\boldsymbol{u}} \in \tilde{\mathscr{K}}_\mu$, such that, for every $t \in [t_0, t_{\text{end}}]$, the RVE is in equilibrium as stated by the Virtual Work Principle

$$\int_{\Omega_{\mu,0}} \boldsymbol{P}_\mu(\boldsymbol{Y},t) : \nabla_0 \boldsymbol{\eta}_\mu \, \mathrm{d}v = 0, \quad \boldsymbol{\eta}_\mu \in \mathscr{V}_\mu, \tag{3.17}$$

where the space of virtual displacements fluctuations, $\mathscr{V}_\mu$, at time t is defined by the set of kinematically admissible displacement fluctuations constrained by the adopted microscale boundary condition.

Another consequence of the PMVP, can be found comparing it to the respective general Virtual Work Principle equilibrium equations in the spatial or material descriptions. These are written, respectively as

$$\int_{\Omega_\mu} \left[\boldsymbol{\sigma}_\mu(\boldsymbol{y},t) : \nabla \boldsymbol{\eta}_\mu - \boldsymbol{b}_\mu \cdot \boldsymbol{\eta}_\mu \right] \mathrm{d}v - \int_{\partial\Omega_\mu} \boldsymbol{t}_\mu(\boldsymbol{y},t) \cdot \boldsymbol{\eta}_\mu \, \mathrm{d}a = 0, \quad \forall \boldsymbol{\eta}_\mu \in \mathscr{V}_\mu, \tag{3.18}$$

and

$$\int_{\Omega_{\mu,0}} \left[\boldsymbol{P}_\mu(\boldsymbol{Y},t) : \nabla_0 \boldsymbol{\eta}_\mu - \boldsymbol{b}_{\mu,0} \cdot \boldsymbol{\eta}_\mu \right] \mathrm{d}v - \int_{\partial\Omega_{\mu,0}} \boldsymbol{t}_{\mu,0}(\boldsymbol{Y},t) \cdot \boldsymbol{\eta}_\mu \, \mathrm{d}a = 0, \quad \forall \boldsymbol{\eta}_\mu \in \mathscr{V}_\mu. \tag{3.19}$$

Thus, it can be concluded that the microscopic body and traction forces do not produce work, i.e.

$$\int_{\partial\Omega_\mu} \boldsymbol{t}_\mu(\boldsymbol{y},t) \cdot \tilde{\boldsymbol{u}}_\mu(\boldsymbol{y},t) \, \mathrm{d}a = 0, \quad \int_{\Omega_\mu} \boldsymbol{b}_\mu(\boldsymbol{y},t) \cdot \tilde{\boldsymbol{u}}_\mu(\boldsymbol{y},t) \, \mathrm{d}v = 0, \tag{3.20}$$

$$\int_{\partial\Omega_{\mu,0}} \boldsymbol{t}_{\mu,0}(\boldsymbol{Y},t) \cdot \tilde{\boldsymbol{u}}_\mu(\boldsymbol{Y},t) \, \mathrm{d}a = 0, \quad \int_{\Omega_{\mu,0}} \boldsymbol{b}_{\mu,0}(\boldsymbol{Y},t) \cdot \tilde{\boldsymbol{u}}_\mu(\boldsymbol{Y},t) \, \mathrm{d}v = 0, \tag{3.21}$$

meaning that the microscopic body and traction forces can be seen as reaction forces arising from the enforcement of the kinematical constraints applied to the microscopic displacement field.

3.3 Microscale boundary conditions

The choice of a suitable microscale boundary condition is of great importance in a multi-scale model, as the microscopic displacement field is directly dependent on the type of constraints imposed on the RVE boundary.

The trivial solution of the microscale equilibrium problem consists in assuming that the microscale displacement fluctuations are null over the entire domain, i.e.

$$\tilde{\boldsymbol{u}}_\mu(\boldsymbol{Y},t) = \boldsymbol{0}, \quad \forall \boldsymbol{Y} \in \Omega_{\mu,0}. \tag{3.22}$$

and it is the most restrictive condition that can be applied to the RVE displacement field, the so-called Taylor hypothesis. This implies that the microscale displacement field is thus entirely defined by the imposed linear displacements as

$$\boldsymbol{u}_\mu(\boldsymbol{Y},t) = \left[\boldsymbol{F}(\boldsymbol{X},t) - \boldsymbol{I} \right] \boldsymbol{Y} = \boldsymbol{u}_\mu^{\text{lin}}, \quad \forall \boldsymbol{Y} \in \Omega_{\mu,0}. \tag{3.23}$$

Accordingly, the set of kinematically admissible microscopic displacement fluctuations constrained by the Taylor hypothesis is defined as

$$\mathscr{K}_{\mu}^{\text{Taylor}} \equiv \left\{ \tilde{\boldsymbol{u}}_{\mu}, \text{ sufficiently regular} \,\middle|\, \tilde{\boldsymbol{u}}_{\mu}(\boldsymbol{Y}, t) = \boldsymbol{0}, \quad \forall \boldsymbol{Y} \in \Omega_{\mu,0} \right\}. \tag{3.24}$$

Regarding non-trivial solutions, there are three microscale boundary conditions that are usually considered in multi-scale models, the so-called homogeneous boundary conditions, linear and uniform traction, and a periodic boundary condition. These are presented below, sorted by decreasing restriction on the microscopic displacement fluctuations.

Linear boundary condition

The linear boundary condition imposes null microscopic displacement fluctuations in the RVE boundary, i.e.

$$\tilde{\boldsymbol{u}}_{\mu}(\boldsymbol{Y}, t) = \boldsymbol{0}, \quad \forall \boldsymbol{Y} \in \partial\Omega_{\mu,0}. \tag{3.25}$$

Therefore, the microscopic displacement field in the RVE boundary is entirely defined by the imposed linear displacements as

$$\boldsymbol{u}_{\mu}(\boldsymbol{y}, t) = \left[\boldsymbol{F}(\boldsymbol{x}, t) - \boldsymbol{I} \right] \boldsymbol{Y} = \boldsymbol{u}_{\mu}^{\text{lin}}, \quad \forall \boldsymbol{y} \in \partial\Omega_{\mu}. \tag{3.26}$$

In accordance, the set of kinematically admissible microscopic displacement fluctuations constrained by the linear boundary condition can be defined as

$$\mathscr{K}_{\mu}^{\text{Linear}} \equiv \left\{ \tilde{\boldsymbol{u}}_{\mu}, \text{ sufficiently regular} \,\middle|\, \tilde{\boldsymbol{u}}_{\mu}(\boldsymbol{Y}, t) = \boldsymbol{0}, \quad \forall \boldsymbol{Y} \in \partial\Omega_{\mu,0} \right\}. \tag{3.27}$$

Periodic boundary condition

The periodic boundary condition assumes that the material microstructure can be represented by tiling the RVE in all directions, thus, implying displacement compatibility between opposite sides of the RVE boundary.

In order to formally state the periodic boundary condition, one considers that the RVE boundary is divided in d disjoint sets such that

$$\partial\Omega_{\mu,0} = \bigcup_{i=1}^{d} \partial\Omega_{\mu,0,i}. \tag{3.28}$$

Each subset $\partial\Omega_{\mu,0,i}$ is defined as

$$\partial\Omega_{\mu,0,i} = (\Gamma_i^- \cup \Gamma_i^+), \tag{3.29}$$

where Γ_i^+ and Γ_i^- are such that each point in the positive side, $\boldsymbol{Y}^+ \in \Gamma_i^+$, has its pair in the opposing negative side, $\boldsymbol{Y}^- \in \Gamma_i^-$. Furthermore, the unitary outward vectors $\boldsymbol{n}^+$ and $\boldsymbol{n}^-$, normal to Γ_i^+ and Γ_i^-, respectively, must be antisymmetric. Accordingly, the periodic boundary condition can now be stated as

$$\tilde{\boldsymbol{u}}_{\mu}(\boldsymbol{Y}^+, t) = \tilde{\boldsymbol{u}}_{\mu}(\boldsymbol{Y}^-, t), \tag{3.30}$$

meaning that the displacement fluctuations are equal in opposing sides of the RVE boundary. As a consequence of the PMVP, one can derive that the constraint just stated is only satisfied if the traction forces field is anti-periodic, i.e.

$$\boldsymbol{t}_{\mu,i}(\boldsymbol{Y}^+, t) = -\boldsymbol{t}_{\mu,i}(\boldsymbol{Y}^-, t). \tag{3.31}$$

Hence, the set of kinematically admissible microscopic displacement fluctuation fields constrained by the periodic boundary condition can be defined as

$$\tilde{\mathscr{K}}_{\mu}^{\text{Periodic}} \equiv \Big\{ \tilde{\boldsymbol{u}}_{\mu}, \text{ sufficiently regular } \Big| \\ \forall i = 1 \dots d \ \forall \{\boldsymbol{Y}^+, \boldsymbol{Y}^-\} \in \partial\Omega_{\mu,0,i} \ \tilde{\boldsymbol{u}}_{\mu,i}(\boldsymbol{Y}^+, t) = \tilde{\boldsymbol{u}}_{\mu,i}(\boldsymbol{Y}^-, t) \Big\} \tag{3.32}$$

Uniform traction boundary condition

The uniform traction boundary condition stands as the least restrictive boundary condition, requiring only that the microscopic displacement fluctuations satisfy the minimal constraint defined by Equation (3.10). This means that the set of kinematically admissible microscopic displacement fluctuations constrained by the uniform traction boundary condition is coincident with the set of kinematically admissible minimally constrained microscopic displacement fluctuations, i.e.

$$\tilde{\mathscr{K}}_{\mu}^{\text{U.Traction}} \equiv \tilde{\mathscr{K}} = \left\{ \tilde{\boldsymbol{u}}_{\mu}, \text{ sufficiently regular } \left| \int_{\partial\Omega_{\mu,0}} \tilde{\boldsymbol{u}}_{\mu}(\boldsymbol{Y}, t) \otimes \boldsymbol{n}(\boldsymbol{Y}) \, \mathrm{d}a = \boldsymbol{0} \right. \right\}. \tag{3.33}$$

Moreover, as a consequence of the PMVP it is possible to conclude that the traction along the RVE boundary is uniform and equal to the homogenized traction, i.e.

$$\boldsymbol{P}_{\mu}(\boldsymbol{Y}, t)\boldsymbol{n}(\boldsymbol{Y}, t) = \boldsymbol{P}(\boldsymbol{X}, t)\boldsymbol{n}(\boldsymbol{Y}, t), \quad \boldsymbol{Y} \in \partial\Omega_{\mu,0}. \tag{3.34}$$

3.3.1 Homogenized stress tensor

After solving the microscale equilibrium problem, the macroscopic stress tensor can be determined by homogenization through the PMVP, setting $\delta\tilde{\boldsymbol{u}}(\boldsymbol{Y}, t) = \boldsymbol{0}$, as a volume average of its microscopic counterpart,

$$\boldsymbol{P}(\boldsymbol{X}, t) = \frac{1}{v_{\mu,0}} \int_{\Omega_{\mu,0}} \boldsymbol{P}_{\mu}(\boldsymbol{Y}, t) \, \mathrm{d}v. \tag{3.35}$$

From the relation between the First Piola-Kirchhoff stress tensor and the Cauchy stress tensor (see Equation (2.32)) one finds

$$\boldsymbol{\sigma} = \frac{1}{J}\boldsymbol{P}\boldsymbol{F}^T. \tag{3.36}$$

3.4 Time discretization of the microscale equilibrium problem

The time discretization of the microscale equilibrium follows the same approach presented in Section 2.7, where an algorithm based in approximated incremental constitutive functions is adopted. Thus, considering the time interval $[t_n, t_{n+1}]$, the same requirements set in Equations (2.86)-(2.88) must be met, denoting the microscopic internal variables as $\boldsymbol{\beta}$ instead. Applying such time discretization scheme, it is then possible to state the incremental version of the microscale equilibrium problem in both spatial and material descriptions as follows

Problem 3.3 | Spatial incremental quasi-static microscale mechanical initial BVP.

For a given macroscale material particle $\boldsymbol{x}$, the associated macroscopic deformation gradient $\boldsymbol{F}(\boldsymbol{x},t)$ at t_{n+1} and the set of internal variables $\boldsymbol{\beta}_n$ at t_n, find the kinematically admissible microscopic displacement fluctuations, $\tilde{\boldsymbol{u}}_{\mu,n+1} \in \tilde{\mathscr{K}}_{\mu,n+1}$, such that the RVE is in equilibrium as stated by the Principle of Multi-scale Virtual Power

$$\int_{\Omega_\mu} \boldsymbol{\sigma}_\mu(\boldsymbol{y},t) : \nabla \boldsymbol{\eta}_\mu \, \mathrm{d}v, \quad \boldsymbol{\eta}_\mu \in \mathscr{V}_\mu, \tag{3.37}$$

where the space of admissible displacement fluctuations, $\tilde{\mathscr{K}}_{\mu,n+1}$, at time t_{n+1}, is defined by the set of kinematically admissible displacement fluctuations constrained by the adopted microscale boundary condition.

and in the material description

Problem 3.4 | Material incremental quasi-static microscale mechanical initial BVP.

For a given macroscale material particle $\boldsymbol{X}$ and the associated macroscopic deformation gradient $\boldsymbol{F}(\boldsymbol{X},t)$, find a kinematically admissible microscopic displacement fluctuation function, $\tilde{\boldsymbol{u}} \in \tilde{\mathscr{K}}_\mu$, such that, for every $t \in [t_0, t_{\text{end}}]$, the RVE is in equilibrium as stated by the Virtual Work Principle

$$\int_{\Omega_{\mu,0}} \boldsymbol{P}_\mu(\boldsymbol{Y},t) : \nabla_0 \boldsymbol{\eta}_\mu \, \mathrm{d}v, \quad \boldsymbol{\eta}_\mu \in \mathscr{V}_\mu, \tag{3.38}$$

where the space of admissible displacement fluctuations, $\tilde{\mathscr{K}}_{\mu,n+1}$, at time t_{n+1}, is defined by the set of kinematically admissible displacement fluctuations constrained by the adopted microscale boundary condition.

3.5 Numerical discretization of the microscale equilibrium problem

The numerical solution of the incremental weak form of the quasi-static microscale initial BVP can be obtained by the Finite Element Method as detailed in Section 2.8. However, additional numerical treatment is required to enforce the microscale boundary conditions as well as to obtain the homogenized consistent tangent modulus. Both these topics are outside the scope of this document and their detailed treatment can be found in de Souza Neto et al. (2011a).

Chapter 4

Random Heterogeneous Materials

This chapter presents a systematic approach for the description of random heterogeneous materials, a class of materials which includes matrix-inclusion composites, whose structure is to be modeled as detailed in Section 1.1. It follows closely the work of Torquato (2013).

4.1 Definition

A material is said to be heterogeneous if it is composed of domains of different materials, so-called phases, such as a composite, or the same material in different states, such as a polycrystal. A subset of these materials is the so-called random heterogeneous materials, whose microstructure can only be characterized statistically, resting on the assumption that any sample of the medium is a realization of a specific random or stochastic process, or random field.

Examples There are numerous examples of heterogeneous materials. In fact, all natural and synthetic materials are heterogeneous at a sufficiently reduced scale. Their random microstructure can range from dispersions with varying degrees of clustering to complex interpenetrating connected multiphase media, including porous media.

Torquato (2013) presents the following example list of synthetic heterogeneous materials

- aligned and chopped fiber composites
- particulate composites
- interpenetrating multiphase composites
- cellular solids
- colloids
- gels
- foams

- microemulsions
- block copolymers
- fluidized beds
- concrete

and natural heterogeneous materials

- polycrystals
- soils
- sandstone
- granular media
- Earth's crust
- sea ice
- wood
- bone
- lungs
- blood
- animal and plant tissue
- cell aggregates and tumors.

Furthermore, one can stress the wide use of composites in automotive and aerospace applications, due to their ability to exhibit the best characteristics of the individual constituents according to their arrangement at microstructural level (Bargmann et al., 2018).

4.2 Impact of the microstructure on the effective properties

Estimates based only on incorporating volume-fraction information, i.e. simple mixture rules, cannot capture crucial microstructural features required to estimate accurately the effective properties of most composites. Thus, since the effective properties depend not only on the phase properties but are also sensitive to the details of the microstructure, it is natural to take the broader approach of predicting the effective properties from a more detailed characterization of the microstructure. One can then relate changes in the microstructure quantitatively to changes in the macroscopic properties.

Furthermore, analytical approaches for the estimation of the effective properties of heterogeneous materials use knowledge of statistical geometrical information about the microstructure, providing improved bounds on a variety of different effective properties of composite materials. In fact, it can be shown that the effective properties are

generally dependent on an infinite amount of statistical information about the microstructure, as a direct consequence of the complex field interactions that occur in the heterogeneous material (see Torquato (2013)).

It has also been established that modeling composite microstructures as periodic leads to computationally efficient models, that allow effective properties to be accurately predicted. However, when applied to failure/damage related predictions, these simple models generally do not perform well (Pyrz, 1994; Trias et al., 2006; Hojo et al., 2009).

4.3 Systematic description

The area of mathematical research that seeks to provide models and methods to characterize random patterns is called stochastic geometry and is the basis of the theory used to describe random heterogeneous materials.

To study random heterogeneous materials in a more meaningful way there is a need for a systematic theory able to describe the "details of the microstructure", such as the phase volume fraction, surface areas of interfaces, orientations, sizes, shapes, and spatial distribution of the phase domains, connectivity of the phases, and so on.

4.3.1 Preliminaries

The term random heterogeneous material implies that any sample of the medium is a realization of a specific random process or field and an ensemble is a collection of all such possible realizations.

To formalize these notions, let $(\Omega, \mathcal{F}, \mathcal{P})$ be some fixed probability space, where Ω is a sample space (set of "outcomes"), $\mathcal{F}$ is a σ-algebra of subsets of Ω (set of "events"), and $\mathcal{P}$ is a probability measure[1]. Let each point $\omega \in \Omega$ denote a realization of the random medium that occupies some subset $\mathcal{V}$ of the d-dimensional Euclidean space, i.e. $\mathcal{V} \subseteq \mathbb{R}^d$. In general, a medium is statistically characterized by a random variable $\xi(\boldsymbol{x};\omega)$, called the structure function, depending on all values of the position vector $\boldsymbol{x} \in \mathcal{V}$.

For a fixed ω, the structure function may be continuously varying function of position, e.g. porosity of geologic media or orientation of crystals in a polycrystal, or it may take on discrete values, e.g., fiber composites or colloids. For the sake of simplicity, the primary focus of this Chapter will be on two-phase random media, i.e., cases in which $\xi(\boldsymbol{x};\omega)$ takes on two different values. However, generalizations to multiphase are possible.

Each realization ω of the two-phase random medium occupies the region of space $\mathcal{V} \subseteq \mathbb{R}^d$ of volume V that is partitioned into two disjoint random sets or phases: phase 1, a region $\mathcal{V}_1(\omega)$ of volume fraction ϕ_1, and phase 2, a region $\mathcal{V}_2(\omega)$ of volume fraction ϕ_2 (see Figure 4.1). The random sets $\mathcal{V}_1(\omega)$ and $\mathcal{V}_2(\omega)$ are the complements of one another, thus, $\mathcal{V}_1(\omega) \bigcup \mathcal{V}_2(\omega) = \mathcal{V}$ and $\mathcal{V}_1(\omega) \bigcap V_2(\omega) = \varnothing$. Let $\partial\mathcal{V}(\omega)$ denote the surface or interface between $\mathcal{V}_1(\omega)$ and $\mathcal{V}_2(\omega)$. For a given realization ω, the structure function $\xi(\boldsymbol{x};\omega)$ is just the indicator function $\mathcal{I}^{(i)}(\boldsymbol{x};\omega)$ for phase i, given for $\boldsymbol{x} \in \mathcal{V}$ by

[1] A probability measure is a real-valued function defined on a set of events in a probability space that satisfies measure properties.

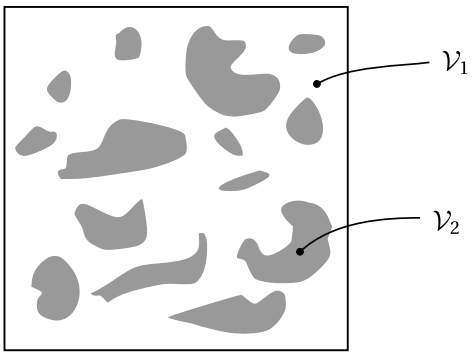

Figure 4.1: A portion of a realization ω of a two-phase random medium, where phase 1 is the white region $\mathcal{V}_1$, phase 2 is the gray region $\mathcal{V}_2$.

$$\mathcal{I}^{(i)}(\boldsymbol{x};\omega) = \begin{cases} 1, & \text{if } \boldsymbol{x} \in \mathcal{V}_i(\omega), \\ 0, & \text{otherwise,} \end{cases} \tag{4.1}$$

for $i = 1,2$ with

$$\mathcal{I}^{(i)}(\boldsymbol{x};\omega) + \mathcal{I}^{(i)}(\boldsymbol{x};\omega) = 1. \tag{4.2}$$

In what follows the probabilistic descriptions of these and other random variables will be considered. It is assumed that the reader is familiar with the basic notion of the probability distribution of a random variable.

4.3.2 n-Point Probability Functions

Definitions

For fixed $\boldsymbol{x}$, the indicator function $\mathcal{I}^{(i)}(\boldsymbol{x})$ has only two possible values; i.e., for some realizations ω it will be 0 and for some others it will be 1. Thus, the random variable $\mathcal{I}^{(i)}(\boldsymbol{x})$ does not possess a probability density. The probabilistic description of $\mathcal{I}^{(i)}(\boldsymbol{x})$ is given simply by the probability that $\mathcal{I}^{(i)}(\boldsymbol{x})$ is 1, which one writes as

$$\mathcal{P}\left\{\mathcal{I}^{(i)}(\boldsymbol{x}) = 1\right\}. \tag{4.3}$$

Given this probability, it follows that

$$\mathcal{P}\left\{\mathcal{I}^{(i)}(\boldsymbol{x}) = 0\right\} = 1 - \mathcal{P}\left\{\mathcal{I}^{(i)}(\boldsymbol{x}) = 1\right\}. \tag{4.4}$$

Moreover, the expectation of any function $f[\mathcal{I}^{(i)}(\boldsymbol{x})]$ can be expressed as

$$\left\langle f\left[\mathcal{I}^{(i)}(\boldsymbol{x})\right]\right\rangle = \mathcal{P}\left\{\mathcal{I}^{(i)}(\boldsymbol{x}) = 1\right\} f(1) + \mathcal{P}\left\{\mathcal{I}^{(i)}(\boldsymbol{x}) = 0\right\} f(0), \tag{4.5}$$

where $\langle(\cdot)\rangle$ denotes an ensemble average, i.e., an average over all realizations ω of the ensemble. In particular, $f\left[\mathcal{I}^{(i)}(\boldsymbol{x})\right] = \mathcal{I}^{(i)}(\boldsymbol{x})$ leads to the definition of the one-point probability function for phase i, denoted by $S_1^{(i)}$, as

$$S_1^{(i)}(\boldsymbol{x}) \equiv \left\langle \mathcal{I}^{(i)}(\boldsymbol{x}) \right\rangle = \mathcal{P}\left\{ \mathcal{I}^{(i)}(\boldsymbol{x}) = 1 \right\}, \tag{4.6}$$

that coincides with the probability of finding phase i at the position $\boldsymbol{x}$. It is sometimes also referred to as the one-point correlation function for the phase indicator function.

Likewise, the n-point probability function for phase i, denoted as $S_n^{(i)}$, is defined as

$$S_n^{(i)}(\boldsymbol{x}_1, \boldsymbol{x}_2, \ldots, \boldsymbol{x}_n) \equiv \left\langle \mathcal{I}^{(i)}(\boldsymbol{x}_1)\mathcal{I}^{(i)}(\boldsymbol{x}_2)\cdots\mathcal{I}^{(i)}(\boldsymbol{x}_n) \right\rangle, \tag{4.7}$$

and is equal to the probability that n points at positions $\boldsymbol{x}_1$, $\boldsymbol{x}_2$,...,$\boldsymbol{x}_n$ are found in phase i. This function can also be referred to as an n-point correlation function.

The special nature of the indicator function makes it possible to specify the general joint distribution

$$\mathcal{P}\left\{ \mathcal{I}^{(i)}(\boldsymbol{x}_1) = j_1, \mathcal{I}^{(i)}(\boldsymbol{x}_2) = j_2, \ldots, \mathcal{I}^{(i)}(\boldsymbol{x}_n) = j_n \right\} = \left\langle \prod_{k\in K} \mathcal{I}^{(i)}(\boldsymbol{x}_k) \prod_{l\in L} [1 - \mathcal{I}^{(i)}(\boldsymbol{x}_l)] \right\rangle, \tag{4.8}$$

where $K = \{k \leq n \mid j_k = 1\}$ and $L = \{l \leq n \mid j_l = 0\}$, in terms of the set of n-point probability functions $S_1^{(i)}$, $S_2^{(i)}$,...,$S_n^{(i)}$ for phase i.

In particular, one can express the probability $S_n^{(2)}$ of finding n points in phase 2 in terms of the set of phase 1 probabilities $S_1^{(1)}$, $S_2^{(1)}$, ..., $S_n^{(1)}$. From the inclusion-exclusion principle, one obtains

$$\begin{aligned} S_n^{(2)}(\boldsymbol{x}_1, \boldsymbol{x}_2, \ldots, \boldsymbol{x}_n) &= \left\langle \prod_{j=1}^{n} [1 - \mathcal{I}^{(1)}(\boldsymbol{x}_j)] \right\rangle \\ &= 1 - \sum_{j=1}^{n} S_1^{(1)}(\boldsymbol{x}_j) + \sum_{j<k}^{n} S_2^{(1)}(\boldsymbol{x}_j, \boldsymbol{x}_k) \\ &\quad - \sum_{j<k<l}^{n} S_3^{(1)}(\boldsymbol{x}_j, \boldsymbol{x}_k, \boldsymbol{x}_l) + \cdots + (-1)^n S_n^{(1)}(\boldsymbol{x}_1, \boldsymbol{x}_2, \ldots, \boldsymbol{x}_n). \end{aligned} \tag{4.9}$$

Furthermore, the probability of finding any subset n_1 of the n points in phase 2 and the remaining $n_2 = n - n_1$ in phase 1 can be expressed purely in terms of the set of phase 1 probabilities $S_1^{(1)}$, $S_2^{(1)}$,..., $S_n^{(1)}$. For example, the probability $S_2^{(12)}$ of two "dissimilar ends", i.e. the probability that a point at $\boldsymbol{x}_1$ is in phase 1 and a point at $\boldsymbol{x}_2$ is in phase 2, is given by

$$S_2^{(12)}(\boldsymbol{x}_1, \boldsymbol{x}_2) = \left\langle \mathcal{I}^{(1)}(\boldsymbol{x}_1)[1 - \mathcal{I}^{(1)}(\boldsymbol{x}_2)] \right\rangle = S_1^{(1)}(\boldsymbol{x}_1) - S_2^{(1)}(\boldsymbol{x}_1, \boldsymbol{x}_2). \tag{4.10}$$

Symmetries and Ergodicity

The n-point probability function $S_n^{(i)}$ may depend on the absolute positions $\boldsymbol{x}_1$, $\boldsymbol{x}_2$,... $\boldsymbol{x}_n$. If that is the case, the medium is said to be statistically inhomogeneous. Figure 4.2 depicts two examples of statistically inhomogeneous media. Indeed, even the one-point function $S_1^{(i)}$ may depend on the local position $\boldsymbol{x}_1$ and then may be interpreted as a position-dependent volume fraction of phase i.

The medium is strictly spatially stationary or strictly statistically homogeneous if the joint probability distributions describing the stochastic process are translationally

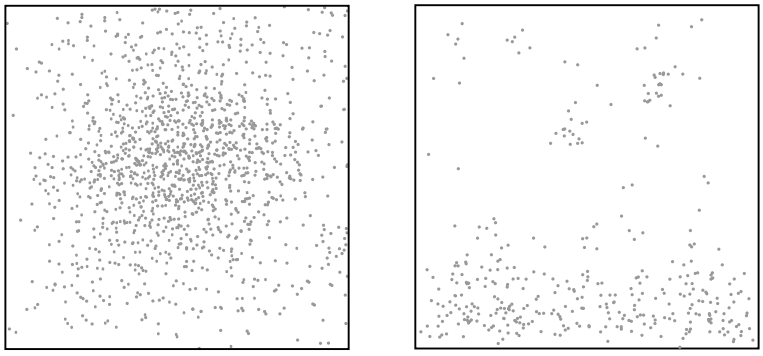

(a) (b)

Figure 4.2: Two examples of statistically inhomogeneous media. (a): Density of the gray phase decreases radially from the center.(b): Density of the gray phase decreseas in the upward direction.

invariant, i.e. invariant under a translation of the space origin. Thus, the random set $\mathcal{V}_i(\omega)$ generated from the stochastic process $\{\mathcal{I}^{(i)}(\boldsymbol{x}) \,|\, \boldsymbol{x} \in \mathcal{V}\}$ is strictly statistically homogeneous, provided that for some constant vector $y \in \mathbb{R}^d$

$$\begin{aligned}\mathcal{P}\left\{\mathcal{I}^{(i)}(\boldsymbol{x}_1) = j_1, \mathcal{I}^{(i)}(\boldsymbol{x}_2) = j_2, \ldots, \mathcal{I}^{(i)}(\boldsymbol{x}_n) = j_n\right\} \\ = \mathcal{P}\left\{\mathcal{I}^{(i)}(\boldsymbol{x}_1 + \boldsymbol{y}) = j_1, \mathcal{I}^{(i)}(\boldsymbol{x}_2 + \boldsymbol{y}) = j_2, \ldots, \mathcal{I}^{(i)}(\boldsymbol{x}_n + \boldsymbol{y}) = j_n\right\}, \quad (4.11)\end{aligned}$$

for all $n \geq 1$, $\boldsymbol{x}_1, \boldsymbol{x}_2, \ldots, \boldsymbol{x}_n$ in $\mathbb{R}^n$ and $j_1, j_2, \ldots, j_n$ in $\{0, 1\}$. This statement is only meaningful if $\mathcal{V}$ and $\mathbb{R}^n$ are equal, i.e. the volume V must be infinite. Equivalently, since such probabilities can be expressed in terms of the n-point probability functions for phase i, $\mathcal{V}_i(\omega)$ is strictly statistically homogeneous if and only if

$$\begin{aligned}S_n^{(i)}(\boldsymbol{x}_1, \boldsymbol{x}_2, \ldots, \boldsymbol{x}_n) &= S_n^{(i)}(\boldsymbol{x}_1 + \boldsymbol{y}, \boldsymbol{x}_2 + \boldsymbol{y}, \ldots, \boldsymbol{x}_n + \boldsymbol{y}) \\ &= S_n^{(i)}(\boldsymbol{x}_{12}, \ldots \boldsymbol{x}_{1n}), \quad (4.12)\end{aligned}$$

for all $n \geq 1$, $\boldsymbol{x}_1$, $\boldsymbol{x}_2$, …, $\boldsymbol{x}_n$ in $\mathbb{R}^n$ and $\boldsymbol{y}$ in in $\mathbb{R}^n$, where $\boldsymbol{x}_{jk} = \boldsymbol{x}_k - \boldsymbol{x}_j$. Therefore, for statistically homogeneous media, the n-point probability function doesn't depend on the absolute positions but rather on the relative displacements. In particular, the one-point probability function is a constant everywhere and it is equal to the volume fraction ϕ_i of phase i, i.e.,

$$S_1^{(i)} = \phi_i. \quad (4.13)$$

Further classification divides statistically homogeneous media into anisotropic if $S_n^{(i)}$ depends on both the orientation and magnitudes of the vectors $\boldsymbol{x}_{12}$, $\boldsymbol{x}_{13}$, …, $\boldsymbol{x}_{1n}$ and into isotropic if $S_n^{(i)}$ depends only on the magnitudes of the vectors $x_{jk} = |\boldsymbol{x}_{jk}|$, $1 \leq j < k \leq n$, …, $\boldsymbol{x}_{1n}$ (see Figure 4.3). For these materials, the two-point function, also

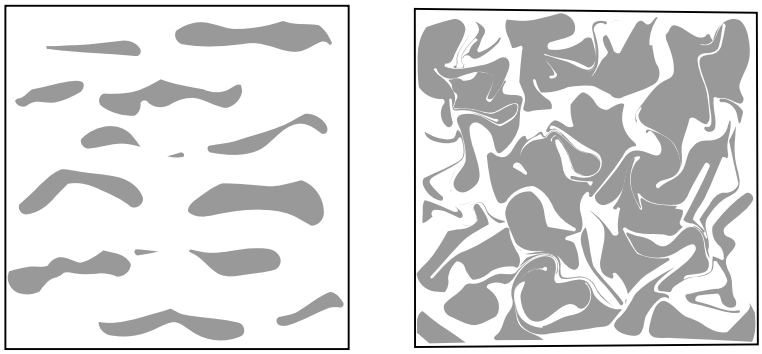

(a) (b)

Figure 4.3: Two examples of portions of statistically homogeneous media with two phase. (a): The layered medium is statistically anisotropic. (b): The medium is statistically isotropic.

known as the autocorrelation function, and the three-point function have the form

$$S_2^{(i)}(\boldsymbol{x}_1, \boldsymbol{x}_2) = S_2^{(i)}(x_{12}), \tag{4.14}$$

$$S_3^{(i)}(\boldsymbol{x}_1, \boldsymbol{x}_2, \boldsymbol{x}_3) = S_3^{(i)}(x_{12}, x_{13}, x_{23}). \tag{4.15}$$

This implies that the two- and three-point functions can be extracted from cross-sections or two-dimensional images of the isotropic sample, as long as the planar representation is sufficiently large, as $S_3^{(i)}$ remains invariant under all permutations of its arguments x_{12}, x_{13}, and x_{23}. Furthermore, the autocorrelation function $S_2^{(i)}$ can also be found from a linear cut through an isotropic medium.

Roughly speaking, the property of statistical homogeneity states that all regions of space are similar as far as the statistical properties of the stochastic process are concerned. When the system is statistically homogeneous, it is meaningful to define volume averages. This suggests an ergodic hypothesis, i.e., the result of averaging over all realizations of the ensemble is equivalent to averaging over the volume for one realization in the infinite-volume limit. Thus, complete probabilistic information can be obtained from a single realization of the infinite medium and ensemble averaging can be replaced with volume averaging when the volume tends to infinity, i.e.,

$$S_n^{(i)}(\boldsymbol{x}_{12}, \ldots, \boldsymbol{x}_{1n}) = \lim_{V\to\infty} \frac{1}{V} \int_{\mathcal{V}} \mathcal{I}^{(i)}(\boldsymbol{y}) \mathcal{I}^{(i)}(\boldsymbol{y}+\boldsymbol{x}_{12}) \cdots \mathcal{I}^{(i)}(\boldsymbol{y}+\boldsymbol{x}_{1n})\, \mathrm{d}y. \tag{4.16}$$

Such systems will be referred to as ergodic media.

In general, the n-point probability functions for $n \geq 2$ cannot be expressed in terms of lower-order q-point functions, $q < n$. Exceptions are the media possessing the so-called phase-inversion symmetry, i.e. media whose morphology of phase 1 at volume fraction ϕ_1 is statistically identical to that of phase 2, where the volume fraction of phase 2 is $1-\phi_1$ and hence

$$S_n^{(1)}(\boldsymbol{x}^n; \phi_1, \phi_2) = S_n^{(2)}(\boldsymbol{x}^n; \phi_2, \phi_1), \tag{4.17}$$

where $\boldsymbol{x}^n \equiv \{\boldsymbol{x}_1, \boldsymbol{x}_2, \ldots, \boldsymbol{x}_n\}$; at $\phi_1 = \phi_2 = 1/2$. From Equation (4.9) it can be seen that the odd-order probability functions $S^{(i)}_{2m+1}$ can be expressed in terms of all the lower-order probability functions. However, the even-order functions $S^{(i)}_{2m}$ cannot be expressed in terms of the lower-order functions.

Asymptotic Properties and Bounds

It is possible to establish asymptotic properties of and bounds on $S^{(i)}_n$ that apply to any statistically inhomogeneous two-phase random medium.

For a given set $\{\boldsymbol{x}_1, \boldsymbol{x}_2, \ldots, \boldsymbol{x}_n\}$, consider a general partition into L sets γ_j, such that $\bigcup_{j=1}^{L} \gamma_j = \{\boldsymbol{x}_1, \boldsymbol{x}_2, \ldots, \boldsymbol{x}_n\}$, each with $m(\gamma_j)$ elements. Let all of the relative distances between the $m(\gamma_j)$ elements of these subsets remain bounded, and let $\boldsymbol{F}^j_{m(\gamma_j)}$ be the polyhedron with $m(\gamma_j)$ vertices located at the positions associated with ith subset. Denoting the centroid of $\boldsymbol{F}^j_{m(\gamma_j)}$ by $\boldsymbol{R}_j$, let $\boldsymbol{R}_{jk}$ be the relative distance between the centroids of $\boldsymbol{F}^j_{m(\gamma_j)}$ and $\boldsymbol{F}^k_{m(\gamma_k)}$, where j and k are all possible values such that $1 \le j < k \le L$. A system is said to possess no long-range order if as $R_{jk} \to \infty$ for all j and k, the $m(\gamma_j)$-point functions corresponding to each γ_j become statistically independent, i.e., the n-point function factorizes into L products as follows

$$\lim_{\text{all } R_{jk}\to\infty} S^{(i)}_n(\boldsymbol{x}_1, \boldsymbol{x}_2, \ldots, \boldsymbol{x}_n) = \prod_{p=1}^{L} S^{(i)}_{m(\gamma_p)}(\boldsymbol{x}_1, \boldsymbol{x}_2, \ldots, \boldsymbol{x}_{m(\gamma_p)}), \tag{4.18}$$

An example of a system with long-range order, and thus one that does not obey the asymptotic result, is an infinitely large crystalline (periodic) array of identical spheres.

As an example, the aforementioned general asymptotic results are presented for the cases $n = 2$ and $n = 3$ for statistically homogeneous media without long-range order. For $n = 2$, one has

$$\lim_{x_{12}\to 0} S^{(i)}_2(\boldsymbol{x}_{12}) = \phi_i, \quad \lim_{x_{12}\to\infty} S^{(i)}_2(\boldsymbol{x}_{12}) = \phi_i^2, \tag{4.19}$$

and for $n = 3$, under permutations of the distances x_{12}, x_{13}, and x_{23},

$$\lim_{x_{12}\to 0, x_{13}\to\infty} S^{(i)}_3(\boldsymbol{x}_{12}, \boldsymbol{x}_{13}) = \phi_i, \quad \lim_{x_{12}\to\infty} S^{(i)}_3(\boldsymbol{x}_{12}, \boldsymbol{x}_{13}) = S^{(i)}_2(\boldsymbol{x}_{12}), \tag{4.20}$$

$$\lim_{\substack{x_{13}\to\infty \\ x_{12}\text{ fixed}}} S^{(i)}_3(\boldsymbol{x}_{12}, \boldsymbol{x}_{13}) = \phi_i S^{(i)}_2(\boldsymbol{x}_{12}), \quad \lim_{\text{all } x_{ij}\to\infty} S^{(i)}_3(\boldsymbol{x}_{12}, \boldsymbol{x}_{13}) = \phi_i^3. \tag{4.21}$$

As for the bounds, since $0 \le \mathcal{I}^{(i)}(\boldsymbol{x}) \le 1$ for all $\boldsymbol{x}$ in $\mathcal{V}$, we have the elementary bounds

$$0 \le S^{(i)}_n(\boldsymbol{x}^n) \le S^{(i)}_{n-1}(\boldsymbol{x}^{n-1}), \quad \text{for all } \boldsymbol{x}^n \text{ and } n \ge 2, \tag{4.22}$$

$$0 \le S^{(i)}_1(\boldsymbol{x}_1) \le 1, \qquad \text{for all } \boldsymbol{x}_1. \tag{4.23}$$

The one-point function $S^{(i)}_1(\boldsymbol{x}_1)$ is an upper bound on $S^{(i)}_n(\boldsymbol{x}^n)$ for all $\boldsymbol{x}^n$ and n.

Geometrical Probability Interpretation

The geometrical-probabilistic significance of the n-point probability function is easily seen for any microstructure. Let $\boldsymbol{F}^{(i)}_n$ be a polyhedron with n vertices located at posi-

tions $\boldsymbol{x}_1$, $\boldsymbol{x}_2$, …, $\boldsymbol{x}_n$. Then, for statistically inhomogeneous media, $S_n^{(i)}$ is the probability that all n vertices of $\boldsymbol{F}_n^{(i)}$ with fixed positions $\boldsymbol{x}_1$,$\boldsymbol{x}_2$, …,$\boldsymbol{x}_n$ lie in $\mathcal{V}_i$. For statistically homogeneous, but anisotropic media, $S_n^{(i)}$ is the probability that all n vertices of $\boldsymbol{F}_n^{(i)}$ lie in $\mathcal{V}_i$ when the polyhedron is randomly placed in the volume at fixed orientation i.e., over all translations of the polyhedron. For statistically isotropic media, $S_n^{(i)}$ can be interpreted as the probability that all n vertices of $\boldsymbol{F}_n^{(i)}$ lie in $\mathcal{V}_i$ when the polyhedron is randomly placed in the volume, i.e., over all translations and rigid-body rotations of the polyhedron.

4.3.3 Lineal-Path Function

For statistically isotropic media, the lineal-path function, denoted by $L^{(i)}$, gives the probability that a line segment of length z lies wholly in phase i when randomly thrown into the sample. The function $L^{(i)}(z)$ contains a coarse level of connectedness information about phase i, although only along a lineal path of length z in phase i. It is a lower-order microstructural function, more precisely a lower-order case of the canonical n-point correlation functions.

The lineal-path function is a monotonically decreasing function of z, since the space available in phase i for a line segment of length z decreases with increasing z. Accordingly, the extreme values of $L^{(i)}(z)$ are

$$L^{(i)}(0) = \phi_i, \quad L^{(i)}(\infty) = 0, \tag{4.24}$$

where ϕ_i is the volume fraction of phase i.

For statistically homogeneous, but anisotropic media, $L^{(i)}(\boldsymbol{z})$ will depend not only on the magnitude of vector $\boldsymbol{z}$ but also on its orientation. For statistically inhomogeneous media, $L^{(i)}(\boldsymbol{x}_1, \boldsymbol{x}_2)$ will depend on the absolute positions $\boldsymbol{x}_1$ and $\boldsymbol{x}_2$ of the end points of the vector $\boldsymbol{z} = \boldsymbol{x}_2 - \boldsymbol{x}_1$.

4.3.4 Two-Point Cluster Function

The formation of very large, on the order of the system's size, clusters[2] of a phase in a heterogeneous material can have a strong influence on its macroscopic properties.

In this context, the definition of the two-point cluster function, denoted as C_2, for general statistically inhomogeneous media, is given through the decomposition of the standard two-point probability function for the phase of interest, say phase 2, into a "connected" part and a "disconnected" part as

$$S_2(\boldsymbol{x}_1, \boldsymbol{x}_2) = C_2(\boldsymbol{x}_1, \boldsymbol{x}_2) + E_2(\boldsymbol{x}_1, \boldsymbol{x}_2), \tag{4.25}$$

where $C_2(\boldsymbol{x}_1, \boldsymbol{x}_2)$ is the probability of finding two points at positions $\boldsymbol{x}_1$ and $\boldsymbol{x}_2$ in the same cluster of phase 2 and $E_2(\boldsymbol{x}_1, \boldsymbol{x}_2)$ is the probability of finding two points at positions $\boldsymbol{x}_1$ and $\boldsymbol{x}_2$ that are not in the same cluster of phase 2. Accordingly, the quantity E_2 is called the two-point blocking function.

It can be seen from its definition, that C_2 generally contains nontrivial connectedness information and therefore is a better signature of the microstructure than S_2.

[2] A cluster of phase i is defined as the part of phase i that can be reached from a point in phase i without passing through phase $j \neq i$.

4.3.5 Nearest Neighbor Function

The aforementioned statistical descriptors are defined for random media of arbitrary microstructure. On the other hand, the following statistical descriptors are used to characterize statistically isotropic media composed of identical spherical particles of diameter, D, at number density[3], ρ, distributed throughout another phase.

One such example is the nearest neighbor function, denoted as H_P. Despite multiple definitions, the one adopted here states that $H_P(r)\,\mathrm{d}r$ is the probability that, at an arbitrary particle center in the system, the center of the nearest particle lies at a distance between r and $r + \mathrm{d}r$. Another similar function, used by Pathan et al. (2017), here denoted as H_P^*, is defined such that $H_P^*(\theta)\,\mathrm{d}\theta$ is the probability that, at an arbitrary point particle center in the system, the center of the nearest particle lies at an angle between θ and $\theta + \mathrm{d}\theta$. Both $H_P(r)$ and $H_P^*(\theta)$ are probability density functions, they are nonnegative for all r and normalize to unity. Furthermore, for statistically inhomogeneous media both functions will also depend upon the location of the central particle.

4.3.6 Voronoi metrics and Minkowski structure metrics

The Voronoi diagram divides the domain into regions, each associated with a seed. A given point of the domain belongs to region R_k, corresponding to seed $\boldsymbol{x}_k$, if $\boldsymbol{x}_k$ is the closest seed to that point. Figure 4.4 presents 2D and 3D examples of Voronoi diagrams.

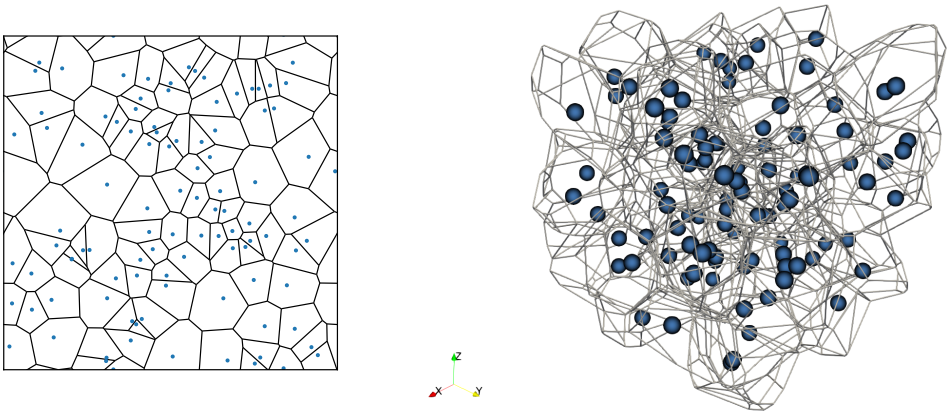

(a) (b)

Figure 4.4: Voronoi diagrams of 100 points obtained through a Poisson point process. (a): 2D and (b): 3D.

Its construction in three-dimensional systems has become a common element of structural analyses of particulate assemblies, including packing problems and granular matter (Schaller et al., 2013).

[3]The number density ρ is defined as the number of particle centers per unit volume.

The Voronoi diagram provides a notion of neighborhood, where neighbors of a given particle are identified as all particles whose corresponding cell has a common edge, or equivalently, that is connected to the particle by a Delaunay edge. For a set of nonoverlapping spheres or circles of the same radius, letting the centers of each particle be the seeds of the Voronoi diagram, the cells will be convex polygons, that do not intersect the particles. However, for a general particle, if the seed is taken to be its center of mass, the cells of the Voronoi diagram may intersect the particles (Schaller et al., 2013).

One way to circumvent this problem is to define the so-called set Voronoi diagram, where the distances used for its construction are not taken relative to the seeds, but instead relative to the surface of the particles. This leads to cells that do not intersect the particles. However, the cells may no longer be convex, or even polyhedra, i.e. the Voronoi facets may be curved, existing even the possibility that at a point not on a Voronoi edge, the Voronoi facet is not smooth. Schaller et al. (2013) presents an algorithm to obtain the set Voronoi of 2D and 3D convex particles based on the triangulation of the particles' bounding surfaces. Figures 4.5 and 4.6 present examples of set Voronoi diagrams. It can be shown that for circles of different sizes or ellipses the edges of the Voronoi cells are no longer straight lines, and these may in some cases be non-convex (see Figures 4.5a and 4.5b). The same applies in 3D for sets of spheres with different sizes and ellipsoids (see Figures 4.6a and 4.6b).

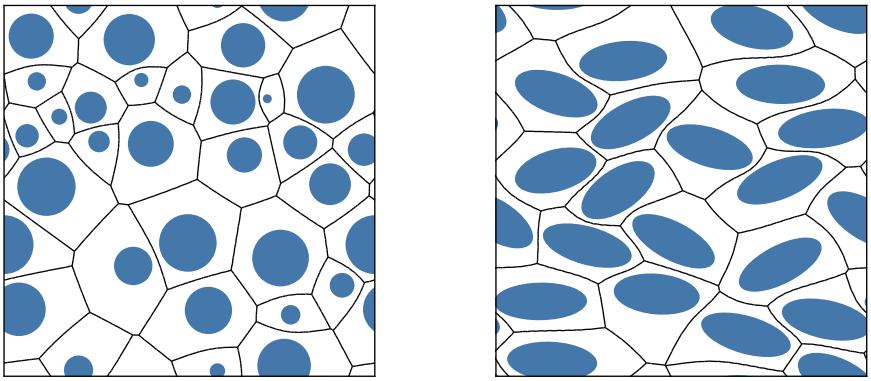

(a) (b)

Figure 4.5: 2D set Voronoi diagrams for (a) disks with different radii, (b) ellipses.

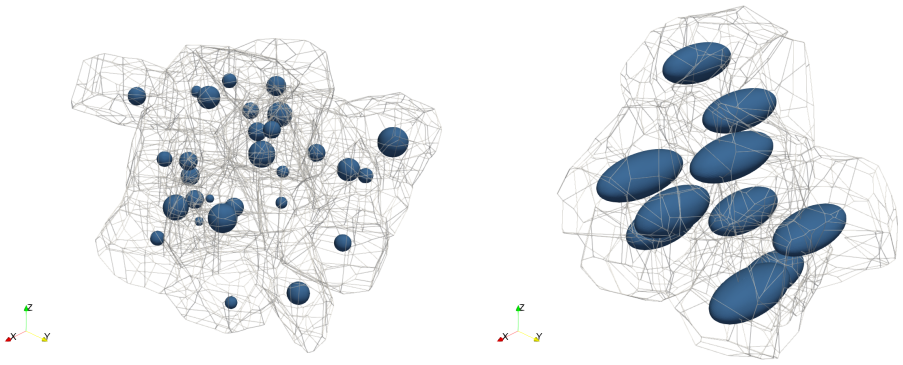

(a) (b)

Figure 4.6: 3D set Voronoi diagrams for (a) spheres with different radii and (b) ellipsoids.

After generating the Voronoi diagram, there is a need to characterize its cells. A set of metrics is their area/volume, perimeter/surface area, and the number of neighbors. Lovrić et al. (2019) presents a detailed analysis of the distribution of such properties of the set Voronoi diagram of 2D packings of ellipses.

A very interesting approach is the use of Minkowski structure metrics, as presented by Mickel et al. (2013), generalizing the bond orientational order parameters introduced by Steinhardt et al. (1983).

For the sake of clarity, they are first presented for two-dimensional convex shapes following Kapfer et al. (2020). Let K be a given convex polygon in the plane, L_k the lengths of the kth edge, and $\boldsymbol{n}_k$ the outer normal vector to the kth edge (see Figure 4.7). Moreover, define the vectors

$$\boldsymbol{L}_k = L_k \boldsymbol{n}_k, \tag{4.26}$$

coinciding with the edges of the polygon rotated by 90º. For a convex polygon, the set of vectors $\{\boldsymbol{L}_k\}$ defines it uniquely. If the vectors $\boldsymbol{L}_k$ are sorted by the angle they span with the x axis, their concatenation retrieves a copy of the original polygon, rotated by 90º.

The normal density function, which characterizes the shape K, denoted by ρ_K, is defined as

$$\rho_K(\varphi) = \sum_k L_k \delta(\varphi - \varphi_k), \quad \text{with } 0 \leq \varphi \leq 2\pi, \tag{4.27}$$

where δ is Dirac's delta function and φ_k is the angle that the outer normal of the kth edge makes with the positive x semi-axis (see Figure 4.7). The function ρ_K characterizes the interface of the shape K, specifying the radius of curvature for each of its points parametrized by φ. Accordingly, the radius of curvature is infinite at the angles corresponding with the edges of the polygon, since they are straight lines, and zero for all remaining angles.

To decompose the normal density into the irreducible representations of the rotation group, i.e. to express it using sines and cosines or imaginary exponentials, one obtains its Fourier series, defining ρ_K has a periodic function with period 2π. The Fourier coefficients $\psi_s(K)$ define the Irreducible Minkowski Tensors and are given by

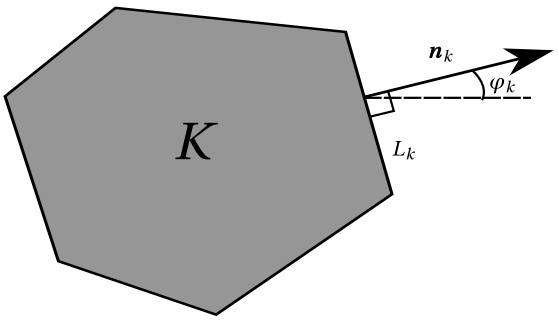

Figure 4.7: Convex polygon K with sides L_k and corresponding outer normals $\boldsymbol{n}_k$, $k = 0,\ldots,6$.

$$\psi_s(K) = \int_0^{2\pi} \exp(is\varphi)\rho_K(\varphi)\,\mathrm{d}\varphi = \sum_{k=-\infty}^{\infty} L_k \exp(is\varphi_k). \tag{4.28}$$

Knowing all ψ_s, one can reconstruct the function $\rho_K(\varphi)$, and thus, the original convex shape K. The zeroth coefficient is precisely the perimeter of the shape, $\psi_0(K) = P(K)$. For any closed contour, the vectors $\boldsymbol{L}_k$ sum to zero, hence, $\psi_{\pm 1} = 0$. Any higher Irreducible Minkowski Tensors contain shape information about the anisotropic nature of the contour. Roughly speaking, the ψ_s tensor describes the component of the interface with s-fold, but not higher, symmetry. Its magnitude quantifies how strong this symmetry is and its argument the orientation at which the symmetry is detected. This information about the shape is disjoint between the coefficients, i.e. they are independent. Figure 4.8 contains the basic shapes retrieved assuming that only one of the coefficients ψ_s, $s \geq 2$ is different from zero, i.e. the density function is given by $\rho_{K_s} = 1 + \cos(s\varphi)$ for $s \geq 2$. These are obtained through integration of the Fourier series, given the relation between the arc length and the radius of curvature (Apostol, 1969).

The mapping between convex shapes K and their set of Irreducible Minkowski Tensors $\{\psi_s(K)\}$ is bijective.

To obtain a set of parameters independent of the orientation and size of an object, a metric must be defined that is invariant under rotation, scaling, and translation. One such set of metrics are the so-called Minkowski Structure Metrics, q_s, defined as

$$q_s(K) \equiv \frac{|\psi_s(K)|}{\psi_0(K)}. \tag{4.29}$$

The q_s are fingerprints of a particular class of shapes and are indifferent to rotation and scaling. Thus, they may be used to classify shapes, ignoring their size and orientation. They are an alternative representation of the cartesian Minkowski tensors $W_1^{0,s}$.

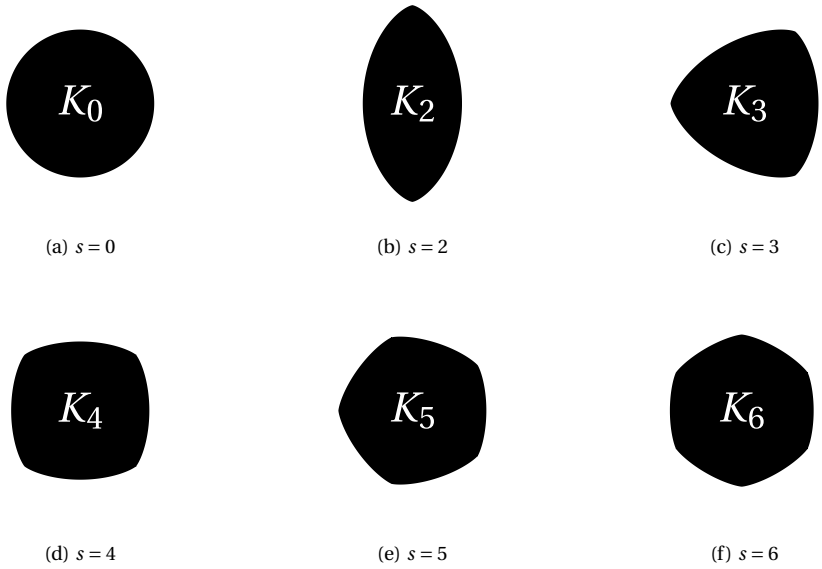

(a) $s = 0$ (b) $s = 2$ (c) $s = 3$

(d) $s = 4$ (e) $s = 5$ (f) $s = 6$

Figure 4.8: Shapes containing s-fold, but not higher, symmetry, obtained from the density function $\rho_{K_s}(\varphi) = 1 + \cos(s\varphi)$, $s = 0$, 2, 3,4, 5, 6, $0 \leq \varphi < 2\pi$.

In 3D, the normal density function of a polyhedron K is given by

$$\rho_K(\boldsymbol{n}) = \sum_k A_k \delta(\boldsymbol{n}_k - \boldsymbol{n}), \tag{4.30}$$

where A_k and $\boldsymbol{n}_k$ are the face areas and the outer normals of K, respectively. The density function in 3D corresponds to the product of the principal radii of curvature at a given point of the polyhedron, whose position is parametrized by the outer normal at that point. As in 2D for polygons, for $\boldsymbol{n}$s coinciding with the outer normals of faces of the polyhedron, the function is infinite, being equal to zero otherwise.

To decompose the normal density into the irreducible representations of the rotation group, one expresses the normal density function using spherical harmonics, $Y_s^m(\boldsymbol{n})$ (see Figure 4.9), a generalization of the Fourier series in 2D. The corresponding coefficients, $\psi_{s,m}$ are

$$\psi_{s,m}(K) = \sum_k A_k Y_s^m(\boldsymbol{n}_k). \tag{4.31}$$

As in 2D, the coefficients $\psi_{s,m}$ provide information about the shape of K. More precisely, the s-fold symmetry is marked by nonzero coefficients $\psi_{s,m}$, i.e. coefficients related to spherical harmonics of degree s. The order m of the spherical harmonic is tied to the orientation at which the symmetry is detected in space. Figure 4.10 displays the basic shapes retrieved using the algorithm proposed by Lamberg and Kaasalainen

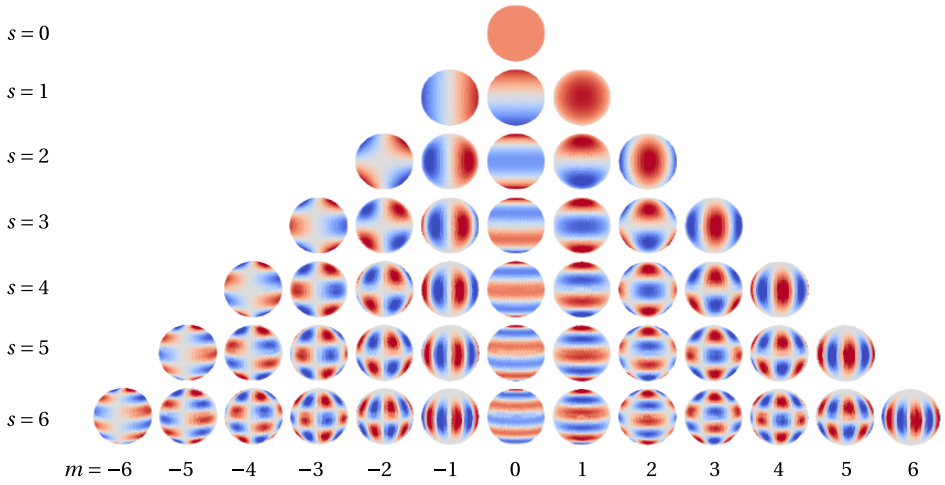

Figure 4.9: Spherical harmonics $Y_s^m(\boldsymbol{n})$, $s = 0, 1, 2, 3, 4, 5, 6$, $-s \le m \le s$, with $\boldsymbol{n} \in S^2$, where S^2 is the unit sphere. Red represents positive values and blue negative values.

(2001) to solve the Minkowski problem[4], with only one coefficient $\psi_{s,m}$, $s \ge 2$, different from zero.

The three-dimensional irreducible Minkowski tensors are defined as

$$q_s(K) = \sqrt{\frac{4\pi}{2s+1}\frac{1}{A^2}\sum_{m=-s}^{s}|\psi_{s,m}(K)|^2}, \tag{4.32}$$

using the quadratic invariants of the spherical harmonics, so that it is invariant under translation, rotation and scaling and so a fingerprint of the body's shape.

Klatt et al. (2017) studies the average values and distribution of theses metrics applied to the Voronoi diagram of points in a plane generated from diverse procedures, such as the Poisson point process, RSA (see Section 5.3.2) and hard-sphere equilibrium arrangements, concluding that they are enough to characterize the generation method. This shows their great sensibility to any order within the system, in this case, related to the generation method. Kapfer et al. (2012) claims that Minkowski's fourth-order tensors, whose information about the shape of the Voronoi cells is the same as the Irreducible Minkowski tensors, are good metrics to detect local crystallinity and hence order in the system.

[4]The Minkowski problem asks for the reconstruction of a convex shape given its curvature.

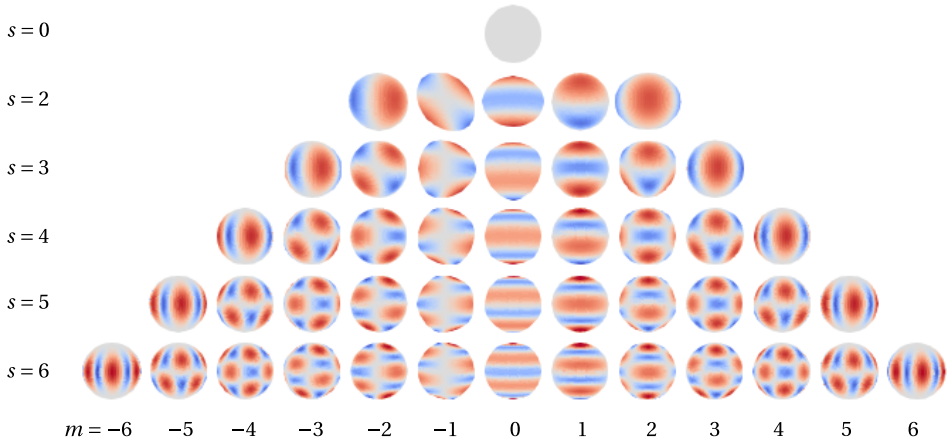

Figure 4.10: Shapes containing s-fold, but not higher, symmetry, obtained from the density function $\rho_{K_{s,m}}(\boldsymbol{n}) = 1 + Y_s^m(\boldsymbol{n})$, $s = 0$, 2, 3,4, 5, 6 and $-s \leq m \leq s$, with $\boldsymbol{n} \in S^2$, where S^2 is the unit sphere. Red marks points with higher curvature and blue points with lower curvature.

4.3.7 n-Particle Probability Densities

Classically, any ensemble of many-particle systems may be completely spatially characterized by the probability density function associated with finding a particular configuration of particles. The following applies to systems of identical spheres, spheres with polydispersivity in size as well as oriented, nonspherical particles. Let $\boldsymbol{r}_i$ denote the center-of-mass coordinate, and eventually the orientation of the particle i, $0 < i \leq N$, and $\boldsymbol{r}^N = \{\boldsymbol{r}_1, \boldsymbol{r}_2, \ldots, \boldsymbol{r}_N\}$ the configuration of a system with N particles.

The configuration of the particles is statistically characterized by the specific N-particle probability density function $P_N(\boldsymbol{r}^N)$ defined such that $P_N(\boldsymbol{r}^N)\,\mathrm{d}\boldsymbol{r}^N$ is the probability of finding the center of particle 1 in volume element $d\boldsymbol{r}_1$ about $\boldsymbol{r}_1$, the center of particle 2 in volume $\mathrm{d}\boldsymbol{r}_2$ about $\boldsymbol{r}_2$, ..., and the center of particle N in volume element $\mathrm{d}\boldsymbol{r}_N$ about $\boldsymbol{r}_N$, where $\mathrm{d}\boldsymbol{r}^N \equiv d\boldsymbol{r}_1\,\mathrm{d}\boldsymbol{r}_2 \cdots \mathrm{d}\boldsymbol{r}_N$.

For ensembles consisting of indistinguishable particles, it is convenient to introduce the generic n-particle probability density function $\rho_n(\boldsymbol{r}^n)$, defined as

$$\rho_n(\boldsymbol{r}^n) = \frac{N!}{(N-n)!} \int P_N(\boldsymbol{r}^N)\,\mathrm{d}\boldsymbol{r}^{N-n}, \tag{4.33}$$

where $d\boldsymbol{r}^{N-n} \equiv \mathrm{d}\boldsymbol{r}_{n+1}\,\mathrm{d}\boldsymbol{r}_{n+2} \cdots \mathrm{d}\boldsymbol{r}_N$. This means that $\rho_n(\boldsymbol{r}^n)\,\mathrm{d}\boldsymbol{r}^n$ is proportional to the probability of finding any subset of n particles with configuration $\boldsymbol{r}^n$ in the volume element $\mathrm{d}\boldsymbol{r}^n$. For statistically homogeneous media, the one-particle function ρ_1 is just equal to the constant number density of particles, ρ, i.e.,

$$\rho_1(\boldsymbol{r}_1) = \rho \equiv \lim_{N,V\to\infty} \frac{N}{V}. \tag{4.34}$$

For statistically homogeneous media, it is convenient to define the so-called n-

particle correlation function as

$$g_n(\boldsymbol{r}^n) = \frac{\rho_n(\boldsymbol{r}^n)}{\rho^n}. \tag{4.35}$$

In systems without long-range order and in which the particles are mutually far from one another, $\rho_n(\boldsymbol{r}^n) \to \rho^n$ and, thus, $g_n(\boldsymbol{r}^n) \to 1$. Hence, the deviation of g_n from unity provides a measure of the degree of spatial correlation between the particles, with unity corresponding to a null spatial correlation.

The important two-particle quantity

$$g_2(\boldsymbol{r}_{12}) = \frac{\rho_2(\boldsymbol{r}_{12})}{\rho^2}, \tag{4.36}$$

is usually referred to as the pair correlation function. In the statistically isotropic case it only depends on the radial distance r_{12}, i.e.,

$$g_2(\boldsymbol{r}_{12}) = g_2(r_{12}), \tag{4.37}$$

and is referred to as the radial distribution function. Hence, $\rho g_2(r)\,\mathrm{d}\boldsymbol{r}$ may be interpreted as the average number of particles at a radial distance between r and $r + \mathrm{d}r$ from a reference particle, since $\rho g_2(\boldsymbol{r})\,\mathrm{d}\boldsymbol{r} = \rho s_1(r) g_2(r)\,\mathrm{d}r$, where $s_1(r)$ is the surface area of of a d-dimensional sphere of radius r.

4.3.8 Ripley's K function

Another widely used function in describing point distributions is Ripley's K function, also known as the second-order intensity function, $K(r)$ (Buryachenko et al., 2003; Melro, 2011; Pathan et al., 2017). It is a tool used to analyze completely mapped spatial point process data. For this particular application, the points are the center-of-mass coordinate of the particles.

According to Dixon (2002), Ripley's K function is defined as the number of points expected to be located within a distance r of an arbitrary point divided by the number of points per unit area, and is obtained from the following expression

$$K(r) = \rho^{-1} E, \tag{4.38}$$

where ρ is the density of points, r is the distance, and E is the number of extra points within distance r of randomly chosen point.

Given the locations of all events within a defined study area, the density of points can be estimated as $\widehat{\rho} = N/A$, where N is the observed number of points and A is the area of the study region. Accordingly, an estimator for $K(r)$ is given by

$$\widehat{K}(r) = \frac{A}{N^2} \sum_i \sum_{j \neq i} \frac{I(d_{ij} \leq r)}{w(l_i, l_j)} \tag{4.39}$$

where A is the area of the study region, N is the total number of particles, d_{ij} is the distance between points i and j, and $I(x)$ is an indicator function having the value 1 if x is true and 0 otherwise. The weight function, $w(l_i, l_j)$, provides an edge correction, needed because points outside the boundary are not counted in the numerator, even

if they are within a distance r of a point in the study area. It has the value 1 when the circle is centered at l_i and passing through the point l_j, i.e. it has a radius equal to d_{ij} and is completely inside the study region. If part of the circle falls outside the area under analysis, then $w(l_i, l_j)$ is the proportion of the circumference of that circle that falls in the study area. The effects of edge corrections are more important for large r because large circles are more likely to be outside the region under examination. Thus, it is common practice to consider only r less than one-half the shortest dimension of the study area.

The information it provides about the medium is different from the one given by the nearest neighbor functions. The latter analyzes short-range interaction between the fibers, while the Ripley's K function also provides some insight about the microstructure at other distances. It is also independent of the direction analyzed since it is a function only of the distance to the origin point.

For a homogeneous Poisson process, also known as complete spatial randomness, it can be shown that

$$K(r) = \pi r^2. \tag{4.40}$$

If the spatial distribution under analysis provides a plot of $\widehat{K}(r)$ below the Poisson curve, it is an indication that exhibits some degree of regularity. On the contrary, if $\widehat{K}(r)$ is above the Poisson curve, the distribution is likely to present clustering. A stair-like pattern for $\widehat{K}(r)$ points to a regular pattern.

The difference between a Poisson distribution and the spatial distribution in the results can be studied using the $\widehat{L}(r)$ function defined as

$$\widehat{L}(r) = \sqrt{\frac{\widehat{K}(r)}{\pi}} - r. \tag{4.41}$$

According to the last paragraph, peaks of positive values in a plot of $\widehat{L}(r)$ would indicate clustering while negative troughs indicate regularity at distance r.

The radial distribution function g_2 is related to Ripley's K function as follows (Melro, 2011)

$$g_2(r) = \frac{1}{2\pi r} \frac{dK(r)}{dr}. \tag{4.42}$$

Chapter 5

Computational Microstructure Generation

This chapter presents an overview of the computational generation schemes used to generate RVEs of matrix-inclusion composites. Its classification scheme is inspired by Bargmann et al. (2018), dividing the methods into three classes: microstructure reconstruction from experimental data, physics-based microstructure generation, and geometrical methods. The last two sections present a brief discussion about the concept of randomness in the context of RVEs and a comparison of the different algorithms from the standpoint of the objectives presented in Section 1.1.

5.1 Microstructure reconstruction from experimental data

The inverse problem to the statistical characterization of a microstructure is its reconstruction from limited microstructural information, typically, lower-order correlation functions. Such reconstructions are nonunique, and thus, this is a distinct problem from data decompression algorithms that restore complete information, e.g. the grayscale of every pixel in an image (Torquato, 2013).

Stereology Stereology is a related area that seeks to investigate 3D spatial structures making use of planar sections (Torquato, 2013), such as the ones obtained by Louis and Gokhale (1995) for a mixture of hollow spherical carbon particles in a polymer, using optical microscopy. Microstructures such as these can be used as 2D RVEs, however in addition to being time-consuming and resource-intensive to obtain. they are not periodic, precluding some types of numerical analysis (Pathan et al., 2017).

In general, some important spatial characteristics cannot be estimated stereologically, and methods based on three-dimensional measurement techniques have been proposed, e.g. confocal microscopy, that dispense the need for physical sections (Buryachenko et al., 2003).

Reconstruction techniques

As reported by Torquato (2013), the first reconstruction procedures were based on thresholding Gaussian random fields. Roberts (1997) presents such a method generating random Gaussian fields using two different methods, a Fourier summation and a

"random-wave". The microstructures are then obtained from level cuts of these fields, chosen so that the two-point probability function of the model coincides with real micrographs. He found that materials with practically identical two-point correlation functions can have very different morphologies and macroscopic properties, showing that reconstructions based on the two-point probability function do not necessarily provide a useful model of the original material. Moreover, this method failed to satisfactorily reproduce a microstructure made up of identical overlapping spheres and, according to Torquato (2013), it is not suitable for extension to non-Gaussian statistics.

Another technique, developed by Torquato et al. (2000), consists of a stochastic optimization technique, based on simulated annealing, to reconstruct random media. The method is highly flexible in that one can include any set of different types of correlation functions as microstructural information. It is, according to Torquato (2013), both a generalization and simplification of the aforementioned Gaussian random field method. Jiao and Chawla (2014) presented a framework to model heterogeneous inclusions of secondary phases based on the directional correlation functions of the inclusions, including the directional two-point cluster functions, using this method.

Fullwood et al. (2008) extended and applied phase-recovery algorithms from the field of signal processing to the problem of reconstructing microstructures from their 2-point statistics. They also present a framework for the fast computation of 2-point statistics of the microstructure using discrete fast Fourier transforms and claim that for so-called eigen microstructures, i.e. two-phase discretized microstructures, their reconstruction is unique, up to translation and inversion.

Tahmasebi and Sahimi (2013) developed a new reconstruction method based on a cross-correlation function and a one-dimensional raster path, providing an accurate description of a wide variety of materials and media. The reconstruction uses a single 2D slice of data to reconstruct an entire 3D medium.

5.2 Physics based microstructure generation

Simulating the manufacturing process is, in most cases, inefficient for matrix inclusion microstructures. Bulk or mixing simulations are far too complex and their simulation times are usually not worth the gained findings on particle distribution (Bargmann et al., 2018).

An approximation to some aspects of the manufacturing process of fiber-reinforced composites can be done with reduced computational effort using rheological models (Bargmann et al., 2018), such as the one presented by Folgar and Tucker III (1984), obtaining a prediction for the fiber orientation in short fiber composites.

5.3 Geometrical methods

Before devising a geometrical generation method for the RVEs, a geometrical definition of the inclusions' shapes is needed, since matrix-inclusion composites are more easily characterized describing the inclusions as simple geometric shapes than using statistical probability functions. Given the parametrization of the geometric bodies, stochastic distributions can be considered for any of the parameters to mimic experimental findings (Bargmann et al., 2018).

The organizational scheme used in this section is inspired by the one used by Buryachenko et al. (2003) and divides the geometrical methods for RVE generation into

methods based on molecular dynamics, methods based on Monte Carlo techniques and methods based on close random packing.

5.3.1 Molecular Dynamics

Molecular dynamics is a widely used computational approach in which the classical equations of motion are solved numerically and the trajectories thus generated are used to extract macroscopic observables (Tuckerman, 2010).

There are at least two types of molecular dynamics simulations: time-driven and event-driven. In a time-driven simulation, one discretizes time and updates the position of each particle after every time interval, checking for overlaps. If there is an overlap, the simulation is rolled back to the time of the collision, the velocities of the colliding particles are updated and the simulation continues (Sedgewick and Wayne, 2011). According to Sedgewick and Wayne (2011), despite their simplicity, time-driven simulations suffer from two major drawbacks, the number of overlap checks, that if done naively is proportional to the square of the number of particles, and the risk of not detecting a collision, if a time interval that is too large is used, as the particles may not overlap when one checks.

Salnikov et al. (2015) present such an algorithm. It starts with a random illegal configuration, i.e. overlapping geometries, and achieves a legal configuration postulating repulsive forces between intersecting particles proportional to the depth of the overlapping domain. The ODEs describing the dynamics of the system governed by these forces are solved numerically to achieve the relaxed configuration. Damping forces are also included to slow the system down and make it stay in the relaxed configuration. They produced RVEs composed of spheres and cylinders at high fractions, in an efficient way and achieving residual intersections between the particles that decrease exponentially with the simulation's time length.

On the other hand, in an event-driven simulation, one focuses only on those times at which noteworthy events occur, e.g. collisions between particles. For example, for a system of hard disks, the particle paths are analytically calculated, as they are straight lines and the particles are non-interacting apart from the collisions. Therefore, the times and places where they collide can be readily found. Ordering these events as a function of the time instant at which they will occur, one considers the time instant corresponding to the first collision. The simulation is advanced up to that moment, moving each particle accordingly and assigning new velocities to the colliding particles. Next, the future collisions are once again computed and ordered according to the time instant at which they will occur, repeating the process. It is also important to note that in event-driven molecular dynamics simulations the configurations of the RVE are always legal, i.e. there are no intersections.

Lubachevsky and Stillinger (1990); Lubachevsky et al. (1991) used an algorithm based on event-driven molecular dynamics able to achieve high volume fractions of disks and spheres. Particles begin as moving points, grow in size at a uniform rate, undergo nonconserving collisions, and eventually jam up. The organization of the particles in the final RVE, more precisely their arrangement into crystals, is highly dependent on the compression rate, i.e. rate of growth, with faster compression leading to more crystallization.

Later, Donev et al. (2005a) generalized the same event-driven molecular dynamics algorithm to ellipsoids, using a partial-update near-neighbor list algorithm, and bounding sphere complexes for very aspherical particles. Ghossein and Lévesque (2013)

also present a similar scheme to produce packings of ellipsoids, computing binary collision times by finding the roots of a non-linear function.

To implement event-driven molecular dynamics simulations one needs to implement contact or approximate contact algorithms to circumvent overlap. For systems of spheres or capsules, the binary collision times can be computed analytically. On the other hand, for systems of with other shapes, e.g. ellipsoids, the collision times are, in general, computed numerically (Bargmann et al., 2018). Ghossein and Lévesque (2013) use an algebraic criterion based on the work of Wang et al. (2001), which implies finding the roots of a non-linear function to determine the relative configuration of two ellipsoids, as separate, tangent or overlapping. Donev et al. (2005b) considers the aforementioned approach, but favors a criterion developed by Perram and Wertheim (1985), declaring that it is both numerically and theoretically superior.

Regarding both types of molecular dynamics simulations, to avoid computing unnecessary collision times or overlap checks, there are methods such as the cell list method and the near-neighbor list method capable of improving significantly the CPU simulation times (Ghossein and Lévesque, 2013; Donev et al., 2005a).

5.3.2 Monte Carlo techniques

The random sequential adsorption (RSA) method, also known as the hardcore model, is the most common method to generate matrix-inclusion RVEs and works by adding filler particles sequentially and randomly in the prescribed RVE domain. If a particle does not intersect previously placed particles, its position is accepted, otherwise it is discarded. The process is repeated until the desired volume fraction is reached (Bargmann et al., 2018). This algorithm, despite being simple and very fast for slow volume fractions, becomes slow at high volume fractions, even presenting a saturation limit, e.g. for cylindrical fibers it is as low as 0.54 (Pathan et al., 2017).

Buryachenko et al. (2003) reports modifications to the RSA method for spheres, where a virtual shaking of the particles through random displacements is employed to better mix the system and allow the placement of more particles, with a saturation limit as high as 0.65.

Melro (2011) developed a more complex RSA-based algorithm, perturbing the particles in order to cause a closer packing of the existing particles, by encouraging fiber attraction, using several arbitrary parameters that make the algorithm hard to implement.

Another variation on the RSA method was presented by Segurado and Llorca (2002). Firstly, they generated a unit cell having a volume fraction lower than the desired value using RSA. The cell was then compressed in several steps and the particle positions and volumes are updated at each compression stage. The eventual intersections between each stage are dealt with using a Markov-chain approach, where intersecting particles are moved randomly until there are no overlaps.

There is also a rejection-free RSA method for disks, described by Krauth (2006) as "faster than the clock". It works by keeping track of the area where disks may still be legally placed using a grid system and sampling the position for the new particle only from this area. This speeds up the algorithm immensely, as the biggest problem for the RSA method at high volume fractions is the high rejection rate. Miranda (2015) implemented a similar algorithm, stating that the algorithm is of linear complexity and that the time taken to place any disk is constant during the process.

Beyond RSA, Vaughan and McCarthy (2010) presented another Monte Carlo scheme

based on a Markov-chain sampling for disks. The first particle is placed randomly in the RVE and then, the position of the next particles is given relative to the last particle placed. The magnitude of the position vector relative to the last particle is sampled from the nearest neighbor function and the angle is sampled from a uniform distribution. The particle is accepted if there is no overlap. The author claims that this scheme better approximates the experimental findings since it tries to mimic statistical distributions found experimentally.

Another approach related to Markov-chain sampling presented by various authors (Bargmann et al., 2018) samples the configuration space starting from a periodic initial configuration of particles by perturbing their positions. One of these authors is Catalanotti (2016) that presents an approach that can produce RVEs of spheres with a volume fraction as high as the theoretical maximum, 0.74, starting from periodic arrangements of spheres derived from the face-centered cubic unit cell.

Other Monte Carlo schemes are used to explore the configuration space, starting from a legal configuration, which allow for moves of an independent particle even if it generates overlaps, the so-called cluster algorithms described by Krauth (2006).

In the avalanche cluster algorithm, an independent particle is randomly moved. If after the move it overlaps another particle, the other particle is then simply moved out of place. This leads to an avalanche, where the particles tip-off each other until a legal configuration is found. The use of this algorithm in statistical mechanics, where the detailed balance[1] must be maintained, implies that there be only one terminal particle, the last particle to be tipped off, before a legal configuration is found. However, this is not a limitation in the case of RVE generation.

Lastly, Bernard et al. (2009) present an event-chain Monte Carlo algorithm capable of exploring the configuration space of systems containing 1024^2 disks at high volume fractions. This allowed them to show that the melting in hard disks proceeds in two steps with a liquid phase, a hexatic phase, and a solid, solving a long standing problem in statistical mechanics (Bernard and Krauth, 2011). This algorithm is rejection-free, allowing for the displacement of arbitrary long chains of particles, and long-range coherent movement to be induced. Each move consists of a deterministic chain of "events": a disk advances until it strikes another one, which is then in turn displaced. The Monte Carlo move starts with a randomly chosen disk and stops when the lengths of all displacements add up to a total displacement parameter. This parameter allows the move to be reversible without rejections. In comparison to a molecular-dynamics algorithm for the same system, the authors showed that it is more efficient, exploring faster the configuration space.

5.3.3 Dense random packing

As the name implies, the goal of these methods is the creation of a random arrangement of particles, whose volume fraction is as high as possible (Torquato et al., 2000). However, according to Torquato et al. (2000), this statement of the problem is ill-defined, as shown by the ample evidence in the literature, in the form of actual and computer experiments. Increasing the degree of coordination, and thus, the bulk system density comes at the expense of disorder. The precise proportion of these competing effects is arbitrary and therein lies the problem. A precise mathematical definition that supplants the inadequate random close packing state is the maximally random

[1] The detailed balance is maintained in a system, if a given Monte Carlo move has the same probability as its reverse.

jammed state, suggested by Torquato et al. (2000). It is defined for systems of disks as the state that minimizes some chosen order metric among all statistically homogeneous and isotropic jammed structures, where a jammed particle is a particle that cannot be translated while fixing the positions of all the other particles in the system.

Notwithstanding this state of affairs, the designation "dense random packing" will still be used to denote the methods presented in the remainder of this section.

Before introducing the methods for dense random packing, it may be of interest to introduce the related problem of cutting and packing. Cutting and packing problems consist of packing a set of geometric objects/items of fixed dimensions and shape into a region of predetermined shape without allowing for intersections and keeping in mind any technological constraints that cannot be reduced to purely geometric constraints (Hifi and M'hallah, 2009). They are NP-hard combinatorial optimization problems, i.e. no procedure can exactly solve them in deterministic polynomial time (Fowler et al., 1981). There are relatively few analytical results relating to the packing of even the simplest geometrical objects. Packing densities for close lattice packing are $\pi/\sqrt{12} \approx 0.9069$, corresponding to a triangular arrangement of disks in the plane, and $\pi/\sqrt{18} \approx 0.7405$, corresponding to the face-centered cubic unit cell in the case of spheres packed into $\mathbb{R}^3$ (Buryachenko et al., 2003).

Buryachenko et al. (2003) divides the dense random packing methods into two types: the sequential generation models and the collective rearrangement models. The present exposition will be based on that classification.

Sequential generation models

There are several sequential generation models for random dense packings, among which the cluster growth method and the advancing front algorithm. None of the works mentioned here presented focus on the generation of RVEs with periodic boundaries.

In the sequential model by Bennett (1972), so-called cluster growth model, aggregates of several thousand hard spheres of equal size were constructed by depositing additional spheres, one at a time, at surface sites on a small seed cluster, placing each new sphere in contact with three already present and not moving it afterward. Despite the author claiming that there is no evidence of crystallinity and that the pair correlation function is similar to that of the dense random packings which have been prepared from ball bearings, and to the pair correlation functions calculated from x-ray diffraction work on amorphous alloys, other reports maintain that the algorithm produces inhomogeneous and anisotropic inclusion fields, whose radial distribution function does not display the characteristic split-second peak observed in experimental packing.

Feng et al. (2002, 2003) presents an advancing front-based algorithm to generate a random packing for disks with different radii within a 2D domain. The same author also extends this approach to ellipses, convex polygons, and spheres.

Ilin and Bernacki (2016) presents a constructive ellipse packing algorithm, so-called advancing layer algorithm, where each ellipse is approximated by a set of circles and placed on the particle that is at the smallest "height" in the domain, checking if there are no intersections with the remaining neighboring particles.

There is also another kind of sequential generation model, called the model of "rigid sphere free fall into a virtual box". It consists in the sequential vertical drop of particles from random points onto the surface of an existing particle cluster growing upwards. The movement of the particles after being dropped is controlled and

influences the density obtained (Buryachenko et al., 2003).

Constructive algorithms from cutting and packing are also presented by Oliveira et al. (2000) and Júnior et al. (2014). The former suggests building the system of non-overlapping geometric shapes by successively adding a new piece to a partial solution, i.e. to the set of pieces previously nested. Every time a new piece is placed, the no-fit-polygon is used to determine the feasible placement points of the layout. This is followed by a local search and/or the use of heuristic algorithms to choose, in each step, the best piece to place, its orientation and the best placement point. Júnior et al. (2014) address the irregular strip packing problem, a particular two-dimensional cutting and packing problem, in which convex or concave shapes have to be packed onto a single rectangular object. They propose an approach that prescribes the use of a metaheuristic engine, a genetic algorithm, and a greedy bottom-left placement rule.

Collective rearrangement models

Collective rearrangement algorithms are typically utilized in combination with random sequential adsorption, which generates an initial configuration with possibly overlapping particles. In a second step, a denser packing with an overlap free configuration is achieved repositioning and shrinking some or all particles (Bargmann et al., 2018).

Jodrey and Tory (1985) present a numerical scheme to realize homogeneous and isotropic packing of spheres by assuming hypothetical spheres having a dual structure whose inner diameter defines the true density and the outer one a nominal density. The algorithm eliminates overlaps among outer spheres using a heuristic, while slowly shrinking the outer diameter. The two diameters approach each other, and the eventual coincidence of true and nominal densities terminates the procedure. A variation of this method is presented by Mościński et al. (1989), where instead of using a heuristic, the displacement of the particles was proportional to the overlap of the particles. Gaiselmann et al. (2013) used this method to obtain their RVEs of non-woven materials.

He and Ekere (2001) also present a method that uses heuristics to decrease the overlap area between randomly generated spheres in cubic space. The relaxation iteration step is repeated a given number of times and then the packing space is expanded, where the scale factor is greater than one and is proportional to the present mean overlap rate. The relaxation and expansion steps are repeated, and the random packing is obtained as the mean overlap rate drops below a preset tolerance.

Another approach to the repositioning of overlapping particles to achieve a legal configuration are optimization schemes that try to minimize the overlap area directly. Pathan et al. (2017) presents a method for generating cylinders and spheres based on a constrained optimization formulation, involving the simultaneous generation of all filler particles using a Poisson point process, followed by an iterative procedure to optimize the location of filler particles subject to certain constraints. The algorithm can be applied to any particle shape whose condition of separation can be defined algebraically such as ellipses and ellipsoids. The volume fractions achieved for cylinders of equal size were 80%; for spheres only up to 40%.

Smirnov and Voloshinov (2018) suggest treating problems of discrete geometry as global optimization problems, to be solved by one of the general-purpose solver implementing branch-and-bound algorithms. The authors apply this scheme to find solutions to the problem of the densest packing of equal circles in a flat torus.

Balzani et al. (2014) proposed a least-square functional including an arbitrary number of statistical measures. By minimization of this functional, the artificially gen-

erated RVE is statistically similar to the included statistical information. They used ellipsoids which are repositioned during the optimization procedure and which may overlap.

The discrete element method is a numerical approach that uses an explicit calculation scheme considering multi-body dynamics to describe the motion and interaction of a large number of small particles (Bargmann et al., 2018). This method generates an RVE through densification under influence of gravity. One could either first randomly generate particles in a container and, then, apply gravity, the so-called mechanical contraction, or let particles of random horizontal direction drop one by one over a set of already equilibrated ones, the so-called drop-and-roll method (Bargmann et al., 2018). Zinchenko (1994) also presents a discrete element method, where the particles are allowed to swell by the numerical solution of the so-called differential equations of densification. As their radius increases the algorithm tries to retain contacts throughout the densification, as far as possible. The algorithm has a well-defined termination point resulting in a perfect contact network. In general, the DEM related methods consume substantial computation time, when a large number of particles interact (Pathan et al., 2017).

Another approach is presented by Wang et al. (2019) to randomly generate 2D packings of a particle assembly for discrete element simulation of convex granules. The proposed approach consists of discretizing the domain using a weighted Voronoi tesselation, that after a few iterations, produces an arrangement of polygonal cells, whose area distribution is as specified. The nonoverlapping particle outlines are generated via cubic-polynomial-curve fitting to polygonal cells.

5.4 Randomness

This section will deal with a common criticism in microstructure generation of materials, such as matrix-inclusion composites: the underlying randomness.

First, there is a need to understand what does "random" mean in this context. It is assumed, as a starting point, that there is an innate sense that allows anyone who looks at a microstructure to say with more or less certainty that it is "random", i.e., microstructures are perceived as "random" or not. But how does this perceived "randomness" tie back to the "quality" of a generated microstructure is an open problem. The ultimate goal of the computer generation of microstructures is to generate microstructures that could plausibly come from the manufacturing process of matrix-inclusion composites. It is a commonly held belief, and a reasonable one, that microstructures perceived as more random are more probable to come from a real manufacturing process.

Looking at the very definition of the materials under analysis (see Section 4.1), they are designated as random heterogeneous materials, as each microstructure is a realization of a random variable $\xi(\boldsymbol{x};\omega)$. However, this in itself does not give away what characteristics of a given microstructure lead to its perception as "random" or not.

Randomness is usually connected to the concept of entropy. The definition of entropy for the discrete random variable X, $H(X)$, is

$$H(X) = -\sum_{i=1}^{n} P(x_i) \log_b P(x_i) \tag{5.1}$$

where $P(X)$ is the corresponding probability mass function and x_i are possible values

taken by X. It can be interpreted as the average number of bits needed to describe a realization of the random variable (Cover and Thomas, 2012).

There are at least two obstacles to its use in this context. The first is that it depends on the probability distribution of the random variable. However, one doesn't have access to it, neither analytically nor numerically through the computational generation method, as the way it samples the configuration space may be different from the real process. The second difficulty is tied to the fact that entropy is a characteristic of the method generating the microstructures. Meanwhile, the goal is to classify specific instances of the random variable, i.e. the microstructures generated, as "random" or not, and not the system as a whole.

From another point of view, according to Uspensky (2009) there are four faces of algorithmic randomness:

1. stability and stochasticness;
2. chaoticness;
3. typicalness;
4. unpredictability.

They are defined for infinite sequences of binary strings and thus are not directly applicable to the case at hand. However, they provide a solid basis for a discussion about randomness. It must also be stressed that they are conditional on the assumed distribution.

Stability and stochasticness are defined as the existence of a limit frequency. For the simplest case of a fair coin, this means that the fraction of zeros in the n-bit prefix of the sequence should converge to $1/2$ as n goes to infinity, for every reasonably chosen subsequence. By chaoticness, it is meant that the string has a complex structure and cannot have a reasonable description, i.e. it is irregular. Typicalness relates to the fact that a random sequence would belong to a reasonable majority. Unpredictability means that betting against this sequence, trying to guess its terms, one cannot systematically win and no clever strategy can help. Trying to apply these concepts to microstructures, the most interesting seem to be chaoticness and typicalness.

As for typicalness, it seems intuitive that most microstructures will belong to a reasonable majority that is perceived as "random". This may be the case for the real manufacturing process and the particular way it samples the configuration space, but it may not be the case for the computational algorithm used to generate the microstructure. i.e. a microstructure with crystallinity at high volume fractions may be more probable than a microstructure perceived as "random". Hence, this may not be an interesting point of view.

Turning to chaoticness, that is, complexity or disorder, it seems reasonable that real microstructures perceived as "random" will be disorderly. Moreover, the probability distribution of the random variable is not needed to define this concept, as the complexity can in theory be gathered from the individual realization of the microstructure. A quantity often associated with complexity is the so-called Komolgorov complexity, defined as the shortest program that would produce the string under analysis (Cover and Thomas, 2012). At first glance this would be the metric one is looking for, however, it is hard to define for microstructures and so has no practical use. Therefore, it appears that no *bona fide* measure for disorder that could be readily applied exists. Still, it seems like the chaoticness of the microstructure is the most fruitful interpretation of the term "random" as it is used in this context.

From a practical standpoint, despite this state of affairs, order metrics such as bond-orientation metric (Steinhardt et al., 1983) and the Minkowski structure metrics (Mickel et al., 2013) (see Section 4.3.6) can be used to detected unwanted order, be it from their average values or their distributions across the particles of the microstructure.

Kansal et al. (2002) gives a list of desirable characteristics for order metrics. It is advised that the order metrics be sensitive to any type of ordering in a system and not be biased toward any reference system. It should also reflect the hierarchy of ordering between prototypical systems given by common physical intuition, as well as, being capable of detecting order at any length. Finally, both the variety of local coordination patterns and the spatial distribution of such patterns should affect the amount of order measured in a system.

Another approach that can be taken to ensure perceived "randomness" is to produce microstructures using as a template real microstructures. For example, if the generated microstructure and the real microstructure have, for example, the same 2-point probability function and the same Ripley's K function, then it is conceivable that the generated microstructure also mimics the perceived randomness of the real material. This approach may be harder to use for some types of microstructures, such as cases where the phases can't be approximated very well by the geometric shapes used to parametrize the RVE. Pathan et al. (2017) used it for distributions of disks achieving good results.

5.5 Comparison

This section presents an attempt to compare the several methods presented previously, in light of the objectives set forth in Section 1.1.

Beginning with the methods based on microstructure reconstruction from experimental data (see Section 5.1), there are a few incompatibilities with the goals already stated. The algorithms of this kind reconstruct the microstructure based on statistical function such as the 2-point probability function and the 2-point cluster function. That information is not available as input and so precludes the use of these approaches in this context. As a general criticism, one might also add that the generated microstructures are not periodic and the source images of the microstructure can be time-consuming to obtain and hard to analyze. It is also true that the easiest statistical metrics of the microstructure to obtain, such as the 2-point probability function, may not characterize the microstructure well enough to be useful for the accurate determination of its effective properties (Roberts, 1997).

Physics-based microstructure generation (see Section 5.2) also seems unsuitable for the purposes at hand, as it requires too much effort for marginal improvements in the quality of the generated RVE (Bargmann et al., 2018). Since the goal here is the efficient generation of RVE for their use in a data-driven framework, it is unacceptable that their generation requires too much effort.

In the context of the geometrical methods presented (see Section 5.3), methods based on Molecular Dynamics, Monte Carlo techniques, and close random packing are examined. Looking at the methods based on event-driven Molecular dynamics, their implementation can be complex, and more so for aspherical particles. Despite their increased accuracy regarding the dynamics of the system, preventing particles from fully travel across each other, this is not a feature highly valued in the present context. Since the final goal is just to find a legal configuration and not an equilibrated system

whose observables, such as temperature or pressure, coincide with real systems, there is no need for such accuracy. It is also the case that all the methods of this kind presented are compression algorithms, that is, the particles start as points and grow. This extra kinematic parameter is strongly tied to the final order of the system, i.e. crystallization, as pointed out by Zinchenko (1994).

On the other hand, time-driven Molecular dynamic simulations may lead to a less accurate prediction of the trajectory of the particles, but as previously stated this is not important for the goals at hand. They are also simpler to implement, but since they start from an overlapping configuration it may be impossible to guarantee zero volume overlap.

Turning now to the Monte Carlo techniques presented, and starting with the RSA, it is widely reported that it has a saturation limit depending on the specific shape of particles and that, for volume fraction close to but below the saturation limit, it is very slow. On the other hand for a small volume fraction, it is extremely fast (Salnikov et al., 2015). The "faster than the clock" improvement reported by Krauth (2006) and Miranda (2015) solves the issue with the slowness of the algorithm near the saturation limit, but still presents a saturation limit and it seems complex to implement in 2D for particles other than disks and particles of any shape in 3D. The other improvements for the RSA, such as the one reported by Melro (2011), make use of arbitrary parameters that are hard to implement with no clear upside for their use.

The perturbation methods presented, such as the one reported by Catalanotti (2016), seem very efficient, but it can be hard to determine if the microstructure has decoupled from its initial configuration. It also needs an initial legal configuration, that for arbitrary shapes at high volume fractions may not be readily available. For spheres and disks, such packings are known up to the maximum volume fraction.

The Monte Carlo event-chain algorithm reported by Bernard et al. (2009) needs an initial legal configuration, but it seems to explore the configuration space very efficiently as can be inferred from the results obtained by Bernard and Krauth (2011) for systems of 10^6 disks.

As for the Random Close Packing approaches, the sequential generation methods, despite being constructive and hence very fast, produce microstructures that are too orderly for them to plausibly represent a real microstructure (Pathan et al., 2017). It is also the case that in 3D, the placing strategies are harder to devise and implement, e.g., the method presented by Feng et al. (2002) for sphere excludes by definition a whole subset of legal configurations. Lastly, the RVEs created in this manner do not present periodic boundary conditions, which is not acceptable for this use case.

Regarding collective rearrangement methods, where the overlaps in the initial configuration are resolved using heuristics, their definition is done through rules that are largely arbitrary. Furthermore, there is no readily available universal rule, be it for all kinds of overlaps between the same shape or accounting for different shapes.

Using optimization schemes to minimize the overlap of the particles in the initial configuration seems at first a very interesting approach. Nevertheless, it may be complex to implement, the optimization problems to be solved are hard, possessing many local minimums not corresponding to legal configurations (Hifi and M'hallah, 2009) and the results obtained may not warrant it. Pathan et al. (2017) using an approach of this type was only able to obtain volume fractions of 40% for spheres, a far cry from the accepted volume fraction for the maximally random jammed state of 64% (Torquato et al., 2000) and the maximum achievable volume fraction of 74%.

Finally, the discrete element methods presented are too complex and effort-intensive

for the final RVEs obtained, as the forces between all the particles have to be modeled, including friction between particles. The approaches using gravity as the driver for densification also exhibit unwanted vertical anisotropy (Bargmann et al., 2018).

With all this in mind, the approach taken will be a time-driven molecular dynamics algorithm, to be detailed in the next chapter, as it fulfills the requirements put forth without unneeded conceptual or practical complexity.

Chapter 6

Molecular Dynamics Algorithm

This chapter fleshes out the proposed approach for microstructure generation based on a time-driven molecular dynamics algorithm, inspired by Salnikov et al. (2015). In what follows, the presentation regarding molecular dynamics simulations in general is based on Frenkel and Smit (2001).

6.1 Introduction

As previously stated the approach used to produce the desired microstructures is a time-driven molecular simulation. It follows, for the most part, the scheme proposed by Salnikov et al. (2015).

As outlined by Frenkel and Smit (2001), the general structure of a time-driven molecular dynamics simulation starts with generating an initial configuration, followed by the computation of the forces between the particles in the system. In this case, the forces are proportional to the overlap area/volume of each particle pair. The differential equations of motion are then integrated using these forces as well as the positions and velocities of the particles. The two last steps are then repeated, one after the other, for the remainder of the simulation.

An algorithm such as the one described in the previous paragraph will produce a simulation of a microcanonical ensemble, which is a system containing a constant number of particles, at constant volume and energy (Frenkel and Smit, 2001). For this work, the most convenient ensemble is the so-called canonical ensemble, where the volume and number of particles are also constant, but now instead of the energy being constant it is the temperature that stays the same (Frenkel and Smit, 2001). This implies the use of a thermostat that will affect the speed of the particles, so that the temperature is constant (see Section 6.7.1). The option to use this ensemble is further discussed later on.

An outline of a general molecular dynamics scheme for a microcanonical ensemble can be seen in Box 6.1. In the following sections, each of these stages are detailed, providing the necessary specifics. First, the types of particles admissible are defined geometrically, followed by the generation of an initial configuration. The concept of legal configuration is introduced and the particulars of the force computation, including the algorithms for the computation of the overlaps between particles and the speed-up schemes, are detailed. Finally, the algorithm used to integrate the equations of motion is explained as well as the developed approach based on thermostats.

Box 6.1: Algorithm for a general molecular dynamics simulation of a microcanonical ensemble.

(i) Generate an initial configuration

(ii) Initialize the increment counter i, $i = 0$

(iii) Compute the interactions between particles

(iv) Integrate the equations of motion for all particles

(v) Check if the simulation has run until the end.
If ($i = i_{\max}$) then

- Exit and report that the maximum number of iterations has been reached

else

- Update the increment counter, $i \leftarrow i + 1$ and go to step (iii)

6.2 Geometrical definition of the particles

The developed program for the generation of RVEs based on a molecular dynamics simulation requires the use of computational geometry to describe the shape of the inclusions admissible in the microstructure. This section details the parameters needed for the full characterization of the particles representing the inclusions, beyond the number of particles and the volume fraction. The precise geometrical definitions are given as needed in the section about force computation from the overlap area/volume (Section 6.5).

6.2.1 Disks

The particles called "Disks" in this program are circles, whose shape is completely defined by their radius, r, or their area, A_{Disk} and are only defined for two-dimensional microstructures (see Figure 6.1). Their position in space is completely defined by the position of their center. The acceptable descriptors for a phase containing Disks are a subset of the radius, r, the area of the Disks, A_{Disk}, the number of particles and the volume fraction of the phase. Different combinations of these parameters can be specified, being related through the formula for the area of a circle

$$A_{\text{Disk}} = \pi r^2. \tag{6.1}$$

6.2.2 Ellipses

The particles called "Ellipses" are elliptical particles, whose shape is fully specified by their major semi-axis, a and minor semi-axis, b, and are only defined for two-dimensional microstructures. Their position in space is defined by their center point and the angle that the major axis makes with the positive semi-axis x, denoted by θ

(see Figure 6.1). The user can specify, for a given phase containing these particles, a subset of the major-semi axis, a, the minor semi-axis, b, their ratio, a/b, the number of particles, and the volume fraction of the phase. The equation for the area of the ellipse establishes the relation between the sets of parameters,

$$A_{\text{Ellipse}} = \pi ab. \tag{6.2}$$

6.2.3 Spheres

The particles called "Spheres" are spherical particles, whose shape is fully specified by their radius, r, and are only defined for three-dimensional microstructures. Their position in space is completely defined by the position of their center (see Figure 6.1). The acceptable descriptors for a phase containing Spheres are a subset of the radius, r, the volume of the Spheres, V_{Sphere}, the number of particles and the volume fraction of the phase. Different combinations of these parameters can be specified, being related through the formula for the volume of a sphere

$$V_{\text{Sphere}} = \frac{4}{3}\pi r^3. \tag{6.3}$$

6.2.4 Ellipsoids

The particles called "Ellipsoids" are ellipsoidal particles, whose shape is fully specified by their principal semi-axis, a, b, and c, and are only defined for three-dimensional microstructures. Their orientation in space is defined by a Euler axis, $\boldsymbol{e}$, an angle, θ, and the position of their center. The aforementioned axis $\boldsymbol{e}$ corresponds to the unit vector, unique except for the sign, which remains unchanged by the rotation. The angle θ specifies the rotation angle around the Euler axis $\boldsymbol{e}$. It is also unique and has its sign determined by the sense of the rotation axis using the right-hand rule. The rotation is applied to the ellipsoid with the a, b, and c axis parallel with the x, y, and z coordinate axis, respectively (see Figure 6.1).

The user can specify, for a given phase containing these particles, a subset of the semi-axis, a, b and c, their ratios, a/b, a/c, the number of particles and the volume fraction of the phase. The equation for the volume of the ellipsoid establishes the relation between the sets of parameters,

$$V_{\text{Ellipsoid}} = \frac{4}{3}\pi abc. \tag{6.4}$$

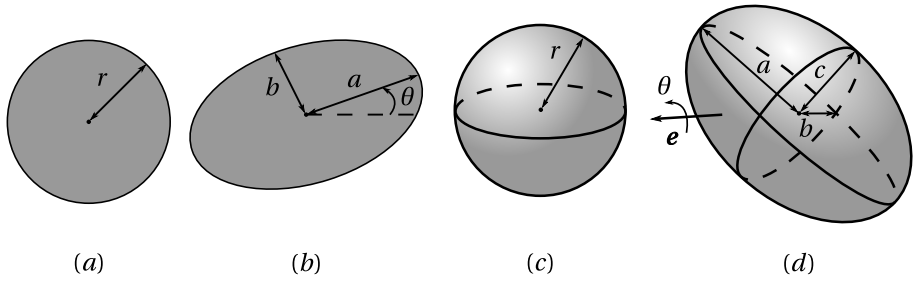

Figure 6.1: Diagram containing the parameters defining geometrically the particles admissible in the microstructures: (a) Disk, (b) Ellipse, (c) Sphere and (d) Ellipsoid.

6.3 Generation of an initial configuration

The initial configuration is generated using a Poisson point process to place the center points of the particles inside the simulation box. Each component of the position vector defining the center of the particles is sampled from a uniform distribution between 0 and the length of the RVE side in the corresponding direction (Bargmann et al., 2018).

As for the geometrical characterization of the particles, all parameters specified, except for the number of particles and the volume fraction, can be supplied as a single value, equal for all the particles in a given phase, or can be made to vary according to a statistical distribution. The supported statistical distributions are the uniform distribution, the Gaussian distribution and the discrete distribution. For the uniform distribution the user must specify its upper and lower bounds. For the Gaussian distribution, its mean and standard deviation must be supplied and for the discrete distribution each value must be provided along with its probability. Allowing also for multiple phases, there is a lot of flexibility in the definition of the inclusions and the ability to closely mimic real matrix-inclusion composites.

6.4 Legal configurations

The legal configurations are determined according to a maximum average area/volume overlap specified by the user. This average area/volume overlap is defined as the total overlap area/volume divided by the number of particles. A successful run of the program will produce a microstructure with an overlap smaller or equal to the specified threshold.

It is also possible to define a minimum distance between particles. The geometrical parameters characterizing the particles' size are increased by half this quantity and the simulation is run as if the particles were bigger. At the end of the simulation, the particles are shrunk, producing a microstructure with the correct volume fraction and respecting the minimum distance specified.

This feature may be useful in some applications as, for example, microstructure generation to perform FEM analyses. The minimum distance between particles contributes to the proper finite element meshing by preventing excessively deformed elements in between particles.

6.5 Force computation

Following Salnikov et al. (2015), the forces applied to each particle are proportional to the overlap area/volume of the interacting particles. It bears to mention that the angular motion of the particles is not included in the simulation, as their orientation may be one of the descriptors specified by the user. As such all forces are applied at the center of mass of the particles. Their direction is along the line defined by the center of the two particles and the sense is opposite to the other particle, as the goal is to eliminate any existing overlap.

Thus, there is a needed to determine the overlap area/volume of two particles. However, if these interactions are computed between every two pairs of particles, the number of computations grows proportional to the square of the number of particles, and this is not desirable for large systems of particles. Therefore, in what follows, it is also presented a set of strategies to avoid the computation of overlap between particles that can be shown a priori not to interact with each other.

6.5.1 Periodic boundary conditions

To account for the periodic boundary conditions, the force computation is always considered between the nearest periodic images of two given particles, as it is the only interaction that needs to be accounted for between a pair of particles. This is the case because particles with one of their characteristic lengths larger than half the smallest length of the RVE are not allowed, as they may interact with themselves.

Thereby, the distance between two particles, $\boldsymbol{d}$, denoted with 1 and 2, for the force computation is obtained as

$$d_i = x_i^{(1)} - x_i^{(2)} - \ell_{\mathrm{RVE}\,i}\,\mathtt{round}\left(\frac{x_i^{(1)} - x_i^{(2)}}{\ell_{\mathrm{RVE}\,i}}\right), \quad i = 1,\ldots,n_{\mathrm{dim}}, \tag{6.5}$$

where $\boldsymbol{x}^{(1)}$ and $\boldsymbol{x}^{(2)}$ are the position vectors of the centers of the particles and $\ell_{\mathrm{RVE}\,i}$ is the length of the RVE in the i direction.

6.5.2 Overlap area/volume

This section presents the approaches used to detect and compute the overlap area/volume between two Disks, two Ellipses, two Spheres and two Ellipsoids. The overlap area between a Disk and an Ellipse and the overlap volume between a Sphere and an Ellipsoid is computed as if the Disk and the Sphere were an Ellipse and an Ellipsoid, respectively. Specific approaches for two Disks and two Spheres are used, as they are much faster and simpler than the general approach used to determine the overlap between two Ellipses or two Ellipsoids.

Overlap Disk-Disk

The detection of the overlap between two Disks is achieved computing the distance between the two centers, denoted by O_1 and O_2, and comparing it to the sum of the radii of the two Disks, denoted by r_1 and r_2. Henceforth, it is assumed that $r_1 \geq r_2$. If $\overline{O_1O_2} < r_1 + r_2$, then there is overlap between the two Disks (see Figure 6.2). Moreover, if $\overline{O_1O_2} \leq r_1 - r_2$, then Disk 2 is entirely contained within Disk 1 and the overlap area is the area of Disk 2.

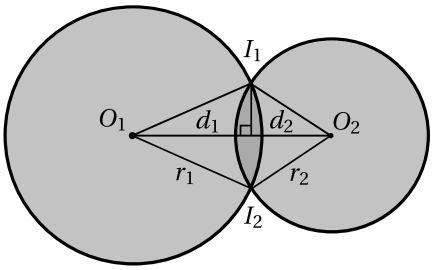

Figure 6.2: Diagram depicting the approach taken to compute the overlap area between two disk of different radii.

On the other hand, if $r_1 - r_2 < \overline{O_1O_2} < r_1 + r_2$, the overlap area is the sum of the segments of Disk 1 and 2 defined by the chord I_1I_2 and can be obtained analytically. To compute the area of the segments, for example, the sector coming from Disk 1, one considers the circular sector $O_1I_1I_2$ and the corresponding triangle, $\triangle O_1I_1I_2$, and subtracts the areas.

The area of the triangle $\triangle O_1I_1I_2$ can be found from

$$A_{\triangle O_1I_1I_2} = \frac{1}{2} d_1 2\sqrt{r_1^2 - d_1^2}, \tag{6.6}$$

where the length of its base is found using Pythagoras theorem, with the height of $\triangle O_1I_1I_2$, d_1, obtained from

$$d_1 = \frac{r_1^2 - r_2^2 + d^2}{2d}. \tag{6.7}$$

In turn, Equation 6.7 can be found from

$$r_1^2 - d_1^2 = r_2^2 - d_2^2, \tag{6.8}$$

coming from the application of Pythagoras theorem, noting that triangles. $\triangle O_1I_1I_2$, and $\triangle O_2I_1I_2$, share a side. The signed height of the triangle $\triangle O_2I_1I_2$, d_2 can be obtained from $d = d_1 + d_2$, and it is negative, only when Disk 2 is smaller than Disk 1 and its center is between the intersection points and the center of Disk 1 (see Figure 6.2).

The area of the sector $O_1I_1I_2$ is found from

$$A_{\text{Sector } O_1I_1I_2} = \frac{1}{2} r_1^2 \, 2 \arccos\left(\frac{d_1}{r_1}\right), \tag{6.9}$$

using the regular formula for the circular sector, with the angle $\arccos(d_1/r_1)$ defining the half arc between I_1 and I_2 computed between 0 and π.

The argument for the segment belonging to Disk 2 is analogous, being the total overlap are given by

$$A_{\text{Total Overlap}} = A_{\text{Sector } O_1I_1I_2} - A_{\triangle O_1I_1I_2} + A_{\text{Sector } O_2I_1I_2} - A_{\triangle O_2I_1I_2}. \tag{6.10}$$

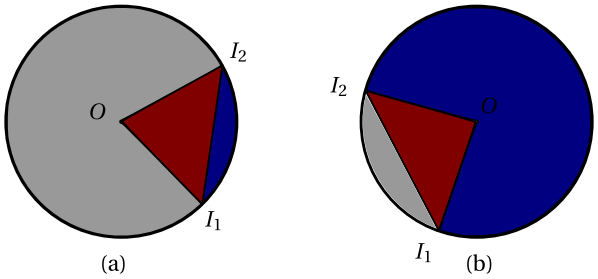

Figure 6.3: Different types of circular segments: (a) less than π radians and (b) more than π radians.

Box 6.2: Algorithm for the computation of the overlap area between two disks.

(i) Denote the larger disk as Disk 1 with radius r_1 and center at O_1 and the smaller disk as Disk 2 with radius r_2 and center at O_2

(ii) Compute the distance between the center of the disks, d

(iii) Check if there is overlap.
If $d > r_1 + r_2$

- There is no overlap, thus, $A_{\text{Overlap}} = 0$

else if $d \leq r_1 - r_2$

- Disk 2 is entirely contained within Disk 1, thus, $A_{\text{Overlap}} = \pi r_2^2$

else if $r_1 - r_2 < d < r_1 + r_2$

- Compute the height of the triangles $\triangle O_1 I_1 I_2$ and $\triangle O_2 I_1 I_2$, where I_1 and I_2 are the two intersection points

$$d_1 = \frac{r_1^2 - r_2^2 + d^2}{2d}, \quad d_2 = d - d_1$$

- Compute the area of the triangles $\triangle O_1 I_1 I_2$ and $\triangle O_2 I_1 I_2$

$$A_{\triangle O_1 I_1 I_2} = \frac{1}{2} d_1 2\sqrt{r_1^2 - d_1^2} \quad A_{\triangle O_2 I_1 I_2} = \frac{1}{2} d_2 2\sqrt{r_2^2 - d_2^2}$$

- Compute the area of the sectors $O_1 I_1 I_2$ and $O_2 I_1 I_2$

$$A_{\text{Sector } O_1 I_1 I_2} = \frac{1}{2} r_1^2 2 \arccos\left(\frac{d_1}{r_1}\right), \quad A_{\text{Sector } O_2 I_1 I_2} = \frac{1}{2} r_2^2 2 \arccos\left(\frac{d_2}{r_2}\right)$$

- The overlap area is the sum of the area of the two segments, thus,

$$A_{\text{Total Overlap}} = A_{\text{Sector } O_1 I_1 I_2} - A_{\triangle O_1 I_1 I_2} + A_{\text{Sector } O_2 I_1 I_2} - A_{\triangle O_2 I_1 I_2}$$

Overlap Ellipse-Ellipse

The detection of overlap and computation of the overlap area between two Ellipses is done following the work of Hughes and Chraibi (2012) and is achieved analytically. Broadly, the approach is similar to the scheme presented in the previous section for Disks. The overlap is detected computing the intersection points of the two ellipses, using their polynomial representation in Cartesian coordinates. After the intersection points are found, as for the case of the Disks, the segments that make up the overlap area are computed considering the areas of the corresponding triangles and sectors. Before addressing the main goal of this section, the detection, and computation of the overlap between two Ellipses, it is shown how to obtain the segment of an ellipse created by an arbitrary chord, defined by points I_1 and I_2.

Area of an Ellipse segment For an arbitrary ellipse with major semi-axis a and minor semi-axis b, centered at the origin, O, whose principal axis are parallel to the coordinate axis of the reference system, the so-called standard parametrization is

$$(x, y) = (a\cos t, b\sin t), \quad 0 \leq t < 2\pi, \tag{6.11}$$

it is remarked that the parameter t is not the angle that the position vector of point (x, y) makes with the positive x semi-axis, i.e. the "visual" angle. Its geometrical interpretation can be found in Figure 6.4.

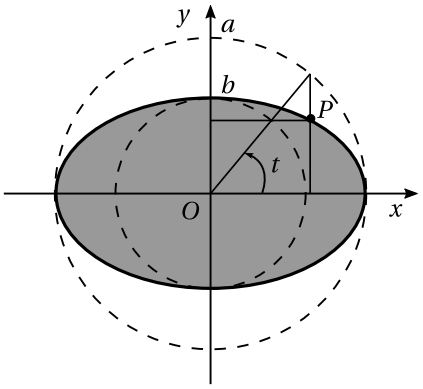

Figure 6.4: Diagram of the standard parametric representation of an ellipse using inscribed and circumscribed circles.

From this parametrization, using the Green-Gauss theorem, the area of the sector is found to be (Hughes and Chraibi, 2012)

$$A_{\text{Sector}} = \frac{ab}{2}\int_{\theta_1}^{\theta_2} dt = \frac{(\theta_2 - \theta_1)\, ab}{2}, \tag{6.12}$$

where θ_1 and θ_2 are the values of the parameter t corresponding to the points I_1 and I_2, respectively. They are found from the standard parametrization (Equation (6.11)), taking care to notice the quadrant where the point is located,

$$\theta = \begin{cases} \arccos\left(\dfrac{x}{a}\right), & y \geq 0, \\ 2\pi - \arccos\left(\dfrac{x}{a}\right), & y < 0, \end{cases} . \tag{6.13}$$

The area of the corresponding triangle can be found directly from the coordinates of its points as

$$\begin{aligned} A_{\triangle OI_1I_2} &= \frac{1}{2}\left|\det\begin{pmatrix} x_1 & x_2 & x_3 \\ y_1 & y_2 & y_3 \\ 1 & 1 & 1 \end{pmatrix}\right|, \\ &= \frac{1}{2}\left|x_1\left(y_2-y_3\right)-x_2\left(y_1-y_3\right)+x_3\left(y_1-y_2\right)\right|, \end{aligned} \tag{6.14}$$

where $(x_1, y_1) \equiv I_1$, $(x_2, y_2) \equiv I_2$ and $(x_3, y_3) \equiv O$. Since the origin is taken to coincide with O, it is found

$$A_{\triangle OI_1I_2} = \frac{1}{2}|x_1y_2 - x_2y_1|. \tag{6.15}$$

Considering the cases presented in Figure 6.5, in the first, the area of the triangle must be added to the sector to obtain the area of the segment and in the second its area must be subtracted. Thus, the area of the segment is given by

$$A_{\text{Segment } I_1I_2} = \frac{\left(\theta_2 - \widehat{\theta}_1\right) a_1\, b_1}{2} + \frac{\text{sign}\left(\theta_2 - \widehat{\theta}_1 - \pi\right)}{2}\left|x_1\, y_2 - x_2\, y_1\right| \tag{6.16}$$

where $(x_1, y_1) \equiv I_1$ and $(x_2, y_2) \equiv I_2$. To accommodate both cases presented in Figure 6.5, the sign of the term relating to the area of the triangle is computed according to the size of the sector, being negative if it encompasses an angle smaller than π and positive otherwise. Also, the angles of the intersection point are ordered such that

$$\widehat{\theta}_1 = \begin{cases} \theta_1, & \theta_1 < \theta_2 \\ \theta_1 - 2\pi, & \theta_1 > \theta_2 \end{cases}, \tag{6.17}$$

to ensure that their difference $\theta_2 - \widehat{\theta}_1$ is positive.

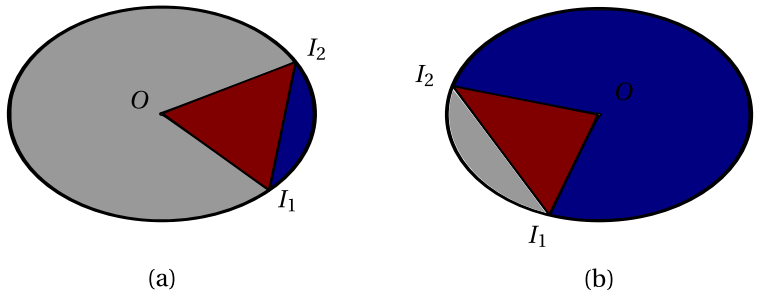

Figure 6.5: Different types of ellipse segments: (a) less than π radians and (b) more than π radians.

Computation of the intersection points In order to obtain the intersection points and detect a possible overlap, the equation describing an ellipse with major semi-axis

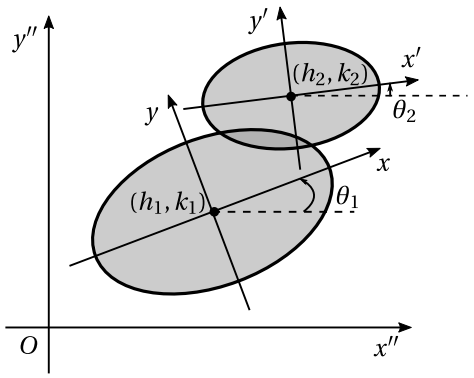

Figure 6.6: Absolute coordinate system an coordinate systems corresponding to Ellipse 1 and Ellipse 2.

a and minor semi-axis b, centered at the origin and whose principal axis coincide with the coordinate axis in Cartesian coordinates, is given as

$$\frac{x^2}{a^2} + \frac{y^2}{b^2} = 1. \tag{6.18}$$

Assume that there are two ellipses, Ellipse 1, with major semi-axis a_1 and minor semi-axis b_1 and angle θ_1 between the major semi-axis and the positive x semi-axis, center located at (h_1, k_1), and Ellipse 2, with major semi-axis a_2 and minor semi-axis b_2 and angle θ_2 between the major semi-axis and the positive x semi-axis, center located at (h_2, k_2), relative to an arbitrary absolute referential (see Figure 6.6). Using the reference system corresponding to Ellipse 1, i.e. the reference system defined by its principal axis, its points (x, y) satisfy

$$\frac{x^2}{a_1^2} + \frac{y^2}{b_1^2} = 1. \tag{6.19}$$

Likewise, the polynomial corresponding to Ellipse 2 in its reference system, denoted by a prime, is

$$\frac{x'^2}{a_2^2} + \frac{y'^2}{b_2^2} = 1. \tag{6.20}$$

To obtain the coordinates of the points satisfying both Equation (6.19) and (6.20), i.e. the intersection points of the two Ellipses, Equation (6.20) must first be written in the coordinates corresponding to Ellipse 1, so that it can be substituted in Equation (6.19). The relation between the two coordinate system is given by

$$\begin{bmatrix} x' \\ y' \end{bmatrix} = \begin{bmatrix} \cos(\theta_2 - \theta_1) & -\sin(\theta_2 - \theta_1) \\ \sin(\theta_2 - \theta_1) & \cos(\theta_2 - \theta_1) \end{bmatrix} \begin{bmatrix} x - (h_1 - h_2) \\ y - (k_1 - k_2) \end{bmatrix}. \tag{6.21}$$

This transformation can be interpreted as a translation to the center of the Ellipse 2 and subsequent rotation through the angle difference between the two systems of reference relative to the absolute referential considered. Substitution in Equation (6.20)

yields

$$\frac{\Big(\cos\big(\theta_2-\theta_1\big)\Big(x-\big(h_1-h_2\big)\Big)-\sin\big(\theta_2-\theta_1\big)\Big(y-\big(k_1-k_2\big)\Big)\Big)^2}{a_2^2} + \frac{\Big(\sin\big(\theta_2-\theta_1\big)\Big(x-\big(h_1-h_2\big)\Big)+\cos\big(\theta_2-\theta_1\big)\Big(y-\big(k_1-k_2\big)\Big)\Big)^2}{b_2^2} = 1.$$

Hence, the polynomial characterizing Ellipse 2 written in the coordinate system corresponding to Ellipse 1 is given by

$$AA\,x^2 + BB\,x\,y + CC\,y^2 + DD\,x + EE\,y + FF = 0, \tag{6.22}$$

where the coefficients of the polynomial, after factoring and regrouping, are found to be

$$AA = a_2^2\sin^2(\theta_2-\theta_1) + b_2^2\cos^2(\theta_2-\theta_1), \tag{6.23}$$
$$BB = 2(b_2^2-a_2^2)\sin(\theta_2-\theta_1)\cos(\theta_2-\theta_1), \tag{6.24}$$
$$CC = a_2^2\cos^2(\theta_2-\theta_1) + b_2^2\sin^2(\theta_2-\theta_1), \tag{6.25}$$
$$DD = -2AA(h_1-h_2) - BB(k_1-k_2), \tag{6.26}$$
$$EE = -BB(h_1-h_2) - 2CC(k_1-k_2), \tag{6.27}$$
$$FF = AA(h_1-h_2)^2 + BB(h_1-h_2)(k_1-k_2) + CC(k_1-k_2)^2 - a_2^2\,b_2^2. \tag{6.28}$$

It is now possible to substitute

$$x = \pm\sqrt{a_1^2\left(1-\frac{y^2}{b_1^2}\right)}, \tag{6.29}$$

found from rewriting Equation (6.19), in Equation (6.22), and obtain the quartic polynomial in y, whose solutions are the ordinates of the intersection points. It reads

$$cy[4]\,y^4 + cy[3]\,y^3 + cy[2]\,y^2 + cy[1]\,y + cy[0] = 0, \tag{6.30}$$

where the coefficients are

$$cy[0] = -CC^2\,b_1^4 + 2\,(AA\,CC - BB^2/2)\,a_1^2\,b_1^2 - a_1^4\,AA^2, \tag{6.31}$$
$$\begin{aligned} cy[1] = &-\big((-a_1\,BB+EE)\,CC + CC\,(a_1\,BB+EE)\big)\,b_1^4 \\ &+2\,(AA\,EE - BB\,DD)\,a_1^2\,b_1^2, \end{aligned} \tag{6.32}$$
$$\begin{aligned} cy[2] = &-\Big((a_1^2\,AA - a_1\,DD + FF)\,CC + (-a_1\,BB+EE)\,(a_1\,BB+EE) \\ &+CC\,(a_1^2\,AA + a_1\,DD + FF)\Big)\,b_1^4 \\ &+2\,(AA^2\,a_1^2 + AA\,FF - 1/2\,DD^2)\,a_1^2\,b_1^2, \end{aligned} \tag{6.33}$$
$$\begin{aligned} cy[3] = &-\Big((a_1^2\,AA - a_1\,DD + FF)\,(a_1\,BB+EE) \\ &+(-a_1\,BB+EE)\,(a_1^2\,AA + a_1\,DD + FF)\Big)\,b_1^4, \end{aligned} \tag{6.34}$$
$$cy[4] = -(a_1^2\,AA - a_1\,DD + FF)\,(a_1^2\,AA + a_1\,DD + FF)\,b_1^4. \tag{6.35}$$

These coefficients are obtained by the author, as the ones supplied by Hughes and Chraibi (2012) were not producing the correct results.

First, there is a need to obtain the intersection points of the ellipses. Each distinct real root of the polynomial represents a y-value where the two ellipses intersect and may correspond to either one or two potential points of intersection. The first case corresponds to the case when $y = b_1$ or $y = -b_1$, and so the y-value produces a single intersection point at $(0, b_1)$ or $(0, -b_1)$, respectively. In the second case, if the y-value is in in the open interval $(-b_1, b_1)$, there are two potential intersection points

$$\left(a_1 \sqrt{1 - \frac{y^2}{b_1^2}}, y \right) \text{ and } \left(-a_1 \sqrt{1 - \frac{y^2}{b_1^2}}, y \right), \tag{6.36}$$

corresponding to the points in Ellipse 1 with the corresponding y-value. To determine if these points are in fact intersection points, they are substituted in Equation (6.22), and if the equality is satisfied, then the point is an intersection point.

Box 6.3 presents the pseudo-code for the computation of the intersection points between two ellipses.

Box 6.3: Algorithm for the computation of the intersection points between two ellipses.

(i) Compute the roots of the polynomial

$$cy[4]\, y^4 + cy[3]\, y^3 + cy[2]\, y^2 + cy[1]\, y + cy[0] = 0$$

(ii) For each real root y^*, check how many intersection points correspond to it.
If $y^* = b_1$ or $y^* = b_1$

- there is only one intersection point corresponding to y^*, i.e. $(0, b_1)$ and $(0, -b_1)$, respectively.

else

- Compute the tentative intersection points corresponding to y^*, as the two points from Ellipse 1

$$\left(a_1 \sqrt{1 - \frac{y^{*2}}{b_1^2}}, y^* \right) \text{ and } \left(-a_1 \sqrt{1 - \frac{y^{*2}}{b_1^2}}, y^* \right)$$

- For each tentative intersection point, check if it also belongs to Ellipse 2, using its definition in Cartesian coordinates

$$AA\, x^2 + BB\, x\, y + CC\, y^2 + DD\, x + EE\, y + FF = 0.$$

If it does, then it is an intersection point.

Computing the overlap area The following steps regarding the computation of the overlap area depend on the number of intersection points found from the polynomial in Equation (6.30). Being a quartic polynomial it may have

1. no real roots (two complex-conjugate pairs), which means that the ellipse curves do not intersect;

2. two real roots (distinct or not) and one complex-conjugate pair, so the ellipse curves intersect;

3. four real roots (distinct or not), meaning that the ellipse curves intersect.

Case (1) represents two possibilities, either the ellipses do not intersect, or one is contained in the other (see Figure 6.7). To understand which of the two cases is being handled, it is checked if the center of the Ellipse with the smaller area, Ellipse 2, is inside the larger Ellipse, Ellipse 1. If so, the overlap area is equal to the area of the Ellipse 2. Otherwise, there is no intersection and the overlap area is zero.

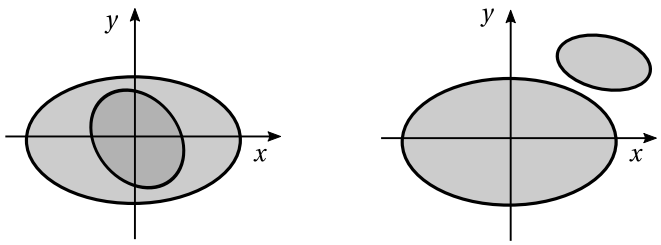

Figure 6.7: Possible cases for the intersection of two ellipses, when the number of intersection points is 0: (a) Ellipse 2 is entirely inside Ellipse 1 and (b) the two Ellipses do not intersect.

Case (2) also represents two possibilities, either the ellipses intersect each other at one point, i.e. the two real roots are equal, or they intersect at two points, i.e. the two real roots are different. Regarding the former case, the argument is the same as in case (1), and either the overlap area is zero or it corresponds to the area of the Ellipse with the smaller area (see Figure 6.8).

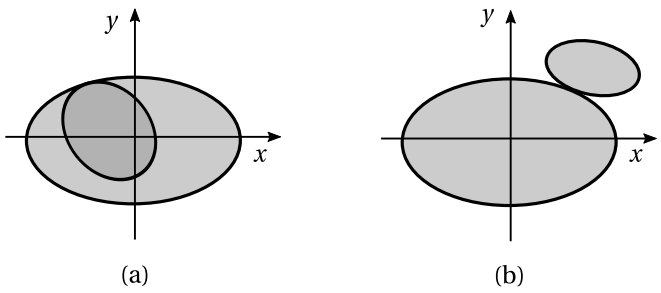

Figure 6.8: Possible cases for the intersection of two ellipses, when the number of intersection points is 1: (a) Ellipse 2 is entirely inside Ellipse 1 and (b) the two Ellipses do not intersect.

On the other hand, when the two real roots are different, the situation is very similar to the one presented in the previous section regarding the overlap area of two disks. The general argument is much the same, and the overlap area is composed of the two segments $I_1 I_2$ corresponding to each Ellipse (see Figure 6.9).

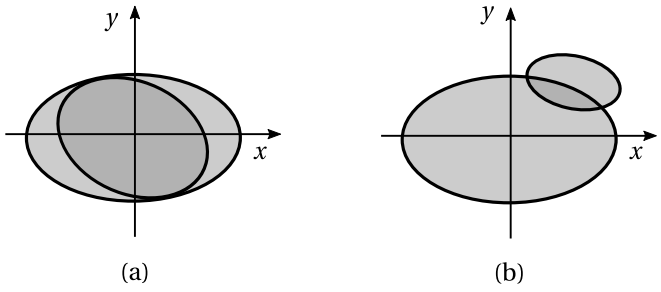

Figure 6.9: Possible cases for the intersection of two ellipses, when the number of intersection points is 2.

Since the approach to compute the area of an ellipse segment is presented at the beginning of this section, it remains to show what are the segments that need to be computed. Assuming that the two intersection points, I_1 and I_2, are ordered clockwise according to their parametric angles, θ_1 and θ_2, computed from Equation (6.13), a point in Ellipse 1 is found, such that it is a midpoint between I_1 and I_2, as it relates to its parametric angle

$$x_{\text{mid}} = a_1 \cos\left(\frac{\theta_1 + \theta_2}{2}\right), \tag{6.37}$$

$$y_{\text{mid}} = b_1 \sin\left(\frac{\theta_1 + \theta_2}{2}\right). \tag{6.38}$$

If the point is also inside Ellipse 2, then the segment to be computed belongs to Ellipse 1 and is computed according to Equation (6.16). Otherwise, the segment to be

computed belongs to Ellipse 2.

The other segment is computed plugging the angles in reverse order in Equation (6.16), as it assumes that the points must be given in counter-clockwise order. The decision to compute it relative to Ellipse 1 or 2 is taken using the same rule as the first segment, with the parametric angle of the midpoint given by $(\theta_1+\theta_2)/2+\pi$. Thus, both cases presented in Figure 6.9 are covered.

Case (3) also encapsulates two further cases, that is, three different intersection points and four intersection points (see Figure 6.10). For the former case, there are two possible sub-cases. One of the three intersection points must be a tangent point in both cases. After detecting which of the three points is the tangent point, the overlap area can be computed as in the case of two intersection points, considering the tangent intersection point as the midpoint used to decide which segments to compute.

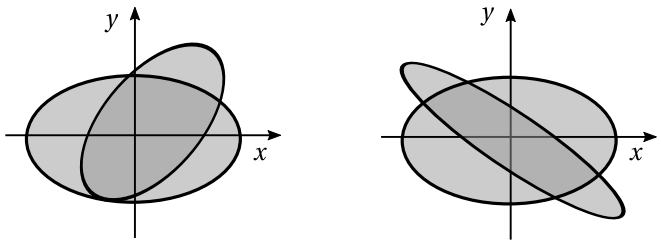

Figure 6.10: Possible cases for the intersection of two ellipses, when the number of intersection points is 3, (a), or 4, (b).

When the ellipses intersect at four different points there is only one case to consider (see Figure 6.10). The points are once again assumed to be sorted counter-clockwise according to their parametric angle, and hence the area of the quadrilateral $I_1I_2I_3I_4$ is given by

$$\begin{aligned} A_{\text{Quadrilateral } I_1I_2I_3I_4} &= \frac{1}{2}\left|\left(x_3-x_1, y_3-y_1\right)\times\left(x_4-x_2, y_4-y_2\right)\right|, \\ &= \frac{1}{2}\left|\left(x_3-x_1\right)\left(y_4-y_2\right)-\left(x_4-x_2\right)\left(x_3-x_1\right)\right|, \end{aligned} \tag{6.39}$$

as half the cross-product of the two diagonals.

The point order also simplifies the search for the appropriate segments of each ellipse that contribute to the overlap area. This is done in the same way as in the case of only two intersection points. A midpoint is defined in Ellipse 1 as it relates to the parametric angle between I_1 and I_2, checking if it is inside Ellipse 2. The corresponding segment is computed relative to Ellipse 1 if this the case and relative to Ellipse 2, otherwise. The segment I_2I_3 is computed in the same way as described above, plugging the points in reverse order in Equation (6.16) and relative to the other Ellipse. Segments I_3I_4 and I_4I_1 are computed relative to the same Ellipses that I_1I_2 and I_2I_3 were computed, respectively. This algorithm is validated using Monte Carlo integration (see Section 6.5.2).

Box 6.4 presents the full pseudo-code for the computation of the overlap area between two ellipses is given the intersection points.

Box 6.4: Algorithm for the computation of the overlap area between two ellipses.

If there are no intersection points or just one intersection point

(i) Denote the ellipse with larger area as Ellipse 1 and the ellipse with smaller area as Ellipse 2

(ii) Check if Ellipse 2 is entirely inside Ellipse 1
If the center of Ellipse 2 is inside Ellipse 1

- Ellipse 2 is entirely contained inside Ellipse 1, thus

$$A_{\text{Total Overlap}} = \pi a_2 b_2$$

else

- Ellipse 2 is entirely outside Ellipse 1, thus

$$A_{\text{Overlap}} = 0$$

else if there are two or three intersection points

(i) Obtain the point $(x_{\text{mid}}, y_{\text{mid}})$, according to the number of intersection points.
If there are two intersection points, $(x_1, y_1) \equiv I_1$ and $(x_2, y_2) \equiv I_2$

- Compute their respective parametric angles, θ_1 and θ_2 relative to Ellipse 1

$$\theta_i = \begin{cases} \arccos\left(\dfrac{x_i}{a_1}\right), & y_i \geq 0, \\ 2\pi - \arccos\left(\dfrac{x_i}{a_1}\right), & y_i < 0, \end{cases} \qquad \text{for } i = 1,2$$

- Compute $(x_{\text{mid}}, y_{\text{mid}})$ as

$$x_{\text{mid}} = a_1 \cos\left(\frac{\theta_1 + \theta_2}{2}\right), \quad y_{\text{mid}} = b_1 \sin\left(\frac{\theta_1 + \theta_2}{2}\right)$$

else if there are three intersection points, I_1, I_2 and I_3,

- Determine which of the three intersection points is the tangent point. Assume it is I_3, and make $(x_{\text{mid}}, y_{\text{mid}}) \equiv I_3$.

(ii) Compute the relevant segments that constitute the overlap area.
If $(x_{\text{mid}}, y_{\text{mid}})$ is in Ellipse 2

- Compute the area of segment $I_1 I_2$ from Ellipse 1, $A_{\text{Segment } I_1 I_2}$, and the area of segment $I_2 I_1$ from Ellipse 2, $A_{\text{Segment } I_2 I_2}$

else

- Compute the area of segment $I_1 I_2$ from Ellipse 2, $A_{\text{Segment } I_1 I_2}$, and the area of segment $I_2 I_1$ from Ellipse 1, $A_{\text{Segment } I_2 I_2}$

(iii) The overlap area is

$$A_{\text{Total Overlap}} = A_{\text{Segment } I_1 I_2} + A_{\text{Segment } I_2 I_1}$$

Box 6.4: (continuation)

else if there are four intersection points

(i) Order the intersection points in counter-clockwise fashion according to their parametric angle, such that I_1 has the smallest parametric angle, θ_1, and I_4 the largest parametric angle, θ_4.

(ii) Compute the area of the quadrilateral defined by the four intersection points $I_1 \equiv (x_1, y_1)$, $I_2 \equiv (x_2, y_2)$, $I_3 \equiv (x_3, y_3)$ and $I_4 \equiv (x_4, y_4)$

$$A_{\text{Quadrilateral } I_1 I_2 I_3 I_4} = \frac{1}{2}\left|\left(x_3 - x_1\right)\left(y_4 - y_2\right) - \left(x_4 - x_2\right)\left(x_3 - x_1\right)\right|$$

(iii) Compute the midpoint-point between I_1 and I_2 relative to their parametric angles,

$$x_{\text{mid}} = a_1 \cos\left(\frac{\theta_1 + \theta_2}{2}\right), \quad y_{\text{mid}} = b_1 \sin\left(\frac{\theta_1 + \theta_2}{2}\right)$$

(iv) Compute the relevant segments that constitute the overlap area
If $(x_{\text{mid}}, y_{\text{mid}})$ is in Ellipse 2

- Compute the area of segment $I_1 I_2$, $A_{\text{Segment } I_1 I_2}$, and segment $I_3 I_4$, $A_{\text{Segment } I_3 I_4}$ from Ellipse 1 and the area of segment $I_2 I_1$, $A_{\text{Segment } I_1 I_2}$, and segment $I_4 I_1$, $A_{\text{Segment } I_4 I_1}$ from Ellipse 2

else

- Compute the area of segment $I_1 I_2$, $A_{\text{Segment } I_1 I_2}$, and segment $I_3 I_4$, $A_{\text{Segment } I_3 I_4}$ from Ellipse 2 and the area of segment $I_2 I_1$, $A_{\text{Segment } I_1 I_2}$, and segment $I_4 I_1$, $A_{\text{Segment } I_4 I_1}$ from Ellipse 1

(v) The overlap area is

$$\begin{aligned} A_{\text{Total Overlap}} = {} & A_{\text{Quadrilateral } I_1 I_2 I_3 I_4} \\ & + A_{\text{Segment } I_1 I_2} + A_{\text{Segment } I_2 I_3} + A_{\text{Segment } I_3 I_4} + A_{\text{Segment } I_1 I_4} \end{aligned}$$

Overlap Sphere-Sphere

The detection of the overlap between two Spheres is achieved computing the distance between the two centers, denoted by O_1 and O_2, and comparing it to the sum of the radii of the two Spheres, denoted by r_1 and r_2. Henceforth, it is assumed that $r_1 \geq r_2$, as in the case regarding the overlap of two Disks. If $\overline{O_1 O_2} < r_1 + r_2$, then there is an overlap between the two Spheres (see Figure 6.11). Moreover, if $\overline{O_1 O_2} \leq r_1 - r_2$ then Sphere 2 is entirely contained within Sphere 1 and the overlap volume is the volume of Sphere 2.

On the other hand, if $r_1 - r_2 < \overline{O_1 O_2} < r_1 + r_2$, the overlap volume is the sum of the caps of Sphere 1 and 2 defined by the plane containing the intersection points and

can be obtained analytically. To compute the volume of the caps, for example, the cap coming from Sphere 1, one considers the corresponding spherical sector as well as the corresponding cone and subtracts the volumes.

The volume of the cone can be found from

$$V_{\text{Cone}} = \frac{1}{3} d_1 \pi \sqrt{r_1^2 - d_1^2}, \tag{6.40}$$

where the radius of its base is found using Pythagoras theorem. The height of cone, d_1, is obtained from

$$d_1 = \frac{r_1^2 - r_2^2 + d^2}{2d}. \tag{6.41}$$

This result can be found from

$$r_1^2 - d_1^2 = r_2^2 - d_2^2, \tag{6.42}$$

where d_2 is the signed height of the cone corresponding to the cap from Sphere 2. Equation 6.42 comes from the application of Pythagoras theorem to the triangles formed by the height of each triangle, their respective radii and generatrices. The signed height of the cone corresponding to the cap from Sphere 2, can be obtained from $d = d_1 + d_2$. It is negative, only when Sphere 2 is smaller than Sphere 1 and its center is between the intersection points and the center of Sphere 1 (see Figure 6.11).

The volume of the spherical sector related to the cap coming from Sphere 1 is found from

$$V_{\text{Sector}} = r_1^3 \frac{2}{3} \pi \left(1 - \frac{d_1}{r_1} \right), \tag{6.43}$$

where $d_1 / r_1 = \cos\varphi$ is half the respective cone angle.

The argument for the cap belonging to Sphere 2 is analogous being the total overlap volume given by

$$V_{\text{Total Overlap}} = V_{\substack{\text{Sector} \\ \text{Sphere 1}}} - V_{\substack{\text{Cone} \\ \text{Sphere 1}}} + V_{\substack{\text{Sector} \\ \text{Sphere 2}}} - V_{\substack{\text{Cone} \\ \text{Sphere 2}}}. \tag{6.44}$$

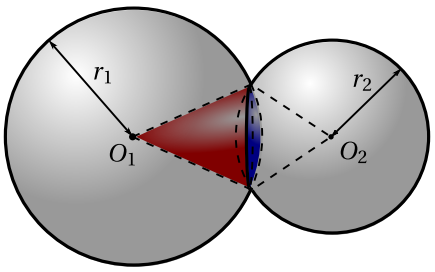

Figure 6.11: Diagram depicting the approach taken to compute the overlap volume between two Spheres of different radii.

Box 6.5: Algorithm for the computation of the overlap area between two spheres.

(i) Denote the larger sphere as Sphere 1 with radius r_1 and center at O_1 and the smaller sphere as Sphere 2 with radius r_2 and center at O_2

(ii) Compute the distance between the center of the spheres, d

(iii) Check if there is overlap.
If $d > r_1 + r_2$

- There is no overlap, thus, $V_{\text{Overlap}} = 0$.

else if $d \leq r_1 - r_2$

- Disk 2 is entirely contained within Disk 1, thus, $V_{\text{Overlap}} = \frac{4}{3}\pi r_2^3$

else if $r_1 - r_2 < d < r_1 + r_2$

- Compute the height of the cones defined by the plane containing the intersection points and the spherical sector

$$d_1 = \frac{r_1^2 - r_2^2 + d^2}{2d}, \quad d_2 = d - d_1$$

- Compute the volume of the cones

$$V_{\text{Cone 1}} = \frac{1}{3} d_1 \pi \sqrt{r_1^2 - d_1^2} \quad V_{\text{Cone 2}} = \frac{1}{3} d_2 \pi \sqrt{r_2^2 - d_2^2}$$

- Compute the area of the spherical sectors

$$V_{\text{Sector 1}} = r_1^3 \frac{2}{3}\pi \left(1 - \frac{d_1}{r_1}\right), \quad A_{\text{Sector } O_2 I_1 I_2} = r_2^3 \frac{2}{3}\pi \left(1 - \frac{d_2}{r_2}\right)$$

- The overlap volume is the sum of the area of the two segments, thus,

$$V_{\text{Total Overlap}} = V_{\substack{\text{Sector} \\ \text{Sphere 1}}} - V_{\substack{\text{Cone} \\ \text{Sphere 1}}} + V_{\substack{\text{Sector} \\ \text{Sphere 2}}} - V_{\substack{\text{Cone} \\ \text{Sphere 2}}}$$

Overlap Ellipsoid-Ellipsoid

In the developed program the detection of the overlap between two Ellipsoids is done analytically following Wang et al. (2001) and Ghossein and Lévesque (2013) using an algebraic criterion related to the coefficients of the characteristic equation, and the computation of the overlap volume is done using a Monte Carlo integration scheme.

Detection of overlap Following Ghossein and Lévesque (2013), the representation in Cartesian coordinates of a generic ellipsoid with principal semi-axis a, b and c is given

by

$$\frac{x^2}{a^2}+\frac{y^2}{b^2}+\frac{z^2}{c^2}=1, \tag{6.45}$$

where the axis of the coordinate system are parallel to its principal axis.

Making use of homogeneous coordinates, such that the point (x,y,z,w) corresponds to $(x/w, y/w, z/w)$ in Cartesian coordinates, Equation (6.45) can be written as

$$\boldsymbol{x}^T \boldsymbol{A}\boldsymbol{x}=0, \tag{6.46}$$

with $\boldsymbol{x}=(x,y,z,1)^{\mathrm{T}}$ and

$$\boldsymbol{A}=\begin{bmatrix} 1/a^2 & 0 & 0 & 0 \\ 0 & 1/b^2 & 0 & 0 \\ 0 & 0 & 1/c^2 & 0 \\ 0 & 0 & 0 & -1 \end{bmatrix}. \tag{6.47}$$

The orientation of a given ellipsoid is defined by a rotation angle θ around an axis oriented along a unit vector $\boldsymbol{e}$, and its position in space by the position vector of its center point, $\boldsymbol{r}$. Thus, the representation of an ellipsoid in the global coordinate system in homogeneous coordinates, denoted by a prime, can be found combining rotation and translation from

$$\boldsymbol{x}'=\mathbf{M}\boldsymbol{x}, \tag{6.48}$$

where

$$\mathbf{M}=\begin{bmatrix} \mathbf{R} & \boldsymbol{r} \\ \mathbf{0}^{\top} & 1 \end{bmatrix}, \tag{6.49}$$

with $\boldsymbol{R}$ the rotation matrix corresponding to the unit vector $\boldsymbol{e}$ and the angle θ.

To assist in the computation of the rotation matrix, normalized quaternions are introduced. The quaternion of the Ellipsoid under analysis, $\boldsymbol{q}$, consists of a scalar α and a vector $\boldsymbol{\psi}$ and is written as follows

$$\boldsymbol{q}=[\alpha,\boldsymbol{\psi}]=\left[\cos\frac{\theta}{2},\boldsymbol{e}\sin\frac{\theta}{2}\right]. \tag{6.50}$$

The rotation matrix can be obtained from the quaternion in the following manner

$$\mathbf{R}=\left[2\alpha^2-1\right]\mathbf{I}+2\boldsymbol{\psi}\boldsymbol{\psi}^T+2\alpha\mathbf{S}, \tag{6.51}$$

where $\mathbf{I}$ is the identity matrix and $\mathbf{S}$ is given by

$$\boldsymbol{S}=\begin{bmatrix} 0 & -\psi_3 & \psi_2 \\ \psi_3 & 0 & -\psi_1 \\ -\psi_2 & \psi_1 & 0 \end{bmatrix}, \tag{6.52}$$

where ψ_k denotes the kth term of vector $\boldsymbol{\psi}$.

Consider now two Ellipsoids, Ellipsoid 1, with principal semi-axis a_1, b_1 and c_1, position of the center point $\boldsymbol{r}_1$ and associated rotation matrix $\boldsymbol{R}_1$, and Ellipsoid 2, with principal semi-axis a_2, b_2 and c_2, position of the center point $\boldsymbol{r}_2$ and associated rotation matrix $\boldsymbol{R}_2$. Accordingly, these Ellipsoids can be expressed in their respective coordinate systems as

$$\boldsymbol{x}^T\boldsymbol{A}_i\boldsymbol{x}=0, \quad i=1,2, \tag{6.53}$$

and in the global coordinate system as

$$\boldsymbol{x}'^{T}\boldsymbol{A}_i'\boldsymbol{x} = 0, \quad i = 1,2, \tag{6.54}$$

with $\boldsymbol{A}_i' = (\boldsymbol{M}_i)^{-T}\boldsymbol{A}_i(\boldsymbol{M}_i)^{-1}$ for $i = 1,2$.

The algebraic criterion presented by Wang et al. (2001) makes use of the so-called characteristic polynomial of the two Ellipsoids, which is defined as

$$f(\lambda) = \det(\lambda\boldsymbol{A}_1' + \boldsymbol{A}_2'). \tag{6.55}$$

According to the roots of Equation 6.55, one can conclude that

1. Ellipsoid 1 and 2 are separate if Equation (6.55) admits two negative and two positive roots,
2. Ellipsoid 1 and 2 are externally tangent if Equation (6.55) admits two negative roots and a double positive root,
3. Ellipsoid 1 and 2 overlap in all other cases.

Equation (6.55) can be rewritten as

$$\det\left(\lambda\boldsymbol{A}_1' + \boldsymbol{A}_2'\right) = p_1\lambda^4 + p_2\lambda^3 + p_3\lambda^2 + p_4\lambda + p_5 = 0, \tag{6.56}$$

where the coefficients p_i, $i = 1,2,3,4,5$ can be obtained from

$$p_1 = -\delta_1\delta_2\delta_3, \tag{6.57}$$

$$p_2 = -\left(\delta_2\delta_3 C_{11} + \delta_1\delta_3 C_{22} + \delta_1\delta_2 C_{33} - \delta_1\delta_2\delta_3 C_{44}\right), \tag{6.58}$$

$$\begin{aligned} p_3 = {} & \delta_1\delta_2\left(C_{33}C_{44} - C_{34}C_{43}\right) + \delta_2\delta_3\left(C_{11}C_{44} - C_{14}C_{41}\right) \\ & + \delta_1\delta_3\left(C_{22}C_{44} - C_{24}C_{42}\right) + \delta_1\left(C_{23}C_{32} - C_{22}C_{33}\right) + \delta_2\left(C_{13}C_{31} - C_{11}C_{33}\right) \\ & + \delta_3\left(C_{12}C_{21} - C_{11}C_{22}\right), \end{aligned} \tag{6.59}$$

$$\begin{aligned} p_4 = {} & \\ & \delta_1\left(C_{22}C_{33}C_{44} - C_{22}C_{34}C_{43} - C_{33}C_{42}C_{24} - C_{44}C_{32}C_{23} + C_{32}C_{24}C_{43} + C_{42}C_{23}C_{34}\right) \\ & +\delta_2\left(C_{11}C_{33}C_{44} - C_{11}C_{34}C_{43} - C_{33}C_{14}C_{41} - C_{44}C_{13}C_{31} + C_{31}C_{14}C_{43} + C_{41}C_{13}C_{34}\right) \\ & +\delta_3\left(C_{11}C_{22}C_{44} - C_{11}C_{24}C_{42} - C_{22}C_{14}C_{41} - C_{44}C_{12}C_{21} + C_{21}C_{14}C_{42} + C_{41}C_{12}C_{24}\right) \\ & +C_{11}C_{23}C_{32} + C_{22}C_{13}C_{31} + C_{33}C_{12}C_{21} - C_{11}C_{22}C_{33} - C_{21}C_{13}C_{32} - C_{31}C_{12}C_{23}, \end{aligned} \tag{6.60}$$

$$p_5 = \det\left(\boldsymbol{A}_2\right), \tag{6.61}$$

with

$$\mathbf{C} = \left(\mathbf{M}_1\right)^{\top}\boldsymbol{A}_2\left(\mathbf{M}_1\right) \tag{6.62}$$

and auxiliary variables δ_i, $i = 1,2,3$ defined as

$$\delta_1 = \left(1/a_1\right)^2, \quad \delta_2 = \left(1/b_1\right)^2, \quad \delta_3 = \left(1/c_1\right)^2. \tag{6.63}$$

Following Ghossein and Lévesque (2013), instead of solving Equation (6.55) directly it suffices to compute five coefficients, denoted by η_i, $i = 1,2,3,4,5$, from the coefficients p_k, $k = 1,2,3,4,5$ such that their values determine the relative position of the two Ellipsoids. This is the case as the exact value of the roots are of no importance. The technique is based on the Sylvester-Habicht matrix of the characteristic equation and its first derivative (Ghossein and Lévesque, 2013).

To compute the coefficients η_i, $i = 1,2,3,4,5$, define the auxiliary variables $\bar{p}_k$, $k = 1,2,3,4$ as

$$\bar{p}_1 = -\frac{p_2}{4p_1}, \quad \bar{p}_2 = \frac{p_3}{6p_1}, \quad \bar{p}_3 = -\frac{p_4}{4p_1}, \quad \bar{p}_4 = \frac{p_5}{p_1}. \tag{6.64}$$

From these compute β_k, $k = 1,2$

$$\beta_1 = \left(\bar{p}_4 - \bar{p}_1\bar{p}_3\right) + 3\left(\bar{p}_2^2 - \bar{p}_1\bar{p}_3\right), \tag{6.65}$$

$$\beta_2 = -\bar{p}_3\left(\bar{p}_3 - \bar{p}_1\bar{p}_2\right) - \bar{p}_4\left(\bar{p}_1^2 - \bar{p}_2\right) - \bar{p}_2\left(\bar{p}_2^2 - \bar{p}_1\bar{p}_3\right). \tag{6.66}$$

Finally, the coefficients η_i, $i = 1,2,3,4,5$ are computed as

$$\eta_1 = \beta_1^3 - 27\beta_2^2, \tag{6.67}$$

$$\eta_2 = -9\left(\bar{p}_3 - \bar{p}_1\bar{p}_2\right)^2 + 27\left(\bar{p}_1^2 - \bar{p}_2\right)\left(\bar{p}_2^2 - \bar{p}_1\bar{p}_3\right) - 3\left(\bar{p}_4 - \bar{p}_1\bar{p}_3\right)\left(\bar{p}_1^2 - \bar{p}_2\right), \tag{6.68}$$

$$\eta_3 = \beta_1\left(\bar{p}_3 - \bar{p}_1\bar{p}_2\right) - 3\bar{p}_1\beta_2, \tag{6.69}$$

$$\eta_4 = \beta_1\left(\bar{p}_3 - \bar{p}_1\bar{p}_2\right) - 3\bar{p}_1\beta_2, \tag{6.70}$$

$$\eta_5 = \left(\bar{p}_1^2 - \bar{p}_2\right). \tag{6.71}$$

The relative position of the Ellipsoids can be found from the value of the coefficients η_i, $i = 1,2,3,4,5$ according to Table 6.1.

Table 6.1: Correspondence between the values of the coefficients η_i, $i = 1,\ldots,5$, found from the coefficients of the characteristic equation of the two Ellipsoid, p_k, $k = 1,\ldots 5$, and the relative configuration of the two Ellipsoids.

Cases	η_1	η_2	η_3	η_4	η_5	Ellipsoids configuration
1	$=0$	>0	>0		>0	separate
2	>0	>0			>0	separate
3	$=0$	>0	<0		>0	externally tangent
4	$=0$	$=0$		<0	>0	externally tangent
5	For all other cases					overlap

Box 6.6 summarizes in pseudo-code the necessary steps to detect overlap between two Ellipsoids.

Box 6.6: Algorithm for the detection of overlap between two ellipsoid.

(i) Compute the matrices relating the global coordinate system and the coordinate system corresponding to Ellipse 1 and Ellipse 2

$$\mathbf{M}_i = \begin{bmatrix} \mathbf{R}_i & \boldsymbol{r}_i \\ \mathbf{0}^\top & 1 \end{bmatrix}, \quad i = 1,2$$

(ii) Compute the matrix $\boldsymbol{A}_2'$, defining Ellipsoid 2 in global homogeneous coordinates.

$$\boldsymbol{A}_2' = (\boldsymbol{M}_2)^{-T} \boldsymbol{A}_2 (\boldsymbol{M}_2)^{-1}$$

where $\boldsymbol{A}_2 = \text{diag}(1/(a_2)^2, 1/(b_2)^2, 1/(b_2)^2, 1)$.

(iii) Compute the matrix $\boldsymbol{C}$

$$\mathbf{C} = \left(\mathbf{M}_1\right)^\top \boldsymbol{A}_2 \left(\mathbf{M}_1\right)$$

(iv) Compute the δ_i, $i = 1,2,3$

$$\delta_1 = \left(1/a_1\right)^2, \quad \delta_2 = \left(1/b_1\right)^2, \quad \delta_3 = \left(1/c_1\right)^2$$

(v) Compute the coefficients p_i, $i = 1,2,3,4,5$

$$\begin{aligned}
p_1 &= -\delta_1\delta_2\delta_3 \\
p_2 &= -\left(\delta_2\delta_3 C_{11} + \delta_1\delta_3 C_{22} + \delta_1\delta_2 C_{33} - \delta_1\delta_2\delta_3 C_{44}\right) \\
p_3 &= \delta_1\delta_2\left(C_{33}C_{44} - C_{34}C_{43}\right) + \delta_2\delta_3\left(C_{11}C_{44} - C_{14}C_{41}\right) \\
&\quad + \delta_1\delta_3\left(C_{22}C_{44} - C_{24}C_{42}\right) + \delta_1\left(C_{23}C_{32} - C_{22}C_{33}\right) + \delta_2\left(C_{13}C_{31} - C_{11}C_{33}\right) \\
&\quad + \delta_3\left(C_{12}C_{21} - C_{11}C_{22}\right) \\
p_4 &= \\
&\quad \delta_1\left(C_{22}C_{33}C_{44} - C_{22}C_{34}C_{43} - C_{33}C_{42}C_{24} - C_{44}C_{32}C_{23} + C_{32}C_{24}C_{43} + C_{42}C_{23}C_{34}\right) \\
&\quad +\delta_2\left(C_{11}C_{33}C_{44} - C_{11}C_{34}C_{43} - C_{33}C_{14}C_{41} - C_{44}C_{13}C_{31} + C_{31}C_{14}C_{43} + C_{41}C_{13}C_{34}\right) \\
&\quad +\delta_3\left(C_{11}C_{22}C_{44} - C_{11}C_{24}C_{42} - C_{22}C_{14}C_{41} - C_{44}C_{12}C_{21} + C_{21}C_{14}C_{42} + C_{41}C_{12}C_{24}\right) \\
&\quad +C_{11}C_{23}C_{32} + C_{22}C_{13}C_{31} + C_{33}C_{12}C_{21} - C_{11}C_{22}C_{33} - C_{21}C_{13}C_{32} - C_{31}C_{12}C_{23} \\
p_5 &= \det\left(\boldsymbol{A}_2'\right)
\end{aligned}$$

(vi) Compute $\bar{p}_i$, $i = 1,2,3,4$

$$\bar{p}_1 = -\frac{p_2}{4p_1}, \quad \bar{p}_2 = \frac{p_3}{6p_1}, \quad \bar{p}_3 = -\frac{p_4}{4p_1}, \quad \bar{p}_4 = \frac{p_5}{p_1}$$

(vii) Compute β_1 and β_2

$$\begin{aligned}
\beta_1 &= \left(\bar{p}_4 - \bar{p}_1\bar{p}_3\right) + 3\left(\bar{p}_2^2 - \bar{p}_1\bar{p}_3\right) \\
\beta_2 &= -\bar{p}_3\left(\bar{p}_3 - \bar{p}_1\bar{p}_2\right) - \bar{p}_4\left(\bar{p}_1^2 - \bar{p}_2\right) - \bar{p}_2\left(\bar{p}_2^2 - \bar{p}_1\bar{p}_3\right)
\end{aligned}$$

Box 6.6: (continuation)

(viii) Compute the coefficients η_i, $i = 1,2,3,4,5$ are computed as

$$\eta_1 = \beta_1^3 - 27\beta_2^2$$
$$\eta_2 = -9\left(\bar{p}_3 - \bar{p}_1\bar{p}_2\right)^2 + 27\left(\bar{p}_1^2 - \bar{p}_2\right)\left(\bar{p}_2^2 - \bar{p}_1\bar{p}_3\right) - 3\left(\bar{p}_4 - \bar{p}_1\bar{p}_3\right)\left(\bar{p}_1^2 - \bar{p}_2\right)$$
$$\eta_3 = \beta_1\left(\bar{p}_3 - \bar{p}_1\bar{p}_2\right) - 3\bar{p}_1\beta_2$$
$$\eta_3 = \beta_1\left(\bar{p}_3 - \bar{p}_1\bar{p}_2\right) - 3\bar{p}_1\beta_2$$
$$\eta_5 = \left(\bar{p}_1^2 - \bar{p}_2\right)$$

(ix) Determine the relative position of the Ellipsoids form η_i, $i = 1,2,3,4,5$.
If $\eta_1 = 0$, $\eta_2 > 0$, $\eta_3 > 0$ and $\eta_5 > 0$

- The Ellipsoids are separate

else, if $\eta_1 > 0$, $\eta_2 > 0$ and $\eta_5 > 0$

- The Ellipsoids are separate

else if $\eta_1 = 0$, $\eta_2 > 0$, $\eta_3 < 0$ and $\eta_5 > 0$

- The Ellipsoids are externally tangent

If $\eta_1 = 0$, $\eta_2 = 0$, $\eta_4 < 0$ and $\eta_5 > 0$

- The Ellipsoids are externally tangent

else

- The Ellipsoids overlap

Computation of the overlap volume This section presents how to compute the overlap volume between two ellipsoids using a Monte Carlo integration scheme without rejection. The approach is based on generating uniform random points inside one of the Ellipsoids, say Ellipsoid 1, and counting how many of these points are also inside Ellipsoid 2. The overlap area is the fraction of generated points that is inside both Ellipsoid 1 and 2 multiplied by the volume of Ellipsoid 1.

A given integral $\int_{-1}^{1}\int_{-1}^{1}\mathcal{O}(x,y)\,\pi(x,y)\,\mathrm{d}x\,\mathrm{d}y$ can be estimated using Monte Carlo integration through (Krauth, 2006)

$$\langle\mathcal{O}\rangle = \frac{\int_{-1}^{1}\int_{-1}^{1}\mathcal{O}(x,y)\,\pi(x,y)\,\mathrm{d}x\,\mathrm{d}y}{\int_{-1}^{1}\int_{-1}^{1}\pi(x,y)\,\mathrm{d}x\,\mathrm{d}y} \simeq \frac{1}{N}\sum_{i=1}^{N}\mathcal{O}_i, \tag{6.72}$$

where $\mathcal{O}(x,y)$ is the observable, $\mathcal{O}_i$ is the value of the observable at the point corresponding to sample i, $\pi(x,y)$ is the probability distribution sampled and N the number of samples.

Assuming that the central limit theorem is valid, which is reasonable for large N,

the value of the integration with 95% confidence is given by

$$\langle \mathcal{O} \rangle = \frac{1}{N} \sum_{i=1}^{N} \mathcal{O}_i \pm \frac{2\sigma}{\sqrt{N}}, \tag{6.73}$$

with σ the standard deviation estimated from the sample.

Using modified spherical coordinates related to Ellipsoid 1, defined as

$$x = a_1\, r\, \sin\theta \cos\varphi, \tag{6.74}$$

$$y = b_1\, r\, \sin\theta \sin\varphi, \tag{6.75}$$

$$z = c_1\, r\, \cos\theta, \tag{6.76}$$

$$r = \frac{x^2}{a_1^2} + \frac{y^2}{b_1^2} + \frac{z^2}{c_1^2}, \tag{6.77}$$

with the radius $r \in [0,1]$, the inclination $\theta \in [0,\pi]$ and the azimuth $\varphi \in [0,2\pi)$, the overlap volume between two Ellipsoids can be expressed as

$$V_{\text{Overlap}} = a_1 b_1 c_1 \int_0^1 \int_{S^2} \mathcal{O}(r,\Omega)\, r^2 \,\mathrm{d}\Omega\,\mathrm{d}r, \tag{6.78}$$

where S^2 is the surface of the unit sphere, with the solid angle Ω related to the inclination θ and the azimuth φ by $\mathrm{d}\Omega = \sin\theta \mathrm{d}\theta \mathrm{d}\varphi$. The function $\mathcal{O}(r,\Omega)$ is defined as

$$\mathcal{O}(r,\Omega) = \begin{cases} 1, & \text{if } (r,\Omega) \text{ is in Ellipsoid 2} \\ 0, & \text{if } (r,\Omega) \text{ is not in Ellipsoid 2} \end{cases}. \tag{6.79}$$

Applying Equation (6.72) to the problem at hand, one finds

$$\frac{\int_0^1 \int_{S^2} \mathcal{O}(r,\Omega)\, r^2 \,\mathrm{d}\Omega\,\mathrm{d}r}{\int_0^1 \int_{S^2} r^2 \,\mathrm{d}\Omega\,\mathrm{d}r} \simeq \frac{1}{N} \sum_{i=1}^{N} \mathcal{O}_i, \tag{6.80}$$

which can be rewritten as

$$V_{\text{Overlap}} = \frac{N_{\text{in}}}{N} V_{\text{Ellipse 1}}, \tag{6.81}$$

since

$$a_1 b_1 c_1 \int_0^1 \int_{S^2} r^2 \,\mathrm{d}\Omega\,\mathrm{d}r = \frac{4}{3}\pi a_1 b_1 c_1 = V_{\text{Ellipsoid 1}}, \tag{6.82}$$

where N is the number of samples and N_{in} is the number of samples inside both Ellipsoid 1 and Ellipsoid 2. Figure 6.12 depicts this approach. Thus, to evaluate the overlap volume one needs to sample the integral in the left-hand side of Equation (6.82), i.e. to uniformly sample Ellipsoid 1.

Following Krauth (2006), to generate uniform random points inside a sphere one raises the error integral of a standard Gaussian, written as

$$\int_{-\infty}^{\infty} \frac{1}{\sqrt{2\pi}} e^{-x^2/2}\,\mathrm{d}x = 1, \tag{6.83}$$

to the third power. Using polar coordinates, with r the radial coordinate and the Ω the solid angle, one obtains

$$\left(\frac{1}{\sqrt{2\pi}}\right)^3 \int_0^{\infty} \int_{S^2} r^2 \exp\left(-r^2/2\right) \mathrm{d}\Omega\,\mathrm{d}r = 1, \tag{6.84}$$

which is sampled by 3 independent Gaussians. It can also be asserted that these 3 independent Gaussians sample the solid angle uniformly, as the integrand does not depend on the solid angle.

Comparing Equation (6.84) with the integral for the volume of the unit sphere

$$V_2(1) = \int_0^1 \int_{S^2} r^2 \mathrm{d},\Omega \, \mathrm{d}r \tag{6.85}$$

also expressed in polar coordinates, one can can conclude that to sample the integral in Equation (6.85), i.e. to uniformly sample the unit sphere, the solid angle must also be uniformly sampled. Thus, the direction of the sample vector (x, y, z) can be found from the direction of the vector (w_1, w_2, w_3), where each w_i, $i = 1,2,3$ is an independent sample from a standard Gaussian. To sample the magnitude of (x, y, z) appropriately, i.e. to sample the integral $\int_0^1 r^2 \mathrm{d}r$, one obtains the value of r for a given sample from $\texttt{ran}(0,1)^{1/3}$, where $\texttt{ran}(0,1)$ denotes a uniform distribution between 0 and 1. Therefore, the random uniform sample inside the unit sphere (x, y, z) can be obtain from

$$(x, y, z) = \frac{r}{\|w\|}(w_1, w_2, w_3). \tag{6.86}$$

To sample a uniform random point inside Ellipsoid 1 one applies an affine transformation, rescaling the axis in each direction by a_1, b_1 and c_1. Hence

$$(x, y, z) = \frac{r}{\|w\|}\left(a_1\, w_1, b_1\, w_2, c_1\, w_3\right). \tag{6.87}$$

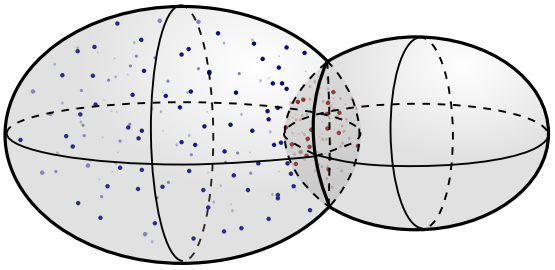

Figure 6.12: Monte Carlo integration of the overlap between two Ellipsoids. The overlap volume is the product of the volume of the Ellipsoid where the random points are generated and the fraction of random points inside both Ellipsoids.

This approach is validated with Ellipsoid 2 completely inside Ellipsoid 1 recovering its volume, as expected. Also, using standard numerical quadrature from the Python library `scipy`, to compute the overlap volume between Ellipsoids in arbitrary relative positions, the same results are obtained, producing results much faster for the same number of points. Lastly, a similar approach was employed to validate the computation of the overlap area between Ellipses.

Box 6.7 summarizes in pseudo-code the approach described to evaluate the overlap volume of two Ellipsoids using Monte Carlo integration.

Box 6.7: Pseudo-code for the evaluation of the overlap volume of two Ellipsoids using Monte Carlo integration.

(i) Initialize the required tolerance tol, the maximum number of iterations, $n_{\max}$ and the counter, i, $i \leftarrow 0$

(ii) Sample the direction of the position vector of the sample point, generating three independent samples from a standard Gaussian distribution, denoting them with w_1, w_2 and w_3

$$\boldsymbol{w} = (w_1, w_2, w_3) \leftarrow \big(\texttt{gauss(1)}, \texttt{gauss(1)}, \texttt{gauss(1)}\big)$$

(iii) Sample the radius of the position vector of the sample point

$$r \leftarrow \texttt{ran}(0,1)^{1/3}$$

(iv) Obtain the coordinates of the sample point as

$$(x, y, z) = \frac{r}{\|w\|}\big(a_1\, w_1, b_1\, w_2, c_1\, w_3\big),$$

with $\|w\| = \sqrt{w_1^2 + w_2^2 + w_3^2}$

(v) Check if (x, y, z) is Ellipsoid 2
If (x, y, z) is in Ellipsoid 2

- $\mathcal{O}_i = 1$

else

- $\mathcal{O}_i = 0$

(vi) If $i > 1$, compute the standard deviation of the samples $\mathcal{O}_k$, $k = 0, \ldots, i$

(vii) Check if the stopping criteria have been reached
If $(2\sigma/\sqrt{i+1})\, V_{\text{Ellipsoid 1}} < \text{tol}$

- End the integration procedure with the estimate for the overlap volume being

$$V_{\text{Overlap}} = \frac{\sum_{k=0}^{i} \mathcal{O}_k}{i+1} V_{\text{Ellipsoid 1}}$$

else if $i = n_{\max}$

- Exit the integration procedure and signal that the required tolerance was not achieved

else

- Update the sample counter, $i \leftarrow i + 1$ and go to step (iii)

6.5.3 Speed-up schemes

This section deals with the speed-up schemes used to avoid the computation of overlap between particles that can be shown a priori not to interact with each other.

A naive approach to computing the forces between all particles is to consider all particle pairs without repetition, which leads to the computation of $n(n-1)/2$ forces. This is undesirable, as it becomes burdensome when the system contains a large amount of particles, and unnecessary, as the force between the majority of the particle pairs is null. To mitigate this problem a few schemes have been proposed. In the remainder of this section the cell list and the Verlet list computed from a cell list are presented.

Cell list

The cell list method is based on the partition of the simulation box using a cell grid such that each particle can only interact with particles in its own or immediately neighboring cells. This is achieved by setting the size of the cells equal or slightly larger than the diameter of the circumscribed circle of the particle (Frenkel and Smit, 2001; Krauth, 2006). Hence the cell list method is most efficient for disks and spheres, providing less and less benefits for ellipses and ellipsoids with large ratios between their principal axis (Donev et al., 2005a).

Since the allocation of a particle to a cell is an operation that scales with the number of particles and the total number of cells that needs to be considered for the calculation of the interaction is independent of the system size, the cell list method scales linearly with the number of particles (Frenkel and Smit, 2001; Krauth, 2006).

Figure 6.13 illustrates this scheme and Box 6.8 presents the pseudo-code for its implementation.

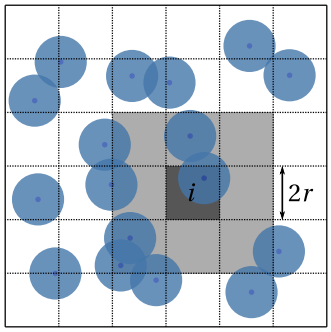

Figure 6.13: Diagram illustrating the cell list method. The Disks with radius r whose center is in the cell i (dark gray) interact only with particles whose center is in the cell i or in the neighboring cells (light gray).

Box 6.8: Pseudo-code for the computation of interactions between particles using cell lists.

(i) Compute a new cell list, saving for each cell the particles whose center is inside them

(ii) For each particle i, in the simulation box

  (1) For each cell k in the neighborhood of the cell containing particle i

    (a) For each particle j in the neighbor cell k, such that $j > i$

      • Compute the force between particle i and particle j

Verlet list computed from a cell list

The Verlet list or neighbor list approach makes use of a list, the so-called Verlet list, computed using a neighborhood with the same shape as the particle, but larger (see Figure 6.14a). All the particles whose neighborhoods intersect are included in each others Verlet lists. In the subsequent calculation of the interactions, only those particles in the list have to be considered. The neighborhood remains fixed in space as the particles move, until a new Verlet list is computed (Frenkel and Smit, 2001).

In the first iteration after the computation of the list no time is saved. However, if the maximum displacement of the particles is such that none of them exits its neighborhood, one only needs to consider the particles in the Verlet list of each particle for the force computation (see Figure 6.14b). This calculation is of the order of the number of particles in the system. As soon as one of the particles moves outside the neighborhood, the Verlet lists must be updated (see Figure 6.14c). This last operation if done according to the naive scheme described in the beginning of this section is proportional to the square of the number of particles, but if it is obtained using a cell list it scales linearly with the number of particles. Although this step is not performed at each iteration, it will dominate for a very large number of particles if the Verlet lists are computed naively (Frenkel and Smit, 2001).

The difference in efficiency between the Verlet list computed from a cell list and the cell list by itself depends on the the specifics of the system and the size of the neighborhood (Frenkel and Smit, 2001). To estimate the difference in efficiency for a system of spheres, consider that, using the cell list, the number of particles for which the distance needs to be calculated is given by

$$n_{\text{Cell}} = 27\rho r^3, \tag{6.88}$$

where ρ is also the particle density and r is the radius of the spheres. For the Verlet list the corresponding number is

$$n_{\text{Verlet}} = \frac{4}{3}\pi\rho r_{\text{Verlet}}^3, \tag{6.89}$$

where ρ is the particle density and r_{Verlet} is the radius of the neighborhood, such that $r_{\text{Verlet}} > r$. Assuming that $r_{\text{Verlet}} = 1.1r$, n_{Verlet} is a fifth of n_{Cell} and if $r_{\text{Verlet}} = 1.5r$, n_{Verlet} is half n_{Cell}. It is also worth noting that smaller r_{Verlet} lead to a shorter Verlet list, but also imply its computation more frequently, so its precise value must be chosen as a compromise between these two constraints (Frenkel and Smit, 2001).

What is shown in the previous paragraph is compounded if the particles are not circular or spherical, leading to a starker difference in favor of the Verlet list computed from the cell list (Donev et al., 2005a). For this reason, the developed program uses a Verlet list computed from a cell list, with an empirical value for the size of the neighborhood equal to one and half times the geometrical parameters defining the particle. Box 6.9 presents the pseudo-code for its implementation.

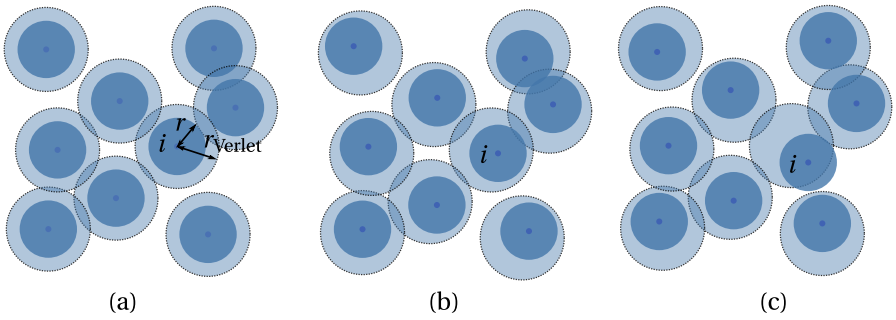

Figure 6.14: Diagram illustrating the Verlet list method: (a) The Verlet list is calculated. (b) Disk i interacts only with the Disks whose neighborhood intersect its own. (c) Disk i exited its neighborhood, so a new Verlet list must be computed.

Box 6.9: Pseudo-code for the computation of interactions between particles using Verlet lists computed from cell lists.

(i) Check if there is a need to compute a new Verlet list
If any of the particles has move outside of its corresponding neighborhood when the current Verlet list was computed

- Compute a new cell list, saving for each cell the particles whose center is inside them
- Compute a new Verlet list using the cell list computed

(ii) For each particle i, in the simulation box

(1) For each particle j in the Verlet list of particle i, such that $j > i$

- Compute the force between particle i and particle j

6.6 Integration schemes for the equations of motion

There are many integration schemes for the equations of motion used in molecular dynamics, such as the Verlet, the leap-frog and the velocity Verlet integration schemes (Frenkel and Smit, 2001). For this application in particular, the integration scheme for the equations of motion that seems more appropriate due to its simplicity, speed and the ability to provide velocities synchronous with position is the Verlet integration scheme.

6.6.1 Verlet integration scheme

The Verlet integration scheme is an explicit integration scheme for the equations of motion that estimates the new position with an error that is of order Δt^4, where Δt is the time step used.

To derive the Verlet integration scheme, one starts with a Taylor expansion of the

particle's position around t obtaining

$$\boldsymbol{x}(t+\Delta t) = \boldsymbol{x}(t) + \boldsymbol{v}(x)\Delta t + \frac{\boldsymbol{f}(t)}{2m}\Delta t^2 + \dddot{\boldsymbol{x}}(t)\frac{\Delta t^3}{3!} + \mathcal{O}(\Delta t^4), \tag{6.90}$$

and similarly

$$\boldsymbol{x}(t-\Delta t) = \boldsymbol{x}(t) - \boldsymbol{v}(x)\Delta t + \frac{\boldsymbol{f}(t)}{2m}\Delta t^2 - \dddot{\boldsymbol{x}}(t)\frac{\Delta t^3}{3!} + \mathcal{O}(\Delta t^4), \tag{6.91}$$

where $\boldsymbol{x}$ is the position of the particle, $\boldsymbol{v}$ its velocity, m its mass, in this case corresponding to the area/volume of the particle, and $\boldsymbol{f}$ the force applied.

Summing the last two equations, the result is

$$\boldsymbol{x}(t+\Delta t) = 2\boldsymbol{x}(t) - \boldsymbol{x}(t-\Delta t) + \frac{\boldsymbol{f}(t)}{m}\Delta t^2 + \mathcal{O}(\Delta t^4). \tag{6.92}$$

Thus, the update formula for the Verlet integration scheme is

$$\boldsymbol{x}(t+\Delta t) = 2\boldsymbol{x}(t) - \boldsymbol{x}(t-\Delta t) + \frac{\boldsymbol{f}(t)}{m}\Delta t^2. \tag{6.93}$$

Usually the velocity is computed from a centered finite difference as

$$\boldsymbol{v}(t) = \frac{\boldsymbol{x}(t+\Delta t) - \boldsymbol{x}(t-\Delta t)}{2\Delta t}, \tag{6.94}$$

which has an error of order Δt^2. Nonetheless, since an isokinetic thermostat is used in the final simulation scheme, it is more desirable to compute the velocity synchronously with the position. Therefore, despite having an error of order Δt, the velocity is computed as

$$\boldsymbol{v}(t) = \frac{\boldsymbol{x}(t) - \boldsymbol{x}(t-\Delta t)}{\Delta t}. \tag{6.95}$$

Lastly, to enforce the periodic boundary conditions, the position of the particle inside the simulation box is found from

$$x_i(\Delta t) = x_i'(\Delta t) - \ell_{\mathrm{RVE}\,i}\,\texttt{floor}(x_i'(\Delta t)/\ell_{\mathrm{RVE}\,i}), \quad i = 1,\ldots,n_{\mathrm{dim}}, \tag{6.96}$$

where $\boldsymbol{x}'$ are the positions obtained from Equation (6.93) and $\ell_{\mathrm{RVE}\,i}$ is the length of the RVE in direction i.

Box 6.10: Pseudo-code for one iteration of the Verlet integration scheme with the computation of the velocity synchronous with the position.

(i) Obtain a virtual position for $-\Delta t$ from the initial position, velocity and force,

$$\boldsymbol{x}(-\Delta t) = \boldsymbol{x}(0) - \boldsymbol{v}(0)\Delta t - \frac{\boldsymbol{f}(0)}{m}\Delta t^2$$

(ii) For each particle i_{particle}

- Compute the new position for particle i_{particle}

$$\boldsymbol{x}(\Delta t) = 2\boldsymbol{x}(0) - \boldsymbol{x}(-\Delta t) + \frac{\boldsymbol{f}(0)}{m}\Delta t^2$$

- Compute the current velocity for particle i_{particle}

$$\boldsymbol{v}(\Delta t) = \frac{\boldsymbol{x}(\Delta t) - \boldsymbol{x}(0)}{\Delta t}$$

- Enforce the periodic boundary conditions

$$x_i(\Delta t) = x_i(\Delta t) - \ell_{\text{RVE}\,i}\,\texttt{floor}(x_i(\Delta t)/\ell_{\text{RVE}\,i}), \quad i = 1,\ldots,n_{\text{dim}},$$

where $\ell_{\text{RVE}\,i}$ is the length of the RVE in direction i.

6.7 Thermostats

This section introduces the concept of temperature in Molecular Dynamics, followed by the isokinetic scheme, ending with the multi-temperature approach based on the isokinetic scheme developed in the present work.

6.7.1 Concept of temperature in molecular dynamics

According to the equipartition theorem (Frenkel and Smit, 2001; Krauth, 2006), the temperature of a classical n-body system is defined as

$$k_b T = \frac{\sum_{i=1}^{N_p} m_i \| v_i \|^2}{N_{\text{DOF}}\, N_p}, \tag{6.97}$$

where k_b is the Boltzmann constant, T is the absolute temperature, m_i and v_i are the mass and velocity of particle i, N_p the number of particles in the system and N_{DOF} the number of degrees of freedom for each particle.

Equation (6.97) can also be rewritten as a function of the kinetic energy of the system in the following way

$$\frac{1}{2} k_b T = \frac{E_{\text{kin}}}{N_{\text{DOF}}\, N_p}, \tag{6.98}$$

where $E_{\text{kin}}/(N_p N_{\text{DOF}})$ is the mean kinetic energy per degree of freedom of the system.

The root mean square of the speed is a good upper estimate of the mean speed and is given by

$$\|v\|_{\text{RMS}} = \sqrt{\frac{N_{\text{DOF}} k_b T}{m}}, \tag{6.99}$$

for a system of particles all with the same mass m. Thus, in the discussion that follows, it is assumed that for the most part the temperature is proportional to the square of the mean speed.

Another useful concept for the discussion that will follow is the concept of mean free-path. It is defined as the mean distance traveled by a particle between two consecutive collisions (Boltzmann, 1995). For disks or spheres it can be found from

$$\ell = \frac{1}{\sqrt{2} N_p \sigma}, \tag{6.100}$$

where the effective cross-sectional length for disks of radius r is

$$\sigma_{\text{Disk}} = 4r, \tag{6.101}$$

and the effective cross-sectional area for spheres of radius r is

$$\sigma_{\text{Sphere}} = \pi (2r)^2. \tag{6.102}$$

6.7.2 Isokinetic scheme

The isokinetic scheme is one of the simplest thermostats that can be devised, keeping the average kinetic energy per particle strictly constant. However, it does not simulate the true constant-temperature ensemble, as in the latter the temperature suffers small fluctuations around the constant temperature value. In practice, the difference between isokinetic and canonical schemes is often negligible (Frenkel and Smit, 2001). In the present case, this is even less relevant, as the goal here is to use the molecular dynamics simulation to find a legal configuration and not to simulate a real system.

As previously mentioned, the temperature is kept rigorously constant in this scheme, say at a reference temperature, denoted as T_{ref}. This is accomplished by rescaling the velocities of all the particles in the system by a factor λ. This factor can be determined from the equipartition theorem (Equation (6.97)), finding the factor λ that leads the mean kinetic energy per degree of freedom to be equal to $1/2 k_b T_{\text{ref}}$. Accordingly, rewriting Equation (6.97), one finds

$$\frac{1}{2} N_p N_{\text{DOF}} k_b T_{\text{ref}} = \frac{1}{2} \sum_{i=1}^{N_p} m_i \|\lambda \boldsymbol{v}_i\|^2, \tag{6.103}$$

and applying the definition of kinetic energy, it follows

$$\frac{1}{2} N_p N_{\text{DOF}} k_b T_{\text{ref}} = \lambda^2 E_{\text{kin}}. \tag{6.104}$$

Therefore, λ is given by

$$\lambda = \sqrt{\frac{N_p N_{\text{DOF}} k_b T_{\text{ref}}}{2 E_{\text{kin}}}}. \tag{6.105}$$

Box 6.11 presents the pseudo-code for a molecular dynamics simulation with constant temperature according to an isokinetic scheme.

Box 6.11: The isokinetic scheme in a molecular dynamics simulation.

(i) Generate an initial configuration

(ii) Initialize the increment counter i, $i = 0$

(iii) Compute the interactions between particles

(iv) Check if the particle configuration is legal.
If a legal configuration has been reached

- Exit with the current configuration being the microstructure sought after

else if ($i = i_{\max}$) then

- Exit and report that the maximum number of iterations has been reached

else

- Update the increment counter, $i \leftarrow i + 1$

(v) Compute the kinetic energy of the system

$$E_{\text{kin}} = \frac{1}{2} \sum_{i=0}^{N_p} m_i \| \boldsymbol{v}_i \|^2$$

(vi) Compute the rescaling factor λ

$$\lambda = \sqrt{\frac{N_p N_{\text{DOF}} k_b T_{\text{ref}}}{2 E_{\text{kin}}}}$$

(vii) Rescale all the velocities by λ

(viii) Integrate the equations of motion for all particles using the resclaed velocities

(ix) Go to step (iii)

Relevant remarks

Two remarks about the behavior of the system under the isokinetic scheme as it relates to the total overlap area/volume in the system are presented shortly. These lend support to the developed strategy, to be described in the next section.

The first remark concerns the existence of a mean overlap area, that decreases with temperature. As the particles move around in the simulation box, they collide with each other. Given that the potential originating the repulsive forces between the particles is soft, they penetrate each other at each collision increasing momentarily the total overlap area. Concurrently with these collisions, overlapping particles are being

driven apart by the repulsive forces between them, contributing to the decrease of the total overlap. As the system reaches equilibrium, the number of collisions oscillates around some constant value, as overlaps are removed and new ones are created. This leads to an oscillating total overlap area around some value with a "period" related to the mean free path and the mean speed of the particles (see Figure 6.15).

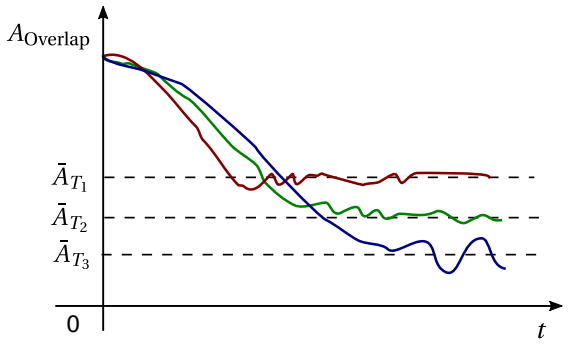

Figure 6.15: Diagram for the prediction related to the behavior of a system of particles applying the isokinetic scheme, as it relates to the elimination of the initial overlap area and the mean overlap area at different temperatures.

This heuristic argument helps establish that the expected behavior of the system regarding the total overlap is oscillatory. To show that the mean overlap area/volume decreases with the reference temperature enforced by the isokinetic scheme, one argues as follows. Consider two disks colliding at the mean speed $\|\boldsymbol{v}_{\text{ref}}\|$ corresponding to some reference temperature T_{ref} (see Figure 6.16).

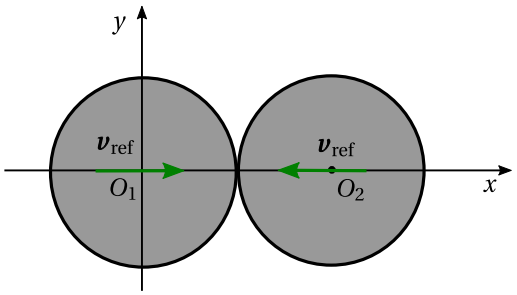

Figure 6.16: Two disks colliding at a velocity $\|\boldsymbol{v}_{\text{ref}}\|$ corresponding to the mean velocity at temperature T_{ref}.

Since the isokinetic scheme artificially keeps the speeds constant during the interaction, it is not possible to analyze the differential equations of motion directly, thus the update formulas for the Verlet integration scheme are used. At each iteration of the Verlet integration scheme, the next position of Disk 1 is determined from

$$\boldsymbol{x}_1(t+\Delta t) = 2\boldsymbol{x}_1(t) - \boldsymbol{x}_1(t-\Delta t) - \frac{\boldsymbol{f}(t)}{m}\Delta t^2. \tag{6.106}$$

Equation (6.106) can be rewritten as

$$\boldsymbol{x}_1(t+\Delta t)-\boldsymbol{x}_1(t)=\boldsymbol{x}_1(t)-\boldsymbol{x}_1(t-\Delta t)-\frac{\boldsymbol{f}(t)}{m}\Delta t^2, \tag{6.107}$$

and since the velocity is always the same, $\boldsymbol{v}_{\text{ref}}$, when applying the isokinetic scheme just to two particles, except for the sense, one finds

$$\boldsymbol{x}_1(t+\Delta t)-\boldsymbol{x}_1(t)=\boldsymbol{v}_{\text{ref}}(t)\Delta t-\frac{\boldsymbol{f}(t)}{m}\Delta t^2. \tag{6.108}$$

Thus, the inversion of the velocity will only happen when

$$\boldsymbol{v}_{\text{ref}}(t)=\frac{\boldsymbol{f}(t)}{m}\Delta t \tag{6.109}$$

keeping in mind that both vectors have the same orientation in space, i.e. a straight line between the centers of the particles. This means that the maximum overlap achieved and as a consequence the mean overlap at equilibrium is positively correlated with the velocity of the particles, and hence with the temperature of the system. Note that the argument just presented is only approximate for systems of particles, as there are interactions between more than two particles. Also, the velocities vary slightly, as the factor λ depends on the velocities of all particles.

The second remark concerns the evolution of the total overlap area/volume in the system starting from an initial random configuration. From the update equation of the Verlet scheme, it can be deduced that the same overlap takes longer to remove at a smaller speed, corresponding to a lower temperature, than at high temperature (see Figure 6.15).

6.7.3 Multi-temperature isokinetic scheme

Firstly, it is explained the need to develop this multi-temperature approach based on the isokinetic scheme. Due to its constant energy, the microcanonical ensemble leads to a conservative system, such that the particles are always colliding with each other. These constant collisions imply a very low probability of finding a legal configuration in a reasonable time.

One possible approach is to introduce a drag force proportional to the speed of the particles, as suggested by Salnikov et al. (2015). This approach solves the problem of perpetual motion as the energy is now dissipated. Despite that, it does not present a natural way to speed up the generation of a legal configuration during the simulation, as the viscous coefficient is set at the beginning of the simulation. One could try to vary the coefficient as the simulation progresses, but it is not readily clear how to devise a fruitful scheme for this variation from physical intuition or by some other means.

As for the approximation to the canonical ensemble using the isokinetic scheme only, there are major roadblocks to its use. On the one side, the choice of a temperature that is too high will lead to a situation similar to the one just mentioned for the microcanonical ensemble. High temperatures entail high particle speeds, and thus lead to a high mean total overlap area/volume, as argued at the end of the last section (see Section 6.7.2) and shown in Section 7.1.1 through experimental results. Conversely, excessively low temperatures result in a very slow removal of the initial overlap. However, they also lead to an equilibrium state at a lower mean overlap area and hence

imply a higher probability of finding a legal configuration as the mean time between collisions decreases (see Equation (6.100)).

To understand the major drawback related to the use of very low temperatures, it is important to define, at least qualitatively, desirable and undesirable microstructures. Given the constraints already presented (see Section 1.1), a desirable microstructure will not present any clear ordering or clustering, with an undesirable one presenting one or the other (see Figure 6.17 for examples of desirable and undesirable microstructures with the same descriptors).

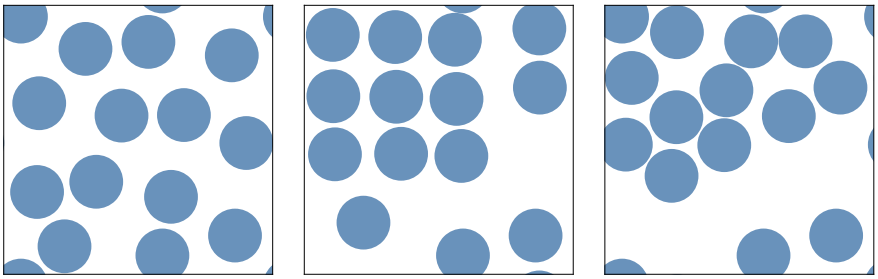

(a) Desirable configuration (b) Partially ordered configuration (c) Clustered configuration

Figure 6.17: Examples of desirable and undesirable, both clustered and partially ordered, configurations.

It can be readily seen that very low temperatures, and hence very low speeds, lead to very clustered microstructures, where even at small volume fractions the particles tend to stay very close, even touch each other, which is undesirable.

The developed approach consists in an isokinetic scheme with stages at progressively lower temperatures until a legal configuration is found. As can be seen in the schematic representation of Figure 6.18, the scheme is characterized, firstly, by an initial temperature, i.e. the temperature at which the simulation starts. One must also specify a temperature lowering scheme, detailing how the temperature is lowered from one stage to the next. The number of iterations spent at each temperature, referred to as the "equilibration time", t_{eq}, is also a parameter that needs to be supplied, such that after the specified number of iterations the temperature is lowered according to the scheme chosen. Lastly, the number of extra iterations allowed after a legal configuration is achieved, referred to as the "relaxation time", t_{relax}, must also be given to fully specify the proposed approach.

Broadly, running the simulation first at higher temperatures seems to be a good way to quickly eliminate the initial overlap. Later running it at lower temperatures appears to be a sound way to remove the remaining overlaps between particles without allowing for the appearance of new overlaps from an excessive number of collisions. This scheme is developed for an arbitrary particle, and it is shown in Section 7.1.2 that the behavior of disks and spheres is identical. Any specificity inherent to ellipses and ellipsoids is disregarded, which is probably not very consequential for small ratios between the principal axis. Further details are provided in what follows.

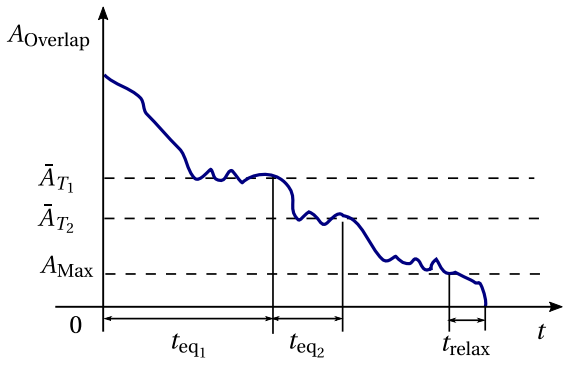

Figure 6.18: Diagram of the evolution of the total overlap area A_{Overlap} using the proposed multi-temperature isokinetic scheme. The system spends t_{eq_1} and t_{eq_2} at temperatures T_1 and T_2, achieving the mean overlap area $\bar{A}_{T_1}$ and $\bar{A}_{T_2}$, respectively. After reaching the maximum total overlap allowed, A_{Max}, the simulation is still run for more t_{relax} and then terminated.

Initial temperature

Firstly, one must choose an initial temperature. The goal at this stage is to remove the large initial overlap (see Figure 6.19) as quickly as possible. This large overlap comes from the way the initial configuration is generated, i.e. through a Poisson point process, making sure that the initial positions of the particles' centers are disordered. Failing to achieve equilibrium, i.e. total overlap oscillating with time, is shown to be very prejudicial in later paragraphs.

With this in mind, a higher temperature appears more desirable, as can be ascertained from Figure 6.15, where the lower temperatures take a much longer time to remove the initial overlap. On the other hand, lower temperatures lead, after removing the initial overlap, to a smaller average overlap and to a higher probability of achieving a legal configuration. Despite this apparent benefit, it produces microstructures with undesirable characteristics. Expanding on this point, the initial configuration has many clusters (see Figure 6.19). A high temperature quickly removes most of the overlap, and the system achieves "equilibrium" with some given mean overlap area/volume. The configuration of the system is now much different from the initial configuration, with some particles overlapping and others free, but for the most part without clusters and large overlaps between anyone pair of particles. A lower temperature would take longer to remove the initial overlap, and due to the low speed of the particles, it will also take a long time for the initial clusters to dissolve, due to its high mean time between collisions (see Equation 6.100).

Having concluded that higher temperatures are in general beneficial in this context, the initial temperature should not be, however, arbitrarily high. This is a poor choice as the particles go through each other and not much is achieved. The average overlap can even be larger than the initial overlap if the temperature is excessively high. In order to avoid that two particles penetrate more than halfway through each other in one iteration, consider the equations of motion of the system and the fact that they are solved numerically using a given time step, Δt. Thus, it must be ensured at least that

$$\|\boldsymbol{v}\|\,\Delta t < r. \tag{6.110}$$

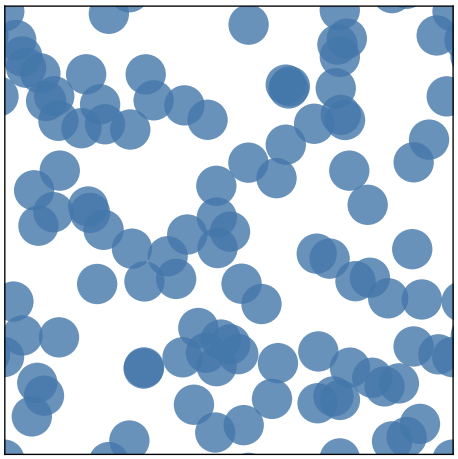

Figure 6.19: Initial configuration generated through a Poisson point process for a system of Disks with the same radius.

With the previous paragraphs in mind, a favorable initial temperature is one that removes the initial overlap in a reasonable number of iterations and whose average collision time is also only a few iterations. It is not straightforward to determine the ideal initial temperature, as described, for all volume fractions and numbers of particles. The last paragraphs of this section show how this problem is dealt with.

Temperature lowering scheme and equilibration time

Regarding the temperature lowering scheme and the equilibration time, they go hand in hand and constrain each other. thus, they are discussed in tandem.

Concerning the equilibration time, i.e. the time spent at some given temperature, it can be seen as composed of two moments. The first, where the overlaps corresponding to the previous temperature are removed and, the second, where the space of configurations is explored at that given temperature and the corresponding mean overlap is achieved.

As already stated in the previous section, determining the time needed to remove a given overlap is not straightforward, but some useful conclusions about the time it takes to remove overlaps at different temperatures can be reached. It is argued below that the equilibration times for two temperature lowering steps are the same, as long as the temperatures are related by a negative exponential law.

To illustrate this point, consider three temperatures T_1, T_2 and T_3, such that $T_1 = k^2 T_2 = k^4 T_3$, with k some arbitrary factor larger than one. Related to each of these three temperatures there is a mean velocity denoted by $\boldsymbol{v}_1$, $\boldsymbol{v}_2$, and $\boldsymbol{v}_3$, and thus related to each other by $\|\boldsymbol{v}_1\| = k\|\boldsymbol{v}_2\| = k^2\|\boldsymbol{v}_3\|$ (see Equation (6.99)). Assume that after reaching equilibrium at a temperature of T_1, the temperature is lowered to T_2. The case of two particles already overlapping, at the moment when the velocity inverts, i.e. maximum overlap for the particle pair, is analyzed (see Figure 6.20). In this situation, the overlap corresponding to T_1 has to be removed at a lower temperature of T_2. Due to the isokinetic scheme, the velocity is assumed constant while the particles overlap. This is not strictly true as the force also contributes to the computation of the next

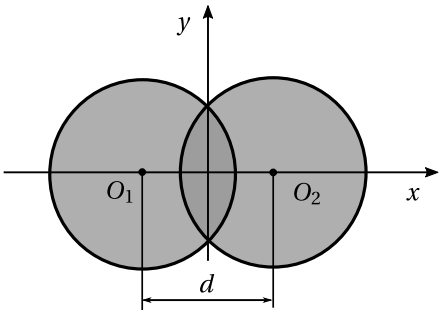

Figure 6.20: Two particles overlapping at the moment of maximum overlap with the coordinate system origin at the center of mass of the particle pair.

position (see Equation (6.9)), and appreciably so when the overlap is at its maximum and the velocity changes direction. Assume that it took $n_{\Delta t}$ to completely remove the overlap.

Suppose that the system has reached equilibrium at temperature T_2 and is now quenched to temperature T_3. One analyzes again the case of two particles already overlapping at the moment when the velocity inverts, i.e. maximum overlap for the particle pair. Now, the overlap corresponding to T_2 has to be removed at a lower temperature of T_3. Due to the isokinetic scheme the velocity is again assumed to be constant while the particles overlap.

Since the maximum force is proportional to the mean velocity (Equation 6.109), the maximum forces between the two cases will also be related by the factor k. From Figure 6.21, detailing the relation between the normalized force $\|\boldsymbol{f}\|/m$ and the distance between particle center d for Disks (Equation (6.9)) and Spheres (Equation (6.44)), it is possible to assert that

$$1 - \frac{x_0^{T_2}}{r} = k\left(1 - \frac{x_0^{T_1}}{r}\right), \tag{6.111}$$

where $x_0^{T_1}$ and $x_0^{T_2}$ are the positions at the moment when the repulsive forces are at their maximum, taken relative to the center of mass of the system (see Figure 6.20), and r is the radius of the particles. So the distance to cover until the overlap disappears is decreased by the factor k. Since the velocities are assumed constant and also related by k, it takes the same number of iterations to remove the overlap, $n_{\Delta t}$.

For a system of particles, these results are not completely accurate, as there are interactions between more than two particles. The higher the volume fraction and the number of particles, the less accurate they will be. Nonetheless, it provides a justification for the use of the same number of iterations for each temperature stage, if the volume fraction and number of particles are not too high. At the end of this section, it is be shown how to deal with those sets of more demanding descriptors.

Regarding the temperature lowering scheme, if the temperature at which legal configurations start to be reasonably probable was known, it could be used as a lower bound for the lowering scheme, but that result is not easy to come by.

To reinforce the importance of spending enough time at a given temperature to achieve equilibrium, it is stressed that if the algorithm fails to spend enough time at

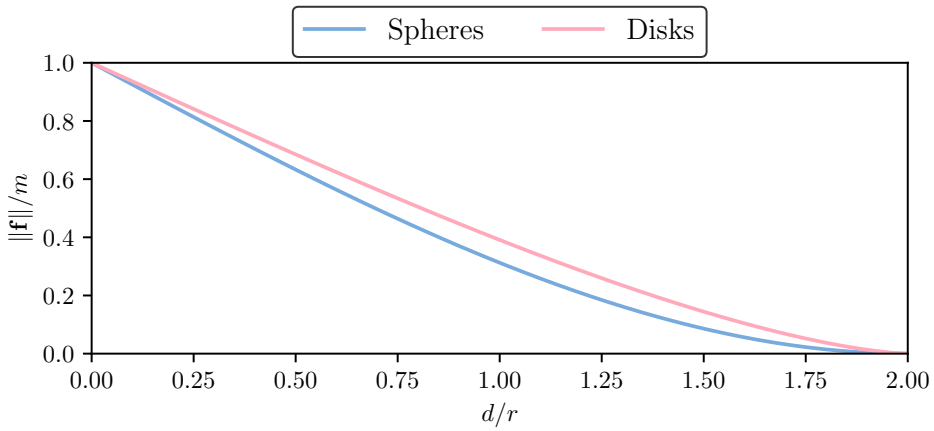

Figure 6.21: Force between two disks and two spheres, where $\|\mathbf{f}\|$ is the area/volume overlap and m is the total area/volume, as a function of the distance between them d/r, where d is the distance between the centers and r is the radius of the Spheres/Disks.

this temperature to dissolve the clusters, lowering the temperature will only aggravate this problem. This is so because the mean speed of the particles will be lower still and even less conducive to the removal of the particle clusters, possibly leading to an overlap are that converges to some known negative value.

Now, for the second moment, as explained before relating to the initial temperature, the temperatures that explore the space of configurations more efficiently are the higher temperatures, so much so that their average collision times are but a few iterations. As one moves to lower temperatures, it becomes untenable to try to explore more fully the space of configurations at that temperature. However, it turns out that this is not needed to achieve good results, the lower temperatures can be used just to remove the residual overlaps, leaving the general layout of the configuration unaltered. Since care is taken to first visit higher temperatures, this is not a problem as any possible clusters are long gone and a disordered microstructure has already been achieved, remaining only minor overlaps.

Relaxation time

The usefulness of allowing for a relaxation time can be seen from the following example. Assume there is only one pair of particles overlapping. As soon as they are driven apart, assuming that no other collision occurred in the meantime, a legal configuration is found, since the total overlap is now zero. Stopping the simulation immediately after reaching a legal configuration may lead to those particles being too close together in the final microstructure. Hence, it seems fruitful to allow the system to "relax" and the particles to move away from each other for a few iterations after reaching a legal configuration.

The suitable number of iterations should be chosen according to the mean free path and the final temperature. This implies a small number of iterations for systems with many particles at high volume fraction and a larger number of iterations for systems with few particles at low volume fractions.

Calibration of the parameters

Since the results presented until here break down for higher volume fractions and number of particles, the approach taken is to obtain reasonable values for the parameters defining the proposed scheme for one combination of descriptors and to develop a "self-calibrating" scheme around that point.

It is found that a reasonable initial temperature for 50 disks with $r = 0.045$ is $T\,k_b = 2.5 \times 10^{-5}$. As for the lowering scheme and the equilibration time, it is found by numerical experience that for $T_{n+1}/T_n = 1/4,\ n = 1,\ldots,\ 25$ iterations produce satisfactory results. A relaxation time of $\ell/\|\boldsymbol{v}\|_{\mathrm{RMS,T_{final}}}$, where ℓ is the mean free path, and $\|\boldsymbol{v}\|_{\mathrm{RMS,T_{final}}}$ is the root mean square velocity corresponding to the final temperature of the system, is also found to be beneficial. These proposed values are justified empirically in Section 7.1.2.

To avoid having to calibrate the algorithm for all combinations of descriptors, and to deal with the breaking down of the assumptions at higher volume fraction and larger number of particles, a "self-calibrating" scheme is developed. The initial temperature, the temperature lowering scheme and the relaxation time remain the same, but the equilibration time, t_{eq}, for each temperature stage changes during the simulation. It starts at 25 iterations and is updated in the following manner. After lowering the temperature, the total overlap is monitored, such that the temperature can only be lowered again if the simulation has spent more time at the current temperature stage than the current equilibration time and if the total overlap area has increased in the last $t_{\mathrm{eq}}/(2\Delta t)$ iterations. This increase in the total overlap area is used as a proxy to detect if the system has reached equilibrium at that temperature. It is a heuristic rule based on experience that is supported by the fact that immediately after lowering the temperature, the overlap tends to fall monotonically. As the equilibrium is reached, due to its oscillatory nature, there will be eventually an uptick in the total overlap area. In future work, a more robust and physically motivated scheme can be developed.

Box 6.12 presents the algorithm for the developed multi-temperature approach based on the isokinetic scheme.

Box 6.12: Multi-temperature molecular dynamics simulation base on the isokinetic scheme.

(i) Generate an initial configuration

(ii) Initialize the increment counter i, $i \leftarrow 0$

(iii) Initialize the relaxation counter i_{relax}, $i_{\text{relax}} \leftarrow 0$

(iv) Initialize the reference temperature T_{ref}, the minimum number of iterations spent at the current temperature stage, n_{eq} and the iteration at which the temperature was last altered, $n_{\text{last alt}} \leftarrow 0$

(v) Compute the interactions between particles from their overlap area/volume and save the total overlap volume/area, $A_{\text{Total Overlap}}$

(vi) Integrate the equations of motion for all particles

(vii) Compute the interactions between particles from their overlap area/volume and save the total overlap volume/area, $A_{\text{Total Overlap}}$

(viii) Check if the system has reached equilibrium at temperature T_{ref}.
If $i > n_{\text{last alt}} + n_{\text{eq}}$, $A_{\text{Total Overlap}} \leq A_{\text{max}}$ and the overlap area has increased in the last n_{eq} iterations

- Lower the temperature, $T_{\text{ref}} = (1/k)\,T_{\text{ref}}$
- Update the number of iterations needed to achieve equilibrium, $n_{\text{eq}} \leftarrow i - n_{\text{last alt}}$
- Save the iteration at which the temperature was lowered, $n_{\text{last alt}} \leftarrow i$

(ix) Compute the rescaling factor λ

$$\lambda = \sqrt{\frac{N_p N_{\text{DOF}} k_b T_{\text{ref}}}{2E_{\text{kin}}}}$$

and multiply all the velocities by λ

(x) Check if the particle configuration is legal.
If $A_{\text{Total Overlap}} \leq A_{\text{max}}$

- Increment the relaxation counter, $i_{\text{relax}} \leftarrow i_{\text{relax}} + 1$

else

- Reset the relaxation counter, $i_{\text{relax}} \leftarrow 0$

(xi) Check if the required number of relaxation iterations has been reached or the maximum number of iterations, n_{relax}.
If $i_{\text{relax}} = n_{\text{relax}}$ or $n_{\text{max}} = i$

- Exit with the current configuration being the microstructure produced

else

- Update the increment counter, $i \leftarrow i + 1$ and go to step (vi)

Page intentionally left blank.

Chapter 7

Results

7.1 Microstructure generation

The first set of results presented concerns the generation of microstructures itself. It includes the study of systems of particles under the isokinetic scheme, the validation of the proposed multi-temperature isokinetic scheme and an analysis of its efficiency.

7.1.1 Results regarding the isokinetic scheme

In this section, the results concerning the isokinetic scheme and the behavior of a system of particles subject to this scheme, more specifically, as it pertains to the total overlap area, are presented.

Results

To understand how the total overlap area/volume of a generic system of particles evolves under the isokinetic scheme at several different temperatures, various molecular dynamics simulations are run at different temperatures.

Figure 7.1 presents the total overlap area for a system containing 100 Disks at a volume fraction 0.65, with the temperatures varying as $T_{\text{ref}}k_b = 2.5 \times 10^{-5}/\sqrt{2}^{-k}$, $k = 5$, 0, -5, -10, -15, -20, -25, -30, enforced through the isokinetic scheme. A similar study is presented in Figure 7.2 using the same temperatures, but for a system of 50 Spheres at a volume fraction of 0.3.

Figure 7.3 presents the total overlap area for a system containing 100 Disks at different volume fractions (0.1, 0.25, 0.5, 0.65, 0.8 and 0.95), with the temperature kept at $T_{\text{ref}}k_b = 2.5 \times 10^{-5}$, enforced through the isokinetic scheme. A similar study is presented in Figure 7.4 using the same temperature but for systems containing 50 Spheres at different volume fractions (0.1, 0.2, 0.3, 0.4, 0.5 and 0.65).

Figure 7.5 presents the total overlap area for systems containing 10, 15, 30, 50, 100 and 200 Disks at a volume fraction of 0.65. The temperature is kept at $T_{\text{ref}}k_b = 2.5 \times 10^{-5}$ and enforced through the isokinetic scheme. A similar study is presented in Figure 7.6 using the same temperature, but for systems containing 10, 15, 30, 50, 100 and 200 Spheres at a volume fraction of 0.3.

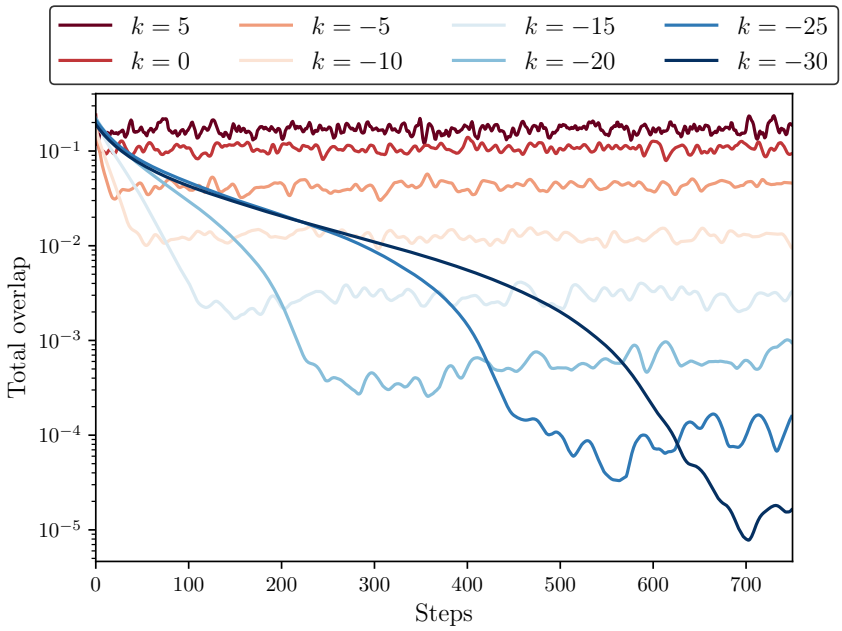

Figure 7.1: Total overlap area for a system of 100 Disks with the volume fraction of 0.65 at different reference temperatures given by $T_{\text{ref}} k_b = 2.5 \times 10^{-5} / \sqrt{2}^{-k}$ with $k = 5$, 0, -5, -10, -15, -20, -25, -30 as a function of the number of iterations.

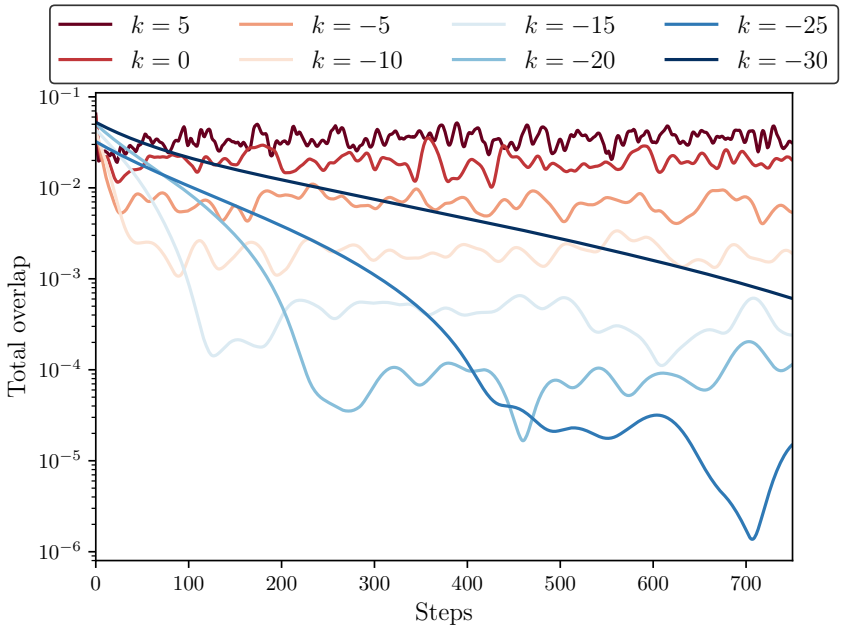

Figure 7.2: Total overlap volume for a system of 50 Spheres with the volume fraction of 0.3 at different reference temperatures given by $T_{\text{ref}} k_b = 2.5 \times 10^{-5} / \sqrt{2}^{-k}$ with $k = 5$, 0, -5, -10, -15, -20, -25, -30 as a function of the number of iterations.

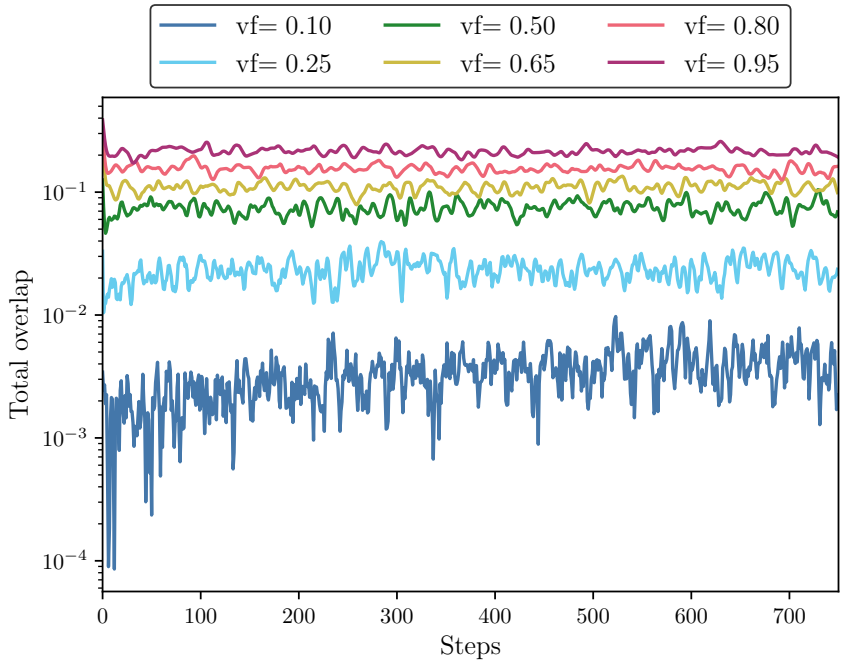

Figure 7.3: Total overlap area for a system of 100 Disks at temperature $T_{\text{ref}}k_b = 2.5 \times 10^{-5}$ with different volume fractions as a function of the number of iterations.

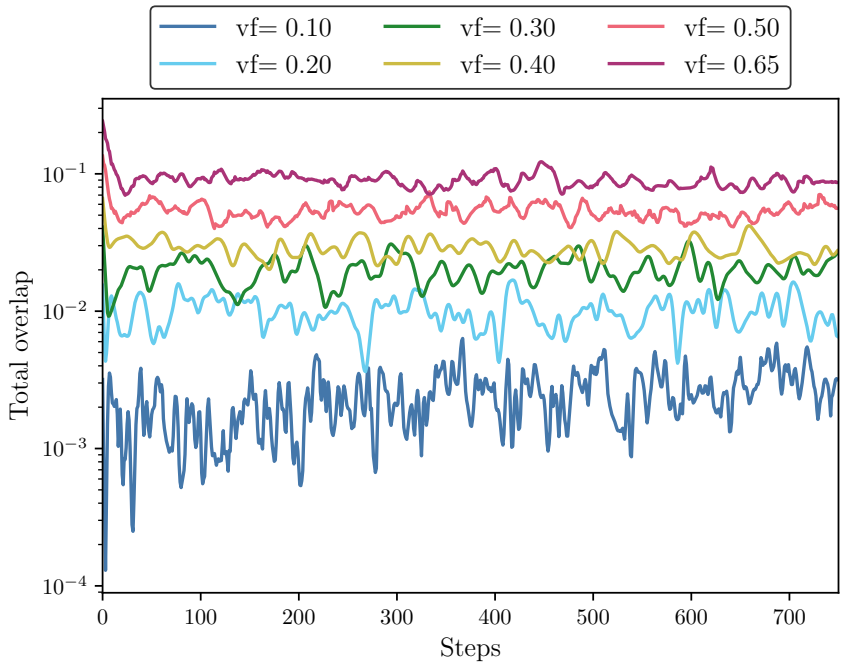

Figure 7.4: Total overlap volume for a system of 50 Spheres at temperature $T_{\text{ref}}k_b = 2.5 \times 10^{-5}$ with different volume fractions, as a function of the number of iterations.

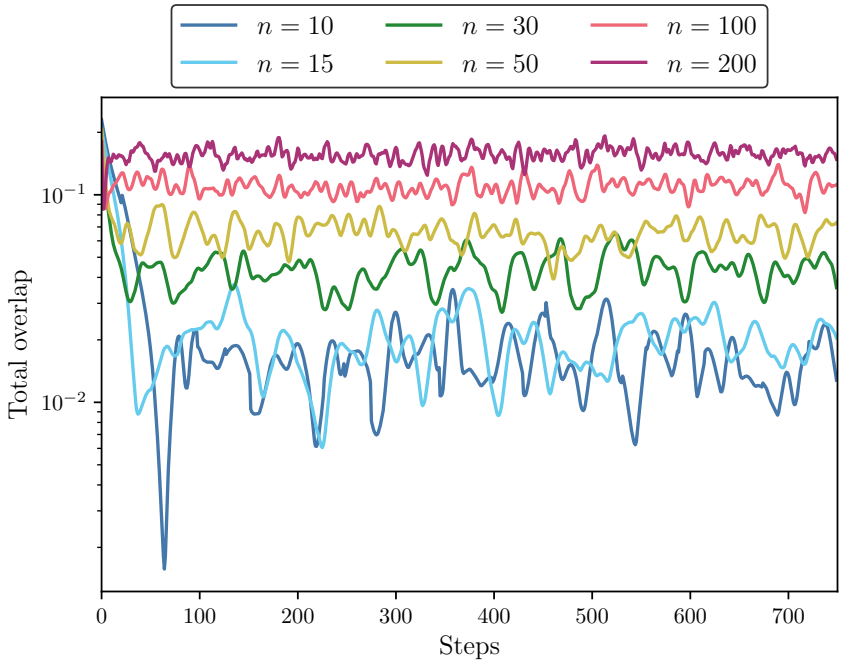

Figure 7.5: Total overlap area for systems of Disks with a volume fraction of 0.65 at temperature $T_{\text{ref}}k_b = 2.5 \times 10^{-5}$ and a different number of particles as a function of the number of iterations.

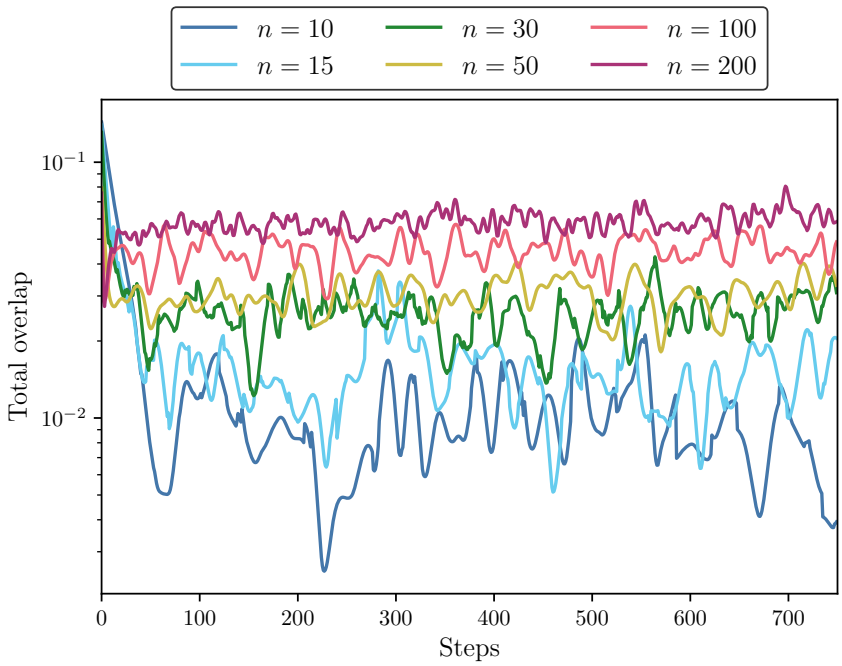

Figure 7.6: Total overlap volume for systems of Spheres with a volume fraction of 0.3 at temperature $T_{\text{ref}}k_b = 2.5 \times 10^{-5}$ and a different number of particles as a function of the number of iterations.

Discussion

From Figures 7.1 and 7.2 it is possible to confirm what is concluded in Section 6.7.2 regarding the oscillatory nature of the total overlap after equilibrium has been reached. Furthermore, the relation between the mean overlap area/volume at a given reference temperature and the reference temperature is also confirmed, with higher temperatures leading to plateaus with a higher mean overlap area/volume and lower temperatures to plateaus with a lower mean overlap/area volume. It is also possible to conclude that lower temperatures take an increasingly longer time to remove the initial overlap as they become lower.

Figures 7.3-7.6 depict how the total overlap area/volume varies as a function of the volume fraction and the number of particles for the same temperature. These results can be interpreted using the concept of the mean free path (Equation (6.100)) and its relation with the two variables just mentioned, the number of particles and the volume fraction. Since the mean free path decreases with the increase in the number of particles and the volume fraction, it is to be expected that from the larger amount of collisions arises a higher mean overlap area/volume. It can also be seen that the "period" of the total overlap area/volume follows an inverse tendency, being lower at higher volume fractions, but higher at larger numbers of particles. Thus, it can be concluded that the interaction between the particles at different volume fractions and the number of particles have a strong impact on the behavior of the system as it relates to the total overlap area/volume.

Lastly, comparing the corresponding examples of systems of Spheres and Disks, one can infer that the behavior of the two types of systems is very similar.

7.1.2 Validation of the multi-temperature approach

With the goal of validating the proposed multi-temperature isokinetic scheme, various microstructures are generated, showing that it produces microstructures with legal configurations.

Results

Firstly, Figure 7.7 and Figure 7.8 show the impact that the number of equilibration iterations allowed has on the total overlap area and the final microstructures. Figure 7.7 presents the evolution of the total overlap area for a system of 100 Disks at a volume fraction of 0.65, with an initial temperature of $T_{\text{ref}}k_b = 2.5 \times 10^{-5}$ and different number of equilibration iterations allowed, $k = 10$, 15, 20, 15, 30 and 35. Figure 7.8 contains the final microstructures obtained, either after finding a legal configuration corresponding to no overlap or after 1000 iterations.

To establish that an initial temperature of $T_{\text{ref}}k_b = 2.5 \times 10^{-5}$ and a number of equilibration iterations equal to 25 in the multi-temperature isokinetic scheme produces acceptable results for a system of 100 Disks at a volume fraction of 0.65, four different random samples are generated. Figure 7.9 presents the evolution of the total overlap area of the system and Figure 7.10 contains the final microstructures obtained, all with no overlap. Thus, all the following simulations begin with an initial temperature of $T_{\text{ref}}k_b = 2.5 \times 10^{-5}$ and a minimum number of equilibration iterations of 25.

To show that allowing only 25 iterations for the system of particles to reach equilibrium at all temperatures, volume fractions and number of particles, is not a robust strategy, a set of microstructures is generated containing 10, 15, 30, 50, 100 and 200

Disks at a volume fraction of 0.65, using the multi-temperature isokinetic scheme allowing only 25 iteration for the equilibration of the system. The simulations are run until a configuration with no overlaps is found or 650 iterations have elapsed. Figures 7.11 and 7.12 illustrate the evolution of the total overlap area and the final microstructures for this set of simulations. With the same purpose, a set of microstructures is generated containing 100 Disks at volume fractions of 0.1, 0.25, 0.5, 0.65, 0.8 and 0.9, using the multi-temperature isokinetic scheme allowing only 25 iteration for the equilibration of the system. The simulations are run until a configuration with no overlaps is found or 1000 iterations have elapsed. Figures 7.13 and 7.14 depict the evolution of the total overlap area and the final microstructures for this set of simulations.

The following two sets of microstructures are generated with the objective of validating the "self-calibrating" multi-temperature isokinetic scheme for Disks. The first set of microstructures, documented in Figures 7.15 and 7.16, is composed of microstructures containing 10, 15, 30, 50, 100 and 200 Disks at a volume fraction of 0.65. The simulations are run until a configuration with no overlaps is found. The second set of microstructures, documented in Figures 7.17 and 7.18, is composed of microstructures containing 100 Disks at high volume fractions (0.7, 0.75, 0.8, 0.85 and 0.9) The simulations are run until a configuration with no overlaps is found or 5000 iterations have elapsed.

So as to also validate the "self-calibrating" multi-temperature isokinetic scheme for Spheres, two more sets of microstructures are generated. The first set of microstructures, documented in Figures 7.19 and 7.20, is composed of microstructures containing 10, 15, 30, 50, 100 and 200 Spheres at a volume fraction of 0.3. The simulations are run until a configuration with a total overlap volume smaller than 1×10^{-10} is found. The second set of microstructures, documented in Figures 7.21 and 7.22, is composed of microstructures containing 100 Spheres at volume fractions of 0.1, 0.2, 0.3, 0.4, 0.5 and 0.6. The simulations are run until a configuration with a total overlap volume smaller than 1×10^{-10} is found or 25000 iterations have elapsed.

Lastly, Figures 7.23 and 7.24 show the evolution of the total overlap area and the final microstructures for systems of particles containing 20 Ellipses with different ratios between the major and the minor axis (1, 1.5, 2, 2.5 and 3).

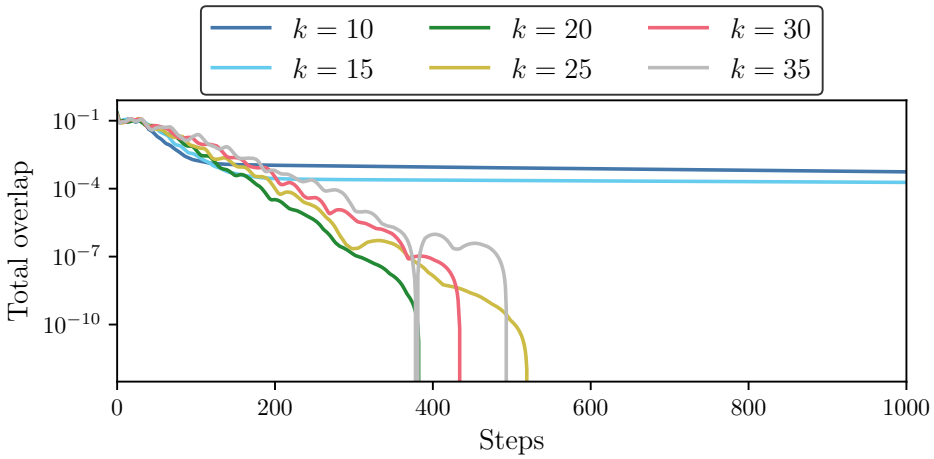

Figure 7.7: Total overlap area for a system of 100 Disks with volume fraction equal to 0.65 as function of the number of iterations, allowing a different number of iterations, k, for the equilibration time in the multi-temperature isokinetic scheme. A configuration is accepted as legal if there are no overlaps.

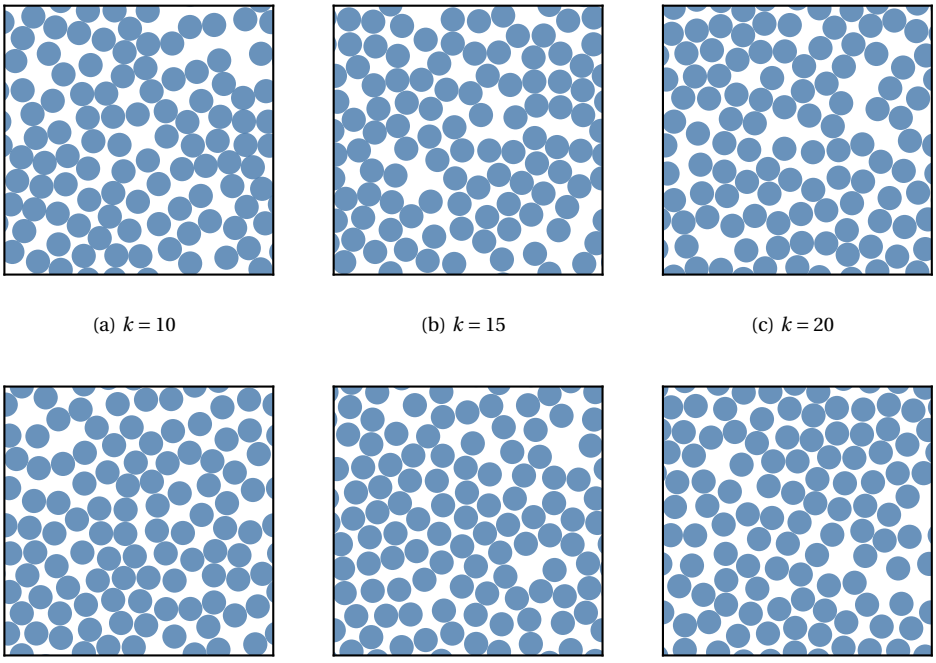

(a) $k = 10$ (b) $k = 15$ (c) $k = 20$

(d) $k = 25$ (e) $k = 30$ (f) $k = 35$

Figure 7.8: Final microstructures containing 100 Disks with a volume fraction equal to 0.65, allowing a different number of iterations, k, for the equilibration time in the multi-temperature isokinetic scheme. A configuration is accepted as legal if there are no overlaps.

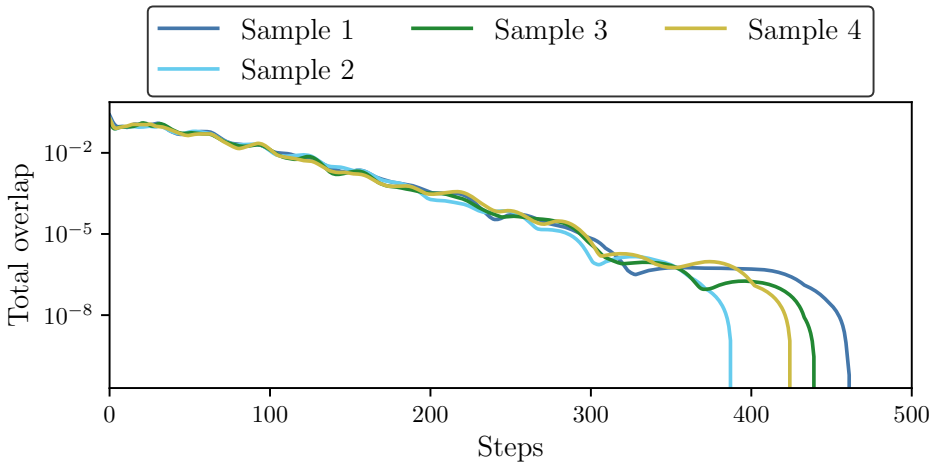

Figure 7.9: Total overlap area for four different random samples of a system containing 100 Disks with volume fraction equal to 0.65 as a function of the number of iterations, allowing 25 iterations for the equilibration time in the multi-temperature isokinetic scheme. A configuration is accepted as legal if there are no overlaps.

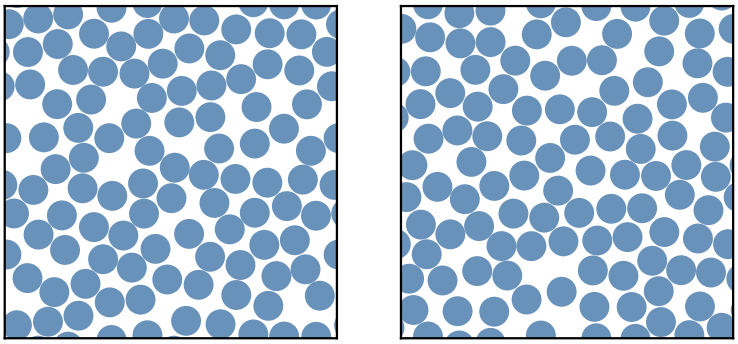

(a) Sample 1

(b) Sample 2

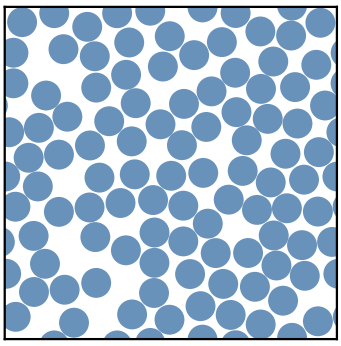

(c) Sample 3

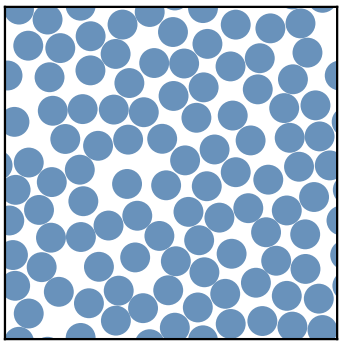

(d) Sample 4

Figure 7.10: Final microstructures corresponding to four different random samples of a system containing 100 Disks with a volume fraction equal to 0.65, allowing 25 iterations for the equilibration time in the multi-temperature isokinetic scheme. A configuration is accepted as legal if there are no overlaps.

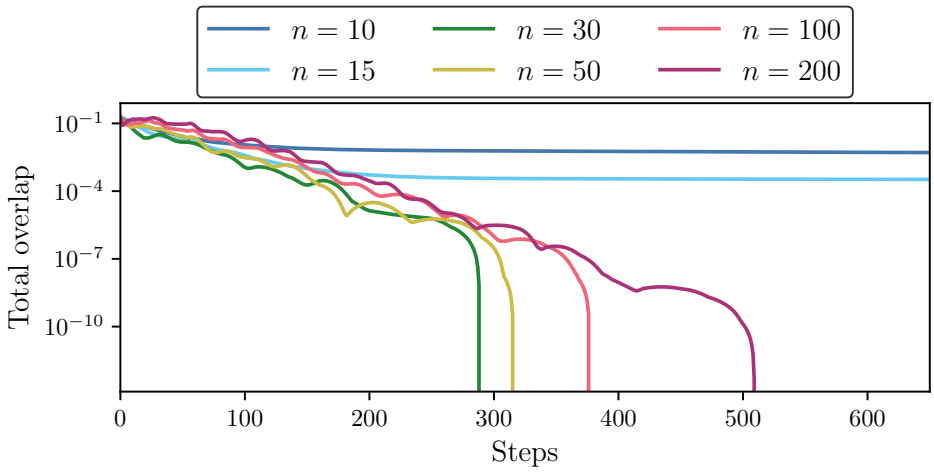

Figure 7.11: Total overlap area for systems containing a different numbers of Disks, n = 10, 15, 30, 50, 100 and 200, with volume fraction equal to 0.65 as a function of the number of iterations, allowing 25 iterations for the equilibration time in the multi-temperature isokinetic scheme. A configuration is accepted as legal if there are no overlaps.

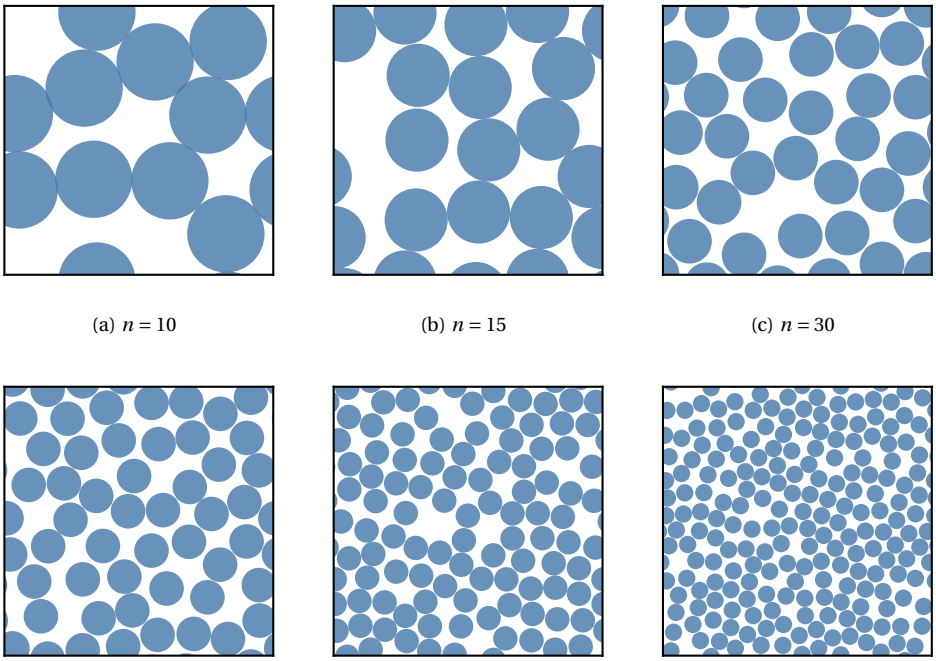

(a) $n = 10$ (b) $n = 15$ (c) $n = 30$

(d) $n = 50$ (e) $n = 100$ (f) $n = 200$

Figure 7.12: Final microstructures for systems containing a different numbers of Disks, n = 10, 15, 30, 50, 100 and 200, with volume fraction equal to 0.65 allowing 25 iterations for the equilibration time in the multi-temperature isokinetic scheme. A configuration is accepted as legal if there are no overlaps.

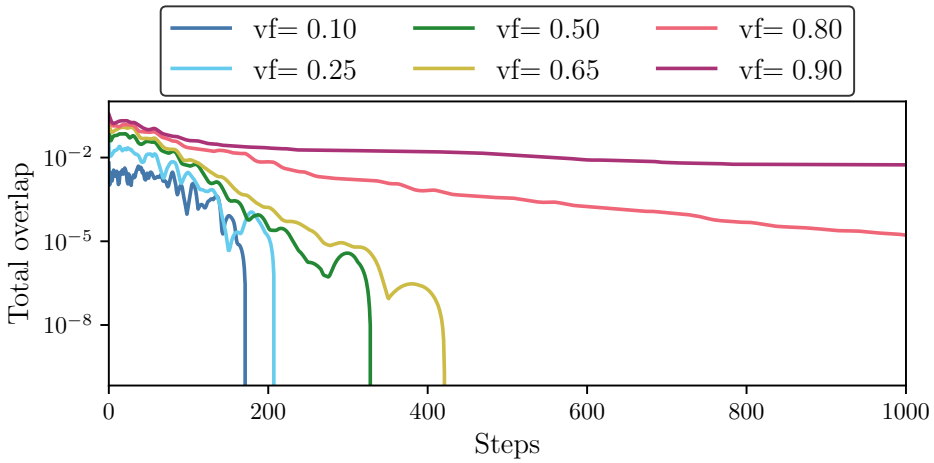

Figure 7.13: Total overlap area for systems containing 100 Disks, with different volume fractions, vf = 0.1, 0.25, 0.50, 0.65, 0.80 and 0.9, as a function of the number of iterations, allowing 25 iterations for the equilibration time in the multi-temperature isokinetic scheme. A configuration is accepted as legal if there are no overlaps.

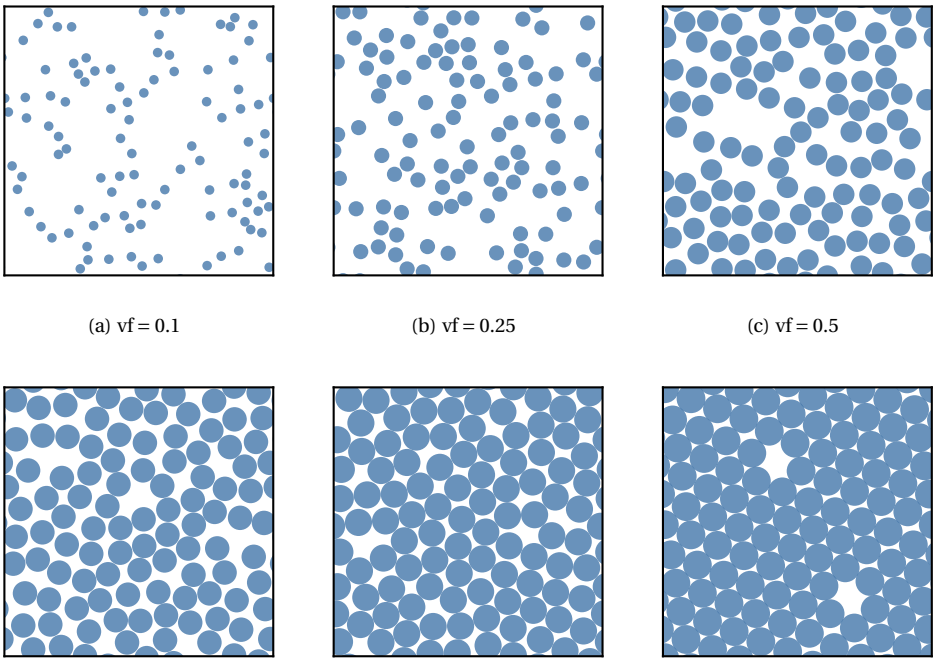

(a) vf = 0.1 (b) vf = 0.25 (c) vf = 0.5

(d) vf = 0.65 (e) vf = 0.8 (f) vf = 0.9

Figure 7.14: Final microstructures for systems containing 100 Disks, with different volume fractions, vf = 0.1, 0.25, 0.50, 0.65, 0.80 and 0.9, allowing 25 iterations for the equilibration time in the multi-temperature isokinetic scheme. A configuration is accepted as legal if there are no overlaps.

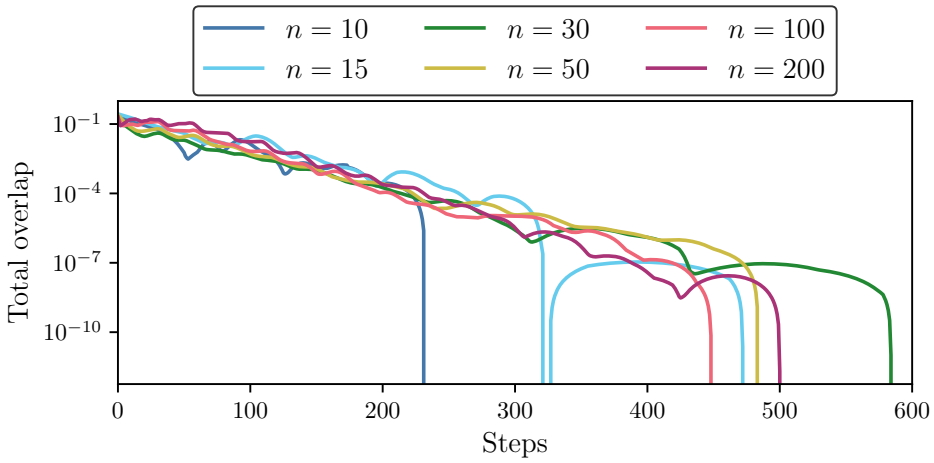

Figure 7.15: Total overlap area for systems containing a different numbers of Disks, n = 10, 15, 30, 50, 100 and 200, with volume fraction equal to 0.65 as a function of the number of iterations, "self-calibrating" the equilibration time in the multi-temperature isokinetic scheme. A configuration is accepted as legal if there are no overlaps.

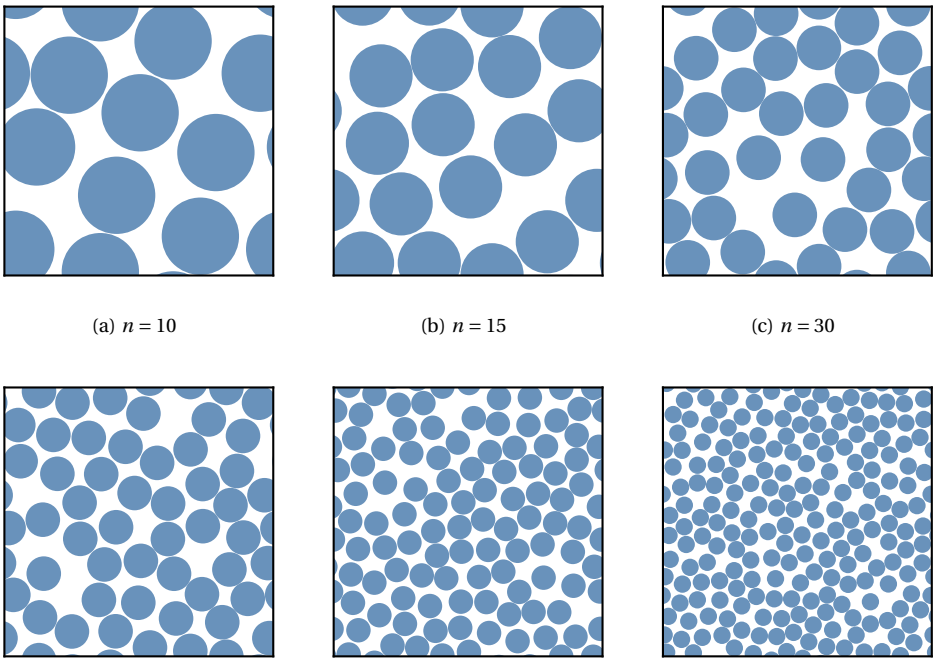

(a) $n = 10$ (b) $n = 15$ (c) $n = 30$

(d) $n = 50$ (e) $n = 100$ (f) $n = 200$

Figure 7.16: Final microstructures for systems containing a different numbers of Disks, n = 10, 15, 30, 50, 100 and 200, with volume fraction equal to 0.65, "self-calibrating" the equilibration time in the multi-temperature isokinetic scheme. A configuration is accepted as legal if there are no overlaps.

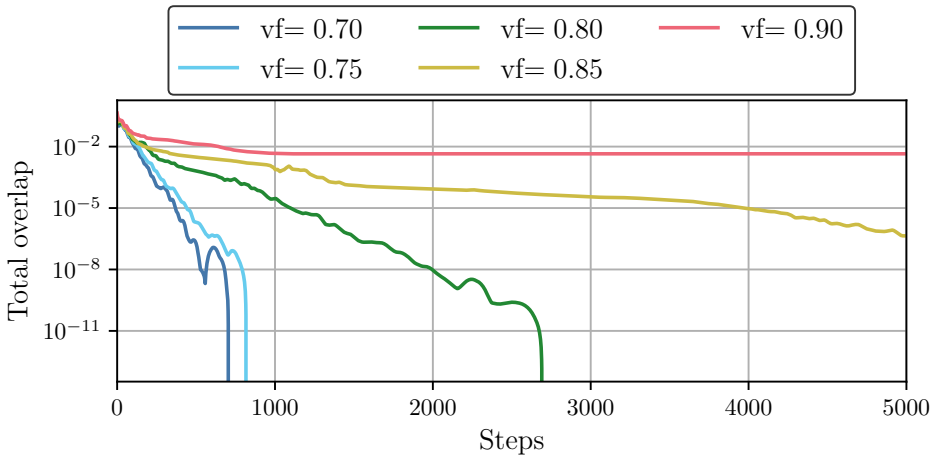

Figure 7.17: Total overlap area for systems containing 100 Disks, with different volume fractions, vf = 0.7, 0.75, 0.80, 0.85 and 0.9, as a function of the number of iterations, "self-calibrating" the equilibration time in the multi-temperature isokinetic scheme. A configuration is accepted as legal if there are no overlaps.

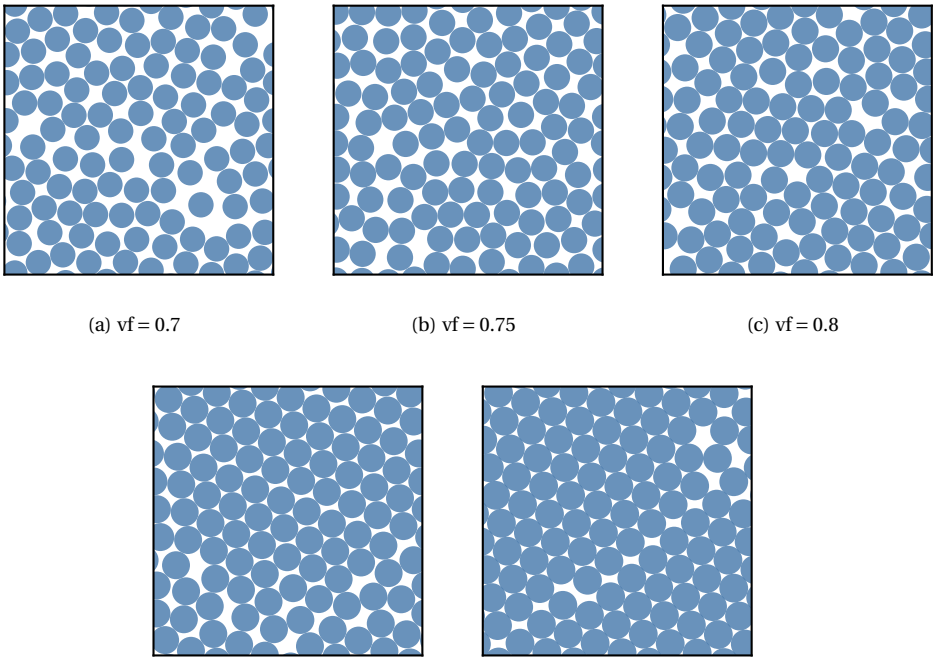

(a) vf = 0.7 (b) vf = 0.75 (c) vf = 0.8

(d) vf = 0.85 (e) vf = 0.9

Figure 7.18: Final microstructures for systems containing 100 Disks, with different volume fractions, vf = 0.7, 0.75, 0.80, 0.85 and 0.9, as a function of the number of iterations, "self-calibrating" the equilibration time in the multi-temperature isokinetic scheme. A configuration is accepted as legal if there are no overlaps.

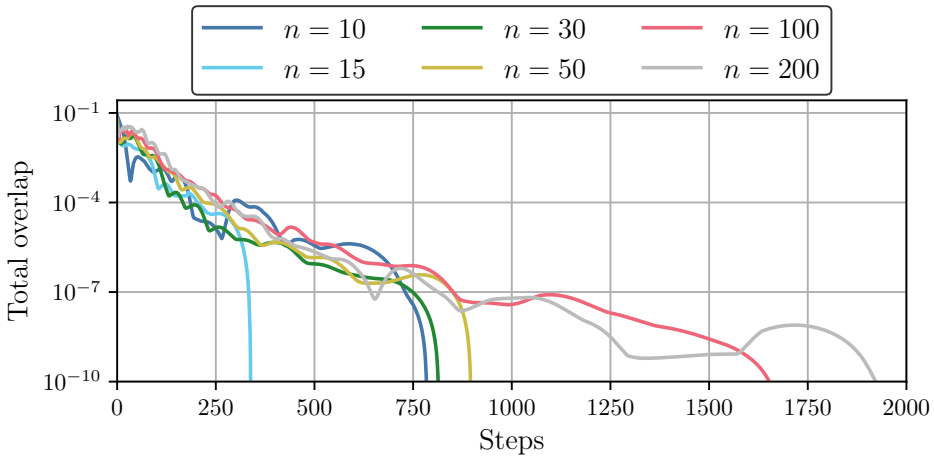

Figure 7.19: Total overlap area for systems containing a different numbers of Spheres, n = 10, 15, 30, 50, 100 and 200, with volume fraction equal to 0.3 as a function of the number of iterations, "self-calibrating" the equilibration time in the multi-temperature isokinetic scheme. A configuration is accepted as legal if the total overlap volume is smaller than 1×10^{-10}.

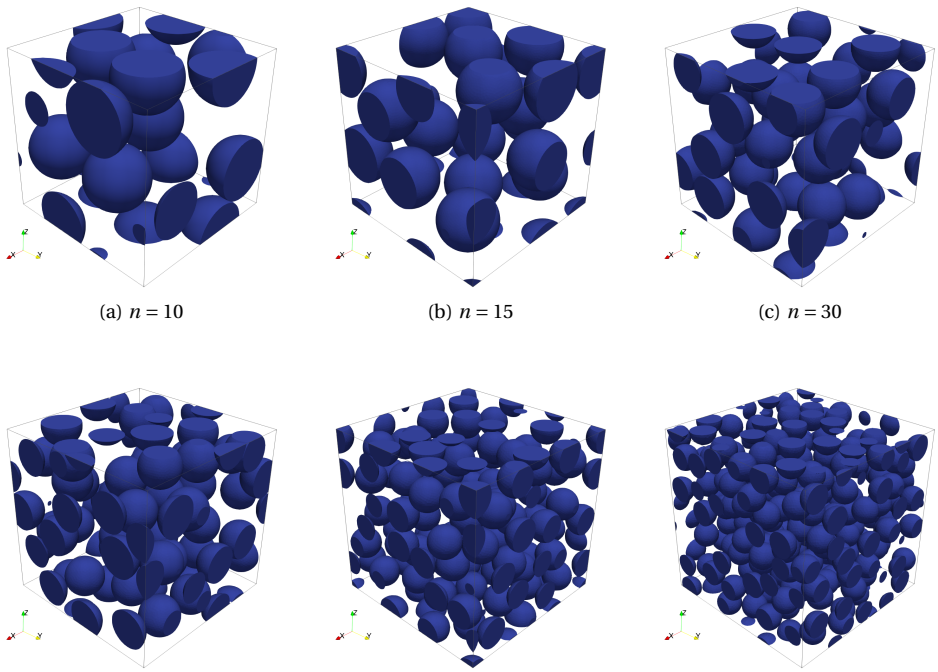

(a) $n = 10$ (b) $n = 15$ (c) $n = 30$

(d) $n = 50$ (e) $n = 100$ (f) $n = 200$

Figure 7.20: Final microstructures for systems containing a different numbers of Spheres, n = 10, 15, 30, 50, 100 and 200, with volume fraction equal to 0.3 as a function of the number of iterations, "self-calibrating" the equilibration time in the multi-temperature isokinetic scheme. A configuration is accepted as legal if the total overlap volume is smaller than 1×10^{-10}.

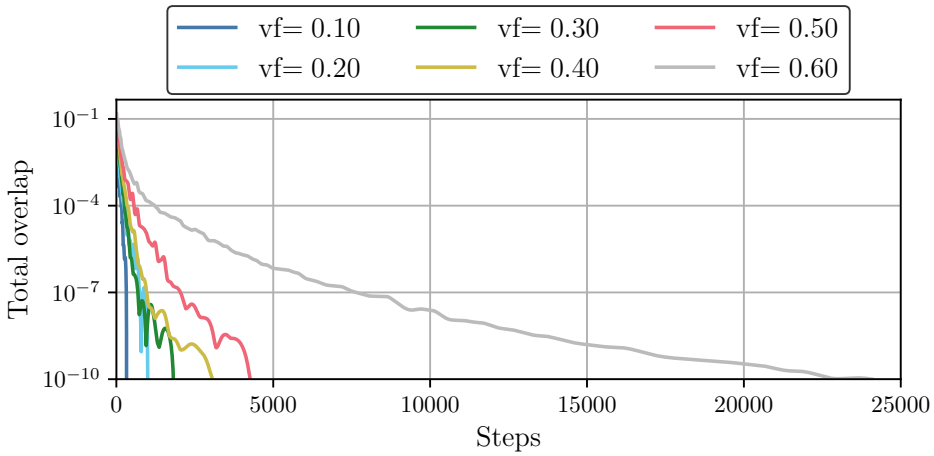

Figure 7.21: Total overlap area for systems containing 100 Spheres, with different volume fractions, vf = 0.1, 0.2, 0.3, 0.4, 0.5 and 0.6, as a function of the number of iterations, "self-calibrating" the equilibration time in the multi-temperature isokinetic scheme. A configuration is accepted as legal if the total overlap volume is smaller than 1×10^{-10}.

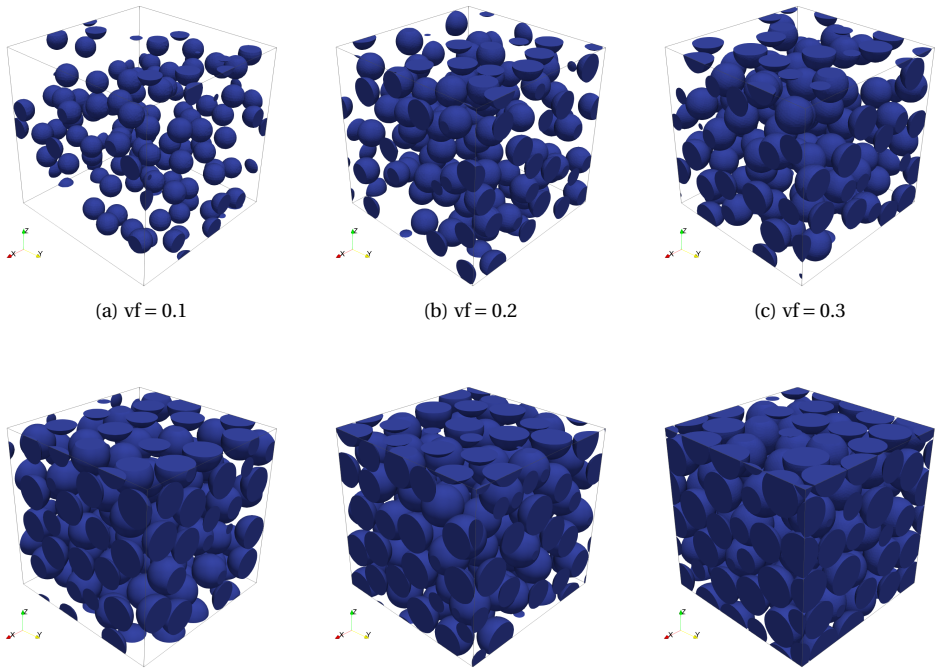

(a) vf = 0.1 (b) vf = 0.2 (c) vf = 0.3

(d) vf = 0.4 (e) vf = 0.5 (f) vf = 0.6

Figure 7.22: Final microstructures for systems containing 100 Spheres, with different volume fractions, vf = 0.1, 0.2, 0.3, 0.4, 0.5 and 0.6, as a function of the number of iterations, "self-calibrating" the equilibration time in the multi-temperature isokinetic scheme. A configuration is accepted as legal if the total overlap volume is smaller than 1×10^{-10}.

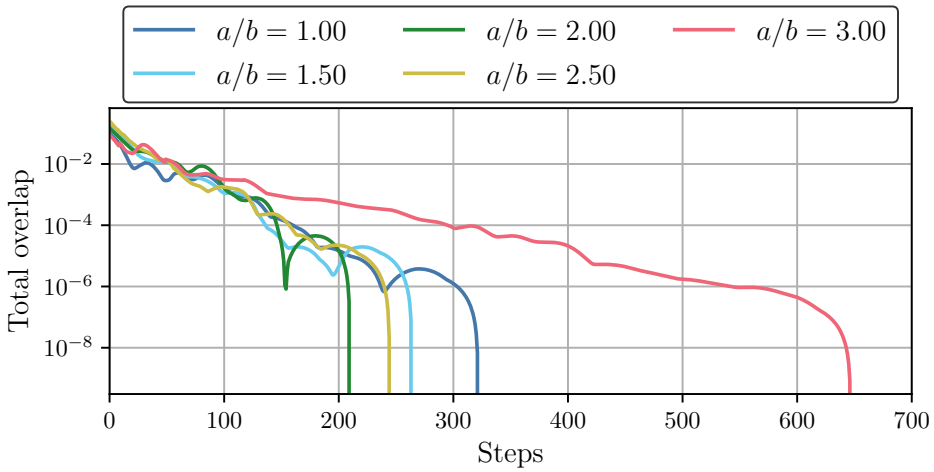

Figure 7.23: Total overlap area for systems containing 20 Ellipses with different ratios between the principal axis, a/b = 1, 1.5, 2, 2.5 and 3, at volume fraction of 0.5, as a function of the number of iterations, "self-calibrating" the equilibration time in the multi-temperature isokinetic scheme. A configuration is accepted as legal if there are no overlaps.

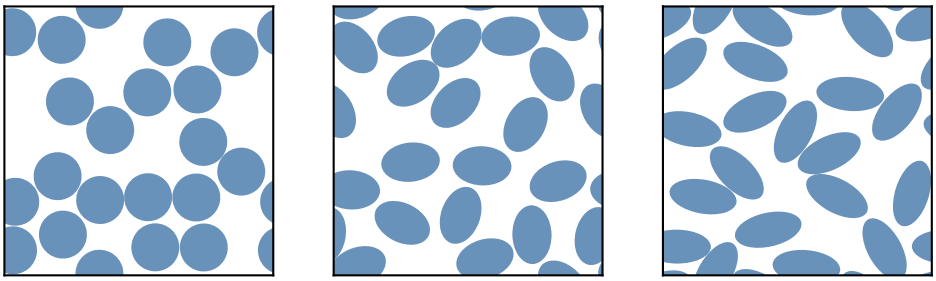

(a) $a/b = 1$ (b) $a/b = 1.5$ (c) $a/b = 2$

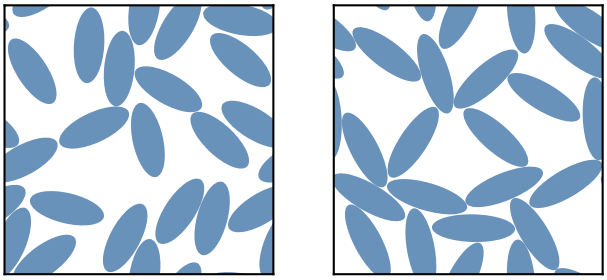

(d) $a/b = 2.5$ (e) $a/b = 3$

Figure 7.24: Total overlap area for systems containing 20 Ellipses with different ratios between the principal axis, a/b = 1, 1.5, 2, 2.5 and 3, at volume fraction of 0.5, as a function of the number of iterations, "self-calibrating" the equilibration time in the multi-temperature isokinetic scheme. A configuration is accepted as legal if there are no overlaps.

Discussion

From Figure 7.7 it is possible to conclude that for a system of 100 Disks at a volume fraction of 0.65, 10 and 15 iterations to reach equilibrium are not enough. Moreover, for these values the temperature is lowered at such a rate that the particles get stuck together and the total overlap area converges to a nonzero value, which is very undesirable. Allowing only for 20 iterations, the simulation produces a legal configuration, but the total overlap area decreases almost monotonically, which may indicate that equilibrium is not reached at each temperature. Thus, so as to not waste iterations after the system reaches equilibrium at a given temperature, the value of 25 iterations is chosen. Looking at the final microstructures, there are no marked differences, even for the microstructures that are not legal, i.e. where there is overlap, since the overlap area is almost imperceptible. This is probably due to the high volume fraction, that masks, for the most part, any clustering, and the disordered nature of the initial configuration, generated through a Poisson point process. Hence, the strategy used to generate the initial configuration seems to be appropriate, contributing to the robustness of the method. Lastly, it is to be noted that only the microstructure generated allowing for 35 equilibration iterations is adversely affected by the presence of the relaxation time, as can be seen in Figure 7.7.

As already stated, Figures 7.9 and 7.10 document the set of four samples generated to establish that an initial temperature of $T_{\text{ref}}k_b = 2.5 \times 10^{-5}$ and a number of equilibration iterations equal to 25 in the multi-temperature isokinetic scheme produces acceptable results for a system of 100 Disks at a volume fraction of 0.65. This is confirmed with the total number of iterations being approximately the same, as can be seen in Figure 7.9 and the final microstructures obtained not showing any glaring flaws.

However, it can be concluded that allowing for only 25 equilibrium iterations is not a robust strategy, and fails for larger particles, as can be seen in Figure 7.11 for 10 and 15 Disks and for higher volume fractions, as can be seen in Figure 7.13 for volume fractions equal to 0.8 and 0.9. Looking at the final microstructures for systems containing 10 and 15 Disks with volume fraction 0.65, Figure 7.12a and 7.12a, respectively, it can be gathered that the particles stuck together preventing the achievement of a legal configuration due to the insufficient number of iterations allowed to reach equilibrium at the different temperature stages. As for the system of particles containing 100 Disks at volume fractions 0.8, from Figure 7.11 it can be posited that due to its slight oscillation, if given more time a legal configuration could be found. Its final configuration (see Figure 7.14e) supports this assertion, as it seems that the particles are fairly close to a legal configuration. On the other hand, the system of particles containing 100 Disks at a volume fraction equal to 0.9 appears to have plateaued (see Figure 7.13). From its final microstructure (see Figure 7.14f), it can be understood why. Despite 0.9 being a volume fraction below the maximum volume fraction possible for a system of Disks (≈ 0.9069), this approach cannot eliminate the point defects present and so its success depends strongly on the initial configuration.

The data presented in Figures 7.15 and 7.17 validates the "self-calibrating" multi-temperature isokinetic scheme, where the equilibration time is updated as the simulation progresses, as it is able to obtain legal configurations for the cases where the use of only 25 iterations for the equilibration time failed. Figures 7.16 and 7.18 present the corresponding final microstructures, whose characteristics seem to be in line with the requirements established for the generation of the microstructures. Regarding the highest volume fractions, this method is not able to produce a legal configuration, as

can be seen in Figure 7.17. This is potentially due to the strong influence of the initial configuration on the defects that will show up in the final microstructure, which at these volume fractions is largely crystallized.

As for the validation of the "self-calibrating" multi-temperature isokinetic scheme for systems of Spheres, the results are presented in Figures 7.19 and 7.21. For systems of Spheres a legal configuration is defined allowing for a residual total overlap volume of 1×10^{-10}, since for these systems achieving zero overlap takes a very long time. This is explained in greater detail in the next section dealing with efficiency, and a solution is proposed when there is a need for no overlap. Regarding the efficacy of the "self-calibrating" multi-temperature isokinetic scheme, a legal configuration is found for all the combinations of descriptors supplied, with Figures 7.20 and 7.22 presenting the final microstructures. The quality of the microstructures generated is addressed in Section 7.22.

Lastly, Figures 7.23 and 7.24 contain the results for systems of Ellipses with different ratios, showing that, as expected, larger ratios lead to longer time to find a legal configuration. It can also be noted, that from Figure 7.23 one cannot detect any obvious difference between the evolution of the total overlap area for ellipses and for disks, except of course for the number of iterations taken to find a legal configuration.

7.1.3 Efficiency

This section seeks to present a set of results related to the efficiency of the proposed method for microstructure generation.

Results

To understand the efficiency in the generation of microstructures containing Disks, the CPU time and number of iterations taken is studied. Figure 7.25 presents the CPU time and the number of iterations averaged over five samples for systems containing 5, 10, 20, 50, 100, 200 and 500 Disks at volume fractions equal to 0.1, 0.2, 0.3, 0.4, 0.5, 0.6 and 0.7. In turn, Table 7.1 presents, in addition to the average CPU time over the five samples, the corresponding standard deviation.

With the same goal but regarding systems of Spheres, another set of simulations is performed. Figure 7.26 presents the CPU time and the number of iterations averaged over five samples for systems containing 10, 20, 50, 100, 200 and 500 Spheres at volume fractions equal to 0.1, 0.2, 0.3, 0.4 and 0.5. In turn, Table 7.2 presents in addition to the average CPU time over the five samples, the corresponding standard deviation. Table 7.3 presents the same results but for systems of Spheres with volume fraction of 0.6. These are excluded from Figure 7.26 and Table 7.2 since it is not possible to reliably generate 5 samples for all numbers of particles.

Lastly, Figure 7.27 and Table 7.4 present the same efficiency related information for systems of 20 Ellipses with the orientation angle varying uniformly between 0 and 2π at a volume fraction of 0.5, and ratio between the major and minor axis equal to 1, 1.5, 2, 2.5 and 3.

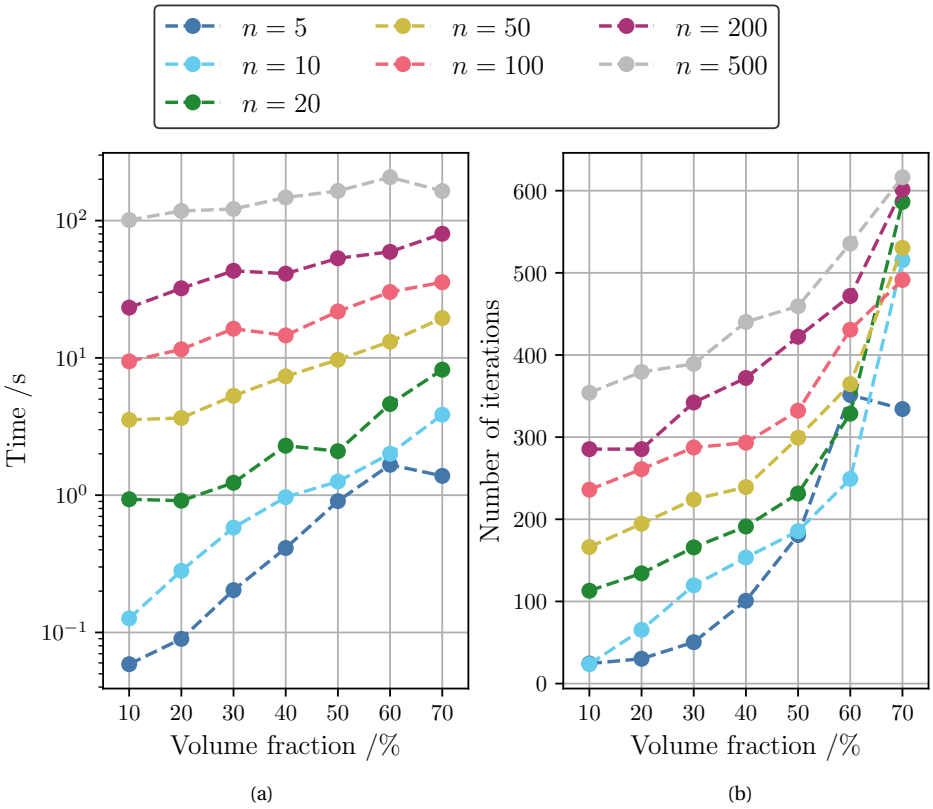

Figure 7.25: (a) Average CPU time and (b) average number of iterations averaged over five samples, for the generation of microstructures containing different numbers of Disks, $n = 5$, 10, 20, 50 , 100, 200 and 500, at various volume fractions, vf = 0.1, 0.2, 0.3, 0.4, 0.5, 0.6 and 0.7, using the "self-calibrating" multi-temperature isokinetic scheme. A configuration is accepted as legal if there are no overlaps.

Table 7.1: Average CPU time and corresponding standard deviation from five samples, for the generation of microstructures containing different numbers of Disks, $n = 5$, 10, 20, 50 , 100, 200 and 500, at various volume fractions, vf = 0.1, 0.2, 0.3, 0.4, 0.5, 0.6 and 0.7, using the "self-calibrating" multi-temperature isokinetic scheme. A configuration is accepted as legal if there are no overlaps.

Number of particles	Time /s	Volume Fraction /%						
		10	20	30	40	50	60	70
5	Mean	0.06	0.09	0.20	0.41	0.90	1.66	1.38
	Std Dev	0.03	0.06	0.03	0.18	0.50	1.64	0.50
10	Mean	0.13	0.28	0.58	0.97	1.26	2.00	3.86
	Std Dev	0.09	0.15	0.24	0.26	0.33	0.83	0.81
20	Mean	0.93	0.91	1.23	2.29	2.09	4.61	8.20
	Std Dev	0.31	0.24	0.25	0.41	0.82	0.80	4.24
50	Mean	3.54	3.65	5.29	7.34	9.69	13.13	19.48
	Std Dev	0.67	0.79	0.47	0.89	1.57	1.52	5.28
100	Mean	9.43	11.55	16.31	14.58	21.78	30.19	35.54
	Std Dev	0.87	2.21	2.11	3.94	3.38	2.99	3.40
200	Mean	23.23	32.12	43.09	41.06	53.13	59.20	80.17
	Std Dev	2.29	5.00	2.68	7.61	5.79	16.34	25.32
500	Mean	100.93	117.57	121.46	147.31	164.38	206.98	164.19
	Std Dev	7.19	4.86	13.26	10.58	21.65	20.23	16.59

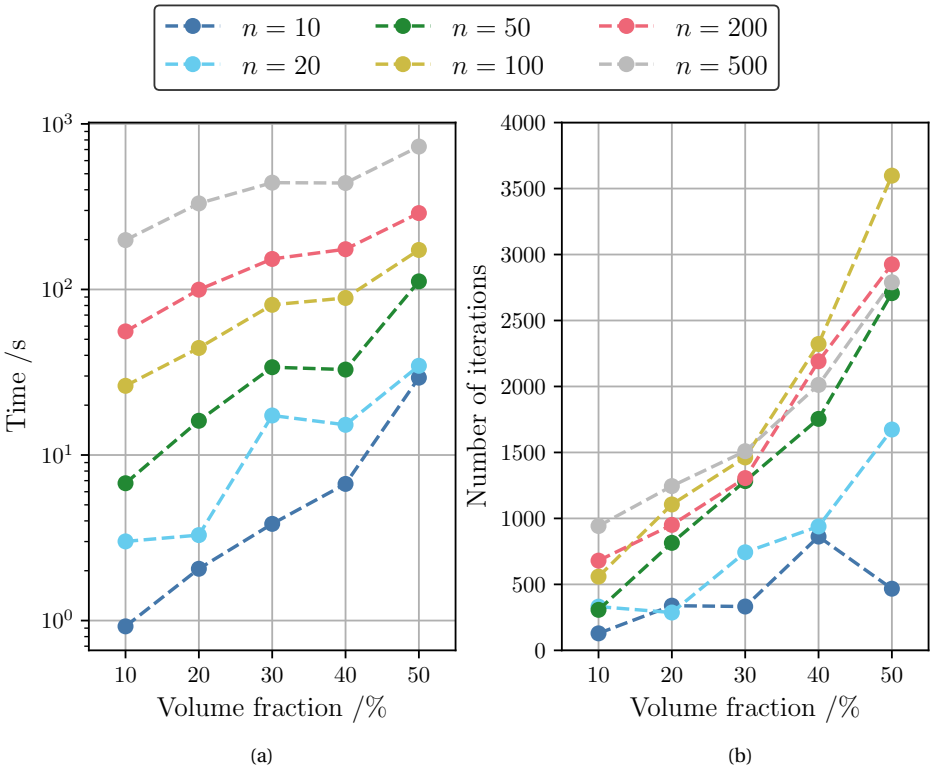

Figure 7.26: (a) Average CPU time and (b) average number of iterations averaged over five samples, for the generation of microstructures containing different numbers of Spheres, n = 10, 20, 50, 100, 200 and 500, at various volume fractions, vf = 0.1, 0.2, 0.3, 0.4, and 0.5, using the "self-calibrating" multi-temperature isokinetic scheme. A configuration is accepted as legal if the average total overlap area per particle is smaller than 1×10^{-12}.

Table 7.2: Average CPU time and corresponding standard deviation from five samples, for the generation of microstructures containing different numbers of Spheres, n = 10, 20, 50, 100, 200 and 500, at various volume fractions, vf = 0.1, 0.2, 0.3, 0.4, and 0.5, using the "self-calibrating" multi-temperature isokinetic scheme.A configuration is accepted as legal if the average total overlap area per particle is smaller than 1×10^{-12}.

Number of particles	Time /s	Volume Fraction /%				
		10	20	30	40	50
10	Mean	0.92	2.06	3.84	6.69	29.33
	Std Dev	0.29	0.68	2.11	3.37	8.47
20	Mean	3.01	3.28	17.33	15.22	34.59
	Std Dev	0.72	0.86	3.26	6.11	10.37
50	Mean	6.75	16.10	33.91	32.82	111.88
	Std Dev	1.09	9.00	8.57	13.08	29.34
100	Mean	26.18	44.32	80.75	88.83	173.18
	Std Dev	7.04	14.19	40.14	31.20	37.84
200	Mean	55.79	99.70	152.86	175.06	289.23
	Std Dev	9.68	28.14	22.30	15.90	26.70
500	Mean	198.71	330.94	441.64	439.53	729.60
	Std Dev	46.22	67.27	78.70	13.65	56.52

Table 7.3: Average CPU time, corresponding standard deviation and average final overlap volume and corresponding standard deviation for systems containing 10, 20, 50, 100, 200 and 500 Spheres at a volume fraction of 0.6.

Number of Spheres	Successful Samples	Final Overlap Volume		Time /s	
		Mean	Std Dev	Mean	Std Dev
10	0	7.27×10^{-3}	6.07×10^{-3}	831.98	378.41
20	1	1.84×10^{-5}	3.69×10^{-5}	521.44	18.46
50	4	1.20×10^{-9}	2.24×10^{-9}	836.89	151.32
100	4	1.03×10^{-8}	2.03×10^{-8}	1187.51	363.65
200	5	2.09×10^{-10}	1.86×10^{-11}	2005.73	939.98
500	5	4.99×10^{-10}	3.39×10^{-13}	2209.93	370.55

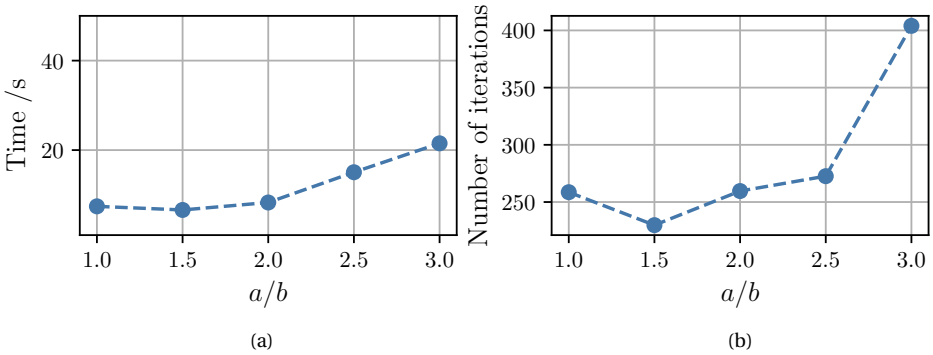

Figure 7.27: (a) Average CPU time and (b) average number of iterations averaged over five samples, for the generation of microstructures containing 20 Ellipses at a volume fraction of 0.5, with different ratios between the principal axis, $a/b = 1$, 1.5, 2, 2.5 and 3, using the "self-calibrating" multi-temperature isokinetic scheme. A configuration is accepted as legal if there are no overlaps.

Table 7.4: Average CPU time and corresponding standard deviation from five samples, for the generation of microstructures containing 20 Ellipses at a volume fraction of 0.5, with different ratios between the principal axis, $a/b = 1$, 1.5, 2, 2.5 and 3, using the "self-calibrating" multi-temperature isokinetic scheme. A configuration is accepted as legal if there are no overlaps.

Time /s	Ratio a/b				
	1	1.5	2	2.5	3
Mean	7.43	6.62	8.29	15.05	21.51
Std Dev	0.59	1.07	1.34	2.18	4.95

Discussion

From Figure 7.25, it can be concluded that the proposed scheme is reasonably efficient, being capable of generating a microstructure containing 500 Disks at a volume fraction of 0.7 in around 165 seconds ($\approx$ 3 mins). As expected, a larger number of Disks at a higher volume fraction implies a larger CPU time to obtain a legal configuration with zero overlap. Table 7.1 hints that the standard variation of the CPU time follows the same tendency, being larger for higher volume fractions and numbers of particles.

For systems of Spheres the same approach, is also shown to be reasonably efficient, being able to produce microstructures containing 500 Spheres at a volume fraction of 0.5 in around 12 mins, with the caveat that the final configuration allows for an average total overlap per particle of 1×10^{-12}. This option, as stated previously, is taken because for systems of Spheres finding a configuration without overlap takes a prohibitive time. A reason for this state of affairs can be deduced from Figure 6.21, depicting the repulsive force as a function of the distance between the centers of two Spheres with the same size. It can be noted that when compared to the repulsive force between two Disks, for distances very close to the diameter of the particle, i.e. no overlap, the force for Spheres decreases more abruptly leading to very small forces when compared to Disks at very small overlaps. Hence, the difference in the ability of the two systems to reach zero overlap.

To mitigate this problem, when a microstructure with Spheres is desired with no overlap, one can simulate the system with larger particles, and hence larger volume fraction, shrinking the particles at the end. For example, if for a system of 500 Spheres at a volume fraction of 0.4, the system is simulated with an increased radius of 0.0001, it implies a virtual volume fraction of 0.402. Assuming that the overlap volume is only due to two particles, the overlap of the virtual particles corresponding to nonoverlapping real particles is 6.3×10^{-7}, and can be found from Equation (6.44). Thus, the increase in volume fraction of just 0.02, carries a negligible increase in CPU time and allows the use of very loose convergence criteria of 6.3×10^{-7} for the total overlap volume.

When it comes to systems of Spheres at a volume fraction of 0.6, Table 7.3 shows that a legal configuration could not be found for all numbers of particles, more precisely, systems with less particles and hence larger particles failed to produce the desired average overlap per particle. At the moment, this behavior cannot be explained, however, it must be noted that for smaller particles corresponding to systems of 200 and 500 Spheres it was always possible to generate microstructures with legal configurations.

Lastly, Figure 7.27 and Table 7.4 confirm, that as expected, systems containing Ellipses with higher ratios between the major and minor axis imply longer simulation times to produce a legal configuration.

7.2 Microstructure Analysis

In this section, it is shown that the Minkowski structure metrics are robust descriptors of the microstructure. Several numerical examples are presented where these metrics are employed to suitably characterize the generated microstructures.

7.2.1 Reconstruction of polygons and detection of s-fold symmetry

This section has the goal of showing that the Minkowski structure metrics and the associated concepts are able to provide a robust description of the shape of convex and non-convex polygons. This is of great importance in the analysis of microstructures, as it allows for the characterization of the Voronoi cells of the Voronoi diagrams, be it standard Voronoi diagrams, obtained from microstructures containing only Disks of the sames size, or set Voronoi diagrams, obtained from microstructures containing Disks of different sizes and/or Ellipses.

Results

In order to fulfill the objectives of this section four convex polygons and four non-convex polygons are created. They are shown in Figures 7.28a, 7.29a, 7.30a, 7.31a, 7.32a, 7.33a, 7.34a and 7.35a, and are obtained by distorting and adding extra vertices to a triangle, a square, a thin rectangle and a hexagon, respectively. The reconstruction of the convex polygons using the first six terms of a Fourier series to approximate the curvature is presented in Figures 7.28b, 7.30b, 7.32b and 7.34b, respectively. The corresponding Minkowski structure metrics for each polygon are shown in Figures 7.28c, 7.29b, 7.30c and 7.31b, 7.32c, 7.33b, 7.34c and 7.35b.

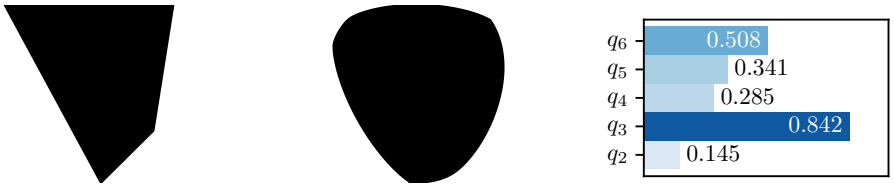

(a) (b) (c)

Figure 7.28: (a): Convex polygon obtained distorting and adding vertices to an equilateral triangle. (b): Reconstruction using the first 6 terms of the Fourier series to approximate the polygon's curvature (c): Minkowski structure metrics of the polygon.

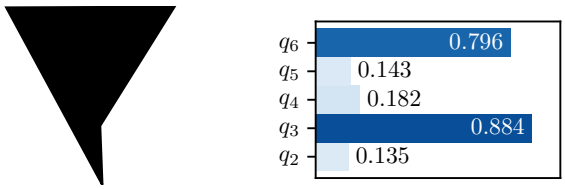

(a) (b)

Figure 7.29: (a): Non-convex polygon obtained distorting and adding vertices to an equilateral triangle. (b): Minkowski structure metrics of the polygon.

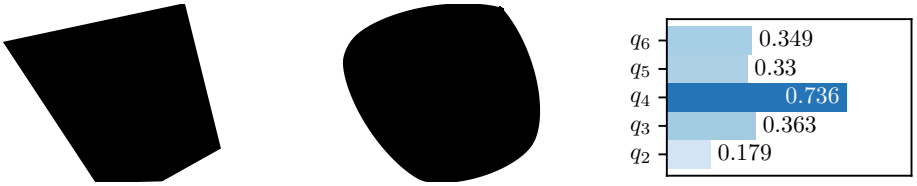

(a) (b) (c)

Figure 7.30: (a): Convex polygon obtained distorting and adding vertices to a square. (b): Reconstruction using the first 6 terms of the Fourier series to approximate the polygon's curvature. (c): Minkowski structure metrics of the polygon.

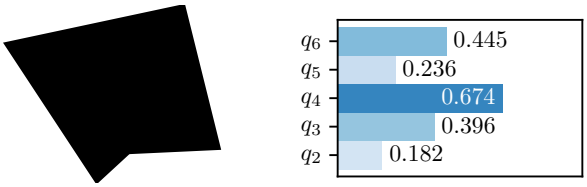

(a) (b)

Figure 7.31: (a): Non-convex polygon obtained distorting and adding vertices to a square. (b): Minkowski structure metrics of the polygon.

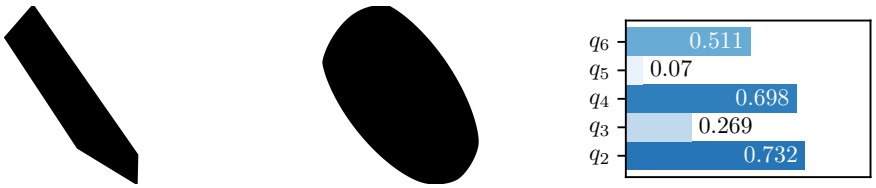

(a) (b) (c)

Figure 7.32: (a): Convex polygon obtained distorting and adding vertices to a thin rectangle. (b): Reconstruction using the first 6 terms of the Fourier series to approximate the polygon's curvature (c): Minkowski structure metrics of the polygon.

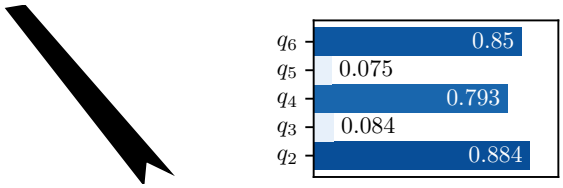

(a) (b)

Figure 7.33: (a): Non-convex polygon obtained distorting and adding vertices to a thin rectangle. (b): Minkowski structure metrics of the polygon.

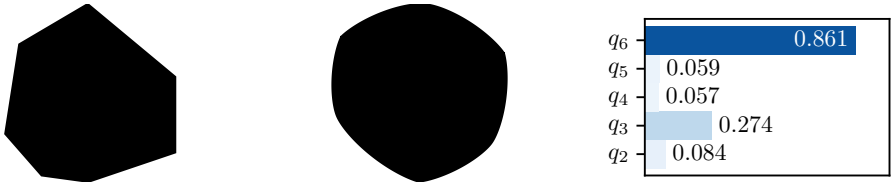

(a) (b) (c)

Figure 7.34: (a): Convex polygon obtained distorting and adding vertices to an equilateral triangle. (b): Reconstruction using the first 6 terms of the Fourier series to approximate the polygon's curvature (c): Minkowski structure metrics of the polygon.

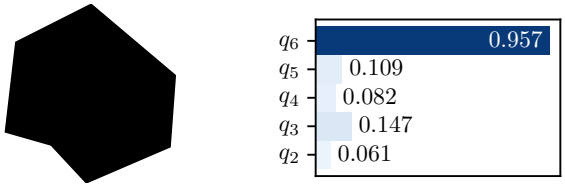

(a) (b)

Figure 7.35: (a): Non-convex polygon obtained distorting and adding vertices to a regular hexagon. (b): Minkowski structure metrics of the polygon.

Discussion

From Figures 7.28b, 7.30b, 7.32b and 7.34b it can be seen that the shapes of the convex polygons are mostly recovered. It must be kept in mind that only 6 terms of the Fourier series are used to produce these shapes. Accordingly, the Minkowski structure metrics presented in Figures 7.28a, 7.30a, 7.32a and 7.34a signal strongly the presence of 3-fold, 4-fold, 2-fold and 6-fold, respectively. The same can be said about the Minkowski structure metrics obtained for the non-convex polygons (see Figures 7.29a, 7.31a, 7.33a and 7.35a). This is expected, as the original polygons are produced from a triangle, a square, a thin rectangle and a hexagon. Therefore, it can be inferred that the Minkowski structures metrics are able to represent robustly the shapes of the Voronoi cells of microstructures containing all the types of particles considered.

7.2.2 Quality analysis of microstructures containing Disks of the same size using Minkowski structure metrics

The results in this section have two goals. Firstly, to show the capability of the Minkowski structure metrics to characterize the Voronoi cells of microstructures containing only Disks of the same size. Secondly, to validate the microstructures generated using the approach introduced as it pertains to their quality.

Results

Figures 7.36-7.41 present typical results obtained from an analysis to a microstructure using Minkowski structure metrics, i.e. the Voronoi diagram with the cells colored according to the value of the corresponding Minkowski structure metric and the respective histogram of the Minkowski structure metrics. The microstructure contains 50 Disks at a volume fraction equal to 0.5. Examples of pathological microstructures with excess order can be found in Figure 7.42.

To understand the typical distribution of the Minkowski structure metrics, q_2, q_3, q_4, q_5 and q_6, for microstructures containing Disks of the same size, five random samples of microstructures containing 100 Disks at volume fractions equal to 0.3, 0.5 and 0.7 are produced. The histograms of the perimeter and Minkowski structures metrics of their Voronoi cells is presented in Figures 7.43-7.45. In the same spirit, Table 7.5 presents the p-values for Anderson-Darling tests probing if the perimeter and Minkowski structure metrics, q_2, q_3, q_4, q_5 and q_6, of the Voronoi cells of five random samples all containing 50, 100, 200 or 500 Disks at volume fractions equal to 0.2, 0.3, 0.4, 0.5, 0.6 or 0.7 come from the same underlying distribution.

Lastly, it is presented a set of results aiming to distinguish between microstructures generated using the "self-calibrating" multi-temperature isokinetic scheme (Method 1) (see Figures 7.46a, 7.46c and 7.46e for examples) and the multi-temperature isokinetic scheme, allowing only a small number of equilibration iterations (Method 2) (see Figures 7.46b, 7.46d and 7.46f for examples). To this effect, Figures 7.47-7.49 present the histograms of the perimeter and Minkowski structures metrics of the Voronoi cells of three samples generated with each method. The microstructures contain 100 Disks at volume fractions equal to 0.3, 0.5 an 0.7, respectively. To check if there are marked differences between the distributions, the mean, standard deviation, skewness and kurtosis of the perimeter and Minkowski structure metrics for each sample are computed an the results are presented in the form of boxplots on Figures 7.50-7.52.

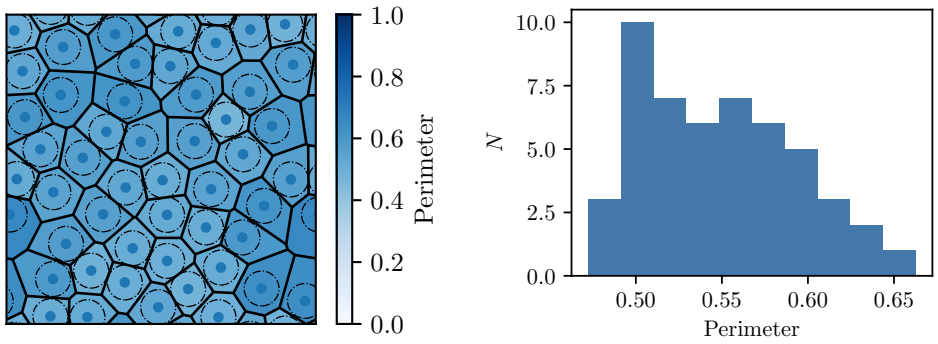

(a) (b)

Figure 7.36: (a) Voronoi diagram of a microstructure containing 50 Disks at a volume fraction equal to 0.5, with the cells colored according to their perimeter. (b) Histogram containing the perimeter of the Voronoi cells.

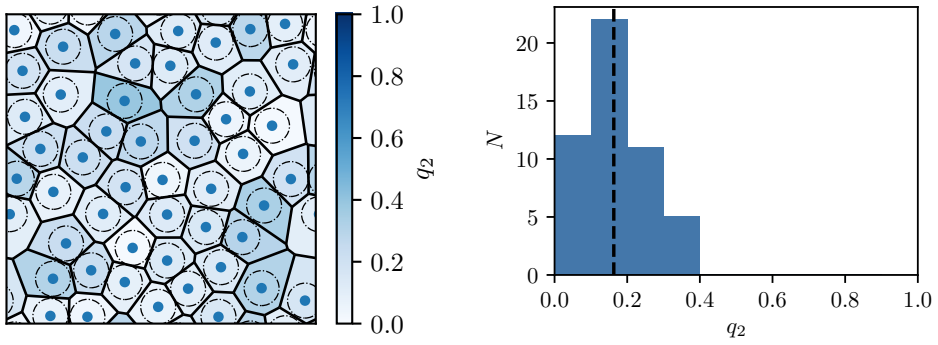

(a) (b)

Figure 7.37: (a) Voronoi diagram of a microstructure containing 50 Disks at a volume fraction equal to 0.5, with the cells colored according to their q_2 Minkowski structure metric. (b) Histogram containing the q_2 Minkowski structure metric of the Voronoi cells, where the dashed line represents the average.

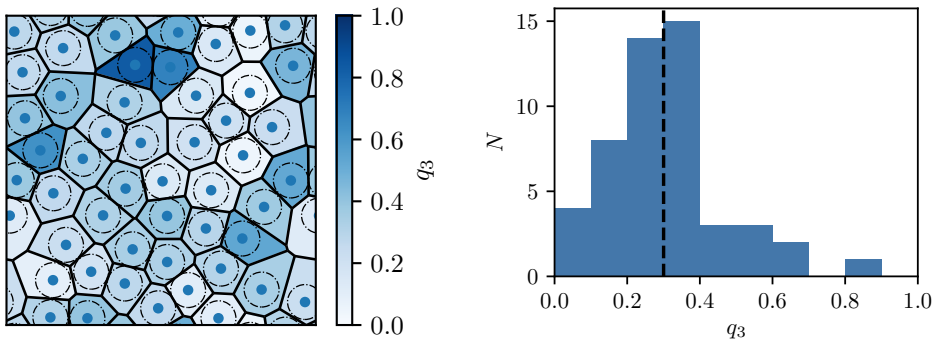

(a) (b)

Figure 7.38: (a) Voronoi diagram of a microstructure containing 50 Disks at a volume fraction equal to 0.5, with the cells colored according to their q_3 Minkowski structure metric. (b) Histogram containing the q_3 Minkowski structure metric of the Voronoi cells, where the dashed line represents the average.

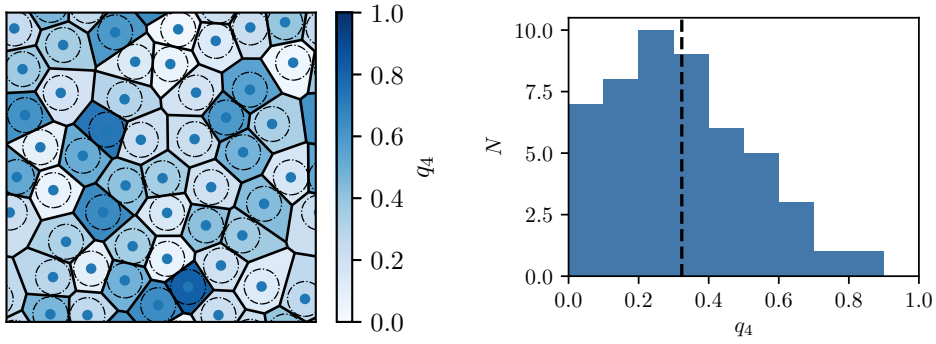

(a) (b) $k = 15$

Figure 7.39: (a) Voronoi diagram of a microstructure containing 50 Disks at a volume fraction equal to 0.5, with the cells colored according to their q_4 Minkowski structure metric. (b) Histogram containing the q_4 Minkowski structure metric of the Voronoi cells, where the dashed line represents the average.

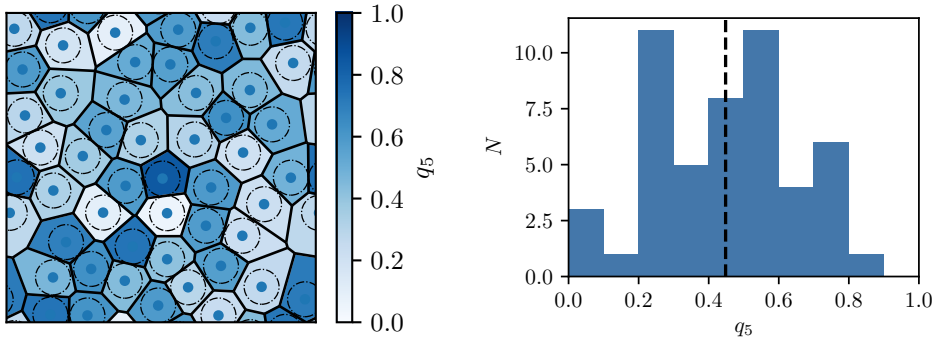

(a) (b)

Figure 7.40: (a) Voronoi diagram of a microstructure containing 50 Disks at a volume fraction equal to 0.5, with the cells colored according to their q_5 Minkowski structure metric. (b) Histogram containing the q_5 Minkowski structure metric of the Voronoi cells, where the dashed line represents the average.

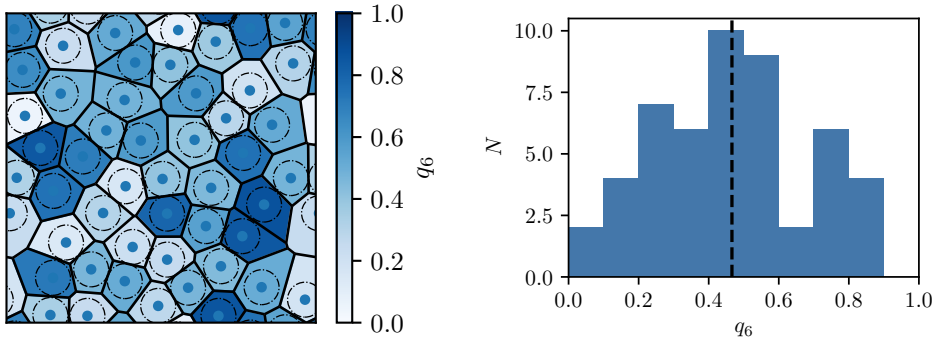

(a) (b)

Figure 7.41: (a) Voronoi diagram of a microstructure containing 50 Disks at a volume fraction equal to 0.5, with the cells colored according to their q_6 Minkowski structure metric. (b) Histogram containing the q_6 Minkowski structure metric of the Voronoi cells, where the dashed line represents the average.

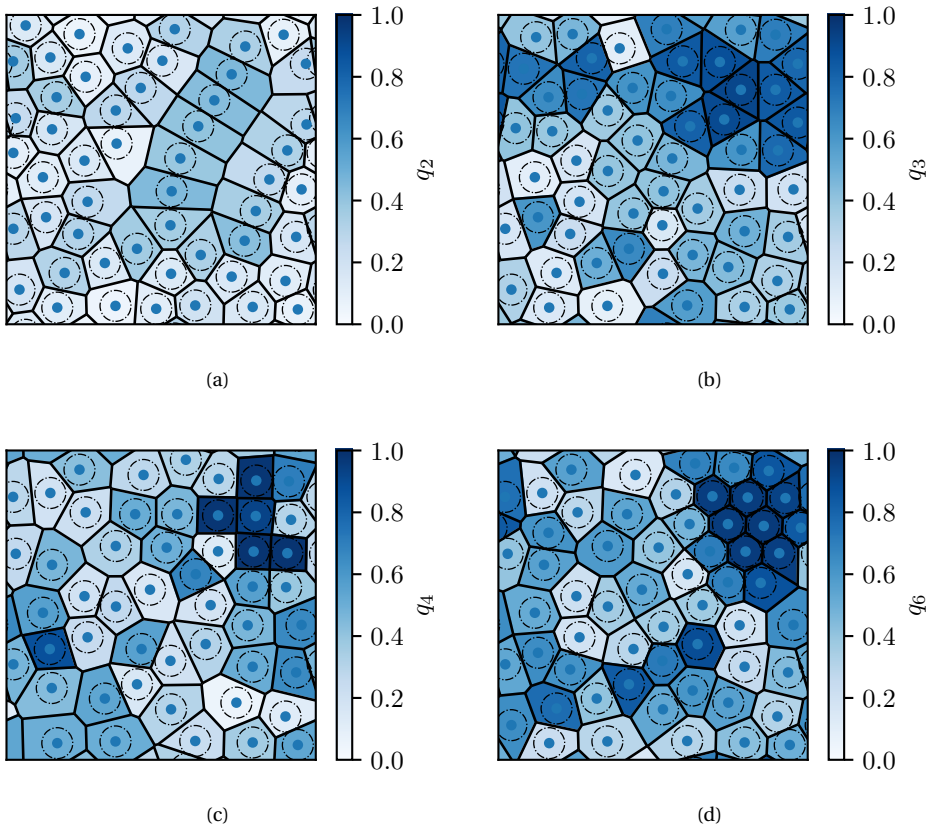

Figure 7.42: Microstructures containing excessive order, signaled by the concentration of cells with high q_2, (a), q_3, (b), q_4, (c) and q_6, (d) Minkowski structure metrics.

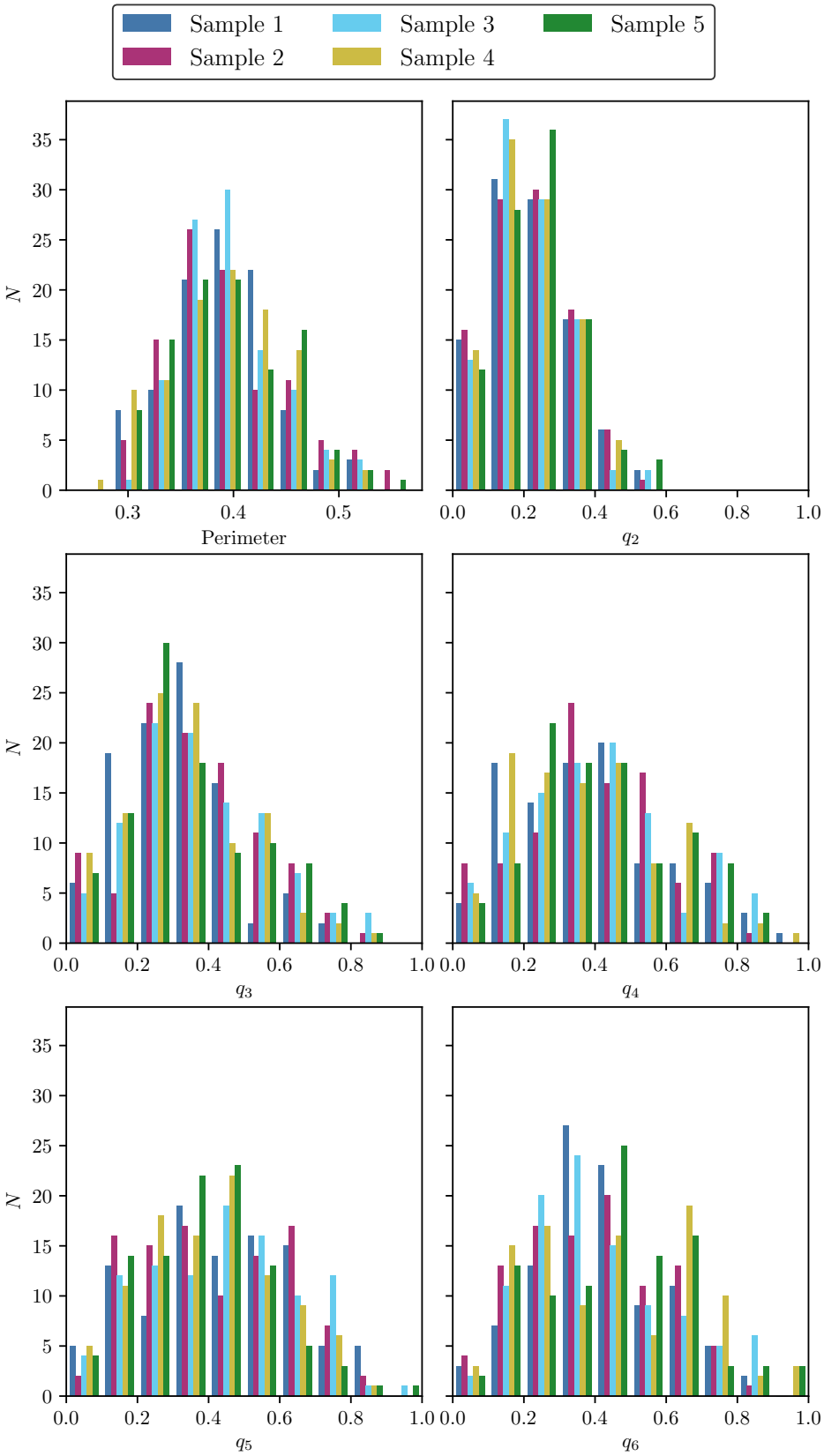

Figure 7.43: Histograms of the perimeter and Minkowski structure metrics, q_2, q_3, q_4, q_5 and q_6, for five random samples containing 100 Disks at a volume fraction of 0.3.

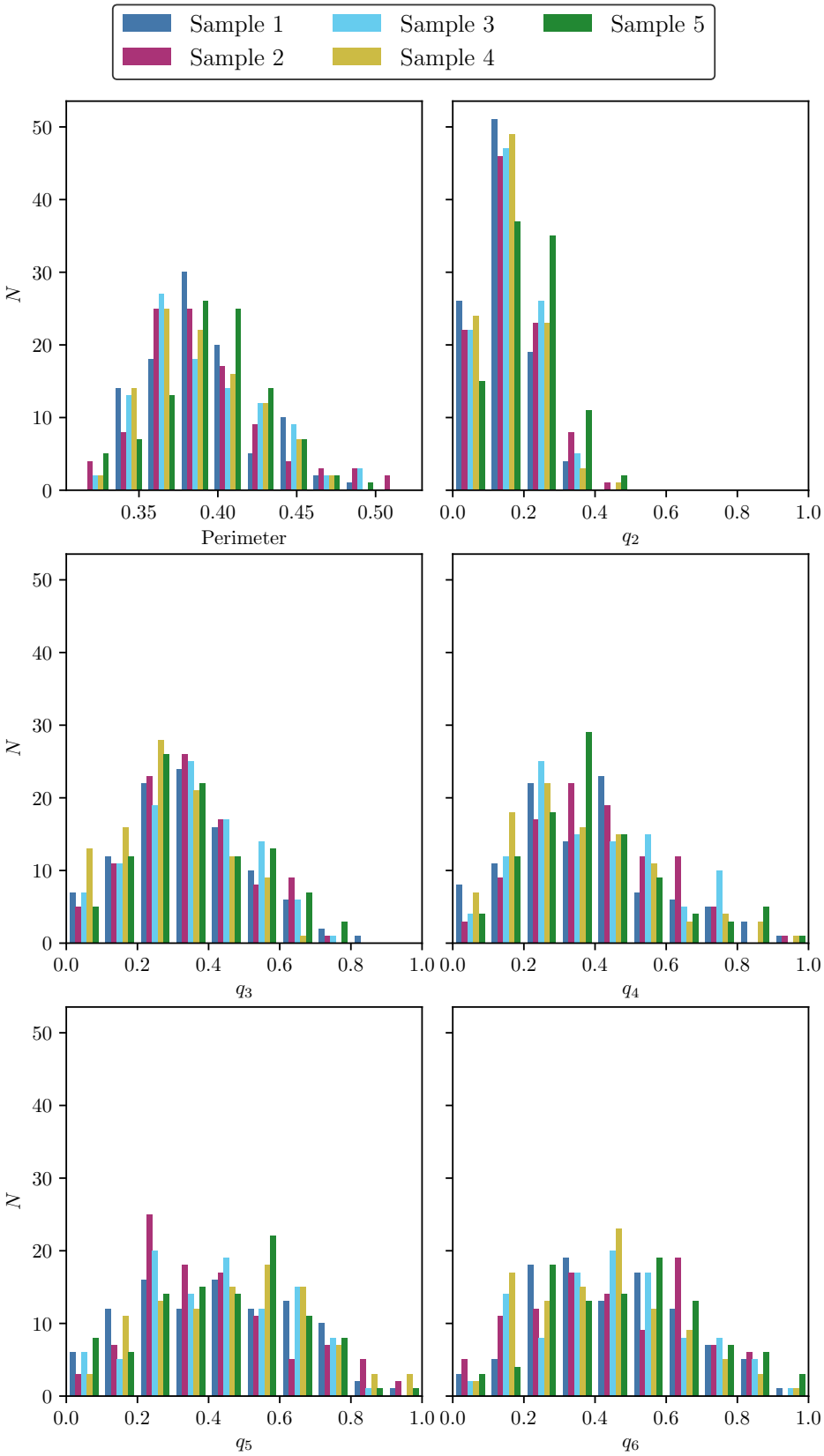

Figure 7.44: Histograms of the perimeter and Minkowski structure metrics, q_2, q_3, q_4, q_5 and q_6, for five random samples containing 100 Disks at a volume fraction of 0.5.

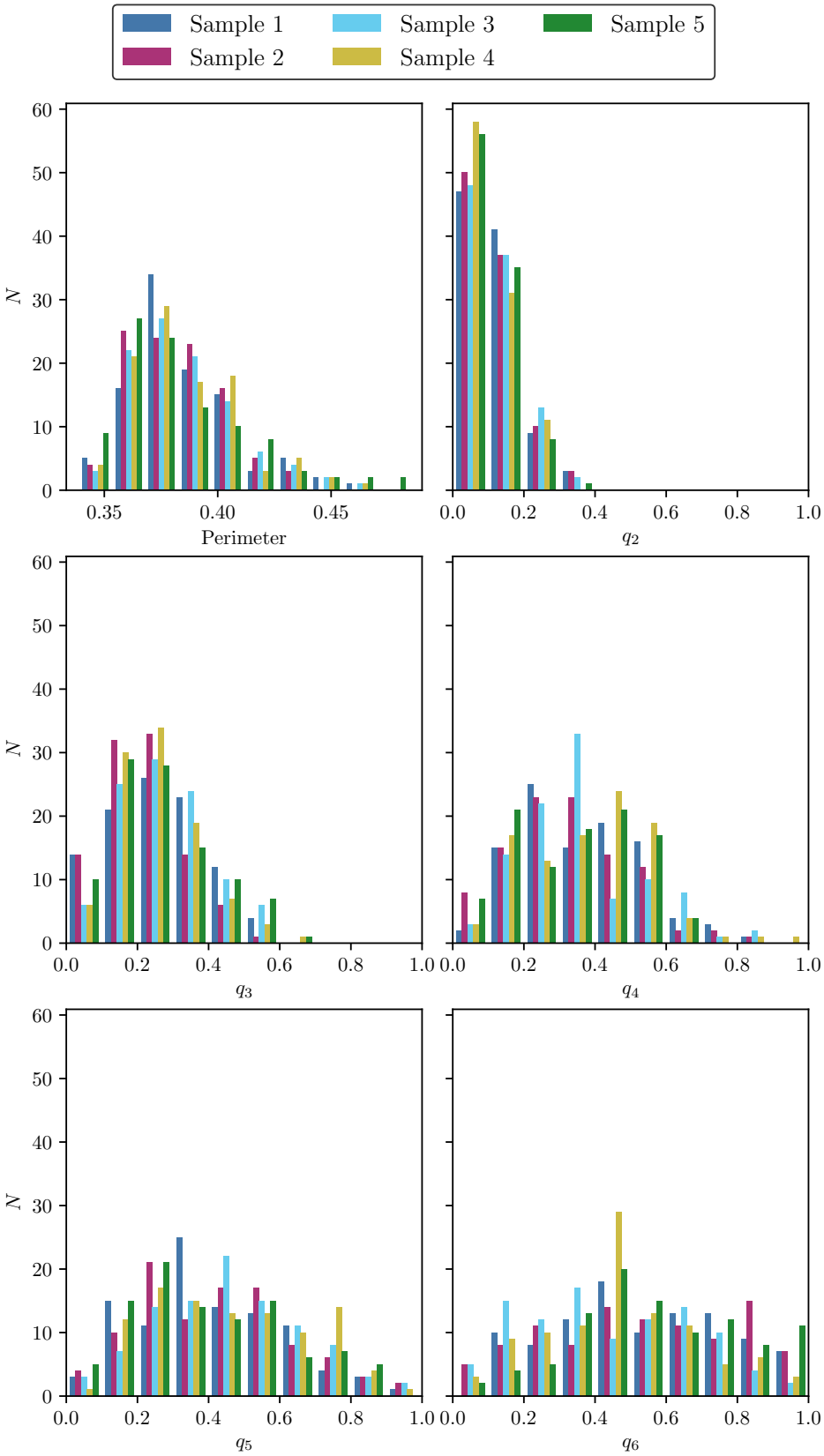

Figure 7.45: Histograms of the perimeter and Minkowski structure metrics, q_2, q_3, q_4, q_5 and q_6, for five random samples containing 100 Disks at a volume fraction of 0.7.

Table 7.5: Anderson-Darling test probing if the perimeter and Minkowski structure metrics, q_2, q_3, q_4, q_5 and q_6 of the Voronoi cells of five samples all containing 50, 100, 200 or 500 Disks at volume fractions equal to 0.2, 0.3, 0.4, 0.5, 0.6 or 0.7 come from the same underlying distribution. The test is also perform including all the microstructures containing different numbers of particles with the same volume fraction under "All". The p-value is floored at 25% and capped at 0.1%.

Volume Fraction /%	Number	p-value / %					
		P	q_2	q_3	q_4	q_5	q_6
20	50	25.00	25.00	25.00	25.00	25.00	25.00
	100	25.00	19.10	23.58	9.81	13.20	14.34
	200	25.00	25.00	13.93	20.88	25.00	25.00
	500	25.00	25.00	0.71	13.54	23.65	25.00
	All	0.10	25.00	0.69	12.34	25.00	25.00
30	50	25.00	25.00	25.00	25.00	8.93	25.00
	100	25.00	25.00	15.18	25.00	12.22	5.89
	200	25.00	25.00	10.99	25.00	25.00	25.00
	500	13.73	4.31	25.00	25.00	25.00	21.40
	All	0.10	3.70	7.71	25.00	25.00	25.00
40	50	25.00	25.00	25.00	25.00	25.00	25.00
	100	22.16	0.10	4.36	25.00	25.00	25.00
	200	25.00	3.56	25.00	25.00	25.00	25.00
	500	25.00	25.00	25.00	20.79	25.00	25.00
	All	0.10	0.10	25.00	25.00	25.00	25.00
50	50	25.00	25.00	2.65	25.00	25.00	25.00
	100	25.00	0.41	5.57	23.54	25.00	25.00
	200	25.00	1.12	16.37	25.00	25.00	1.77
	500	25.00	25.00	25.00	25.00	25.00	25.00
	All	0.10	0.10	0.14	25.00	25.00	8.54
60	50	8.00	8.53	25.00	1.36	25.00	23.16
	100	25.00	25.00	25.00	25.00	25.00	17.10
	200	24.70	0.33	0.10	25.00	22.42	1.95
	500	25.00	25.00	25.00	25.00	25.00	25.00
	All	0.10	0.10	0.10	2.66	25.00	3.03
70	50	25.00	2.38	25.00	21.26	25.00	5.80
	100	25.00	25.00	5.12	10.17	17.17	0.10
	200	22.10	0.81	25.00	25.00	25.00	25.00
	500	17.15	25.00	10.52	25.00	25.00	10.83
	All	0.10	0.10	0.69	0.35	25.00	0.10

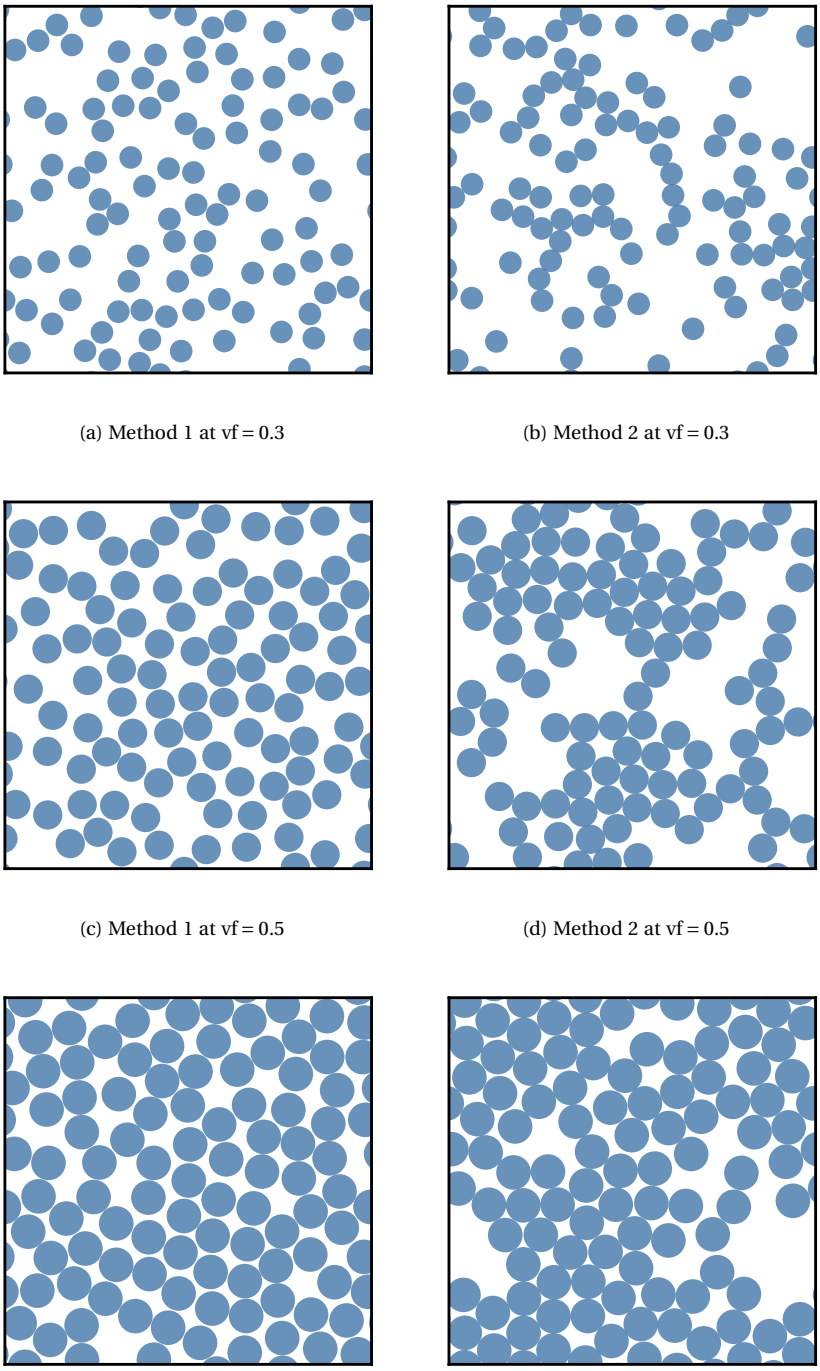

(a) Method 1 at vf = 0.3

(b) Method 2 at vf = 0.3

(c) Method 1 at vf = 0.5

(d) Method 2 at vf = 0.5

(e) Method 1 at vf = 0.7

(f) Method 2 at vf = 0.7

Figure 7.46: Final microstructures for random samples generated with the "self-calibrating" multi-temperature isokinetic scheme (Method 1) and three samples generated using the multi-temperature isokinetic scheme with a low fixed number of equilibration iterations (Method 2), all containing 100 Disks at a volume fractions of 0.3, 0.5 and 0.7.

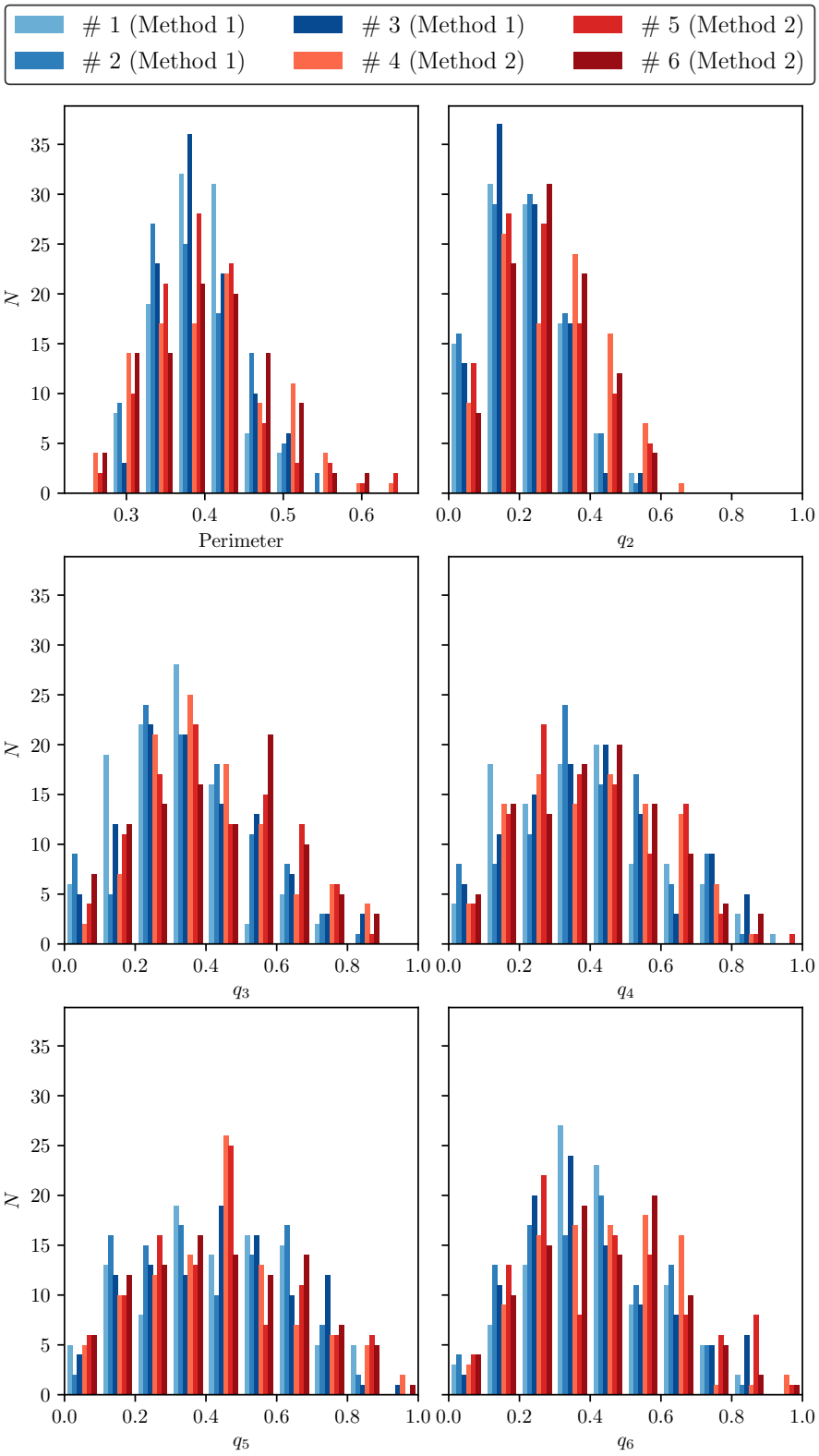

Figure 7.47: Histograms of the perimeter and Minkowski structure metrics, q_2, q_3, q_4, q_5 and q_6, for three random samples generated with the "self-calibrating" multi-temperature isokinetic scheme (Method 1) and three samples generated using the multi-temperature isokinetic scheme with a low fixed number of equilibration iterations (Method 2), all containing 100 Disks at a volume fraction of 0.3.

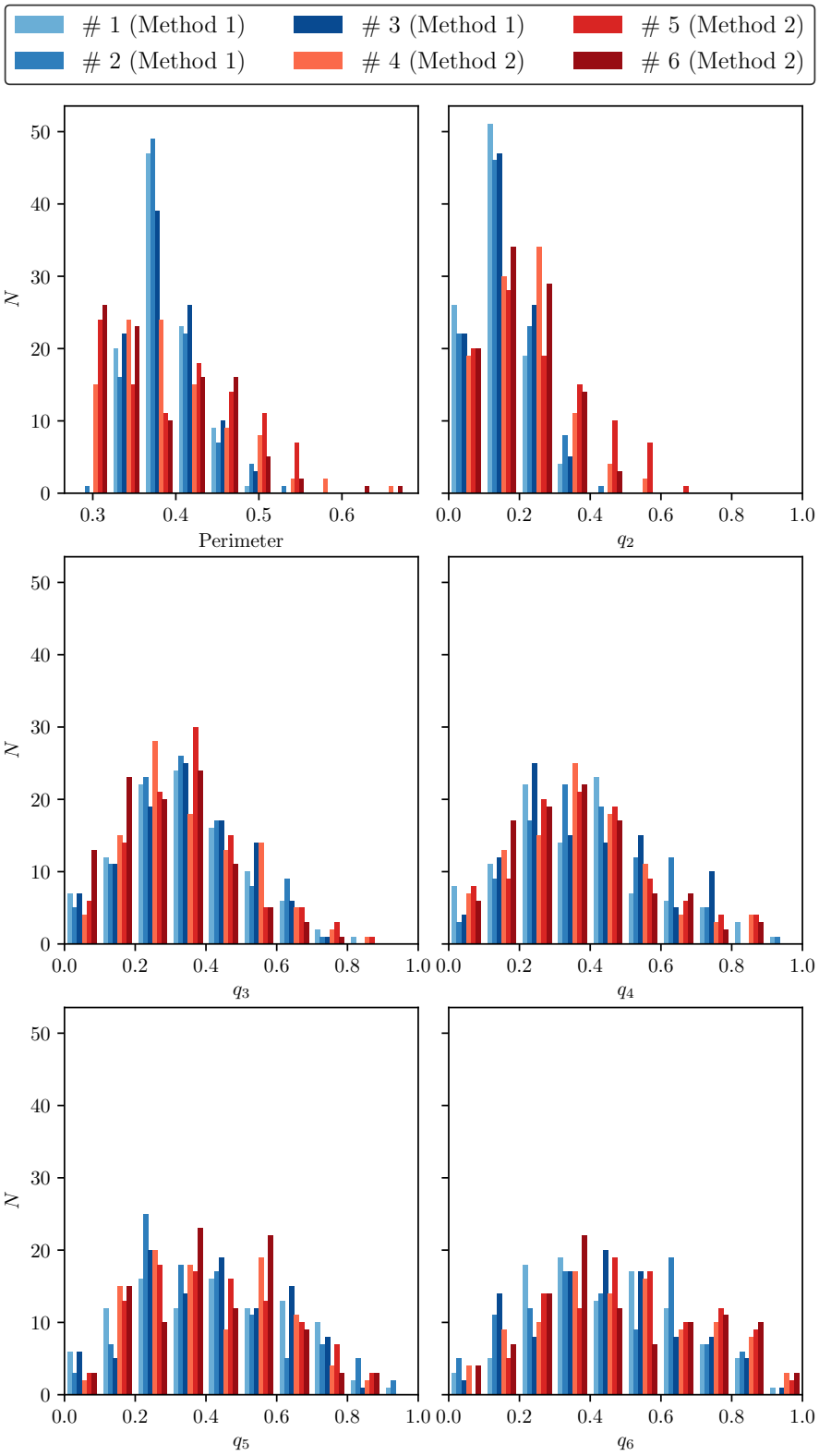

Figure 7.48: Histograms of the perimeter and Minkowski structure metrics, q_2, q_3, q_4, q_5 and q_6, for three random samples generated with the "self-calibrating" multi-temperature isokinetic scheme (Method 1) and three samples generated using the multi-temperature isokinetic scheme with a low fixed number of equilibration iterations (Method 2), all containing 100 Disks at a volume fraction of 0.5.

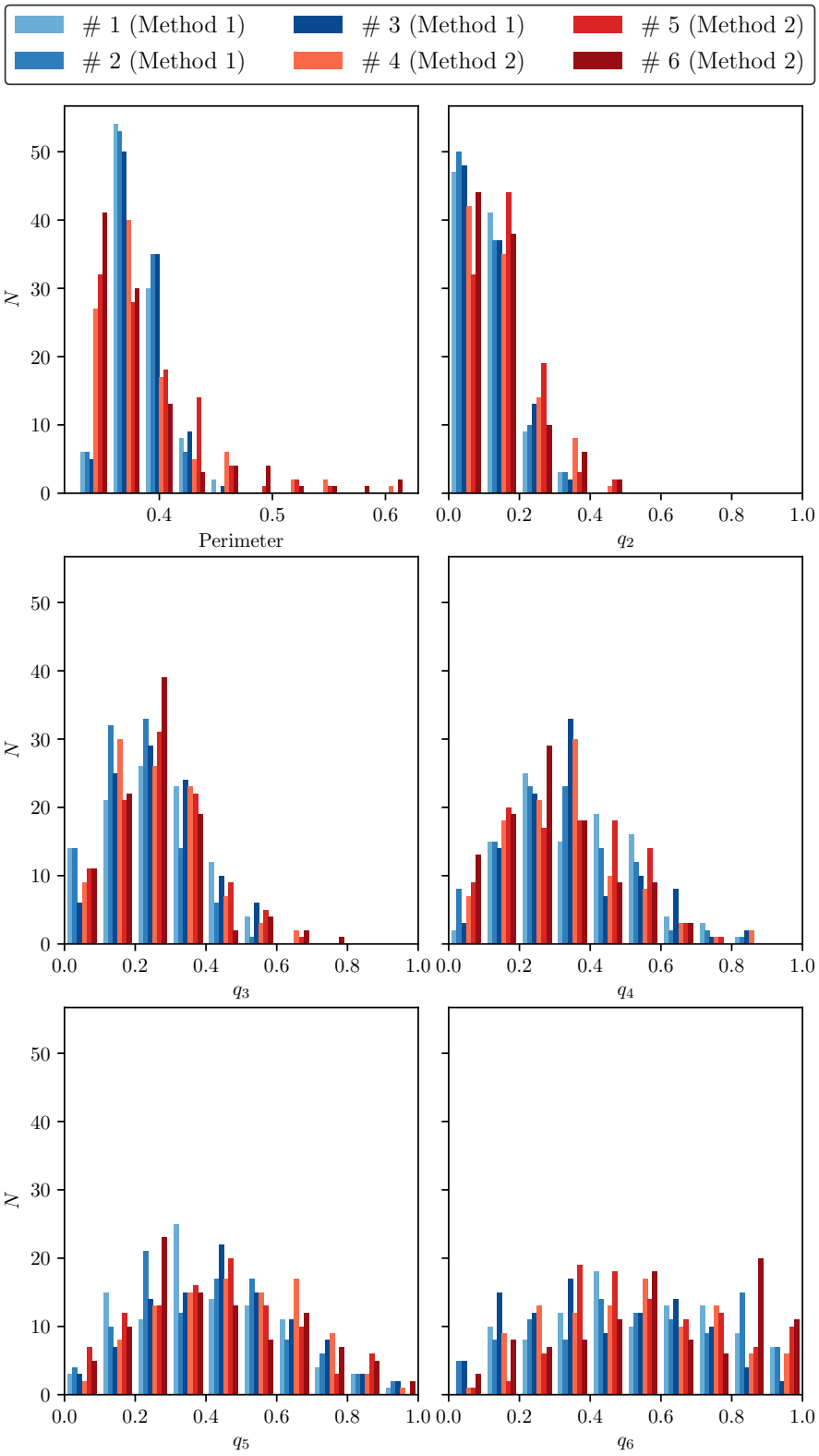

Figure 7.49: Histograms of the perimeter and Minkowski structure metrics, q_2, q_3, q_4, q_5 and q_6, for three random samples generated with the "self-calibrating" multi-temperature isokinetic scheme (Method 1) and three samples generated using the multi-temperature isokinetic scheme with a low fixed number of equilibration iterations (Method 2), all containing 100 Disks at a volume fraction of 0.7.

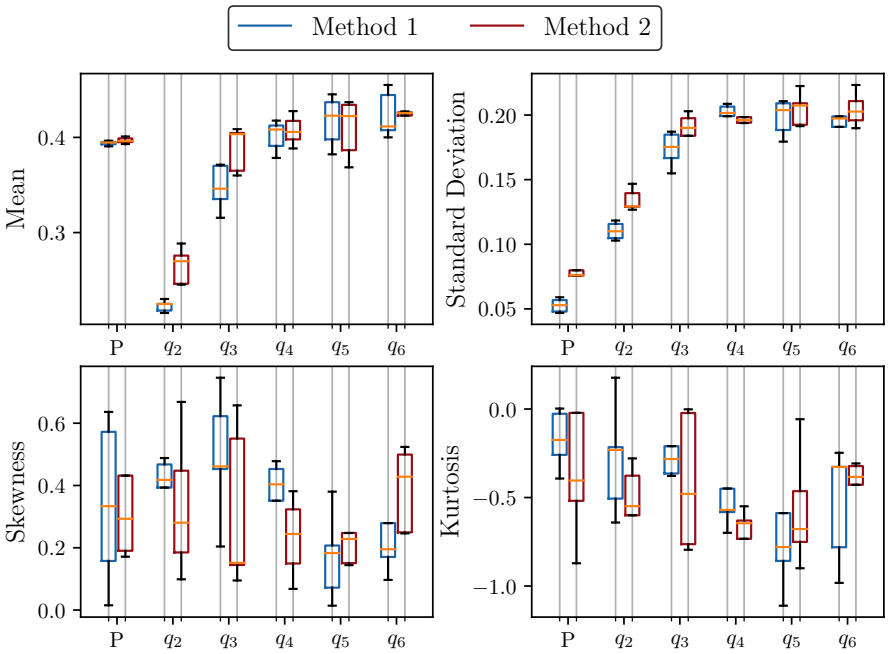

Figure 7.50: Boxplots of the mean, standard deviation, skewness and kurtosis of the perimeter, P, and Minkowski structure metrics, q_2, q_3, q_4, q_5 and q_6 of the Voronoi cells, for five random samples generated with the "self-calibrating" multi-temperature isokinetic scheme (Method 1) and three samples generated using the multi-temperature isokinetic scheme with a low fixed number of equilibration iterations (Method 2), all containing 100 Disks at a volume fraction of 0.3.

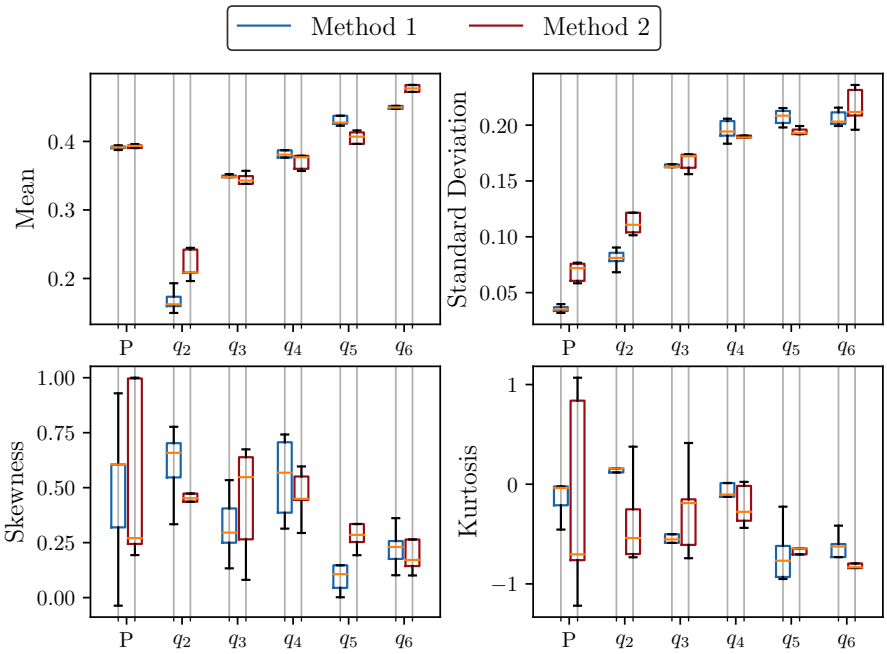

Figure 7.51: Boxplots of the mean, standard deviation, skewness and kurtosis of the perimeter, P, and Minkowski structure metrics, q_2, q_3, q_4, q_5 and q_6 of the Voronoi cells, for five random samples generated with the "self-calibrating" multi-temperature isokinetic scheme (Method 1) and three samples generated using the multi-temperature isokinetic scheme with a low fixed number of equilibration iterations (Method 2), all containing 100 Disks at a volume fraction of 0.5.

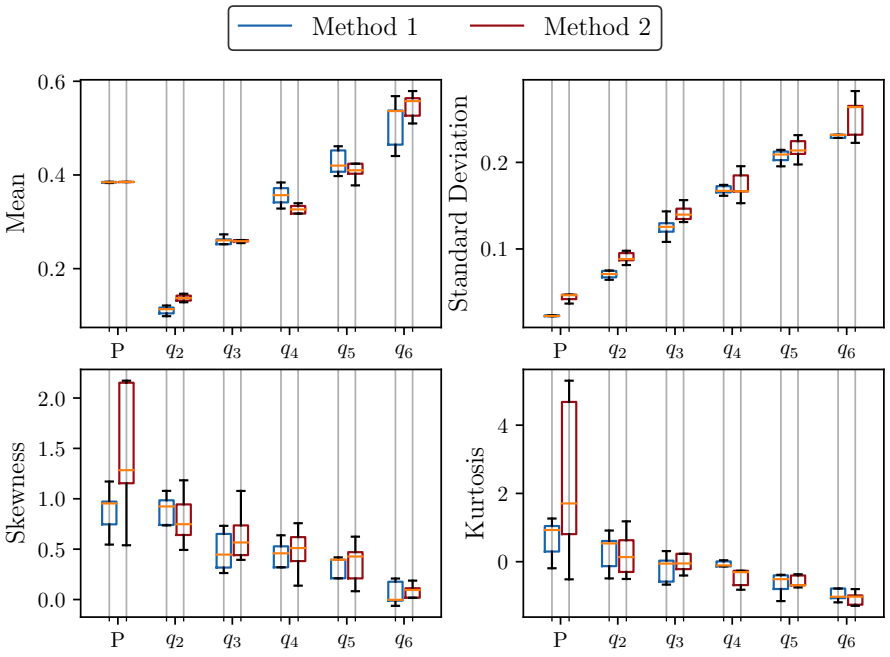

Figure 7.52: Boxplots of the mean, standard deviation, skewness and kurtosis of the perimeter, P, and Minkowski structure metrics, q_2, q_3, q_4, q_5 and q_6 of the Voronoi cells, for five random samples generated with the "self-calibrating" multi-temperature isokinetic scheme (Method 1) and three samples generated using the multi-temperature isokinetic scheme with a low fixed number of equilibration iterations (Method 2), all containing 100 Disks at a volume fraction of 0.7.

Discussion

Figures 7.36-7.41 present the typical results obtained from an analysis to a microstructure using Minkowski structure metrics. There are no clusters of Voronoi cells with high values of any Minkowski structure metric, which would indicate excess order in that region. In contrast, the microstructures presented in Figure 7.42 display a region where there is an excess of Voronoi cells with high values for a given Minkowski structure metric. In Figure 7.42a there are isolated strings of particles leading to elongated cells with higher q_2 than expected. The microstructure in Figure 7.42b shows a high concentration of Voronoi cells with high q_3 in its top right region, due to the arrangement of the Disks in an hexagonal pattern with the center particle missing. As for the microstructure depicted in Figure 7.42c, a quadrangular grid of particles is detected in the top right due to the high values of the q_4 Minkowski structure metric. Lastly, Figure 7.42d exhibits a microstructure with possibly the most common type of order at high volume fractions, crystallization in a hexagonal pattern, detected due to the high q_6 Minkowski structure metric. Thus, it is shown that a larger number of Voronoi cells with larger values of any Minkowski structure metric signals undesirable order and that a typical microstructure will not display this behavior.

To better understand the typical distribution of the Minkowski structure metrics, q_2, q_3, q_4, q_5 and q_6, for microstructures containing Disks of the same size, five random samples of microstructures containing 100 Disks at volume fractions equal to 0.3, 0.5 and 0.7 are produced. From the histograms of the perimeter and Minkowski structures metrics of the Voronoi cells for microstructures containing 100 Disks at a volume fraction of 0.3, presented in Figure 7.43, it can be ascertained that there are no glaring cases of an excessive number of cells with a high value for any Minkowski structure metric. The same can be said for the microstructures containing 100 Disks at a volume fraction of 0.5 (see Figure 7.44). However, for a volume fraction equal to 0.7, a volume fraction reasonably high, a marked difference in the histogram containing the q_6 Minkowski structure metric can be observed (see Figure 7.45). This signals that the microstructure presents crystallization in an hexagonal pattern, which is to be expected as the volume fraction is quite elevated. Also, one can observe that the q_2 Minkowski structure metric gets progressively shifted to the the left as the volume fraction increases from 0.3 to 0.5 and to 0.7. This is probably due to the fact that at higher volume fractions the distance between the particles is more uniform, i.e. the distance between the particles is mostly the same, leading to Voronoi cells that are less elongated and thus have a smaller q_2 Minkowski structure metric. Still, it must be highlighted that for the remaining Minkowski structure metrics a marked difference is not observable, suggesting that the corresponding particle arrangements are not prevalent at any of the volume fractions studied.

Looking a the histograms in Figures 7.43-7.45, it is plausible that they are generated sampling the same distribution, as they don't look too dissimilar. To test this hypothesis k-sample Anderson-Darling tests are performed. Looking at Table 7.5 it can be understood that for many volume fraction, number of particles, Minkowski structure metric combinations, the null hypothesis could not be rejected. Notwithstanding, for a sizable amount of the cases considered at least one of the tests succeeds in rejecting the null hypothesis. Moreover, when the samples of different sizes at the same volume fractions are all considered in the same test, there seems to be a tendency to reject the null hypothesis at higher rates, e.g. at the volume fraction of 0.7 the null hypothesis is rejected with a p-value smaller than 1% for all Minkowski structure metrics, except for q_5. These results do not support the conclusion that the Minkowski structure met-

rics for microstructures containing only Disks described by the same descriptors come from the same underlying distribution. Despite this, it could still be that while they do not come from the same underlying distribution, they are generated from the same family of distributions, explaining somewhat the similarity between the histograms in Figures 7.43-7.45.

Lastly, it is presented a set of results aiming to distinguish between microstructures generated using the "self-calibrating" multi-temperature isokinetic scheme (Method 1) and the multi-temperature isokinetic scheme, allowing only a small number of equilibration iterations (Method 2). Comparing Figures 7.46a, 7.46c and 7.46e with Figures 7.46b, 7.46d and 7.46f, respectively, a marked visual difference can be detected. The latter microstructures, generated through Method 2, all present clustering and, at volume fractions equal to 0.5 and 0.7, also ordered arrangements of particles. For the purpose of showing that the Minkowski structure metrics are useful tools in distinguishing between the results produced by the two methods, Figures 7.47-7.49 are generated, presenting the histograms of the perimeter and Minkowski structures metrics of the Voronoi cells of three samples generated with each method The microstructures contain 100 Disks at volume fractions equal to 0.3, 0.5 and 0.7, respectively. To better quantify the differences between the distributions, the mean, standard deviation, skewness and kurtosis of the perimeter and Minkowski structure metrics for each sample are computed and the results are presented in the form of boxplots on Figures 7.50, 7.51 and 7.52.

For the microstructures at a volume fraction equal to 0.3, the biggest difference that can be detected regarding the means of the perimeter and the Minkowski structure metrics of the Voronoi cells is in the q_2 Minkowski structure metric, which is larger for all samples generated through Method 2. This is probably a consequence of the clustering in strings of particles (see Figure 7.46b) that leads to elongated Voronoi cells with higher q_2. For the means of the other Minkowski structure metrics there is overlap between the values coming from microstructures generated using the two different methods. Regarding the standard deviations, for the perimeter and Minkowski structure metrics q_2 and q_3, the distributions of these parameters seem to be larger for the microstructures generated using Method 2. Concerning the skewness and the kurtosis, there is for the most part a big overlap for all the parameters. In general, it can be concluded that the distributions are asymmetric and skewed to the right, possessing "light-tails" when compared to a normal distribution. Thus, it can be concluded that the strongest differences between the two methods found at the volume fraction of 0.3 are in q_2 Minkowski structure metric, both in its mean and in its standard deviation, both higher for Method 2. It can also be asserted that the standard deviation of the perimeter is larger for microstructures generated with Method 2.

With respect to microstructures at a volume fraction equal to 0.5, the most marked differences are again in the mean and standard deviation of the q_2 Minkowski structure metric and the standard deviation of the perimeter of the Voronoi cells. The explanation is much the same as the one given above for microstructures at a volume fraction equal to 0.3. In addition, one can also observe that the mean for the q_6 Minkowski structure metric is distinctly higher for the microstructures generated using the Method 2. This is again due to the clustering, that because of the higher volume fraction leads now also to the formation of stronger hexagonal patterns increasing the mean of the Minkowski structure metric q_6. In general, the distributions are again skewed to the right, and more heavily so, but now the kurtosis is not as negative, implying tails comparable to a normal distribution. Therefore, one can conclude that the

strongest differences between the two methods found at the volume fraction of 0.5 are in the q_2 and q_6 Minkowski structure metrics, both in their mean and in their standard deviation, both higher for Method 2. It can also be asserted the standard deviation of the perimeter is larger for microstructures generated with Method 2.

Finally, for microstructures at a volume fraction equal to 0.7, the conclusions are the same as the ones found for volume fractions equal to 0.5, in the previous paragraph. Apart from minor differences, the only clear change to be noticed is the kurtosis of the data, that is for this case for the most part positive implying heavier tails. Despite not being clear from the statistical measures computed, it can be seen from Figure 7.49 that for the q_6 Minkowski metric the Method 2 leads to a higher number of cells containing values close to 1, strongly suggesting the presence of large arrangement of particles in undesirable hexagonal patterns.

7.2.3 Detection of anisotropy in microstructures containing Ellipses using Minkowski structure metrics

This section has the goal of providing an example where the Minkowski structure metrics and associated concepts are used to detect and characterize anisotropy.

Results

Two microstructures are generated containing 30 particles at a volume fraction equal to 0.6. The first containing Ellipses with a ratio between the major and minor axis equal to 2.5 and oriented along $\pi/4$. The second containing Disks, all of the same size. Figures 7.53a and 7.53b present the corresponding Voronoi diagrams with their cells colored according to the Minkowski structure metric q_2. Figure 7.53c presents the histogram of the Minkowski structure metric q_2 of both microstructures, and Figure 7.53d shows the histogram of the argument of the irreducible Minkowski tensor ψ_2 for both microstructures.

Discussion

From Figures 7.53a and 7.53b it is clear that the microstructure containing Ellipses presents Voronoi cells with a higher Minkowski structure metric q_2. This is confirmed by Figure 7.53c, thus affirming the ability of the Minkowski structure metric q_2 to detect anisotropy. Moreover, the argument of the corresponding irreducible Minkowski tensor ψ_2 provides a way to identify the direction of the anisotropy. From Figure 7.53d, it can be gathered that the Voronoi cells from the microstructure containing Ellipses have for the most part ψ_2s with the same argument, i.e. $-\pi/2$. From the definition of the irreducible Minkowski tensor ψ_2, in Equation (4.28), and the corresponding fundamental shape, depicted in Figure 4.8b, it can be concluded that the normal direction to the orientation of the particles is $-\pi/4$, which is the correct result. On the other hand, the arguments of the ψ_2s of the Voronoi cells from the microstructure containing Disks do not present a particular value, implying that the microstructure is isotropic. Therefore, it has been shown that the Minkowski structure metric q_2 and the corresponding irreducible Minkowski tensor ψ_2 may be useful tools in detecting and characterizing anisotropy in microstructures.

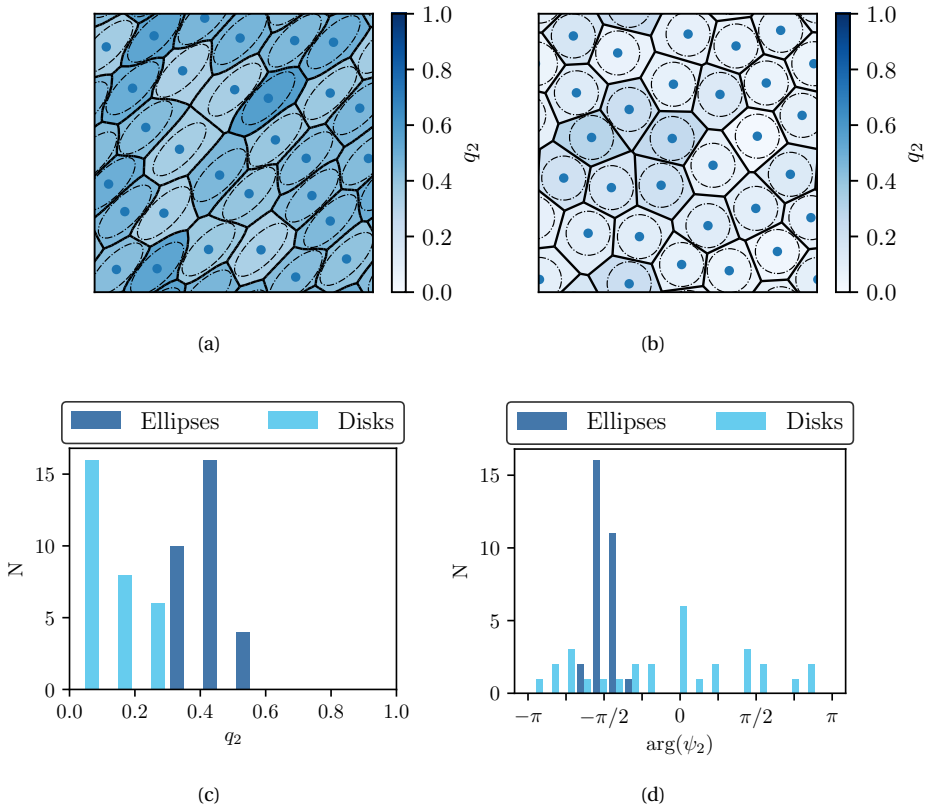

Figure 7.53: (a): Set Voronoi diagram for a microstructure containing 30 Ellipses with ratio a/b equal to 2.5 oriented along $\pi/4$ at a volume fraction of 0.6, with the Voronoi cells colored according to their Minkowski structure metric q_2. (b): Voronoi diagram for a microstructure containing 30 Disks at a volume fraction of 0.6, with the Voronoi cells colored according to their Minkowski structure metric q_2. (c): Histogram of the Minkowski structure metric q_2 of both microstructures. (d) Histogram of the argument of the irreducible Minkowski tensor ψ_2 of both microstructures.

7.2.4 Reconstruction of polyhedra and detection of s-fold symmetry

This section has the goal of showing that the Minkowski structure metrics and the associated concepts are able to provide a robust description of the shape of convex polyhedra. As stated before, this is of great importance in the analysis of microstructures, as it allows for the characterization of the Voronoi cells of the Voronoi diagrams obtained from microstructures containing only Spheres of the same size.

Results

In order to fulfill the objectives of this section, four convex polyhedra are created. They are shown in Figures 7.54a, 7.55a, 7.56a and 7.57a, and are a hexagonal prism, a tetrahedron, a cube and a thin parallelepiped, respectively. The reconstruction of the convex polyhedra approximating the curvature through spherical harmonics of degree 6

at most is presented in Figures 7.54b, 7.55b, 7.56b and 7.57b, respectively. The corresponding Minkowski structure metrics for each polygon are shown in Figures 7.54c, 7.55c, 7.56c and 7.57c.

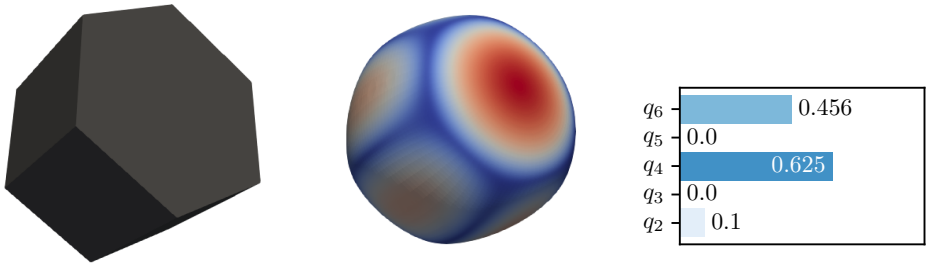

(a) (b) (c)

Figure 7.54: (a): Hexagonal prism. (b): Reconstruction found approximating the curvature through a series of spherical harmonics, where points in red represent high curvature and points in blue low curvature. (c) Minkowski structure metrics of the hexagonal prism.

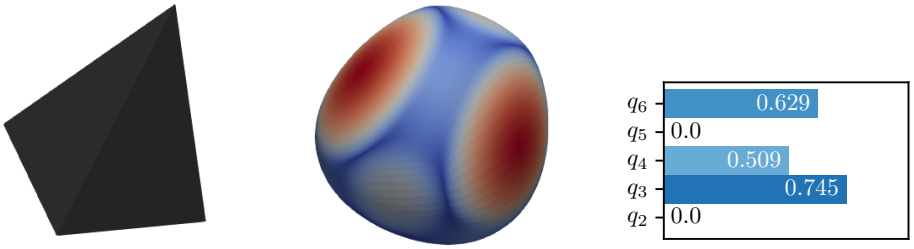

(a) (b) (c)

Figure 7.55: (a): Tetrahedron. (b): Reconstruction found approximating the curvature through a series of spherical harmonics, where points in red represent high curvature and points in blue low curvature. (c) Minkowski structure metrics of the tetrahedron.

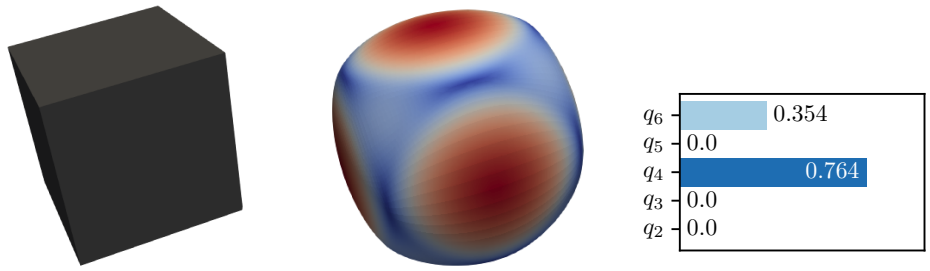

(a) (b) (c)

Figure 7.56: (a): Cube. (b): Reconstruction found approximating the curvature through a series of spherical harmonics, where points in red represent high curvature and points in blue low curvature. (c) Minkowski structure metrics of the cube.

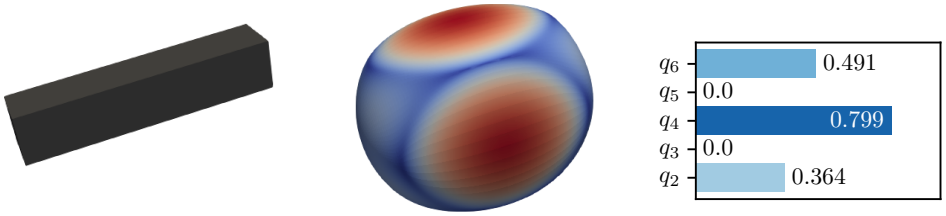

(a) (b) (c)

Figure 7.57: (a): Thin parallelepiped. (b): Reconstruction found approximating the curvature through a series of spherical harmonics, where points in red represent high curvature and points in blue low curvature. (c) Minkowski structure metrics of the thin parallelepiped.

Discussion

From Figures 7.54b, 7.55b, 7.56b and 7.57b it can be seen that the shapes of the convex polyhedra are mostly recovered. It must be kept in mind that only spherical harmonics of degree 6 at most are used to produce these shapes.

The Minkowski structure metrics presented in Figure 7.54c, corresponding to the hexagonal prism, signal the presence of 4-fold and 6-fold symmetry, as expected. As for the tetrahedron, the highest Minkowski structure metric is q_3, as shown in Figure 7.55c, which is also expected. Likewise, Figure 7.56c signals strongly the presence of 4-fold symmetry for the cube. Comparing the Minkowski structure metrics computed for the thin paralleliped, presented in Figure 7.57c, with the ones just mentioned computed for the cube, one can observe a strong increase in the q_2 due to the elongated form of the polyhedron. For the q_2 to signal more strongly 2-fold symmetry, the parallelipiped would have to be even thinner. Nonetheless, a marked difference between its Minkowski structure metrics and the ones obtained for the cube can be detected.

Therefore, it can be inferred that the Minkowski structures metrics are able to represent robustly the shapes of the Voronoi cells of microstructures containing only Spheres of the same size.

7.2.5 Quality analysis of microstructures containing Spheres of the same size using Minkowski structure metrics

The results in this section have as a goal to show the capability of the Minkowski structure metrics to characterize the Voronoi cells of microstructures containing only Spheres of the same size and validate the microstructures generated using the proposed approach as it pertains to their quality.

Results

Figures 7.58-7.63 present typical results obtained from an analysis to a microstructure using Minkowski structure metrics, i.e. the Voronoi diagram with the cells colored according to the value of the corresponding Minkowski structure metric and the respective histogram of the Minkowski structure metrics. The microstructure contains 100 Spheres at a volume fraction equal to 0.4. Examples of pathological microstructures with excess order can be found in Figure 7.64.

To understand the typical distribution of the Minkowski structure metrics, q_2, q_3, q_4, q_5 and q_6, for microstructures containing Spheres of the same size and to validate the generation method concerning the quality of the microstructures, five random samples of microstructures containing 100 Spheres at volume fractions equal to 0.1, 0.3 and 0.5 are produced. The histograms of the surface area and Minkowski structures metrics of their Voronoi cells is presented in Figure 7.65-7.67.

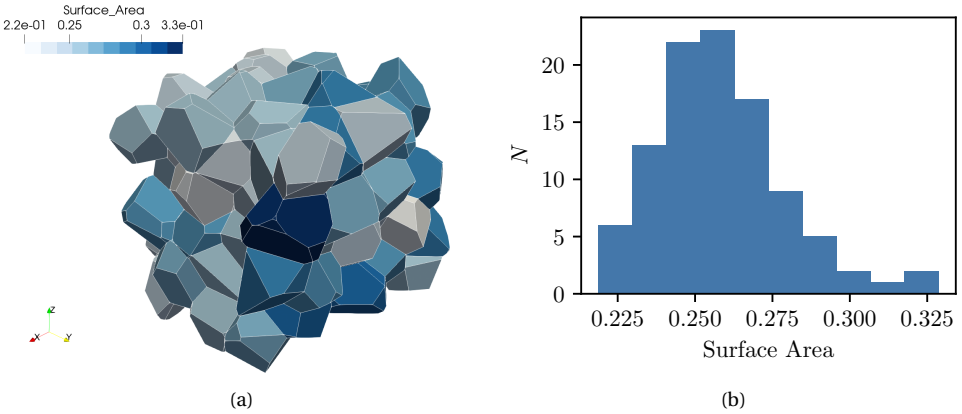

(a) (b)

Figure 7.58: (a) Voronoi diagram of a microstructure containing 100 Spheres at a volume fraction equal to 0.4, with the cells colored according to their surface area. (b) Histogram containing the surface area of the Voronoi cells.

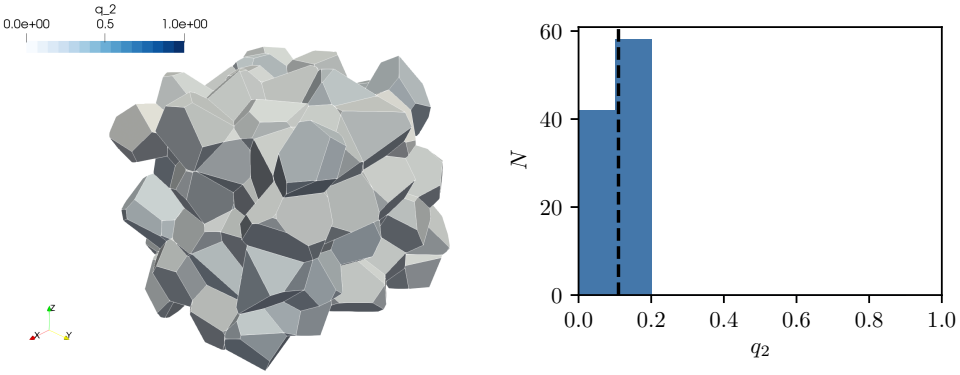

(a) (b)

Figure 7.59: (a) Voronoi diagram of a microstructure containing 100 Spheres at a volume fraction equal to 0.4, with the cells colored according to their q_2 Minkowski metric. (b) Histogram containing the q_2 Minkowski metric of the Voronoi cells, where the dashed line represents the average.

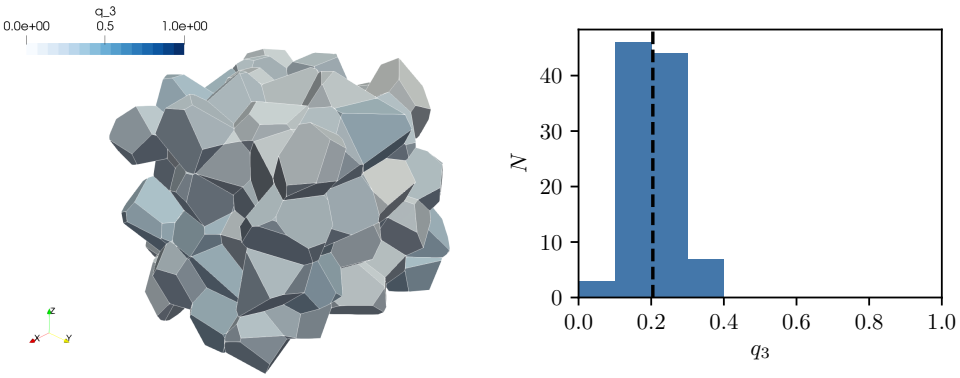

(a) (b)

Figure 7.60: (a) Voronoi diagram of a microstructure containing 100 Spheres at a volume fraction equal to 0.4, with the cells colored according to their q_3 Minkowski metric. (b) Histogram containing the q_3 Minkowski metric of the Voronoi cells, where the dashed line represents the average.

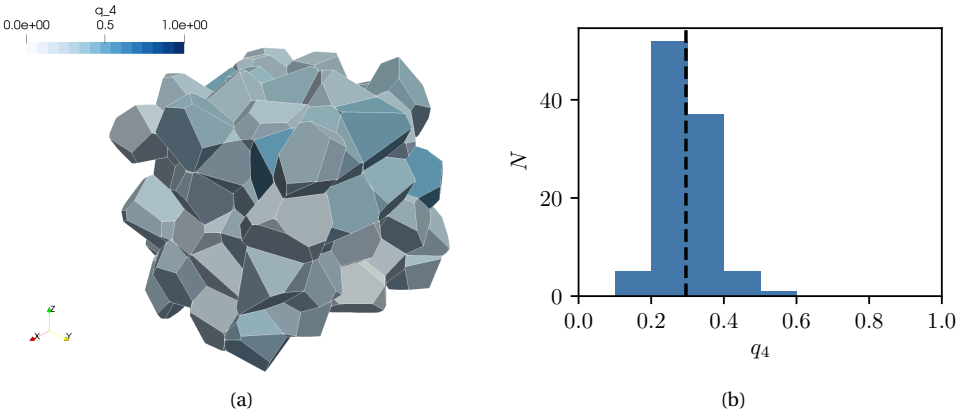

(a) (b)

Figure 7.61: (a) Voronoi diagram of a microstructure containing 100 Spheres at a volume fraction equal to 0.4, with the cells colored according to their q_4 Minkowski metric. (b) Histogram containing the q_4 Minkowski metric of the Voronoi cells, where the dashed line represents the average.

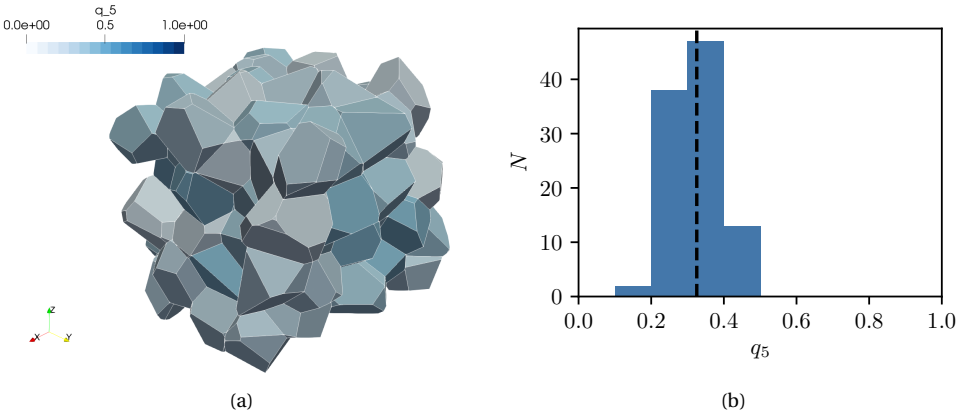

(a) (b)

Figure 7.62: (a) Voronoi diagram of a microstructure containing 100 Spheres at a volume fraction equal to 0.4, with the cells colored according to their q_5 Minkowski metric. (b) Histogram containing the q_5 Minkowski metric of the Voronoi cells, where the dashed line represents the average.

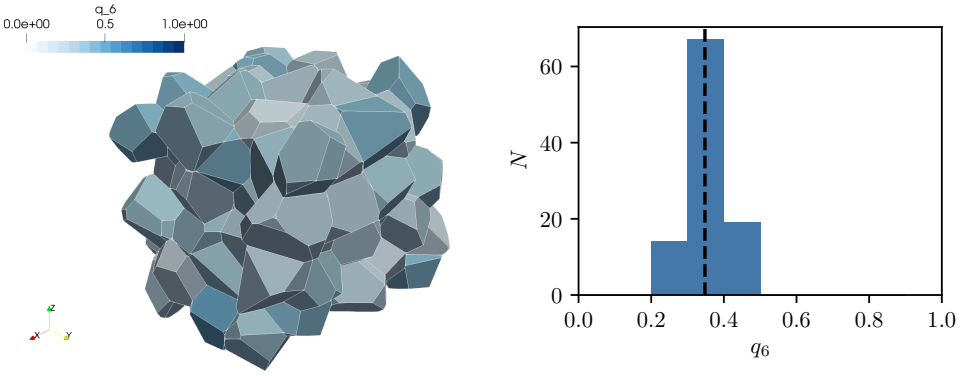

(a) (b)

Figure 7.63: (a) Voronoi diagram of a microstructure containing 100 Spheres at a volume fraction equal to 0.4, with the cells colored according to their q_6 Minkowski metric. (b) Histogram containing the q_6 Minkowski metric of the Voronoi cells, where the dashed line represents the average.

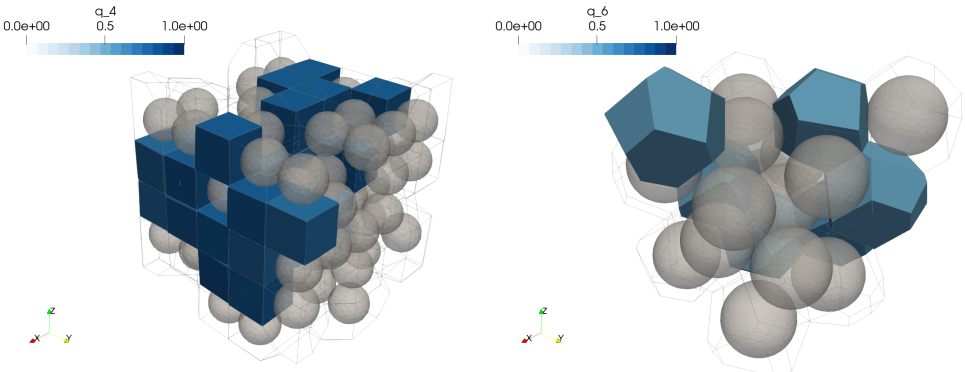

(a) (b)

Figure 7.64: (a): Voronoi diagram of a microstructure containing Spheres arranged in a cubic grid with random vertices missing. Only the cells with Minkowski structure metric q_4 higher than 0.7 are shown. (b): Voronoi diagram of a microstructure containing Spheres at a volume fraction of 0.7. Only the cells with Minkowski structure metric q_6 higher than are 0.5 shown.

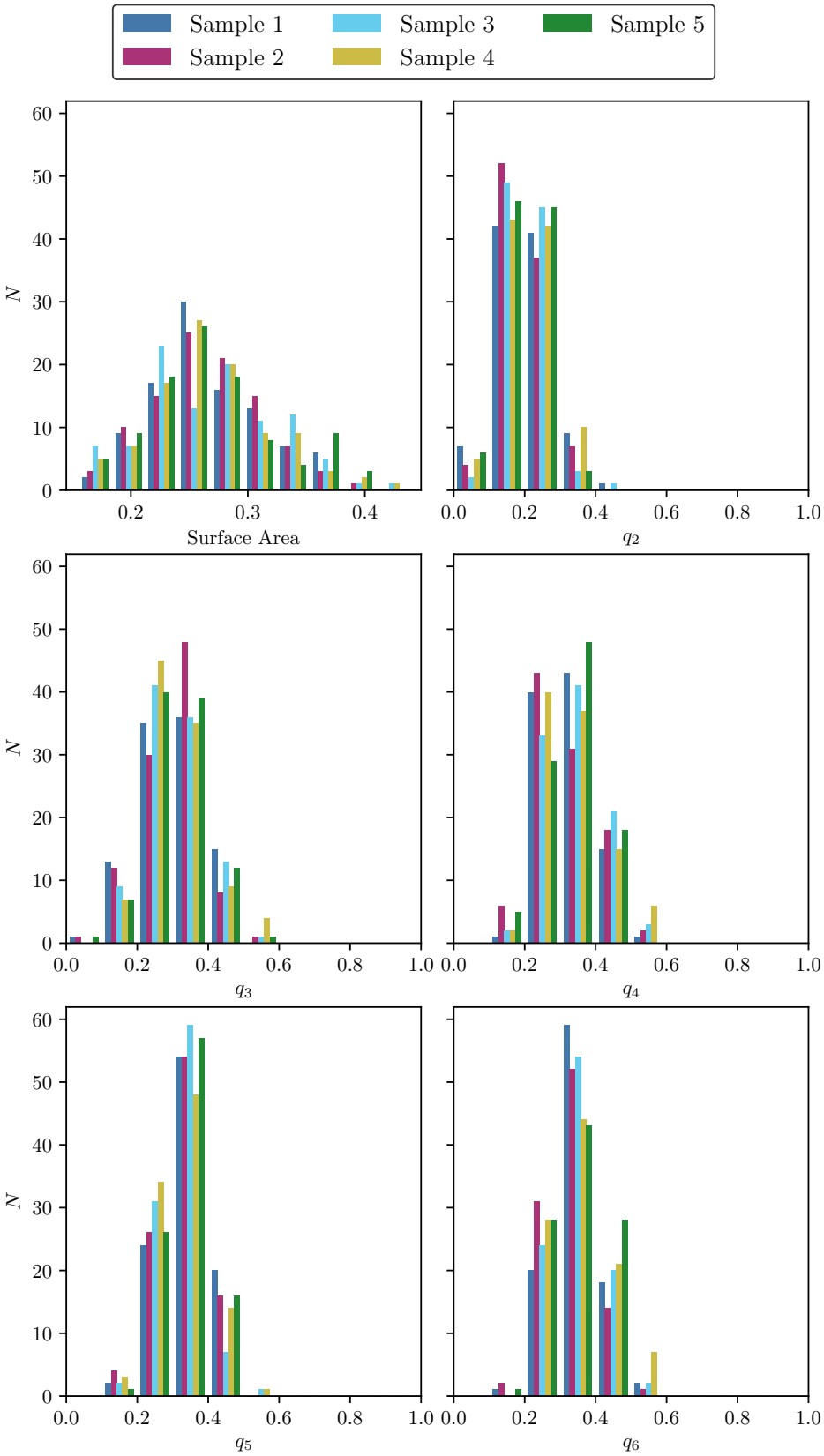

Figure 7.65: Histograms of the surface area and Minkowski structure metrics, q_2, q_3, q_4, q_5 and q_6, for five random samples containing 100 Spheres at a volume fraction of 0.1.

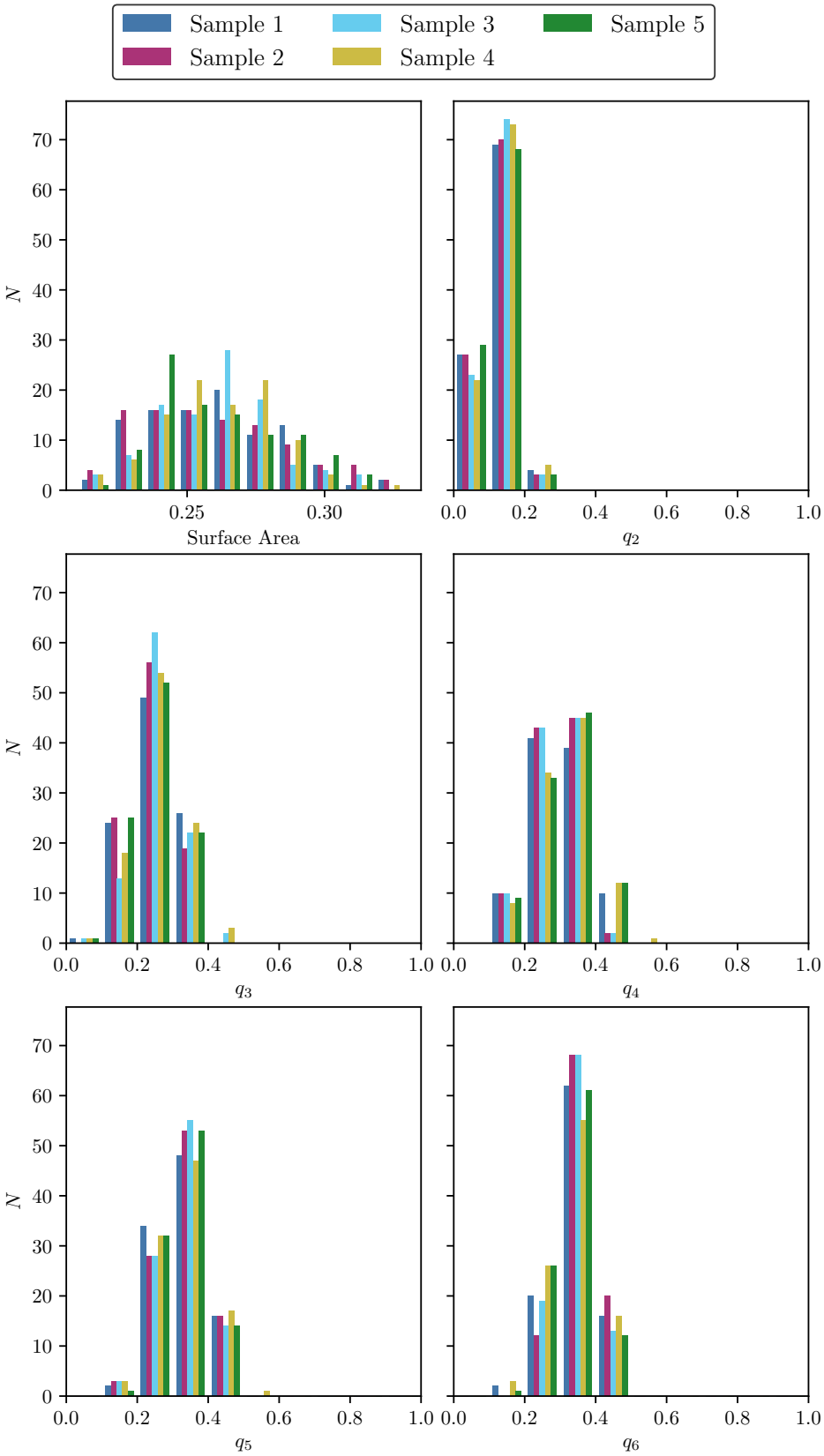

Figure 7.66: Histograms of the surface area and Minkowski structure metrics, q_2, q_3, q_4, q_5 and q_6, for five random samples containing 100 Spheres at a volume fraction of 0.3.

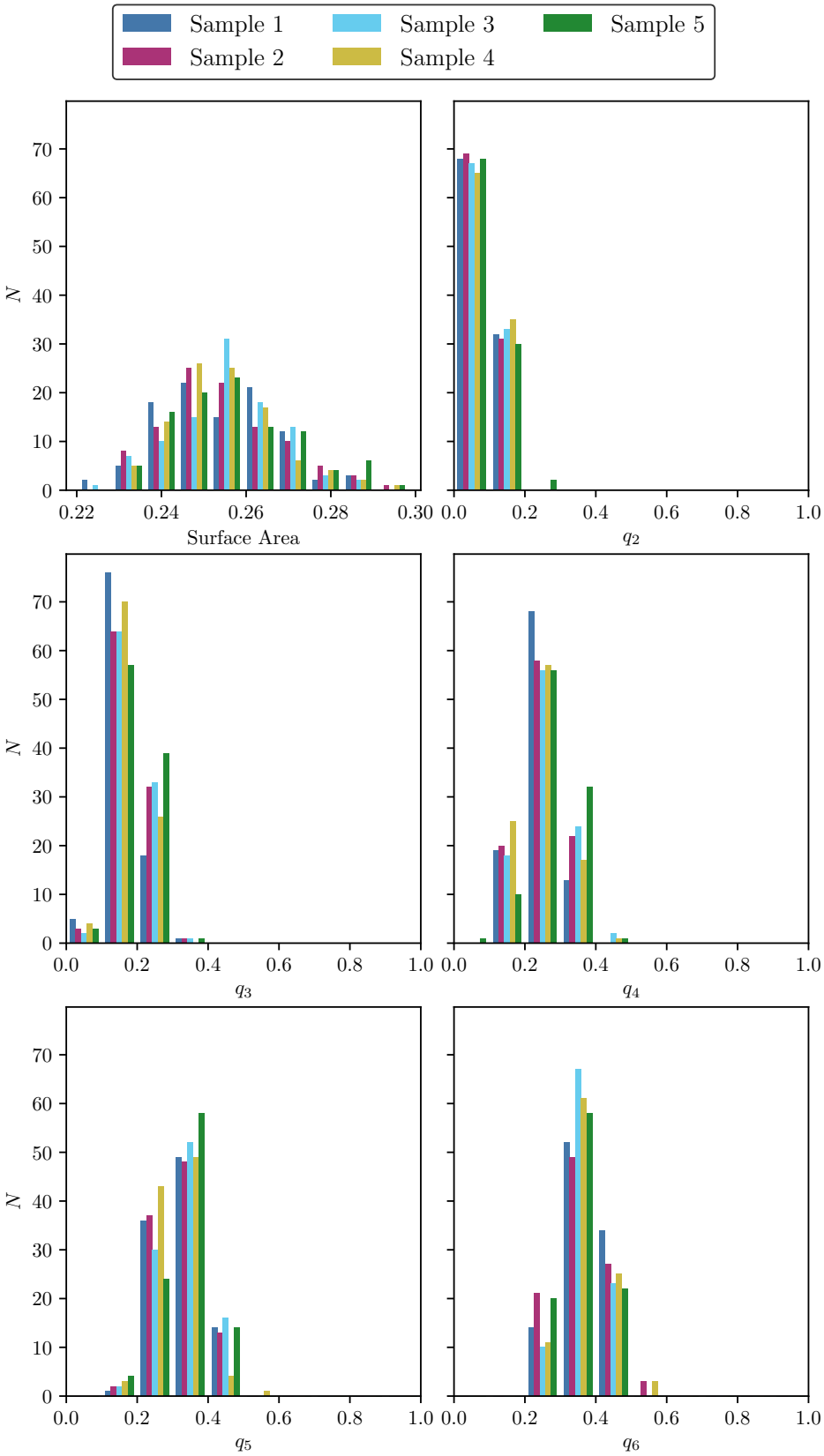

Figure 7.67: Histograms of the surface area and Minkowski structure metrics, q_2, q_3, q_4, q_5 and q_6, for five random samples containing 100 Spheres at a volume fraction of 0.5.

Discussion

Figures 7.58-7.63 present the typical results obtained from an analysis to a microstructure using Minkowski structure metrics. There are no clusters of Voronoi cells with high values of any Minkowski structure metric, which would indicate excess order in that region. Contrast this with the microstructures presented in Figure 7.64. Figure 7.64a presents a clearly undesirable microstructure obtained by removing random points from a cubic grid. As expected, the Minkowski structure metric q_4 flags very strongly this arrangement. As for the microstructure presented in Figure 7.64b containing 20 Spheres at the high volume fraction of 0.7, it would be expected that crystallization with 6-fold symmetry would occur. The Minkowski structure metric q_6 is higher than 0.5 for 6 particles, that is more than 25% of all the particles in the microstructure. Still these values of q_6 do not go over 0.6. In fact, from all the microstructures generated during this work, it was never registered a Voronoi cell with a q_6 higher than 0.6. Looking at the results of the previous section, none of the polyhedra analyzed produces results over 0.6 for q_6, except for the tetrahedron, with a value slightly higher. Thus, it may be that a value q_6 equal to 0.6 should be considered high for the purpose of interpreting the results, as it pertains to the detection of undesirable 6-fold order in the microstructure. This is the approach taken in the next paragraphs.

To better understand the typical distribution of the Minkowski structure metrics, q_2, q_3, q_4, q_5 and q_6, for microstructures containing Spheres of the same size and to validate the microstructure generation method, as it relates to the quality of the microstructures produced, five random samples of microstructures containing 100 Disks at volume fractions equal to 0.1, 0.3 and 0.5 are produced. From the histograms of the surface area and Minkowski structures metrics of the Voronoi cells for all sets of microstructures considered, it can be ascertained there is are no glaring cases of an excessive number of cells with a high value for any Minkowski structure metric.

Comparing the results for the different volume fractions, one can observe that the q_2 Minkowski structure metric gets progressively shifted to the the left as the volume fraction increases from 0.1 to 0.3 and to 0.5. This is probably due to the fact that at higher volume fractions the distance between the particles is more uniform, i.e. the distance between the particles is mostly the same, leading to Voronoi cells that are less elongated and thus have a smaller q_2 Minkowski structure metric. Still, it must be highlighted that for the remaining Minkowski structure metrics a marked difference is not observable, suggesting that the difference between these volume fractions regarding the relative position of the particles is not pronounced.

7.3 Multi-scale analyses based on computational homogenization

This section presents a set of results concerning multi-scale analyses based on computational homogenization. Its goal is to understand the relation between the number of particles included in the RVE and its representativity. The number of particles needed to achieve isotropy is also considered in the following sections.

For an RVE to be representative, the response of the material must be independent of the choice of boundary conditions imposed (Saeb et al., 2016). According to Hill (1963), an RVE is well defined when it contains a sufficient number of inclusions and the responses under linear displacement and constant traction boundary conditions coincide. It has also been shown that in pure mechanical linear problems, the effective behavior derived under periodic boundary conditions is bounded by linear displacement boundary conditions from above and constant traction boundary conditions from below for a finite size of the RVE (Saeb et al., 2016). Despite the results obtained under periodic boundary conditions not always being the closest ones to the exact solutions, they provide reasonable estimates for the mechanical behavior, in the sense that they are always bounded by the other boundary conditions (Saeb et al., 2016). Thus, they are used to gauge what is the influence of the number of particles included in the RVE, as it relates to isotropy.

With this in view, microstructures with different number of phases and types of particles are generated containing an increasing number of particles at the same volume fraction. These are submitted to various loading schemes and the first Piola-Kirchhoff stress tensor is obtained, using linear, periodic and uniform traction boundary conditions. All materials are considered elastic and follow the so-called Henky constitutive model.

7.3.1 One phase containing Disks with same radius

This section presents the results concerning microstructures containing only Disks of the same size belonging to a single phase. The sides of the RVE are unitary, the volume fraction is fixed at 0.3 and samples with n, particles are created, with n given by

$$n = \texttt{round}(10^k) \quad \text{for } k = 0.5, 0.75, 1, \ldots, 3. \tag{7.1}$$

To perform the multi-scale analyses based on computational homogenization simulations, the microstructure is discretized in a nonconform TRI6 mesh. The materials considered are for Phase 1, corresponding to the matrix, $E = 100\,\text{MPa}$ and $\nu = 0.3$, and for Phase 2, the phase containing the Disks, $E = 500\,\text{MPa}$ and $\nu = 0.3$. Assuming a plain strain condition, three different deformation gradients are imposed, characterizing an uniaxial loading along xx, an uniaxial loading along yy and a simple shear across xy defined as

$$\text{Uniaxial along } xx: \quad \boldsymbol{F} = \begin{bmatrix} 1.1 & 0 \\ 0 & 1.0 \end{bmatrix}, \tag{7.2}$$

$$\text{Uniaxial along } yy: \quad \boldsymbol{F} = \begin{bmatrix} 1.0 & 0 \\ 0 & 1.1 \end{bmatrix}, \tag{7.3}$$

$$\text{Simple shear across } xy: \quad \boldsymbol{F} = \begin{bmatrix} 1.0 & 0.3 \\ 0 & 1.0 \end{bmatrix}, \tag{7.4}$$

respectively.

Results

Figure 7.68 presents examples of the RVEs considered, including in Figures 7.68a and 7.68b the TRI6 nonconform mesh.

The homogenized first Piola-Kirchhoff stress for various loading schemes as a function of the number of particles is presented in Figure 7.69. The results for uniaxial traction along xx are shown in Figure 7.69a, for uniaxial traction along yy in Figure 7.69b and for simple shear across xy in Figure 7.69c. To ease the interpretation of these results as it relates to the representativity of the RVE, they are presented in Tables 7.6-7.8, including the relative variation between the boundary conditions considered. In the same vein, Table 7.9 presents the same results only for the periodic boundary condition and the uniaxial loading conditions with the goal of helping to reach conclusions about the isotropy of the RVEs.

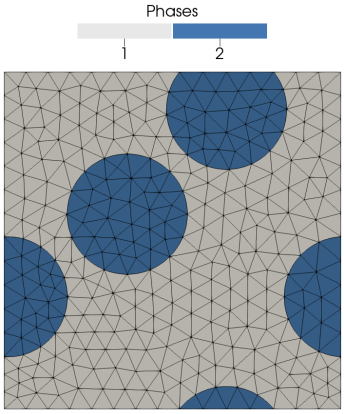

(a) $n = 3$

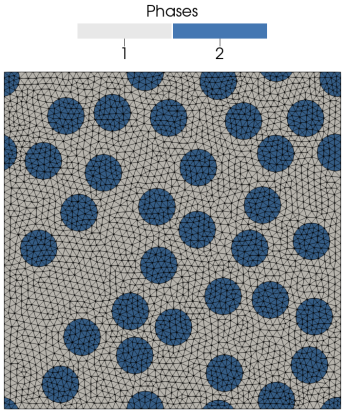

(b) $n = 32$

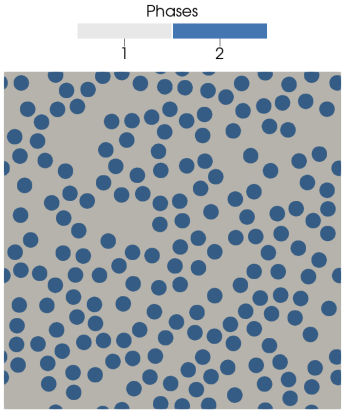

(c) $n = 178$

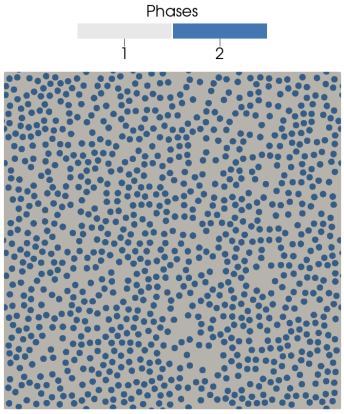

(d) $n = 1000$

Figure 7.68: Microstructures containing (a): 3, (b): 32, (c):178 and (d):1000 Disks of the same size belonging to the same phase at a volume fraction equal to 0.3. The TRI6 nonconform mesh is only represented for (a) and (b) (only the vertex nodes shown).

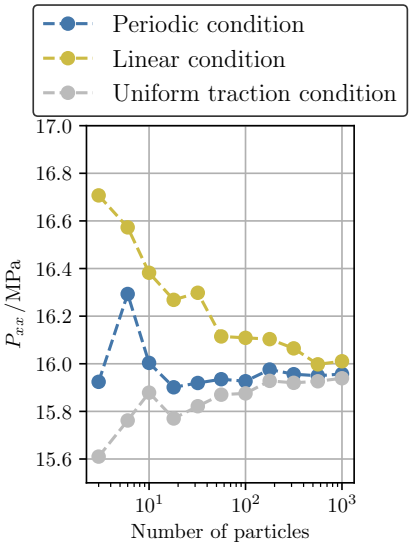

(a) Uniaxial traction along xx

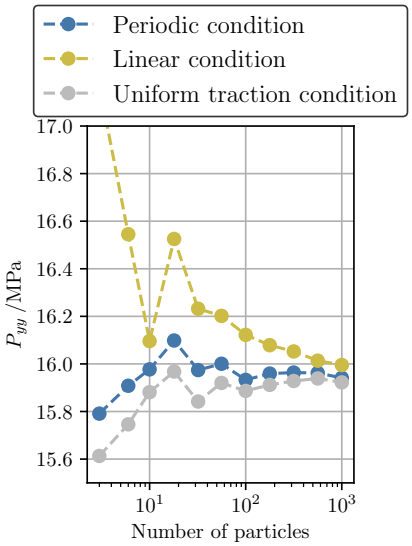

(b) Uniaxial traction along yy

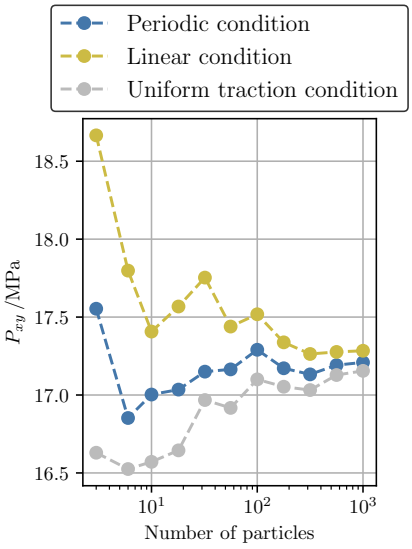

(c) Simple shear across xy

Figure 7.69: Homogenized first Piola-Kirchhoff stress for various loading schemes ((a): uniaxial traction along xx - P_{xx}, (b): uniaxial traction along yy - P_{yy}, (c): simple shear across xy - P_{xy}) as a function of the number of particles, for microstructures containing only Disks of the same size at a volume fraction equal to 0.3 belonging to the same phase.

Table 7.6: Homogenized first Piola-Kirchhoff component P_{xx} under uniaxial loading condition along xx for linear, periodic, and uniform traction boundary conditions as a function of the number of particles, for microstructures containing only Disks of the same size at a volume fraction equal to 0.3 belonging to the same phase. The relative variation with reference to the periodic boundary is also presented as $\varepsilon_{\text{Periodic}}$.

Number of Particles	Linear condition		Periodic condition	U. Traction condition	
	P_{xx} /MPa	$\varepsilon_{\text{Periodic}}$ /%	P_{xx} /MPa	P_{xx} /MPa	$\varepsilon_{\text{Periodic}}$ /%
3	16.71	4.92	15.92	15.61	−1.97
6	16.57	1.72	16.29	15.76	−3.26
10	16.38	2.37	16.00	15.88	−0.78
18	16.27	2.31	15.90	15.77	−0.82
32	16.30	2.38	15.92	15.82	−0.61
56	16.11	1.13	15.94	15.87	−0.41
100	16.11	1.14	15.93	15.88	−0.32
178	16.10	0.80	15.98	15.93	−0.30
316	16.06	0.68	15.96	15.92	−0.23
562	16.00	0.30	15.95	15.93	−0.15
1000	16.01	0.34	15.96	15.94	−0.11

Table 7.7: Homogenized first Piola-Kirchhoff component P_{yy} under uniaxial loading condition along yy for linear, periodic, and uniform traction boundary conditions as a function of the number of particles, for microstructures containing only Disks of the same size at a volume fraction equal to 0.3 belonging to the same phase. The relative variation with reference to the periodic boundary is also presented as $\varepsilon_{\text{Periodic}}$.

Number of Particles	Linear condition		Periodic condition	U. Traction condition	
	P_{yy} /MPa	$\varepsilon_{\text{Periodic}}$ /%	P_{yy} /MPa	P_{yy} /MPa	$\varepsilon_{\text{Periodic}}$ /%
3	17.17	8.74	15.79	15.61	−1.13
6	16.55	4.00	15.91	15.75	−1.02
10	16.10	0.74	15.98	15.88	−0.60
18	16.53	2.65	16.10	15.97	−0.81
32	16.23	1.61	15.97	15.84	−0.83
56	16.20	1.26	16.00	15.92	−0.50
100	16.12	1.19	15.93	15.89	−0.29
178	16.08	0.75	15.96	15.91	−0.30
316	16.05	0.56	15.96	15.93	−0.22
562	16.01	0.32	15.96	15.94	−0.14
1000	16.00	0.34	15.94	15.92	−0.12

Table 7.8: Homogenized first Piola-Kirchhoff component P_{xy} under simple shear across xy for linear, periodic, and uniform traction boundary conditions as a function of the number of particles, for microstructures containing only Disks of the same size at a volume fraction equal to 0.3 belonging to the same phase. The relative variation with reference to the periodic boundary is also presented as $\varepsilon_{\text{Periodic}}$.

Number of Particles	Linear condition		Periodic condition	U. Traction condition	
	P_{xy} /MPa	$\varepsilon_{\text{Periodic}}$ /%	P_{xy} /MPa	P_{xy} /MPa	$\varepsilon_{\text{Periodic}}$ /%
3	18.67	6.34	17.55	16.63	−5.26
6	17.80	5.61	16.85	16.53	−1.94
10	17.41	2.38	17.00	16.57	−2.54
18	17.57	3.13	17.03	16.64	−2.29
32	17.75	3.52	17.15	16.97	−1.06
56	17.44	1.60	17.16	16.92	−1.44
100	17.52	1.32	17.29	17.10	−1.10
178	17.34	0.97	17.17	17.05	−0.69
316	17.26	0.76	17.13	17.03	−0.59
562	17.28	0.49	17.19	17.13	−0.37
1000	17.28	0.43	17.21	17.15	−0.32

Table 7.9: Homogenized first Piola-Kirchhoff component P_{xx} and P_{yy} under uniaxial loading condition along xx and yy, respectively, for periodic boundary conditions as a function of the number of particles, for microstructures containing only Disks of the same size at a volume fraction equal to 0.3 belonging to the same phase. The relative variation with reference to the homogenized first Piola-Kirchhoff component P_{xx} under uniaxial loading condition along xx is also presented as ε_{xx}.

Number of Particles	Uniaxial traction along y		Uniaxial traction along x
	P_{yy} /MPa	ε_{xx} /%	P_{xx} /MPa
3	15.79	0.84	15.92
6	15.91	2.36	16.29
10	15.98	0.17	16.00
18	16.10	−1.24	15.90
32	15.97	−0.34	15.92
56	16.00	−0.41	15.94
100	15.93	−0.04	15.93
178	15.96	0.10	15.98
316	15.96	−0.05	15.96
562	15.96	−0.08	15.95
1000	15.94	0.10	15.96

Discussion

The results presented in Figure 7.69 regarding the stiffness of the response as a function of the boundary condition used are as expected, with the linear boundary condition leading to a stiffer behavior, the uniform boundary traction leading to a more flexible behavior and the periodic boundary condition corresponding to an intermediate response. This can be confirmed from the sign of the relative variations in Tables 7.6, 7.7 and 7.8.

Regarding the representativity of the RVE, an increasing number of particles leads to a more representative RVE, as can be inferred from the decreasing difference between the corresponding homogenized first Piola-Kirchhoff components. For the two uniaxial loading schemes considered, the RVE containing a 1000 particles leads to relative differences between the boundary conditions of well below half a percent. The results are slightly higher for the simple shear across xy, but of the same magnitude.

Concerning isotropy, it can be gathered from Table 7.9 that for all numbers of particles considered the relative variation between the homogenized Piola-Kirchhoff P_{xx} in the uniaxial traction along xx and the homogenized Piola-Kirchhoff P_{yy} in the uniaxial traction along yy is below 2.5% with a sligth tendency to decrease with an increase in the number of particles included in the RVE.

7.3.2 Three phases containing Disks with different radii

This section presents the results concerning microstructures containing three different particle phases. Each phase contains n Disks of the same size, with n given by

$$n = \texttt{round}(10^k/3) \quad \text{for } k = 0.5, 0.75, 1, \ldots, 3. \tag{7.5}$$

Considering a unitary RVE, for Phase 2 the volume fraction is fixed at 0.1, for Phase 3 at 0.05 and for Phase 4 at 0.15. To perform the multi-scale analyses based on computational homogenization simulations, the microstructure is discretized in a nonconform TRI6 mesh. The materials considered are for Phase 1, corresponding to the matrix, $E = 100\,\text{MPa}$ and $\nu = 0.3$, for Phase 2, $E = 700\,\text{MPa}$ and $\nu = 0.3$, for Phase 3, $E = 500\,\text{MPa}$ and $\nu = 0.3$ and for Phase 4, $E = 300\,\text{MPa}$ and $\nu = 0.3$. Assuming a plain strain condition, three different deformation gradients are imposed, characterizing an uniaxial loading along xx, an uniaxial loading along yy and a simple shear across xy defined as

$$\text{Uniaxial along } xx: \quad \boldsymbol{F} = \begin{bmatrix} 1.1 & 0 \\ 0 & 1.0 \end{bmatrix}, \tag{7.6}$$

$$\text{Uniaxial along } yy: \quad \boldsymbol{F} = \begin{bmatrix} 1.0 & 0 \\ 0 & 1.1 \end{bmatrix}, \tag{7.7}$$

$$\text{Simple shear across } xy: \quad \boldsymbol{F} = \begin{bmatrix} 1.0 & 0.3 \\ 0 & 1.0 \end{bmatrix}, \tag{7.8}$$

respectively.

Results

Figure 7.70 presents examples of the RVEs considered, including in Figures 7.70a and 7.70b the TRI6 nonconform mesh.

The homogenized first Piola-Kirchhoff stress for various loading schemes as a function of the number of particles is presented in Figure 7.71. The results for uniaxial traction along xx are shown in Figure 7.71a, for uniaxial traction along yy in Figure 7.71b and for simple shear across xy in Figure 7.71c. To ease the interpretation of these results as it relates to the representativity of the RVE, they are presented in Tables 7.10-7.12, including the relative variation between the boundary conditions considered. In the same vein, Table 7.13 presents the same results only for the periodic boundary condition and the uniaxial loading conditions with the goal of helping to reach conclusions about the isotropy of the RVEs.

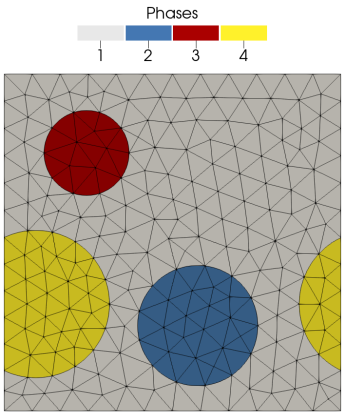

(a) $n = 3$

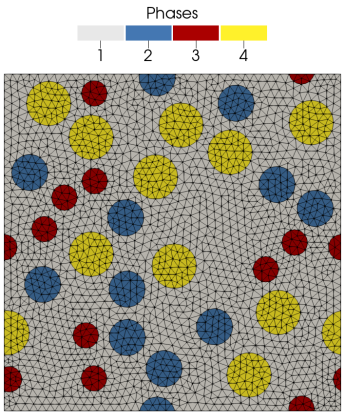

(b) $n = 32$

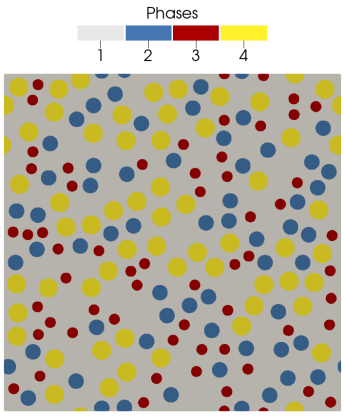

(c) $n = 178$

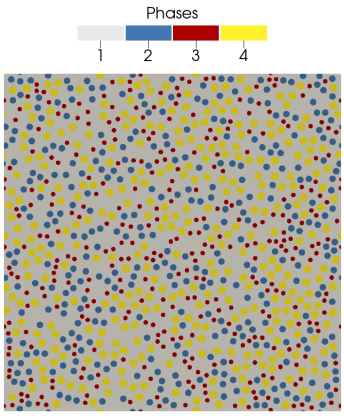

(d) $n = 1000$

Figure 7.70: Microstructures containing (a): 3, (b): 32, (c):178 and (d):1000 Disks of the same size belonging to the three different phases (Phase 2: vf = 0.1, Phase 3: vf = 0.05, Phase 4: vf = 0.15). The TRI6 nonconform mesh is only represented for (a) and (b) (only the vertex nodes shown).

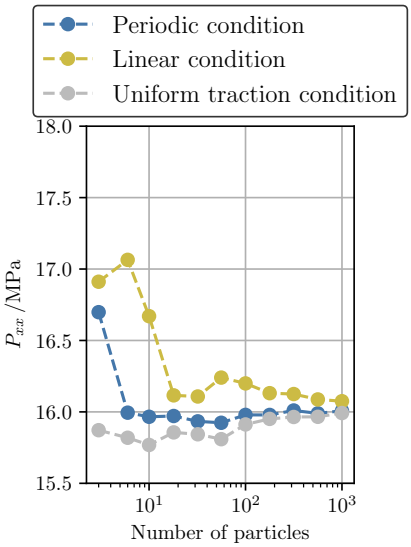

(a) Uniaxial traction along xx

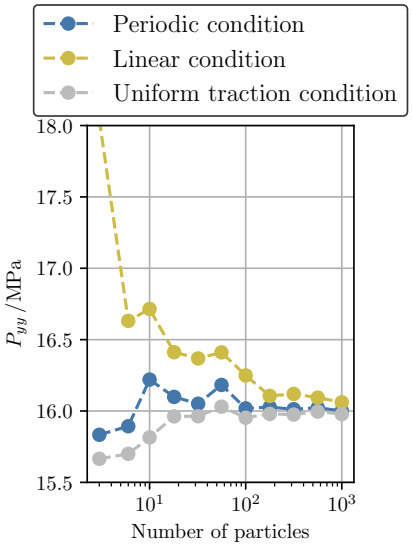

(b) Uniaxial traction along yy

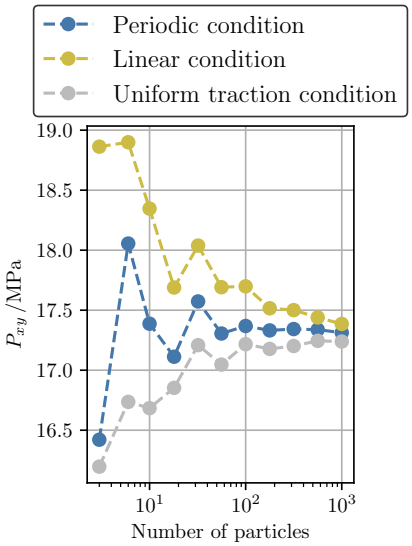

(c) Simple shear across xy

Figure 7.71: Homogenized first Piola-Kirchhoff stress for various loading schemes ((a): uniaxial traction along xx - P_{xx}, (b): uniaxial traction along yy - P_{yy}, (c): simple shear across xy - P_{xy}) as a function of the number of particles, for microstructures containing Disks of the same size belonging to the three different phases (Phase 2: vf = 0.1, Phase 3: vf = 0.05, Phase 4: vf = 0.15).

Table 7.10: Homogenized first Piola-Kirchhoff component P_{xx} under uniaxial loading condition along xx for linear, periodic, and uniform traction boundary conditions as a function of the number of particles, for microstructures containing Disks of the same size belonging to the three different phases (Phase 2: vf = 0.1, Phase 3: vf = 0.05, Phase 4: vf = 0.15). The relative variation with reference to the periodic boundary is also presented as $\varepsilon_{\text{Periodic}}$.

Number of Particles	Linear condition		Periodic condition	U. Traction condition	
	P_{xx} /MPa	$\varepsilon_{\text{Periodic}}$ /%	P_{xx} /MPa	P_{xx} /MPa	$\varepsilon_{\text{Periodic}}$ /%
3	16.91	1.28	16.70	15.87	−4.95
6	17.06	6.69	15.99	15.82	−1.10
10	16.67	4.41	15.97	15.77	−1.24
18	16.12	0.90	15.97	15.86	−0.72
32	16.11	1.09	15.93	15.84	−0.57
56	16.24	1.99	15.92	15.81	−0.72
100	16.20	1.38	15.98	15.91	−0.42
178	16.13	0.95	15.98	15.95	−0.17
316	16.12	0.72	16.01	15.96	−0.28
562	16.09	0.61	15.99	15.97	−0.15
1000	16.07	0.42	16.01	15.99	−0.10

Table 7.11: Homogenized first Piola-Kirchhoff component P_{yy} under uniaxial loading condition along yy for linear, periodic, and uniform traction boundary conditions as a function of the number of particles, for microstructures containing Disks of the same size belonging to the three different phases (Phase 2: vf = 0.1, Phase 3: vf = 0.05, Phase 4: vf = 0.15). The relative variation with reference to the periodic boundary is also presented as $\varepsilon_{\text{Periodic}}$.

Number of Particles	Linear condition		Periodic condition	U. Traction condition	
	P_{yy} /MPa	$\varepsilon_{\text{Periodic}}$ /%	P_{yy} /MPa	P_{yy} /MPa	$\varepsilon_{\text{Periodic}}$ /%
3	18.04	13.94	15.83	15.67	−1.06
6	16.63	4.64	15.89	15.70	−1.22
10	16.71	3.05	16.22	15.82	−2.50
18	16.41	1.94	16.10	15.96	−0.85
32	16.37	1.98	16.05	15.96	−0.55
56	16.41	1.41	16.18	16.03	−0.94
100	16.25	1.44	16.02	15.95	−0.41
178	16.11	0.49	16.03	15.98	−0.30
316	16.12	0.67	16.01	15.98	−0.23
562	16.09	0.44	16.02	16.00	−0.17
1000	16.06	0.37	16.00	15.98	−0.14

Table 7.12: Homogenized first Piola-Kirchhoff component P_{xy} under simple shear across xy for linear, periodic, and uniform traction boundary conditions as a function of the number of particles, for microstructures containing Disks of the same size belonging to the three different phases (Phase 2: vf = 0.1, Phase 3: vf = 0.05, Phase 4: vf = 0.15). The relative variation with reference to the periodic boundary is also presented as $\varepsilon_{\text{Periodic}}$.

Number of Particles	Linear condition		Periodic condition	U. Traction condition	
	P_{xy} /MPa	$\varepsilon_{\text{Periodic}}$ /%	P_{xy} /MPa	P_{xy} /MPa	$\varepsilon_{\text{Periodic}}$ /%
3	18.86	14.87	16.42	16.20	−1.37
6	18.90	4.67	18.06	16.74	−7.31
10	18.35	5.52	17.39	16.68	−4.05
18	17.69	3.37	17.11	16.85	−1.52
32	18.04	2.65	17.57	17.21	−2.07
56	17.69	2.23	17.31	17.05	−1.50
100	17.70	1.90	17.37	17.22	−0.87
178	17.52	1.06	17.33	17.18	−0.89
316	17.50	0.91	17.34	17.20	−0.82
562	17.44	0.59	17.34	17.24	−0.54
1000	17.39	0.42	17.31	17.24	−0.43

Table 7.13: Homogenized first Piola-Kirchhoff component P_{xx} and P_{yy} under uniaxial loading condition along xx and yy, respectively, for periodic boundary conditions as a function of the number of particles, for microstructures containing Disks of the same size belonging to the three different phases (Phase 2: vf = 0.1, Phase 3: vf = 0.05, Phase 4: vf = 0.15). The relative variation with reference to the homogenized first Piola-Kirchhoff component P_{xx} under uniaxial loading condition along xx is also presented as ε_{xx}.

Number of Particles	Uniaxial traction along y		Uniaxial traction along x
	P_{yy} /MPa	ε_{xx} /%	P_{xx} /MPa
3	15.83	5.18	16.70
6	15.89	0.63	15.99
10	16.22	−1.59	15.97
18	16.10	−0.80	15.97
32	16.05	−0.74	15.93
56	16.18	−1.63	15.92
100	16.02	−0.25	15.98
178	16.03	−0.30	15.98
316	16.01	−0.02	16.01
562	16.02	−0.21	15.99
1000	16.00	0.04	16.01

Discussion

The results presented in Figure 7.71 regarding the stiffness of the response as a function of the boundary condition used are as expected, with the linear boundary condition leading to a stiffer behavior, the uniform boundary traction leading to a more flexible behavior and the periodic boundary condition corresponding to an intermediate response. This can be confirmed from the sign of the relative variations in Tables 7.10, 7.11 and 7.12.

Regarding the representativity of the RVE, an increasing number of particles leads to a more representative RVE, as can be inferred from the decreasing difference between the corresponding homogenized first Piola-Kirchhoff components. For the two uniaxial loading schemes considered, the RVE containing a 1000 particles leads to relative differences between the boundary conditions of below half a percent. The results are slightly higher for the simple shear across xy, but of the same magnitude. A comparison with the results of the previous section regarding the number of particles to achieve a representative RVE are presented in the next section.

Concerning isotropy, it can be gathered from Table 7.13 that for all numbers of particles considered the relative variation between the homogenized Piola-Kirchhoff P_{xx} in the uniaxial traction along xx and the homogenized Piola-Kirchhoff P_{yy} in the uniaxial traction along yy is below 2% with a slight tendency to decrease with an increase in the number of particles included in the RVE, except for the microstructure containing only 3 particles.

7.3.3 One phase containing Disks and one phase containing Ellipses

This section presents the results concerning microstructures containing two different particle phases. Each phase contains n particles, with n given by

$$n = \texttt{round}(10^k/2) \quad \text{for } k = 0.5, 0.75, 1, \ldots, 3. \tag{7.9}$$

Considering an unitary RVE, Phase 2 contains Disks of the same size at a volume fraction of 0.1, and Phase 3 contains Ellipses at volume fraction of 0.2. The ratio between the major and minor axis varies uniformly between 1 and 2.5. As for the orientation, the angle between the major axis and the positive semi-axis x varies according to a Gaussian of mean 0 and standard deviation $\pi/10$. To perform the multi-scale analyses based on computational homogenization simulations, the microstructure is discretized in a nonconform TRI6 mesh. the materials considered are for Phase 1, corresponding to the matrix, $E = 100\,\text{MPa}$ and $\nu = 0.3$, for Phase 2, $E = 500\,\text{MPa}$ and $\nu = 0.3$ and for Phase 3, $E = 300\,\text{MPa}$. Assuming a plain strain condition, three different deformation gradients are imposed, characterizing an uniaxial loading along xx, an uniaxial loading along yy and a simple shear across xy defined as

$$\text{Uniaxial along } xx: \quad \boldsymbol{F} = \begin{bmatrix} 1.1 & 0 \\ 0 & 1.0 \end{bmatrix}, \tag{7.10}$$

$$\text{Uniaxial along } yy: \quad \boldsymbol{F} = \begin{bmatrix} 1.0 & 0 \\ 0 & 1.1 \end{bmatrix}, \tag{7.11}$$

$$\text{Simple shear across } xy: \quad \boldsymbol{F} = \begin{bmatrix} 1.0 & 0.3 \\ 0 & 1.0 \end{bmatrix}, \tag{7.12}$$

respectively.

Results

Figure 7.72 presents examples of the RVEs considered, including in Figures 7.72a and 7.72b the TRI6 nonconform mesh.

The homogenized first Piola-Kirchhoff stress for various loading schemes as a function of the number of particles is presented in Figure 7.73. The results for uniaxial traction along xx are shown in Figure 7.73a, for uniaxial traction along yy in Figure 7.73b and for simple shear across xy in Figure 7.73c. To ease the interpretation of these results as it relates to the representativity of the RVE, they are presented in Tables 7.14-7.16, including the relative variation between the boundary conditions considered. Figure 7.74 aggregates these results for all the 2-D microstructures considered under uniaxial loading along xx. In the same vein as Tables 7.14-7.16, Table 7.17 present the same results only for the periodic boundary condition and the uniaxial loading conditions with the goal of helping to reach conclusions about the isotropy of the RVEs.

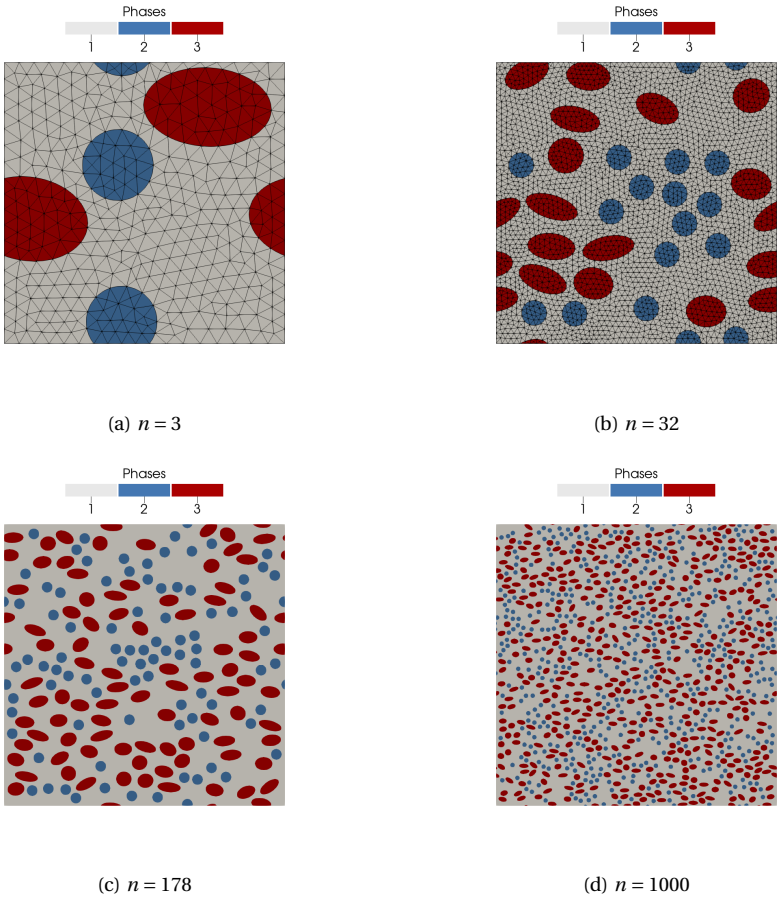

(a) $n = 3$ (b) $n = 32$

(c) $n = 178$ (d) $n = 1000$

Figure 7.72: Microstructures containing (a): 4, (b): 32, (c):178 and (d):1000 particles including two particle phases, Phase 2 containing Disks of the same size at vf = 0.1 and Phase 3 containing Ellipses oriented along xx at vf = 0.2. The TRI6 nonconform mesh is only represented for (a) and (b) (only the vertex nodes shown).

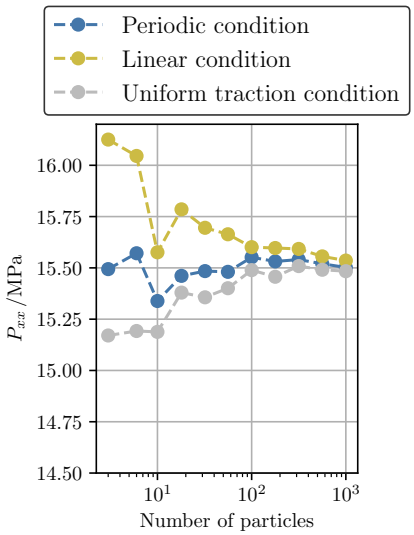

(a) Uniaxial traction along xx

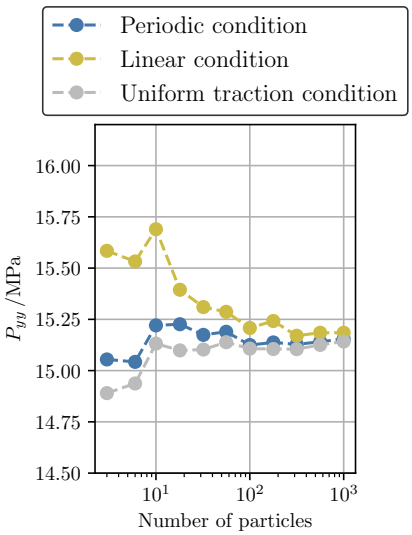

(b) Uniaxial traction along yy

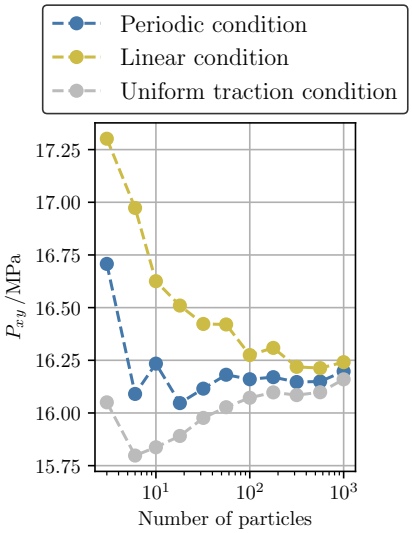

(c) Simple shear across xy

Figure 7.73: Homogenized first Piola-Kirchhoff stress for various loading schemes ((a): uniaxial traction along xx - P_{xx}, (b): uniaxial traction along yy - P_{yy}, (c): simple shear across xy - P_{xy}) as a function of the number of particles, for microstructures containing two particle phases, Phase 2 containing Disks of the same size at vf = 0.1 and Phase 3 containing Ellipses oriented along xx at vf = 0.2.

Table 7.14: Homogenized first Piola-Kirchhoff component P_{xx} under uniaxial loading condition along xx for linear, periodic, and uniform traction boundary conditions as a function of the number of particles, for microstructures containing two particle phases, Phase 2 containing Disks of the same size at vf = 0.1 and Phase 3 containing Ellipses oriented along xx at vf = 0.2. The relative variation with reference to the periodic boundary is also presented as $\varepsilon_{\text{Periodic}}$.

Number of Particles	Linear condition		Periodic condition	U. Traction condition	
	P_{xx} /MPa	$\varepsilon_{\text{Periodic}}$ /%	P_{xx} /MPa	P_{xx} /MPa	$\varepsilon_{\text{Periodic}}$ /%
3	16.13	4.08	15.49	15.17	−2.09
6	16.05	3.05	15.57	15.19	−2.43
10	15.58	1.55	15.34	15.19	−0.98
18	15.79	2.10	15.46	15.38	−0.53
32	15.70	1.36	15.48	15.36	−0.83
56	15.66	1.18	15.48	15.40	−0.52
100	15.60	0.32	15.55	15.49	−0.40
178	15.60	0.42	15.53	15.46	−0.48
316	15.59	0.33	15.54	15.51	−0.20
562	15.56	0.23	15.52	15.49	−0.19
1000	15.54	0.22	15.50	15.48	−0.12

Table 7.15: Homogenized first Piola-Kirchhoff component P_{yy} under uniaxial loading condition along yy for linear, periodic, and uniform traction boundary conditions as a function of the number of particles, for microstructures containing two particle phases, Phase 2 containing Disks of the same size at vf = 0.1 and Phase 3 containing Ellipses oriented along xx at vf = 0.2. The relative variation with reference to the periodic boundary is also presented as $\varepsilon_{\text{Periodic}}$.

Number of Particles	Linear condition		Periodic condition	U. Traction condition	
	P_{yy} /MPa	$\varepsilon_{\text{Periodic}}$ /%	P_{yy} /MPa	P_{yy} /MPa	$\varepsilon_{\text{Periodic}}$ /%
4	15.58	3.52	15.05	14.89	−1.09
6	15.53	3.26	15.04	14.94	−0.70
10	15.69	3.08	15.22	15.13	−0.58
18	15.39	1.10	15.23	15.10	−0.84
32	15.31	0.89	15.17	15.10	−0.47
56	15.29	0.64	15.19	15.14	−0.33
100	15.21	0.55	15.12	15.11	−0.11
178	15.24	0.69	15.14	15.11	−0.21
316	15.17	0.28	15.13	15.10	−0.15
562	15.18	0.29	15.14	15.13	−0.10
1000	15.18	0.20	15.15	15.14	−0.08

Table 7.16: Homogenized first Piola-Kirchhoff component P_{xy} under simple shear across xy for linear, periodic, and uniform traction boundary conditions as a function of the number of particles, for microstructures containing two particle phases, Phase 2 containing Disks of the same size at vf = 0.1 and Phase 3 containing Ellipses oriented along xx at vf = 0.2. The relative variation with reference to the periodic boundary is also presented as $\varepsilon_{\text{Periodic}}$.

Number of Particles	Linear condition		Periodic condition	U. Traction condition	
	P_{xy} /MPa	$\varepsilon_{\text{Periodic}}$ /%	P_{xy} /MPa	P_{xy} /MPa	$\varepsilon_{\text{Periodic}}$ /%
4	17.30	3.56	16.71	16.05	−3.93
6	16.97	5.49	16.09	15.80	−1.82
10	16.63	2.41	16.23	15.84	−2.45
18	16.51	2.89	16.05	15.89	−0.97
32	16.42	1.91	16.12	15.98	−0.86
56	16.42	1.48	16.18	16.03	−0.95
100	16.27	0.71	16.16	16.07	−0.54
178	16.31	0.86	16.17	16.10	−0.45
316	16.22	0.45	16.15	16.08	−0.39
562	16.21	0.39	16.15	16.10	−0.32
1000	16.24	0.27	16.20	16.16	−0.23

Table 7.17: Homogenized first Piola-Kirchhoff component P_{xx} and P_{yy} under uniaxial loading condition along xx and yy, respectively, for periodic boundary conditions as a function of the number of particles, for microstructures containing two particle phases, Phase 2 containing Disks of the same size at vf = 0.1 and Phase 3 containing Ellipses oriented along xx at vf = 0.2. The relative variation with reference to the homogenized first Piola-Kirchhoff component P_{xx} under uniaxial loading condition along xx is also presented as ε_{xx}.

Number of Particles	Uniaxial traction along y		Uniaxial traction along x
	P_{yy} /MPa	ε_{xx} /%	P_{xx} /MPa
4	15.05	2.84	15.49
6	15.04	3.40	15.57
10	15.22	0.77	15.34
18	15.23	1.52	15.46
32	15.17	2.00	15.48
56	15.19	1.88	15.48
100	15.12	2.74	15.55
178	15.14	2.54	15.53
316	15.13	2.65	15.54
562	15.39	3.95	16.02
1000	15.41	3.63	15.99

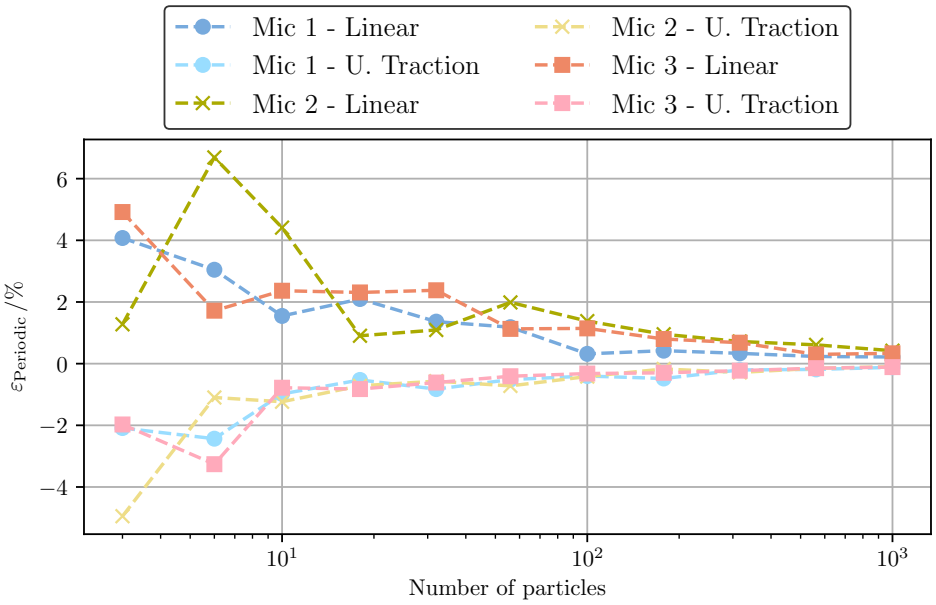

Figure 7.74: Relative variation of the homogenized first Piola-Kirchhoff P_{xx} under uniaxial loading along xx between the linear and uniform traction boundary conditions and the periodic boundary condition as a function of the number of particles. Microstructure 1 includes one particle phase containing Disks of the same size at a volume fraction equal to 0.3. Microstructure 2 includes three particle phases containing Disks of the same size, Phase 2 at a volume fraction of 0.1, Phase 3 at a volume fraction of 0.05 and Phase 4 at a volume fraction 0.15. Microstructure 3 comprises two particle phase. Phase 2 containing Disks of the same size at a volume fraction equal to 0.1 and Phase 3 containing Ellipses at a volume fraction equal to 0.2 oriented along xx.

Discussion

The results presented in Figure 7.73 regarding the stiffness of the response as a function of the boundary condition used are as expected, with the linear boundary condition leading to a stiffer behavior, the uniform boundary traction leading to a more flexible behavior and the periodic boundary condition corresponding to an intermediate response. This can be confirmed from the sign of the relative variations in Tables 7.14-7.16.

Regarding the representativity of the RVE, an increasing number of particles leads to a more representative RVE, as can be inferred from the decreasing difference between the corresponding homogenized first Piola-Kirchhoff components. For the two uniaxial loading schemes considered, the RVE containing a 1000 particles leads to relative differences between the boundary conditions of below half a percent. The results are slightly higher for the simple shear across xy, but of the same magnitude. A cursory look at Tables 7.6-7.8, 7.10-7.12 and 7.14-7.16 suggests that there isn't a strong difference in the number of particles needed for the RVE to be representative between all the 2D microstructures considered. Figure 7.74 confirms visually this assertion for uniaxial loading along xx.

Concerning isotropy, it can be gathered from Table 7.17 that for all numbers of particles considered the relative variation between the homogenized Piola-Kirchhoff P_{xx} in the uniaxial traction along xx and the homogenized Piola-Kirchhoff P_{yy} in the uniaxial traction along yy is always below 4% but never smaller than 1.5%, except for the microstructure containing 10 particles. This is to be expected given the orientation of the Ellipses, which leads to the anisotropy detected.

7.3.4 One phase containing Spheres with same radius

This section presents the results concerning microstructures containing only Spheres of the same size belonging to a single phase. Assuming that the RVE is unitary, the volume fraction is fixed at 0.2 and samples with n particles are created, with n given by

$$n = \texttt{round}(10^k) \quad \text{for } k = 0.5, 0.75, 1, \ldots, 2.75. \tag{7.13}$$

To perform the multi-scale analyses based on computational homogenization simulations, the microstructure is discretized in a nonconform TETRA10 mesh. The materials considered are for Phase 1, corresponding to the matrix, $E = 100\,\text{MPa}$ and $\nu = 0.3$, and for Phase 2, $E = 500\,\text{MPa}$ and $\nu = 0.3$. Four different deformation gradients are imposed, characterizing an uniaxial loading along xx, an uniaxial loading along yy, an uniaxial loading along zz and a simple shear across xy defined as

$$\text{Uniaxial along } xx: \quad \boldsymbol{F} = \begin{bmatrix} 1.1 & 0 & 0 \\ 0 & 1.0 & 0 \\ 0 & 0 & 1.0 \end{bmatrix}, \tag{7.14}$$

$$\text{Uniaxial along } yy: \quad \boldsymbol{F} = \begin{bmatrix} 1.0 & 0 & 0 \\ 0 & 1.1 & 0 \\ 0 & 0 & 1.0 \end{bmatrix}, \tag{7.15}$$

$$\text{Uniaxial along } zz: \quad \boldsymbol{F} = \begin{bmatrix} 1.0 & 0 & 0 \\ 0 & 1.0 & 0 \\ 0 & 0 & 1.1 \end{bmatrix}, \tag{7.16}$$

$$\text{Simple shear across } xy: \quad \boldsymbol{F} = \begin{bmatrix} 1.0 & 0.3 & 0 \\ 0 & 1.0 & 0 \\ 0 & 0 & 1.0 \end{bmatrix}, \tag{7.17}$$

respectively.

Results

Figure 7.75 presents examples of the RVEs considered, including in Figures 7.75a and 7.75b the TETRA10 nonconform mesh.

The homogenized first Piola-Kirchhoff stress for various loading schemes as a function of the number of particles is presented in Figure 7.76. The results for uniaxial traction along xx are shown in Figure 7.76a, for uniaxial traction along yy in Figure 7.76b, for uniaxial traction along zz in Figure 7.76c and for simple shear across xy in Figure 7.76d. To ease the interpretation of these results as it relates to the representativity of the RVE, they are presented in Tables 7.18-7.20, including the relative variation between the boundary conditions considered. In the same vein, Table 7.21 presents the same results only for the periodic boundary condition and the uniaxial loading conditions with the goal of helping to reach conclusions about the isotropy of the RVEs.

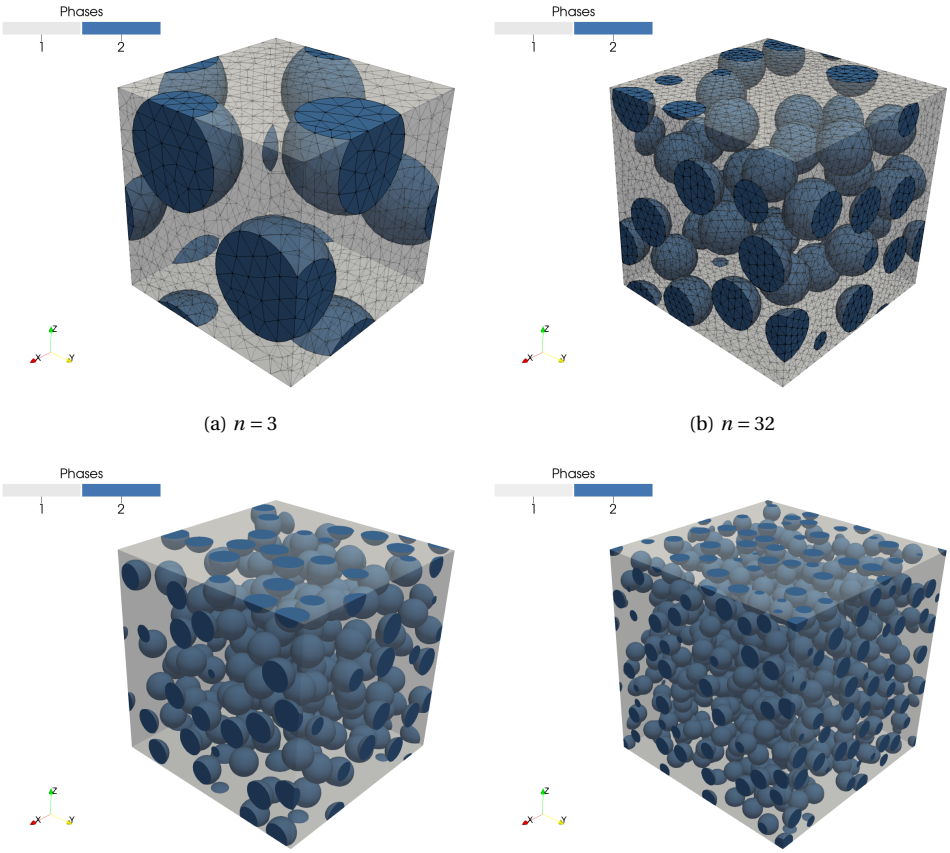

(a) $n = 3$ (b) $n = 32$

(c) $n = 178$ (d) $n = 562$

Figure 7.75: Microstructures containing (a): 3, (b): 32, (c):178 and (d):562 Spheres of the same size belonging to the same phase at a volume fraction equal to 0.2. The TETRA10 nonconform mesh is only represented for (a) and (b) (only the vertex nodes shown).

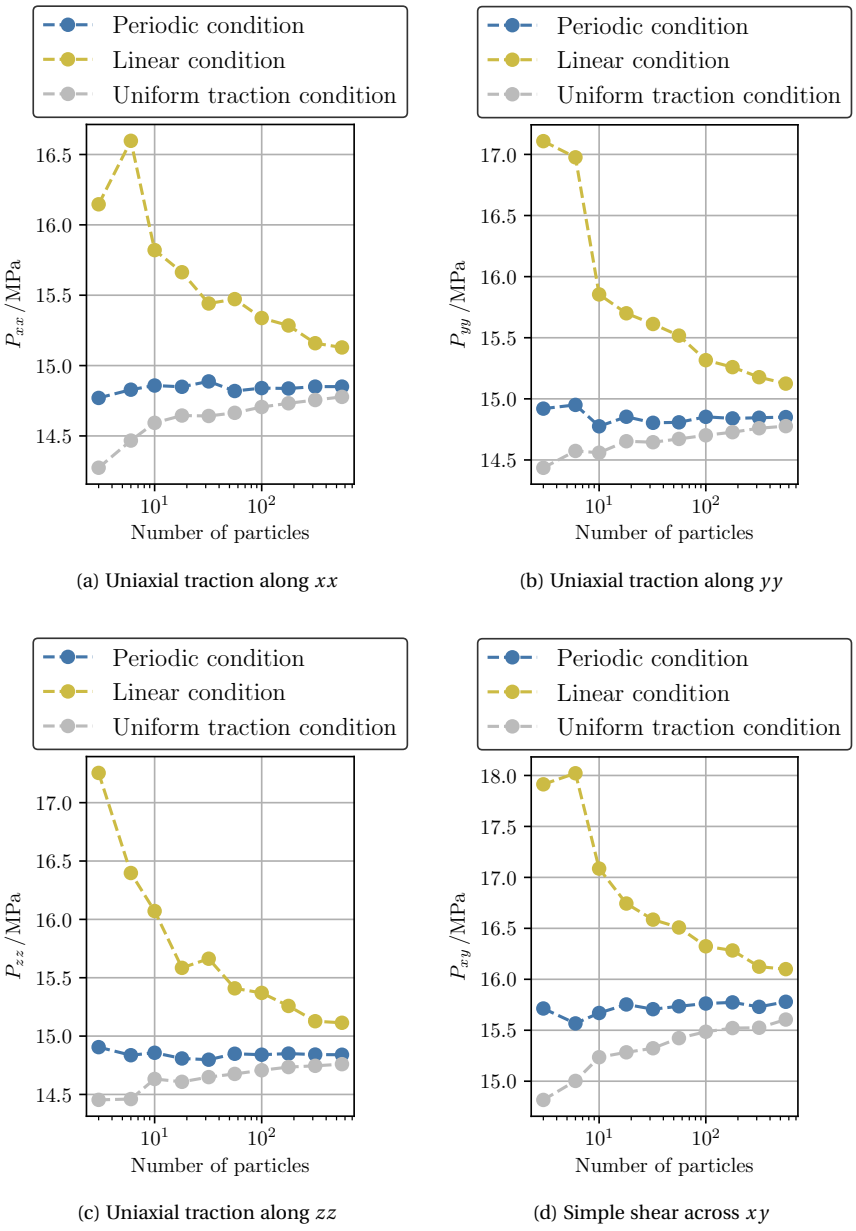

(a) Uniaxial traction along xx

(b) Uniaxial traction along yy

(c) Uniaxial traction along zz

(d) Simple shear across xy

Figure 7.76: Homogenized first Piola-Kirchhoff stress for various loading schemes ((a): uniaxial traction along xx - P_{xx}, (b): uniaxial traction along yy - P_{yy}, (c): uniaxial traction along zz - P_{zz}, (d): simple shear across xy - P_{xy}) as a function of the number of particles, for microstructures containing only Spheres of the same size at a volume fraction equal to 0.2 belonging to the same phase.

Table 7.18: Homogenized first Piola-Kirchhoff component P_{xx} under uniaxial loading condition along xx for linear, periodic, and uniform traction boundary conditions as a function of the number of particles, for microstructures containing only Spheres of the same size at a volume fraction equal to 0.2 belonging to the same phase. The relative variation with reference to the periodic boundary is also presented as $\varepsilon_{\text{Periodic}}$.

Number of Particles	Linear condition		Periodic condition	U. Traction condition	
	P_{xx} /MPa	$\varepsilon_{\text{Periodic}}$ /%	P_{xx} /MPa	P_{xx} /MPa	$\varepsilon_{\text{Periodic}}$ /%
3	16.15	9.32	14.77	14.27	−3.36
6	16.60	11.93	14.83	14.47	−2.44
10	15.82	6.48	14.86	14.59	−1.79
18	15.66	5.48	14.85	14.64	−1.38
32	15.44	3.72	14.89	14.64	−1.65
56	15.47	4.41	14.82	14.66	−1.05
100	15.34	3.35	14.84	14.71	−0.91
178	15.28	3.02	14.84	14.73	−0.71
316	15.16	2.08	14.85	14.76	−0.64
562	15.13	1.87	14.85	14.78	−0.49

Table 7.19: Homogenized first Piola-Kirchhoff component P_{yy} under uniaxial loading condition along yy for linear, periodic, and uniform traction boundary conditions as a function of the number of particles, for microstructures containing only Spheres of the same size at a volume fraction equal to 0.2 belonging to the same phase. The relative variation with reference to the periodic boundary is also presented as $\varepsilon_{\text{Periodic}}$.

Number of Particles	Linear condition		Periodic condition	U. Traction condition	
	P_{xx} /MPa	$\varepsilon_{\text{Periodic}}$ /%	P_{xx} /MPa	P_{xx} /MPa	$\varepsilon_{\text{Periodic}}$ /%
3	17.11	14.67	14.92	14.44	−3.25
6	16.98	13.55	14.95	14.57	−2.52
10	15.85	7.30	14.78	14.56	−1.46
18	15.70	5.70	14.85	14.65	−1.35
32	15.61	5.46	14.80	14.65	−1.07
56	15.52	4.79	14.81	14.67	−0.92
100	15.32	3.12	14.85	14.70	−1.02
178	15.26	2.83	14.84	14.73	−0.76
316	15.18	2.23	14.85	14.76	−0.58
562	15.12	1.84	14.85	14.78	−0.50

Table 7.20: Homogenized first Piola-Kirchhoff component P_{zz} under uniaxial loading condition along zz for linear, periodic, and uniform traction boundary conditions as a function of the number of particles,for microstructures containing only Spheres of the same size at a volume fraction equal to 0.2 belonging to the same phase. The relative variation with reference to the periodic boundary is also presented as $\varepsilon_{\text{Periodic}}$.

Number of Particles	Linear condition		Periodic condition	U. Traction condition	
	P_{xx} /MPa	$\varepsilon_{\text{Periodic}}$ /%	P_{xx} /MPa	P_{xx} /MPa	$\varepsilon_{\text{Periodic}}$ /%
3	17.25	15.76	14.91	14.45	−3.03
6	16.40	10.52	14.84	14.46	−2.53
10	16.07	8.17	14.86	14.63	−1.51
18	15.58	5.24	14.81	14.61	−1.35
32	15.66	5.85	14.80	14.65	−1.01
56	15.41	3.77	14.85	14.68	−1.16
100	15.37	3.57	14.84	14.71	−0.90
178	15.26	2.75	14.85	14.73	−0.78
316	15.13	1.92	14.84	14.75	−0.65
562	15.11	1.85	14.84	14.76	−0.54

Table 7.21: Homogenized first Piola-Kirchhoff component P_{xx}, P_{yy} and P_{zz} under uniaxial loading condition along xx, yy and zz, respectively, for periodic boundary conditions as a function of the number of particles, for microstructures containing only Spheres of the same size at a volume fraction equal to 0.2 belonging to the same phase. The relative variation with reference to the homogenized first Piola-Kirchhoff component P_{xx} under uniaxial loading condition along xx is also presented as ε_{xx}.

Number of Particles	Uniaxial traction along x	Uniaxial traction along y		Uniaxial traction along z	
	P_{xx} /MPa	P_{yy} /MPa	ε_{xx} /%	P_{zz} /MPa	ε_{xx} /%
3	14.770	14.920	−1.015	14.905	−0.916
6	14.829	14.951	−0.822	14.836	−0.049
10	14.778	14.836	−0.390	14.857	−0.530
18	14.849	14.854	−0.029	14.808	0.276
32	14.887	14.804	0.561	14.798	0.603
56	14.819	14.808	0.076	14.849	−0.199
100	14.840	14.853	−0.086	14.840	−0.002
178	14.837	14.840	−0.020	14.850	−0.086
316	14.850	14.846	0.033	14.842	0.059
562	14.851	14.851	−0.002	14.840	0.070

Discussion

The results presented in Figure 7.76 regarding the stiffness of the response as a function of the boundary condition used are as expected, with the linear boundary condition leading to a stiffer behavior, the uniform boundary traction leading to a more flexible behavior and the periodic boundary condition corresponding to an intermediate response. This can be confirmed from the sign of the relative variations in Tables 7.18-7.20.

Regarding the representativity of the RVE, an increasing number of particles leads to a more representative RVE, as can be inferred from the decreasing difference between the corresponding homogenized first Piola-Kirchhoff components in Figure 7.76. For the three uniaxial loading schemes considered, the RVE containing a 562 particles leads to a relative differences between the periodic and the linear boundary condition of around 2% and between the periodic and the uniform traction boundary condition of about 0.5%.

Concerning isotropy, it can be gathered from Table 7.21 that for all numbers of particles considered the relative variation between the homogenized Piola-Kirchhoff P_{xx} in the uniaxial traction along xx, the homogenized Piola-Kirchhoff P_{yy} in the uniaxial traction along yy, and the homogenized Piola-Kirchhoff P_{yy} in the uniaxial traction along zz is below 1% with a strong tendency to decrease with an increase in the number of particles included in the RVE.

7.3.5 Three phases containing Spheres with different radii

This section presents the results concerning microstructures containing three different particle phases. Each phase contains n Spheres of the same size, with n given by

$$n = \texttt{round}(10^k/3) \quad \text{for } k = 0.5, 0.75, 1, \ldots, 2.75. \tag{7.18}$$

Assuming an unitary RVE, for Phase 2 the volume fraction is fixed at 0.075, for Phase 3 at 0.025, and for Phase 4 at 0.1. To perform the multi-scale analyses based on computational homogenization simulations, the microstructure is discretized in a nonconform TETRA10 mesh. The materials considered are for Phase 1, corresponding to the matrix, $E = 100\,\text{MPa}$ and $\nu = 0.3$, and for Phase 2, the phase containing the Disks, $E = 500\,\text{MPa}$ and $\nu = 0.3$, for Phase 3, $E = 700\,\text{MPa}$ and $\nu = 0.3$, and for Phase 4, $E = 1000\,\text{MPa}$ and $\nu = 0.3$. Four different deformation gradients are imposed, characterizing an uniaxial loading along xx, an uniaxial loading along yy, an uniaxial loading along zz and a simple shear across xy defined as

$$\text{Uniaxial along } xx: \quad \boldsymbol{F} = \begin{bmatrix} 1.1 & 0 & 0 \\ 0 & 1.0 & 0 \\ 0 & 0 & 1.0 \end{bmatrix}, \tag{7.19}$$

$$\text{Uniaxial along } yy: \quad \boldsymbol{F} = \begin{bmatrix} 1.0 & 0 & 0 \\ 0 & 1.1 & 0 \\ 0 & 0 & 1.0 \end{bmatrix}, \tag{7.20}$$

$$\text{Uniaxial along } zz: \quad \boldsymbol{F} = \begin{bmatrix} 1.0 & 0 & 0 \\ 0 & 1.0 & 0 \\ 0 & 0 & 1.1 \end{bmatrix}, \tag{7.21}$$

$$\text{Simple shear across } xy: \quad \boldsymbol{F} = \begin{bmatrix} 1.0 & 0.3 & 0 \\ 0 & 1.0 & 0 \\ 0 & 0 & 1.0 \end{bmatrix}, \tag{7.22}$$

respectively.

Results

Figure 7.77 presents examples of the RVEs considered, including in Figures 7.77a and 7.77b the TETRA10 nonconform mesh.

The homogenized first Piola-Kirchhoff stress for various loading schemes as a function of the number of particles is presented in Figure 7.78. The results for uniaxial traction along xx are shown in Figure 7.78a, for uniaxial traction along yy in Figure 7.78b, for uniaxial traction along zz in Figure 7.78c and for simple shear across xy in Figure 7.78d. To ease the interpretation of these results as it relates to the representativity of the RVE, they are presented in Tables 7.22-7.24, including the relative variation between the boundary conditions considered. In the same vein, Table 7.25 presents the same results only for the periodic boundary condition and the uniaxial loading conditions with the goal of helping to reach conclusions about the isotropy of the RVEs.

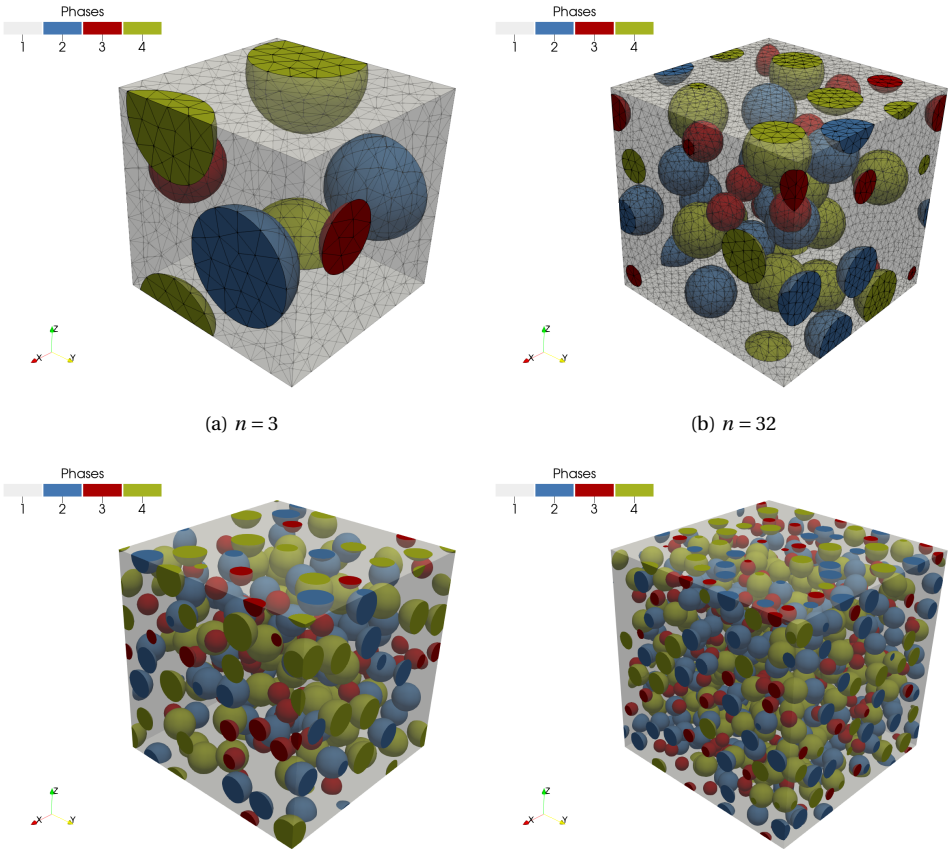

(a) $n = 3$ (b) $n = 32$

(c) $n = 178$ (d) $n = 562$

Figure 7.77: Microstructures containing (a): 3, (b): 32, (c):178 and (d):562 Spheres of the same size belonging to three different phases (Phase 2: vf = 0.075, Phase 3: vf = 0.025, Phase 4: vf = 0.1). The TETRA10 nonconform mesh is only represented for (a) and (b) (only the vertex nodes shown).

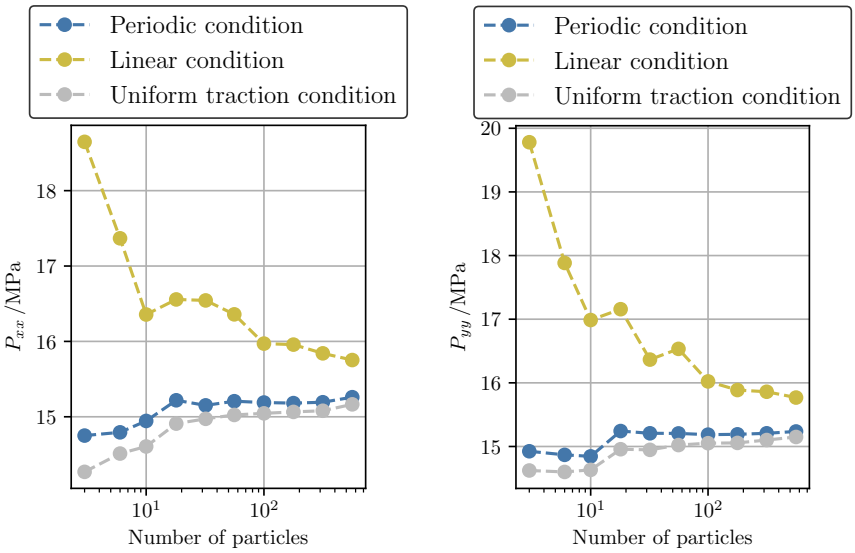

(a) Uniaxial traction along xx

(b) Uniaxial traction along yy

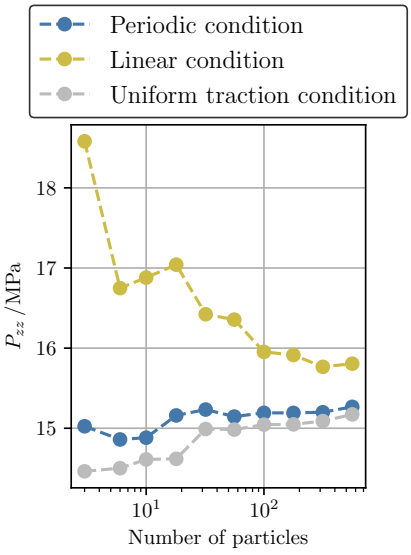

(c) Uniaxial traction along zz

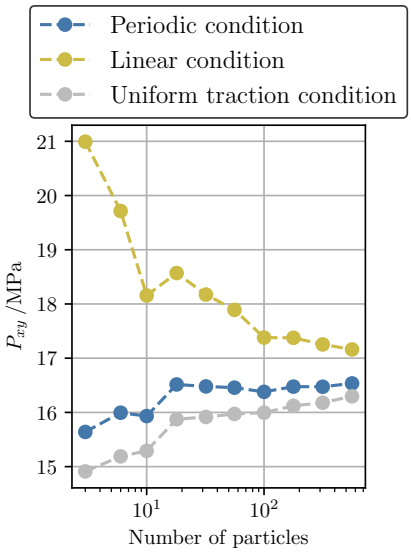

(d) Simple shear across xy

Figure 7.78: Homogenized first Piola-Kirchhoff stress for various loading schemes ((a): uniaxial traction along xx - P_{xx}, (b): uniaxial traction along yy - P_{yy}, (c): uniaxial traction along zz - P_{zz}, (d): simple shear across xy - P_{xy}) as a function of the number of particles, for microstructures containing Spheres of the same size belonging to three different phases (Phase 2: vf = 0.075, Phase 3: vf = 0.025, Phase 4: vf = 0.1).

Table 7.22: Homogenized first Piola-Kirchhoff component P_{xx} under uniaxial loading condition along xx for linear, periodic, and uniform traction boundary conditions as a function of the number of particles, for microstructures containing Spheres of the same size belonging to three different phases (Phase 2: vf = 0.075, Phase 3: vf = 0.025, Phase 4: vf = 0.1). The relative variation with reference to the periodic boundary is also presented as $\varepsilon_{\text{Periodic}}$.

Number of Particles	Linear condition		Periodic condition	U. Traction condition	
	P_{xx} /MPa	$\varepsilon_{\text{Periodic}}$ /%	P_{xx} /MPa	P_{xx} /MPa	$\varepsilon_{\text{Periodic}}$ /%
3	18.65	26.42	14.75	14.27	−3.26
6	17.37	17.40	14.79	14.51	−1.90
10	16.36	9.45	14.94	14.61	−2.27
18	16.56	8.79	15.22	14.91	−2.03
32	16.54	9.19	15.15	14.97	−1.18
56	16.36	7.58	15.21	15.02	−1.20
100	15.97	5.15	15.19	15.05	−0.94
178	15.96	5.11	15.18	15.06	−0.77
316	15.84	4.27	15.19	15.08	−0.74
562	15.75	3.23	15.26	15.16	−0.62

Table 7.23: Homogenized first Piola-Kirchhoff component P_{yy} under uniaxial loading condition along yy for linear, periodic, and uniform traction boundary conditions as a function of the number of particles, for microstructures containing Spheres of the same size belonging to three different phases (Phase 2: vf = 0.075, Phase 3: vf = 0.025, Phase 4: vf = 0.1). The relative variation with reference to the periodic boundary is also presented as $\varepsilon_{\text{Periodic}}$.

Number of Particles	Linear condition		Periodic condition	U. Traction condition	
	P_{xx} /MPa	$\varepsilon_{\text{Periodic}}$ /%	P_{xx} /MPa	P_{xx} /MPa	$\varepsilon_{\text{Periodic}}$ /%
3	19.78	32.53	14.92	14.62	−2.02
6	17.88	20.28	14.87	14.60	−1.81
10	16.99	14.43	14.84	14.63	−1.43
18	17.16	12.56	15.24	14.96	−1.87
32	16.37	7.61	15.21	14.95	−1.71
56	16.53	8.74	15.21	15.02	−1.20
100	16.02	5.51	15.19	15.05	−0.88
178	15.89	4.58	15.19	15.06	−0.89
316	15.86	4.29	15.21	15.10	−0.70
562	15.77	3.50	15.24	15.15	−0.57

Table 7.24: Homogenized first Piola-Kirchhoff component P_{zz} under uniaxial loading condition along zz for linear, periodic, and uniform traction boundary conditions as a function of the number of particles, for microstructures containing Spheres of the same size belonging to three different phases (Phase 2: vf = 0.075, Phase 3: vf = 0.025, Phase 4: vf = 0.1). The relative variation with reference to the periodic boundary is also presented as $\varepsilon_{\text{Periodic}}$.

Number of Particles	Linear condition		Periodic condition	U. Traction condition	
	P_{xx} /MPa	$\varepsilon_{\text{Periodic}}$ /%	P_{xx} /MPa	P_{xx} /MPa	$\varepsilon_{\text{Periodic}}$ /%
3	18.58	23.67	15.02	14.46	−3.74
6	16.75	12.71	14.86	14.50	−2.41
10	16.88	13.42	14.88	14.61	−1.82
18	17.04	12.41	15.16	14.62	−3.57
32	16.42	7.81	15.23	14.99	−1.59
56	16.36	7.99	15.15	14.98	−1.07
100	15.95	5.01	15.19	15.05	−0.97
178	15.91	4.75	15.19	15.05	−0.94
316	15.77	3.73	15.20	15.09	−0.73
562	15.81	3.53	15.27	15.17	−0.62

Table 7.25: Homogenized first Piola-Kirchhoff component P_{xx}, P_{yy} and P_{zz} under uniaxial loading condition along xx, yy and zz, respectively, for periodic boundary conditions as a function of the number of particles, for microstructures containing Spheres of the same size belonging to three different phases (Phase 2: vf = 0.075, Phase 3: vf = 0.025, Phase 4: vf = 0.1). The relative variation with reference to the homogenized first Piola-Kirchhoff component P_{xx} under uniaxial loading condition along xx is also presented as ε_{xx}.

Number of Particles	Uniaxial traction along x	Uniaxial traction along y		Uniaxial traction along z	
	P_{xx} /MPa	P_{yy} /MPa	ε_{xx} /%	P_{zz} /MPa	ε_{xx} /%
3	14.750	14.925	−1.183	15.025	−1.859
6	14.794	14.869	−0.507	14.860	−0.449
10	14.945	14.845	0.668	14.882	0.418
18	15.219	15.243	−0.157	15.160	0.386
32	15.151	15.207	−0.369	15.233	−0.542
56	15.206	15.205	0.007	15.145	0.401
100	15.189	15.186	0.020	15.192	−0.023
178	15.181	15.191	−0.064	15.192	−0.067
316	15.193	15.207	−0.094	15.200	−0.047
562	15.260	15.236	0.157	15.267	−0.049

Discussion

The results presented in Figure 7.78 regarding the stiffness of the response as a function of the boundary condition used are not always as expected, with the linear boundary condition leading to a stiffer behavior, the uniform boundary traction leading to a more flexible behavior and the periodic boundary condition corresponding to an intermediate response. This can be confirmed from the sign of the relative variations in Tables 7.22-7.24.

Regarding the representativity of the RVE, an increasing number of particles leads to a more representative RVE, as can be inferred from the decreasing difference between the corresponding homogenized first Piola-Kirchhoff components. For the three uniaxial loading schemes considered, the RVE containing a 562 particles leads to a relative differences between the periodic and the linear boundary condition of around 3.5% and between the periodic and the uniform traction boundary condition of about 0.6%. Compared with the results from the previous section regarding Spheres of the same size, the results hint at the need to add more particles to achieve an equally representative RVE. This is possibly the cases due to the more varied nature of the particles included in the current microstructure.

Concerning isotropy, it can be gathered from Table 7.25 that for all numbers of particles considered the relative variation between the homogenized Piola-Kirchhoff P_{xx} in the uniaxial traction along xx, the homogenized Piola-Kirchhoff P_{yy} in the uniaxial traction along yy, and the homogenized Piola-Kirchhoff P_{yy} in the uniaxial traction along zz is below 1% with a slight tendency to decrease with an increase in the number of particles included in the RVE.

7.3.6 One phase containing Spheres and one phase containing Ellipsoids

This section presents the results concerning microstructures containing two different phases. Each phase contains n particles, with n given by

$$n = \texttt{round}(10^k/2) \quad \text{for } k = 0.5, 0.75, 1, \ldots, 2.75. \tag{7.23}$$

Assuming an unitary RVE, Phase 2 contains Spheres of the same size at a volume fraction of 0.1, and Phase 3 contains Ellipsoids at volume fraction of 0.1. The semi-axis a of the Ellipsoids are aligned along the xx axis, with the ratio a/b equal to 2 and the ratio a/c varying uniformly between 2 and 3. The ratio between the major and minor axis varies uniformly between 1 and 2.5. To perform the multi-scale analyses based on computational homogenization simulations, the microstructure is discretized in a nonconform TETRA10 mesh The materials considered are for Phase 1, corresponding to the matrix, $E = 100\,\text{MPa}$ and $\nu = 0.3$, for Phase 2 $E = 500\,\text{MPa}$ and $\nu = 0.3$ and for Phase 3 $E = 700\,\text{MPa}$. Four different deformation gradients are imposed, characterizing an uniaxial loading along xx, an uniaxial loading along yy and a simple shear across xy defined as

$$\text{Uniaxial along } xx: \quad \boldsymbol{F} = \begin{bmatrix} 1.1 & 0 & 0 \\ 0 & 1.0 & 0 \\ 0 & 0 & 1.0 \end{bmatrix}, \tag{7.24}$$

$$\text{Uniaxial along } yy: \quad \boldsymbol{F} = \begin{bmatrix} 1.0 & 0 & 0 \\ 0 & 1.1 & 0 \\ 0 & 0 & 1.0 \end{bmatrix}, \tag{7.25}$$

$$\text{Uniaxial along } zz: \quad \boldsymbol{F} = \begin{bmatrix} 1.0 & 0 & 0 \\ 0 & 1.0 & 0 \\ 0 & 0 & 1.1 \end{bmatrix}, \tag{7.26}$$

$$\text{Simple shear across } xy: \quad \boldsymbol{F} = \begin{bmatrix} 1.0 & 0.3 & 0 \\ 0 & 1.0 & 0 \\ 0 & 0 & 1.0 \end{bmatrix}, \tag{7.27}$$

respectively.

Results

Figure 7.79 presents examples of the RVEs considered, including in Figures 7.79a and 7.79b the TETRA10 nonconform mesh.

The homogenized first Piola-Kirchhoff stress for various loading schemes as a function of the number of particles is presented in Figure 7.80. The results for uniaxial traction along xx are shown in Figure 7.80a, for uniaxial traction along yy in Figure 7.80b and for simple shear across xy in Figure 7.80d. To ease the interpretation of these results as it relates to the representativity of the RVE, they are presented in Tables 7.26-7.28, including the relative variation between the boundary conditions considered. Some data points are missing due to difficulties in generating nonconform meshes. Also, it was not possible to generate periodic nonconform meshes, so this boundary condition is enforced using Mortar's condition. In the same vein of Tables 7.26-7.28, Table 7.29 presents the same results only for the linear boundary condition and the

uniaxial loading conditions with the goal of helping to reach conclusions about the isotropy of the RVEs. In this study the linear boundary condition is used instead of the periodic boundary condition, because it is the one with most data points available.

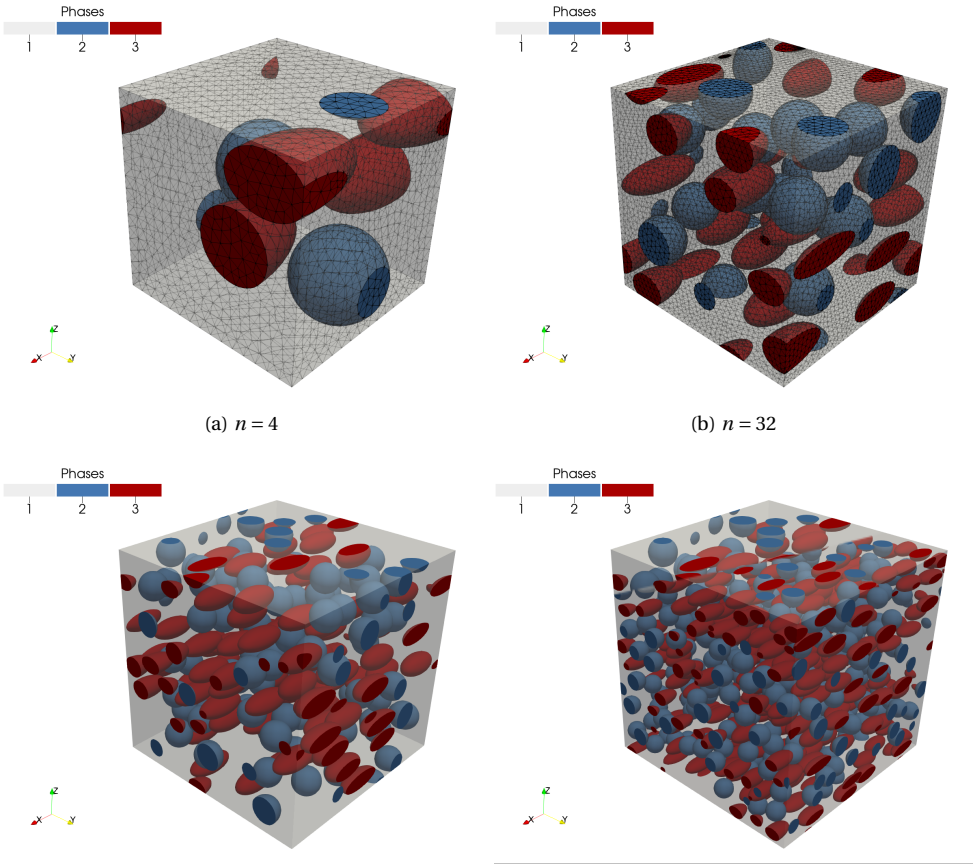

(a) $n = 4$ (b) $n = 32$

(c) $n = 178$ (d) $n = 562$

Figure 7.79: Microstructures containing (a): 4, (b): 32, (c):178 and (d):562 particles including two particle phases, Phase 2 containing Spheres of the same size at vf = 0.1 and Phase 3 containing Ellipsoids with the largest principal axis oriented along xx at vf = 0.1. The TETRA10 nonconform mesh is only represented for (a) and (b) (only the vertex nodes shown).

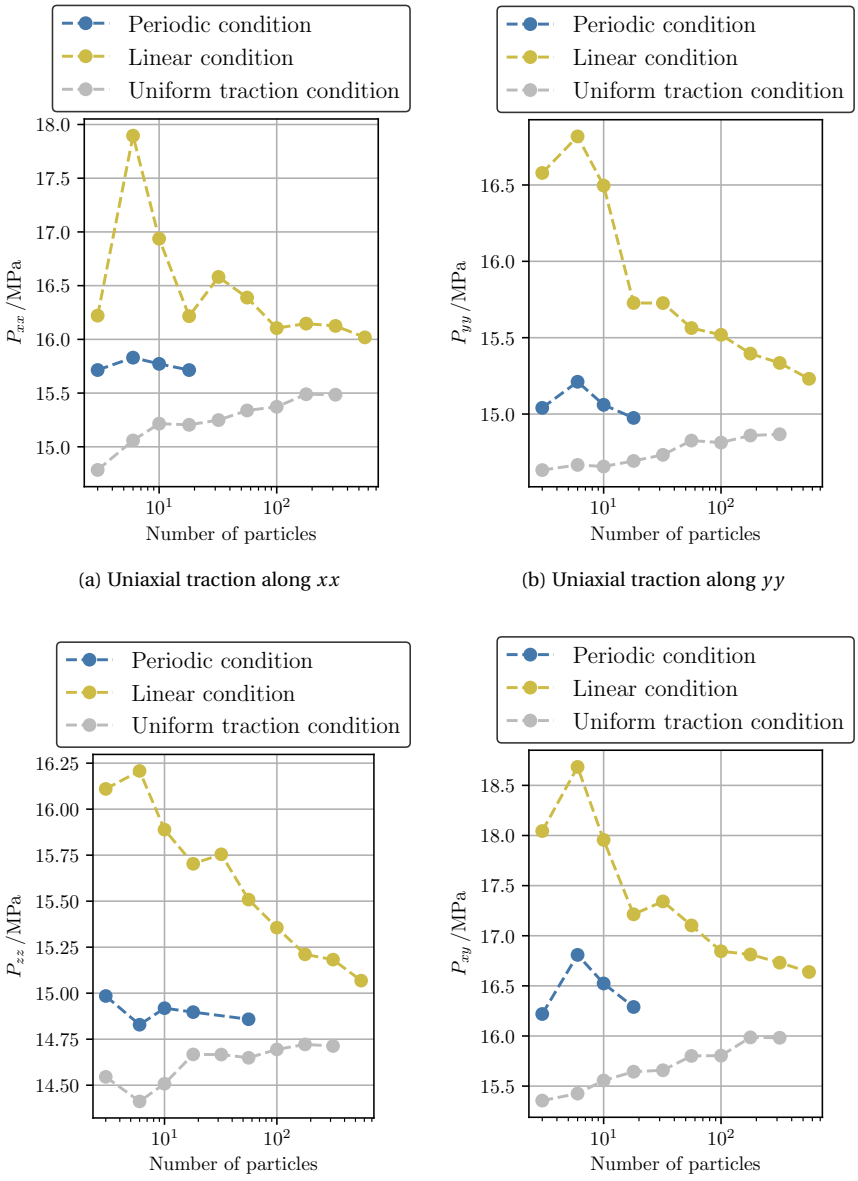

(a) Uniaxial traction along xx

(b) Uniaxial traction along yy

(c) Uniaxial traction along zz

(d) Simple shear across xy

Figure 7.80: Homogenized first Piola-Kirchhoff stress for various loading schemes ((a): uniaxial traction along xx - P_{xx}, (b): uniaxial traction along yy - P_{yy}, (c): uniaxial traction along zz - P_{zz}, (d): simple shear across xy - P_{xy}) as a function of the number of particles, for microstructures including two particle phases, Phase 2 containing Spheres of the same size at vf = 0.1 and Phase 3 containing Ellipsoids with the largest principal axis oriented along xx at vf = 0.1.

Table 7.26: Homogenized first Piola-Kirchhoff component P_{xx} under uniaxial loading condition along xx for linear, periodic, and uniform traction boundary conditions as a function of the number of particles, for microstructures including two particle phases, Phase 2 containing Spheres of the same size at vf = 0.1 and Phase 3 containing Ellipsoids with the largest principal axis oriented along xx at vf = 0.1. The relative variation with reference to the periodic boundary is also presented as $\varepsilon_{\text{Periodic}}$.

Number of Particles	Linear condition		Periodic condition	U. Traction condition	
	P_{xx} /MPa	$\varepsilon_{\text{Periodic}}$ /%	P_{xx} /MPa	P_{xx} /MPa	$\varepsilon_{\text{Periodic}}$ /%
4	16.22	3.22	15.71	14.78	−5.92
6	17.90	13.05	15.83	15.06	−4.87
10	16.94	7.39	15.77	15.22	−3.53
18	16.22	3.19	15.71	15.20	−3.24
32	16.58	-	-	15.25	-
56	16.39	-	-	15.34	-
100	16.10	-	-	15.37	-
178	16.15	-	-	15.49	-
316	16.13	-	-	15.48	-
562	16.02	-	-	-	-

Table 7.27: Homogenized first Piola-Kirchhoff component P_{yy} under uniaxial loading condition along yy for linear, periodic, and uniform traction boundary conditions as a function of the number of particles, for microstructures including two particle phases, Phase 2 containing Spheres of the same size at vf = 0.1 and Phase 3 containing Ellipsoids with the largest principal axis oriented along xx at vf = 0.1. The relative variation with reference to the periodic boundary is also presented as $\varepsilon_{\text{Periodic}}$.

Number of Particles	Linear condition		Periodic condition	U. Traction condition	
	P_{xx} /MPa	$\varepsilon_{\text{Periodic}}$ /%	P_{xx} /MPa	P_{xx} /MPa	$\varepsilon_{\text{Periodic}}$ /%
4	16.58	10.23	15.04	14.63	−2.71
6	16.82	10.56	15.21	14.67	−3.58
10	16.50	9.53	15.06	14.66	−2.68
18	15.73	5.03	14.97	14.69	−1.88
32	15.73	-	-	14.73	-
56	15.56	-	-	14.83	-
100	15.52	-	-	14.81	-
178	15.40	-	-	14.86	-
316	15.33	-	-	14.87	-
562	15.23	-	-	-	-

Table 7.28: Homogenized first Piola-Kirchhoff component P_{zz} under uniaxial loading condition along zz for linear, periodic, and uniform traction boundary conditions as a function of the number of particles, for microstructures including two particle phases, Phase 2 containing Spheres of the same size at vf = 0.1 and Phase 3 containing Ellipsoids with the largest principal axis oriented along xx at vf = 0.1. The relative variation with reference to the periodic boundary is also presented as $\varepsilon_{\text{Periodic}}$.

Number of Particles	Linear condition		Periodic condition	U. Traction condition	
	P_{xx} /MPa	$\varepsilon_{\text{Periodic}}$ /%	P_{xx} /MPa	P_{xx} /MPa	$\varepsilon_{\text{Periodic}}$ /%
4	16.11	7.51	14.98	14.55	−2.93
6	16.21	9.30	14.83	14.41	−2.81
10	15.89	6.50	14.92	14.51	−2.75
18	15.70	5.41	14.90	14.67	−1.54
32	15.75	-	-	14.67	-
56	15.51	4.38	14.86	14.65	−1.41
100	15.36	-	-	14.69	-
178	15.21	-	-	14.72	-
316	15.18	-	-	14.71	-
562	15.07	-	-	-	-

Table 7.29: Homogenized first Piola-Kirchhoff component P_{xx}, P_{yy} and P_{zz} under uniaxial loading condition along xx, yy and zz, respectively, for linear boundary conditions as a function of the number of particles, for microstructures including two particle phases, Phase 2 containing Spheres of the same size at vf = 0.1 and Phase 3 containing Ellipsoids with the largest principal axis oriented along xx at vf = 0.1. The relative variation with reference to the homogenized first Piola-Kirchhoff component P_{xx} under uniaxial loading condition along xx is also presented as ε_{xx}.

Number of Particles	Uniaxial traction along x	Uniaxial traction along y		Uniaxial traction along z	
	P_{xx} /MPa	P_{yy} /MPa	ε_{xx} /%	P_{zz} /MPa	ε_{xx} /%
4	16.221	16.579	−2.207	16.110	0.682
6	17.896	16.818	6.023	16.208	9.433
10	16.937	16.496	2.604	15.889	6.190
18	16.216	15.727	3.015	15.703	3.164
32	16.581	15.727	5.153	15.755	4.984
56	16.389	15.563	5.038	15.508	5.372
100	16.105	15.519	3.640	15.356	4.650
178	16.147	15.396	4.650	15.211	5.794
316	16.125	15.334	4.903	15.182	5.847
562	16.019	15.231	4.918	15.068	5.933

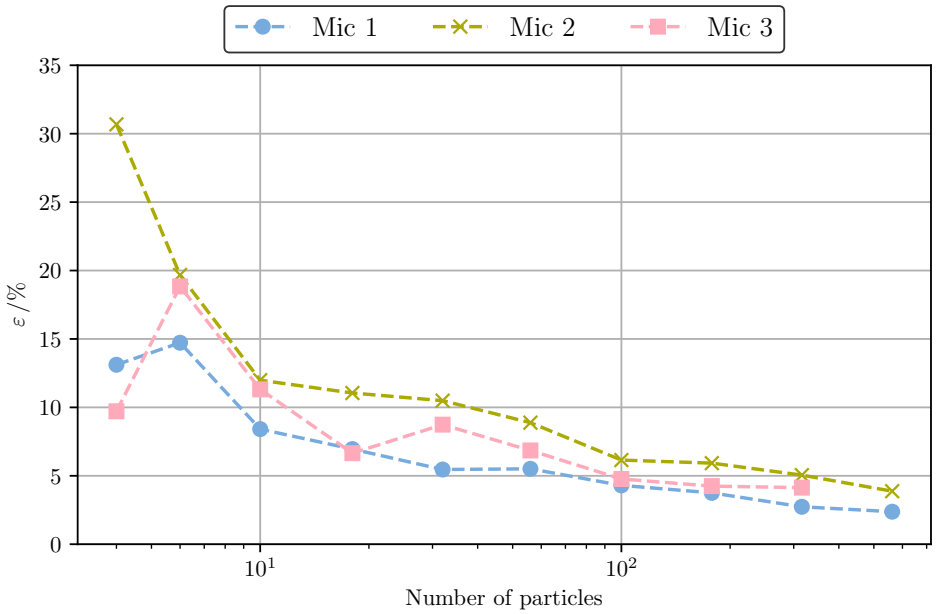

Figure 7.81: Relative variation of the homogenized first Piola-Kirchhoff P_{xx} under uniaxial loading along xx between the linear and uniform traction boundary conditions, with reference to the latter, as a function of the number of particles. Microstructure 1 includes one particle phase containing Spheres of the same size at a volume fraction equal to 0.2. Microstructure 2 includes three particle phases containing Spheres of the same size, Phase 2 at a volume fraction of 0.075, Phase 3 at a volume fraction of 0.025 and Phase 4 at a volume fraction 0.1. Microstructure 3 comprises two particle phase. Phase 2 containing Spheres of the same size at a volume fraction equal to 0.1 and Phase 3 containing Ellipsoids at a volume fraction equal to 0.1 oriented along xx.

Discussion

The results presented in Figure 7.80 regarding the stiffness of the response as a function of the boundary condition used are as expected, with the linear boundary condition leading to a stiffer behavior, the uniform boundary traction leading to a more flexible behavior and the periodic boundary condition corresponding to an intermediate response. This can be confirmed from the sign of the relative variations in Tables 7.26-7.28.

Regarding the representativity of the RVE, an increasing number of particles leads to a more representative RVE, as can be inferred from the decreasing difference between the corresponding homogenized first Piola-Kirchhoff components in Figure 7.80. A cursory look at Tables 7.18-7.20, 7.22-7.24 and 7.26-7.28 suggests that there is a marked difference in the number of particles needed for the RVE to be representative between all the 3D microstructures considered. Figure 7.81 confirms this and one can conclude that the single particle phase with Spheres of the same size needs less particles for the RVE to be representative. On the other hand, from all the 3D microstructures considered, the three particle phase comprised of Spheres of different radii needs the most particles. Such a result is not unexpected, as it contains four different phases while the other microstructures analyzed only contain two and three. The microstructure containing Spheres and Ellipsoids presents intermediate results between the other two.

Concerning isotropy, it can be gathered from Table 7.29 that for all numbers of particles considered the relative variation between the homogenized Piola-Kirchhoff P_{xx} in the uniaxial traction along xx and the homogenized Piola-Kirchhoff P_{yy} in the uniaxial traction along yy hovers around 5%. This is to be expected given the orientation of the Ellipsoids along xx, which leads to the anisotropy detected.

Page intentionally left blank.

Chapter 8

Conclusions and Future Research

8.1 Conclusions

Microstructure generation

The main goal of the present work is the design of a program to generate RVEs ranging from the specification of the input descriptors to the finite element discretization of the spatial domain. The program is implemented in an object-oriented Python framework and it allows for the generation of 2D and 3D RVEs with simple geometrical features, such as Disks, Ellipses, Spheres and Ellipsoids. It also provides the ability to specify the parameters characterizing these geometrical features as fixed values or according to statistical distributions, such as uniform, Gaussian or discrete distributions. An arbitrary number of phases is supported, allowing great flexibility in the modeling of real materials, such as polymer blends.

The proposed approach is based in a molecular dynamics simulation where the initial configuration is created using a Poisson point process for the center of the particles and the repulsive forces between particles are proportional to the overlap area/volume of the particles. The algorithms for the computation of the overlap have been validated providing the correct results. A "self-calibrating" multi-temperature isokinetic scheme is proposed, based on results regarding the behavior of a system of particles under an isokinetic scheme. It is concluded that for a given reference temperature, the system of particles, after some time, achieves equilibrium. This equilibrium is characterized by an oscillatory behavior of the total overlap area/volume of the system around a given mean total overlap area/volume positively correlated with the reference temperature. A higher volume fraction and number of particles also leads to larger mean total overlap areas/volumes. Using a multi-temperature isokinetic scheme allowing always the same number of iterations to achieve equilibrium at each temperature stage, very satisfactory results are found for moderate volume fractions and number of particles. However, this approach fails for higher volume fractions and smaller numbers of particles. The "self-calibrating" multi-temperature scheme is introduced as solution to this problem. It updates the number of iterations that a system is allowed to spend at a given temperature stage, using an uptick in the total overlap area/volume as a sign that the system as reached equilibrium. It is an heuristic rule, based on the fact that after lowering the temperature the total overlap area/volume of the system tends to decrease monotonically, and after reaching equilibrium the total overlap area/volume exhibits an oscillatory behavior.

This proposed scheme is validated generating microstructures with the desired descriptors in a very reasonable time frame. Microstructures containing from 10 to 1000 Disks at volume fractions from 0.1 to 0.8 are created with no overlaps and containing from 10 to 500 Spheres at volume fractions from 0.1 to 0.5 with a maximum total overlap of 1×10^{-10}. Microstructures containing 200 and 500 Spheres at a volume fraction of 0.6 are also generated reliably. For smaller numbers of particles at this volume fraction it is not always possible to find a legal configuration. Regarding the CPU time spent, it is able to generate microstructures containing 500 Disks of the same size at a volume fraction of 0.7 with no overlap in less than 3 mins. Regarding Spheres, it is able to produce microstructures containing 500 Spheres of the same size at a volume fraction of 0.5 with a total overlap smaller than 1×10^{-10} in around 12 mins. Generating microstructures containing Spheres with zero overlap takes unreasonably long, so if microstructures with no overlap containing Spheres are required, it is possible to run the simulation at a slightly higher volume fraction, shrinking the particles at the end. The increase in volume fraction can be negligible, even allowing for a higher maximum total overlap volume than 1×10^{-10}, leading to very small differences in the CPU time spent to generate the microstructure.

In conclusion, the developed program is able to generate microstructures according to the specifications of the user in reasonable time frames.

Microstructure quality

The microstructures generated using the approach put forth are analyzed using the so-called Minkowski structure metrics of their Voronoi cells.

The Minkowski structure metrics are first validated for convex and non-convex polygons, and convex polyhedra, detecting the expected symmetries that characterize the shapes under analysis. Thus, they are able to identify clearly the original shape and are useful in characterizing the Voronoi cells obtained from the generated microstructures.

The typical microstructures containing only Disks and Spheres of the same size at different volume fractions generated by the proposed approach are shown to possess no clustering or ordered arrangement of the particles. This is in contrast to examples provided of pathological microstructures with excess order, that are strongly flagged by the corresponding Minkowski structure metric. Comparing the Minkowski structure metrics for microstructures at different volume fractions, higher volume fractions tend to lead to lower Minkowski structure metrics q_2 and larger Minkowski structure metrics q_6. Despite the histograms of the Minkowski structure metrics for different samples with the same descriptors not looking to dissimilar it is not possible to reach a conclusion regarding a common underlying distribution from the k-sample Anderson-Darling tests performed.

It is also possible to conclude that the Minkowski structure metric q_2 and the corresponding irreducible Minkowski tensor ψ_2 may be useful tools in detecting and characterizing anisotropy, including its direction. This is done analyzing two microstructures with the same volume fraction and number of particles, with one containing only Disks and the other Ellipses aligned according to a specified direction.

In summary, it is shown that the Minkowski structure metrics are a very versatile tool to judge the degree of disorder, colloquially referred to as "randomness", providing reassurance that the RVEs produced mimic the disorderliness observed in real materials.

Microscale analyses based on computational homogenization

Multi-scale analyses based on computational homogenization are performed in three different types of 2D and 3D microstructures, fixing the volume fractions of each phase and increasing the number of inclusions. Each phase is assumed linear and follows the so-called Henky constitutive model. The 2D microstructures considered are a microstructure containing a single particle phase of Disks at a volume fraction of 0.3, a microstructure containing three particle phases of Disks with the same size at volume fractions of 0.1, 0.05 and 0.15, and a microstructure containing two particle phases, one composed of Disks at a volume fraction of 0.1 and another composed of aligned Ellipses at a volume fraction of 0.2. The 3D microstructures analyzed are similar: a microstructure containing a single particle phase of Spheres at a volume fraction of 0.2, a microstructure containing three particle phases of Spheres with the same size at volume fractions of 0.025, 0.075 and 0.1, and a microstructure containing two particle phases, one composed of Spheres at a volume fraction of 0.1 and another composed of aligned Ellipsoids at a volume fraction of 0.1.

The microscale analyses based on computational homogenization performed show the expected behavior as it relates to the representativeness of the RVE, highlighting the need to include a sufficient number of particles in the microstructure so that the RVE represents the behavior of the material in an average sense. It is also possible to conclude that for the 2D microstructures examined the same number of particles is needed to achieve a representative RVE. However, for the 3D microstructures studied, the microstructure containing only a single particle phase is shown to need less particles and the microstructure with three different particle phases is shown to need more.

The results regarding isotropy are also in line with what was expected, so that microstructures containing Disks or Spheres when submitted to uniaxial loading along different axis behave in the same manner, as the microstructure comprises more and more particles. The microstructures containing Ellipses and Ellipsoids also perform as expected displaying different responses according to the preferred orientation of the particles.

8.2 Future Research

Despite the objectives set forth in the present MSc thesis being accomplished, some further avenues of research remain that can be addressed in future works. These are listed below along with some brief comments:

Microstructure morphology diversity Under the framework of the proposed program more diverse convex geometrical shapes can be easily added in the future. It also may be of interest to develop approaches allowing for the generation of microstructures with more amorphous structures, that are hard to model using particles with a very precise geometrical definition.

Microstructure generation efficiency Regarding the efficiency of the program put forth there still remain means to improve it, such as more efficient methods for the detection and computation of the interaction between particles. The use of reshuffling techniques can also be an interesting approach to generate efficiently multiple samples with the same descriptors from a first microstructure generated by the proposed program.

Experimental validation Although the present work is purely numerical, it is of great importance to perform experimental validation of the generated microstructures, comparing them to real samples through tools such as the Minkwoski structure metrics.

Microstructure quality analysis Regarding the quality analysis of the generated microstructures using Minkowski structure metrics, it remains to establish a clear set of criteria allowing one to make a distinction between disorderly, and so desirable, microstructures and clustered and overly orderly microstructures, and to link this to the representativeness or lack thereof of such RVEs.

Bibliography

Apostol, T.
1969. *Calculus. Vol. II: Multi-variable Calculus and Linear Algebra, with Applications to Differential Equations and Probability*, Blaisdell international textbook series. Xerox College Publ.

Balzani, D., L. Scheunemann, D. Brands, and J. Schröder
2014. Construction of two-and three-dimensional statistically similar rves for coupled micro-macro simulations. *Computational Mechanics*, 54(5):1269–1284.

Bargmann, S., B. Klusemann, J. Markmann, J. E. Schnabel, K. Schneider, C. Soyarslan, and J. Wilmers
2018. Generation of 3d representative volume elements for heterogeneous materials: A review. *Progress in Materials Science*, 96:322–384.

Bärwinkel, S., A. Seidel, S. Hobeika, R. Hufen, M. Mörl, and V. Altstädt
2016. Morphology formation in pc/abs blends during thermal processing and the effect of the viscosity ratio of blend partners. *Materials*, 9(8):659.

Bennett, C. H.
1972. Serially deposited amorphous aggregates of hard spheres. *Journal of applied physics*, 43(6):2727–2734.

Bernard, E. P. and W. Krauth
2011. Two-step melting in two dimensions: First-order liquid-hexatic transition. *Physical review letters*, 107(15):155704.

Bernard, E. P., W. Krauth, and D. B. Wilson
2009. Event-chain monte carlo algorithms for hard-sphere systems. *Physical Review E*, 80(5):056704.

Bessa, M., R. Bostanabad, Z. Liu, A. Hu, D. W. Apley, C. Brinson, W. Chen, and W. K. Liu
2017. A framework for data-driven analysis of materials under uncertainty: Countering the curse of dimensionality. *Computer Methods in Applied Mechanics and Engineering*, 320:633–667.

Blanco, P. J., P. J. Sánchez, E. A. de Souza Neto, and R. A. Feijóo
2016. Variational foundations and generalized unified theory of rve-based multiscale models. *Archives of Computational Methods in Engineering*, 23(2):191–253.

Boltzmann, L.
1995. *Lectures on Gas Theory*, Dover Books on Physics. Dover Publications.

Buryachenko, V., N. Pagano, R. Kim, and J. Spowart
2003. Quantitative description and numerical simulation of random microstructures of composites and their effective elastic moduli. *International journal of solids and structures*, 40(1):47–72.

Catalanotti, G.
2016. On the generation of rve-based models of composites reinforced with long fibres or spherical particles. *Composite Structures*, 138:84–95.

Cover, T. and J. Thomas
2012. *Elements of Information Theory*. Wiley.

de Souza Neto, E. and R. Feijóo
2006. Variational foundations of multi-scale constitutive models of solid: small and large strain kinematical formulation. *LNCC Research & Development Report*, 16.

de Souza Neto, E. and R. Feijóo
2008. On the equivalence between spatial and material volume averaging of stress in large strain multi-scale solid constitutive models. *Mechanics of materials*, 40(10):803–811.

de Souza Neto, E., D. Peric, and D. Owen
2011a. *Computational Methods for Plasticity: Theory and Applications*. Wiley.

de Souza Neto, E. A., R. A. Feijóo, and A. Novotny
2011b. Variational foundations of large strain multiscale solid constitutive models: kinematical formulation. *Advanced computational materials modeling: from classical to multi-scale techniques-scale techniques*.

Dixon, P. M.
2002. *Encyclopedia of Environmetrics*, chapter Ripley's K function, Pp. Volume 3, pp 1796–1803. John Wiley & Sons.

Donev, A., S. Torquato, and F. H. Stillinger
2005a. Neighbor list collision-driven molecular dynamics simulation for non-spherical hard particles. I. Algorithmic details. *Journal of computational physics*, 202(2):737–764.

Donev, A., S. Torquato, and F. H. Stillinger
2005b. Neighbor list collision-driven molecular dynamics simulation for nonspherical hard particles.: II. Applications to ellipses and ellipsoids. *Journal of Computational Physics*, 202(2):765 – 793.

Drugan, W. and J. Willis
1996. A micromechanics-based nonlocal constitutive equation and estimates of representative volume element size for elastic composites. *Journal of the Mechanics and Physics of Solids*, 44(4):497–524.

Feng, Y., K. Han, and D. Owen
2002. An advancing front packing of polygons, ellipses and spheres. In *Discrete Element Methods: Numerical Modeling of Discontinua*, Pp. 93–98.

Feng, Y., K. Han, and D. Owen
2003. Filling domains with disks: an advancing front approach. *International journal for numerical methods in engineering*, 56(5):699–713.

Folgar, F. and C. L. Tucker III
1984. Orientation behavior of fibers in concentrated suspensions. *Journal of reinforced plastics and composites*, 3(2):98–119.

Fowler, R. J., M. S. Paterson, and S. L. Tanimoto
1981. Optimal packing and covering in the plane are np-complete. *Information processing letters*, 12(3):133–137.

Frenkel, D. and B. Smit
2001. *Understanding Molecular Simulation: From Algorithms to Applications*, Computational science. Elsevier Science.

Fullwood, D. T., S. R. Niezgoda, and S. R. Kalidindi
2008. Microstructure reconstructions from 2-point statistics using phase-recovery algorithms. *Acta Materialia*, 56(5):942–948.

Gaiselmann, G., D. Froning, C. Tötzke, C. Quick, I. Manke, W. Lehnert, and V. Schmidt
2013. Stochastic 3d modeling of non-woven materials with wet-proofing agent. *International Journal of Hydrogen Energy*, 38(20):8448 – 8460.

Ghossein, E. and M. Lévesque
2013. Random generation of periodic hard ellipsoids based on molecular dynamics: A computationally-efficient algorithm. *Journal of Computational Physics*, 253:471–490.

He, D. and N. Ekere
2001. Structure simulation of concentrated suspensions of hard spherical particles. *AIChE journal*, 47(1):53–59.

Hifi, M. and R. M'hallah
2009. A literature review on circle and sphere packing problems: Models and methodologies. *Advances in Operations Research*, 2009.

Hill, R.
1963. Elastic properties of reinforced solids: some theoretical principles. *Journal of the Mechanics and Physics of Solids*, 11(5):357–372.

Hojo, M., M. Mizuno, T. Hobbiebrunken, T. Adachi, M. Tanaka, and S. K. Ha
2009. Effect of fiber array irregularities on microscopic interfacial normal stress states of transversely loaded ud-cfrp from viewpoint of failure initiation. *Composites Science and Technology*, 69(11-12):1726–1734.

Hughes, G. B. and M. Chraibi
2012. Calculating ellipse overlap areas. *Computing and visualization in science*, 15(5):291–301.

Ilin, D. and M. Bernacki
2016. A new algorithm for dense ellipse packing and polygonal structures generation in context of fem or dem. *MATEC Web of Conferences*, 80:02004.

Javid, F., P. Wang, A. Shanian, and K. Bertoldi
2016. Architected materials with ultra-low porosity for vibration control. *Advanced materials*, 28(28):5943–5948.

Jiao, Y. and N. Chawla
2014. Modeling and characterizing anisotropic inclusion orientation in heterogeneous material via directional cluster functions and stochastic microstructure reconstruction. *Journal of Applied Physics*, 115(9):093511.

Jodrey, W. and E. Tory
1985. Computer simulation of close random packing of equal spheres. *Physical Review A*, 32(4):2347–2351. cited By 373.

Júnior, B. A., P. R. Pinheiro, R. D. Saraiva, and P. G. C. D. Pinheiro
2014. Dealing with nonregular shapes packing. *Mathematical Problems in Engineering*, 2014.

Kansal, A. R., S. Torquato, and F. H. Stillinger
2002. Diversity of order and densities in jammed hard-particle packings. *Physical Review E*, 66(4):041109.

Kapfer, S., M. Klatt, and F. Schaller
2020. Minkowski Functionals: Robust and Versatile Shape Descriptors. https://morphometry.org. Accessed: 2020-02-30.

Kapfer, S. C., W. Mickel, K. Mecke, and G. E. Schröder-Turk
2012. Jammed spheres: Minkowski tensors reveal onset of local crystallinity. *Physical Review E*, 85(3):030301.

Klatt, M. A., G. Last, K. Mecke, C. Redenbach, F. M. Schaller, and G. E. Schröder-Turk
2017. Cell shape analysis of random tessellations based on minkowski tensors. In *Tensor Valuations and Their Applications in Stochastic Geometry and Imaging*, Pp. 385–421. Springer.

Krauth, W.
2006. *Statistical Mechanics: Algorithms and Computations*, EBSCO ebook academic collection. OUP Oxford.

Lamberg, L. and M. Kaasalainen
2001. Numerical solution of the minkowski problem. *Journal of computational and applied mathematics*, 137(2):213–227.

Lombardo, B. S., H. Keskkula, and D. Paul
1994. Influence of abs type on morphology and mechanical properties of pc/abs blends. *Journal of applied polymer science*, 54(11):1697–1720.

Louis, P. and A. M. Gokhale
1995. Application of image analysis for characterization of spatial arrangements of features in microstructure. *Metallurgical and Materials Transactions A*, 26(6):1449–1456.

Lovrić, J., S. Kaliman, W. Barfuss, G. E. Schröder-Turk, and A.-S. Smith
2019. Geometric effects in random assemblies of ellipses. *Soft matter*, 15(42):8566–8577.

Lubachevsky, B. D. and F. H. Stillinger
1990. Geometric properties of random disk packings. *Journal of statistical Physics*, 60(5-6):561–583.

Lubachevsky, B. D., F. H. Stillinger, and E. N. Pinson
1991. Disks vs. spheres: Contrasting properties of random packings. *Journal of Statistical Physics*, 64(3-4):501–524.

Melro, A. R.
2011. *Analytical and numerical modelling of damage and fracture of advanced composites*. PhD thesis, Faculdade de Engenharia da Universidade do Porto.

Mickel, W., S. C. Kapfer, G. E. Schröder-Turk, and K. Mecke
2013. Shortcomings of the bond orientational order parameters for the analysis of disordered particulate matter. *The Journal of Chemical Physics*, 138(4):044501.

Miranda, H. D.
2015. *Computational Generation and Homogenization of Random Close Packed Materials*. PhD thesis, Faculty of Engineering, University of Porto.

Mościński, J., M. Bargieł, Z. A. Rycerz, and P. W. M. Jacobs
1989. The force-biased algorithm for the irregular close packing of equal hard spheres. *Molecular Simulation*, 3(4):201–212.

Oliveira, J. F., A. M. Gomes, and J. S. Ferreira
2000. Topos–a new constructive algorithm for nesting problems. *OR-Spektrum*, 22(2):263–284.

Pathan, M., V. Tagarielli, S. Patsias, and P. Baiz-Villafranca
2017. A new algorithm to generate representative volume elements of composites with cylindrical or spherical fillers. *Composites Part B: Engineering*, 110:267–278.

Perić, D., E. de Souza Neto, R. Feijóo, M. Partovi, and A. C. Molina
2011. On micro-to-macro transitions for multi-scale analysis of non-linear heterogeneous materials: unified variational basis and finite element implementation. *International Journal for Numerical Methods in Engineering*, 87(1-5):149–170.

Perram, J. W. and M. Wertheim
1985. Statistical mechanics of hard ellipsoids. i. overlap algorithm and the contact function. *Journal of Computational Physics*, 58(3):409–416.

Pyrz, R.
1994. Correlation of microstructure variability and local stress field in two-phase materials. *Materials Science and Engineering: A*, 177(1-2):253–259.

Roberts, A. P.
1997. Statistical reconstruction of three-dimensional porous media from two-dimensional images. *Physical Review E*, 56(3):3203.

Saeb, S., P. Steinmann, and A. Javili
2016. Aspects of computational homogenization at finite deformations: a unifying review from reuss' to voigt's bound. *Applied Mechanics Reviews*, 68(5).

Salnikov, V., D. Choï, and P. Karamian-Surville
2015. On efficient and reliable stochastic generation of rves for analysis of composites within the framework of homogenization. *Computational Mechanics*, 55(1):127–144.

Schaller, F. M., S. C. Kapfer, M. E. Evans, M. J. Hoffmann, T. Aste, M. Saadatfar, K. Mecke, G. W. Delaney, and G. E. Schröder-Turk
2013. Set voronoi diagrams of 3d assemblies of aspherical particles. *Philosophical Magazine*, 93(31-33):3993–4017.

Sedgewick, R. and K. Wayne
2011. *Algorithms*. Addison-Wesley.

Segurado, J. and J. Llorca
2002. A numerical approximation to the elastic properties of sphere-reinforced composites. *Journal of the Mechanics and Physics of Solids*, 50(10):2107 – 2121.

Smirnov, S. A. and V. V. Voloshinov
2018. Packing of circles on square flat torus as global optimization of mixed integer nonlinear problem. *arXiv preprint arXiv:1809.10525*.

Şopu, D., C. Soyarslan, B. Sarac, S. Bargmann, M. Stoica, and J. Eckert
2016. Structure-property relationships in nanoporous metallic glasses. *Acta materialia*, 106:199–207.

Steinhardt, P. J., D. R. Nelson, and M. Ronchetti
1983. Bond-orientational order in liquids and glasses. *Physical Review B*, 28(2):784.

Tahmasebi, P. and M. Sahimi
2013. Cross-correlation function for accurate reconstruction of heterogeneous media. *Physical review letters*, 110(7):078002.

Torquato, S.
2013. *Random Heterogeneous Materials: Microstructure and Macroscopic Properties*, Interdisciplinary Applied Mathematics. Springer New York.

Torquato, S., T. M. Truskett, and P. G. Debenedetti
2000. Is random close packing of spheres well defined? *Physical review letters*, 84(10):2064.

Trias, D., J. Costa, J. Mayugo, and J. Hurtado
2006. Random models versus periodic models for fibre reinforced composites. *Computational materials science*, 38(2):316–324.

Tuckerman, M.
2010. *Statistical Mechanics: Theory and Molecular Simulation*, Oxford Graduate Texts. OUP Oxford.

Uspensky, V.
2009. *Four algorithmic faces of randomness*. MCCME Publishers.

Vaughan, T. and C. McCarthy
2010. A combined experimental–numerical approach for generating statistically equivalent fibre distributions for high strength laminated composite materials. *Composites Science and Technology*, 70(2):291 – 297.

Walkington, W. and N. A. D. C. Association
2003. *Gas Porosity: A Guide to Correcting the Problems*, Publication (North American Die Casting Association). North American Die Casting Association.

Wang, W., J. Wang, and M.-S. Kim
2001. An algebraic condition for the separation of two ellipsoids. *Computer Aided Geometric Design*, 18(6):531 – 539.

Wang, X., J. Gong, A. An, K. Zhang, and Z. Nie
2019. Random generation of convex granule packing based on weighted voronoi tessellation and cubic-polynomial-curve fitting. *Computers and Geotechnics*, 113:103088.

Zinchenko, A. Z.
1994. Algorithm for random close packing of spheres with periodic boundary conditions. *Journal of Computational Physics*, 114(2):298–307.